

The role of fractured terrain on comet 67P for nucleus thermophysics and activity

Von der Fakultät für Elektrotechnik, Informationstechnik, Physik
der Technischen Universität Carolo-Wilhelmina zu Braunschweig

zur Erlangung des Grades eines Doktors
der Naturwissenschaften (Dr. rer. nat.)

genehmigte Dissertation

von Sebastian Höfner

aus München

eingereicht am: 22.11.2021

Disputation am: 12.05.2022

1. Referent: Prof. Dr. Jürgen Blum
2. Referentin: Prof. Dr. Jessica Agarwal

Druckjahr: 2023

Cover Figure: Nucleus of comet 67P/ Churyumov-Gerasimenko on 31st of July 2015, imaged by OSIRIS on Rosetta at a distance of 197 km to the centre of the nucleus. OSIRIS Image Reference:
NAC_2015-07-31T09.49.29.649Z_ID20_1397549400_F22

Dissertation an der Technischen Universität Braunschweig,
Fakultät für Elektrotechnik, Informationstechnik, Physik

1. Referent: Prof. Dr. Jürgen Blum
2. Referentin: Prof. Dr. Jessica Agarwal

eingereicht am: 22.11.2021
Disputation am: 12.05.2022
Druckjahr: 2023

ISBN 978-3-00-075352-7

©Sebastian Höfner

Printed by: <https://www.sdl-online.de>

Printed in Germany

Contents

Summary	7
Zusammenfassung	9
1 Cometary exploration	11
1.1 The fascination of comets	11
1.2 A historical view on knowledge about comets	11
1.2.1 Understanding the nature of comets: From portentous interpretation to scientific explanations	11
1.2.2 Scientific perception in the 19th century	13
1.2.3 The role and understanding of comets in modern astronomy	13
1.3 Space missions to comets – an overview	15
1.4 The ESA mission Rosetta to comet 67P/Churyumov-Gerasimenko	19
1.4.1 Challenges of a cometary mission	19
1.4.2 The scientific goals of Rosetta	20
1.4.3 Instrumentation on Rosetta	21
1.4.4 OSIRIS - the scientific camera system	21
1.5 Cometary activity - the motivation for this thesis	22
2 A thermal model for the nucleus of comet 67P	25
2.1 The cometary nucleus - a portrait	25
2.1.1 67P - A member of the Jupiter Family Comets	25
2.1.2 Temporal evolution	25
2.1.3 Properties of the nucleus	27
2.1.4 Topographic diversity of 67P	28
2.2 Thermophysical processes of nucleus surfaces	30
2.2.1 Conduction	30
2.2.2 Convection	30
2.2.3 Radiation	31
2.2.4 Insolation	32
2.2.5 Dust mantle heat transport	32
2.2.6 Internal heat sinks and sources	36
2.3 The effect of surface roughness	37
2.3.1 Beaming effect on atmosphereless planetary bodies	37
2.3.2 Surface roughness of comet 67P	39
2.3.3 Modeling surface roughness	40

2.3.4	Heat balance of rough surface patches	43
2.3.5	Temperature maps for rough surfaces	44
2.4	Simple models of surface temperatures	46
2.4.1	Radiative equilibrium model	46
2.4.2	Standard thermal model for planetary bodies	47
2.4.3	Length and time scales of thermal waves	48
2.5	Development of a one dimensional thermal model	49
2.5.1	The impact of orbital parameters	49
2.5.2	Heat capacity of porous agglomerate layers	49
2.5.3	Heat fluxes of a 67P thermal model	50
2.5.4	Orbital and diurnal thermal waves	52
2.5.5	Surface property alteration by impacting objects	55
2.5.6	Model limitations and implications for resolved geometric thermophysical models	56
3	Model application to fractured topographies	59
3.1	Observed fracture morphology and its variety	60
3.1.1	Cometary building blocks or polygonal contraction cracks?	62
3.1.2	Illumination and implications on fracture topography	62
3.2	Parametric fracture geometry and composition	65
3.3	Insolation conditions of fractured terrain	66
3.4	Energy balance in a model fracture	70
3.4.1	Thermophysical model assumptions	70
3.4.2	Heat conductivity in subsurface fracture layers	71
3.4.3	Radiative transport between surfaces facets	71
3.4.4	Absorbed solar irradiation	71
3.4.5	The sublimation front	73
3.4.6	The fracture thermophysical model	73
3.5	Analysis of heat fluxes and temperatures	75
3.5.1	Range of parameter variations	75
3.5.2	Comparison of fractured and flat terrains	75
3.5.2.1	Heat flux characteristics	75
3.5.2.2	Diurnal temperature patterns	77
3.5.3	Resolved fracture geometries	79
3.5.4	Fracture floor size variation	80
3.5.5	Diurnal temperature patterns of ice-free fractures	84
3.5.6	Fracture orientation and solar plane angle	85
3.5.7	Fracture sublimation rates	85
3.5.8	Variation of the sublimation front	89
3.5.9	The influence of heliocentric distance variations	92
3.5.10	Temporal temperature fluctuations and gradients	94
3.5.11	Modeling influence of surface erosion	95
3.6	Conclusions of the parametric fracture analysis	97
3.6.1	Heat trap mechanism of fractures	98
3.6.2	Diffusion and phase-change in porous media	98
3.6.3	Porous agglomerate textures and effective thermal conductivity	99

3.6.4	Thermal inertia of fractured terrains	100
3.6.4.1	Thermal infrared emissions	100
3.6.4.2	Brightness temperature patterns	100
3.6.4.3	Thermal inertia of Philae landing site Abydos	101
3.6.4.4	A solid-state greenhouse effect?	102
3.6.4.5	Influence of illumination on fracture morphology	102
3.6.5	A scenario of fracture evolution	103
4	Model application to a cliff collapse	105
4.1	Outburst characteristics	105
4.2	Topography and evolution of the cliff	106
4.3	Thermophysical analysis of the cliff structure	107
4.3.1	Model of the cliff	107
4.3.2	Cliff illumination	109
4.3.3	Temperatures of the cliff	113
4.3.4	Consequences of sublimation and fracture geometry	114
4.4	Cliff collapse scenarios	116
4.5	Conclusions about the cliff collapse	117
5	Conclusion and Outlook	119
5.1	Main results of thermophysical modelling	119
5.2	Observation of dust jets, activity and erosion	120
5.3	Fractures and cometary activity	121
5.4	Fracture formation and evolution	122
5.5	Outlook	123
	Bibliography	125
	Publications	147
	Acknowledgements	153
	Curriculum Vitae	155

Summary

Cometary nuclei likely preserved the information on physical properties and conditions of planetesimals during the formation of the solar system, and as their remnants, they bear valuable informations about the past. The ESA mission Rosetta to Jupiter Family Comet 67P/Churyumov-Gerasimenko was the first interplanetary probe that performed investigations in an orbit around a cometary nucleus and followed the cometary orbit for more than two years. The scientific camera onboard Rosetta, OSIRIS, delivered images of unprecedented details of a cometary nucleus and its surrounding coma.

Cometary activity, the release of dust particles from the nucleus surface driven by the solar irradiation at low heliocentric distances, and the formation of dust jets are yet not fully understood in respect to the underlying physical mechanisms. This thesis focuses on modelling the thermophysical conditions in the uppermost nucleus layers, and constrains terrain types that may lead to favourable conditions for activity. A thermophysical model of the upper layers of the nucleus of 67P is developed that takes into account conductive and radiative heat transfer through aggregates composed of dust grains, and the sublimation of water ice under a dust mantle. The analysis of comet revolutions around the sun indicates the interplay of a diurnal and an orbital thermal lag that happen on very different time scales and penetration depths of the thermal wave.

OSIRIS images showed the presence of networks of fractured terrain in many regions on the nucleus of 67P. The developed models show that under certain illumination conditions, these fractures act as heat traps; their concave nature making them ideal locations for increased water sublimation rates compared to flat terrain topographies with equivalent properties. Illuminated fractures tend to be generally warmer with smaller diurnal temperature fluctuations in comparison to flat terrain. The rough structure of the fractured terrain leads to a significantly higher inferred surface thermal inertia. Dust mantle quenching effects on sublimation rates are weaker than for flat terrain, and maximum sublimation rates attain higher peak values. These findings are robust to a variety of parameters, such as heliocentric distance, illumination geometry, fracture topography, and the location of volatiles within the fracture. The diurnal peak sublimation rate of water ice located at the bottom of model fractures is enhanced by a factor between 1.2 and 14 compared to icy patches on flat terrain. Dust jet observations, emanating from the surface directly after sunrise and partly even during night times fit to the diurnal sublimation pattern of fractured terrain.

The thermophysical analysis of a cliff collapse, presumably resulting in an outburst which happened shortly before perihelion, indicate that strong illumination on the heavily fractured terrain might have contributed to the weakening of the cliff structures, thus underlining the importance of thermal fracturing for the evolution of cometary nuclei.

Zusammenfassung

Kometen haben Informationen über die physikalischen Eigenschaften und Umgebungsbedingungen von Planetesimalen während der Entstehungsphase des Sonnensystems bewahrt; als deren Überbleibsel konservieren sie wertvolle Informationen über den Ursprung unseres Sonnensystems. Die ESA-Sonde Rosetta zum Kometen 67P/Churyumov-Gerasimenko war die erste interplanetare Mission, die Untersuchungen in der Umlaufbahn eines Kometenkerns durchführte und diesen mehr als zwei Jahre lang verfolgte. OSIRIS, die wissenschaftliche Kamera an Bord von Rosetta, lieferte Aufnahmen in beispielloser Auflösung und Qualität.

Die Aktivität von Kometen, das Loslösen von Staubpartikeln von der Oberfläche durch Sonneneinstrahlung und die Bildung von Fontänen sind hinsichtlich der zugrundeliegenden physikalischen Mechanismen noch nicht vollständig verstanden. Diese Dissertation entwickelt ein thermophysikalisches Modell der oberen Materieschichten von 67P, das die komplexe Wärmeübertragung in Staub- und Eisschichten sowie die Sublimation von Wassereis unter einem kometaren Staubmantel berücksichtigt. Durch die Umlaufbahn um die Sonne und die überlagerte Rotation um seine eigene Achse entstehen thermische Zyklen mit sehr unterschiedlichen Zeitskalen und Eindringtiefen.

Die OSIRIS-Aufnahmen zeigen das Vorhandensein von zerklüftetem und rissigem Gelände in vielen Regionen von 67P. Die Anwendung der in dieser Arbeit entwickelten thermophysikalischen Modelle zeigt, dass Brüche in der Oberfläche bei Beleuchtung als Wärmefallen wirken. Die konkave Morphologie begünstigt erhöhte Sublimationsraten von Wassereis im Vergleich zu flachen Geländetopographien mit gleichwertigen Eigenschaften. Im Inneren sind Risse im Allgemeinen wärmer, weisen zugleich geringere Temperaturschwankungen und eine deutlich höhere thermische Trägheit auf. Lokale Sublimationsraten erreichen höhere Maximalwerte, diese werden durch Sonneneinstrahlung in kürzerer Zeit erreicht. Parametervariationen, wie z.B. Entfernung zur Sonne, Einstrahlungsrichtungen über den Tagesverlauf, Topographie der Rissstrukturen sowie Existenz eines Staubmantels ändern die Tendenz der Analyse nicht. So ist die Sublimationsrate von Wassereis am Rissboden, verglichen mit flachem Gelände um Faktoren zwischen 1,2 und 14 erhöht. Jets, die direkt nach Sonnenaufgang und teilweise sogar während der Nacht von der Oberfläche beobachtet wurden, können mit den entwickelten Modellen besser erklärt werden.

Die thermophysikalische Analyse eines Klippeneinsturzes, der vermutlich zu einer Eruption kurz vor dem Periheldurchgang von 67P führte, deutet darauf hin, dass starke Sonneneinstrahlung zu einer Schwächung der Klippenstrukturen beigetragen haben könnte und unterstreicht damit die Bedeutung von thermisch bedingter Entstehung von Rissstrukturen in der Evolutionsgeschichte der Kometenkerne.

1 Cometary exploration

”Old men and comets have been revered for the same reason: their long beards, and pretenses to foretell events” – *Jonathan Swift*

1.1 The fascination of comets

Apparitions of comets at all times inspired mankind for interpretations, and as such our view on comets has changed through human history. During most of the time, comets were feared to herald and bring inevitable catastrophes. Oddly enough, today’s popular culture still focuses on comets merely as threats - potential impactors on Earth with hazardous implications for life. Today’s scientific community however expects that fundamental questions about the origin of the solar system and the cause for the existence of water and even building blocks of life on Earth can be solved with the investigation of comets.

Beside the impressive and variegating beauty of coma and tail of a comet in the sky, their fascination has an additional aspect: Comets are the only celestial objects that appear irregularly and show a clear evolution and change on timescales of days to months. By doing so, they present a counterbalance to the apparently everlasting lapse of time in the solar system, or even the universe. Cometary activity represents the dynamics of large-scale physical processes, visible for everybody.

1.2 A historical view on knowledge about comets

The history of astronomy is tightly amalgamated with the evolution of knowledge about comets. Curiosity about the nature and orbital behaviour of comets led to a better understanding of the solar system, and contributed to mankind’s perception of objects beyond Earth.

1.2.1 Understanding the nature of comets: From portentous interpretation to scientific explanations

Lacking scientific explanations, many human cultures historically linked comets with harbingers of disasters. The fear of comets reached a maximum after the apparition of C/1618 W1, the ’Great Comet of 1618/19’. It later was often interpreted as forecasting of the Thirty Years’ War and described as terrible comet, e.g. in the left image of Figure 1.2. Ancient sources noted and associated the appearance of short-period comet 1P/Halley



Figure 1.1: Comets in Historical Art. Left: Adoration of the Magi by Giotto di Bondone, eponym of ESA's mission to comet Halley (in Scrovegni Chapel, Padova, 1305) Right: Illustration in Augsburgur Wunderzeichenbuch, around 1552, Augsburg

before the destruction of the Roman city of Pompei by a catastrophic eruption of the Vesuvius volcano, and before the invasion of the British Isles in 1066 AD - to give just a few examples.

First recorded evidence of cometary sightings, when these were described as falling stars, can be dated back until 2500 BC. One of the favourite explanatory models of the Bethlehem star was the appearance of a bright comet; notwithstanding approval to this theory has dwindled over the years. Ancient observation techniques had to deal with the difficulties to distinguish whether a comet is a celestial object, or a phenomenon of the atmosphere. Both Aristotle and Ptolemy expected them to be atmospherical effluvia. Comets, with seemingly erratic trajectories, an unpredictable appearance and their structural diversity of comae and tails did not fit into the well-balanced and mathematically described celestial sphere.

The conception of comets as solar system bodies can be linked with the Copernican Revolution. Regiomontanus first described comets as celestial bodies in 1472 after calculating the distance of comet C/1471 Y1 by using the parallax method (Seargent 2009). Tycho Brahe succeeded in measuring the parallactic deviation of comet C/1577 V1 parallel to the lunar one, and concluding that comets cannot have atmospheric distances. The great sun-grazing comet of 1680 (C/1680 V1) then was the first to be detected by a telescope before becoming visible for the naked eye, and it also became relevant for the study of orbits: George Samuel Doerffels concluded a hyperbolic trajectory from its observations. Isaac Newton verified his theory about gravitation, as a highly elliptical orbit also demonstrated a feasible solution. In 1705, Edmond Halley merged several cometary appearances into the theory of a single cometary body (later named after him 1P/Halley) and successfully predicted its return to the inner solar system and hence visibility for 1758.

Charles Messier, french royal astronomer in the late 18th century, created the famous Messier catalogue of nebular objects that eased systematic observations of far-away astronomical objects – just with the intention to distinguish these celestial objects from comets, of which he detected about 20.



Figure 1.2: From scepticism to scientific exploration. Left: W/1618 V1, the Great Comet of 1618 (Courtesy Ohio State Library); Center: C/1843 D1 in an artists view: Daylight View over Table Bay Showing the Great Comet of 1843 (Charles Piazzi Smyth); Right: C/1858 L1, in: Sketches of Donati's Comet of 1858, by G.P. Bond, engraved by J.W. Watts (in: A popular treatise on comets; J.C. Watson, Philadelphia 1861. Courtesy University of Cambridge).

1.2.2 Scientific perception in the 19th century

The 19th century, with its technological advancements, also saw important progress in understanding the nature of comets. Investigations of short-period comet 2P/Encke, in fact the second comet whose periodicity was proven, revealed its orbital period shortened for every perihelion passage. Orbital perturbations of other planetary bodies could be ruled out, and the only remaining explanatory model involved the action of non-gravitational forces.

Reports about the great comet of 1843 (C/1843 D1) mentioned its extreme brightness that allowed daylight visibility, and a long tail of up to 64 degrees. Its classification as a sungrazing comet raised questions about the origin and physical composition that could survive the extreme thermal loads within the solar atmosphere. The first detailed photograph of filaments and jet-like structures succeeded for comet C/1858 L1 (see Figure 1.2 right), as exposure time and image resolution allowed the detection of several spiralling jets.

The 1880s allowed spectrometry of the constituents of the cometary coma and tail, and hydrocarbon constituents could be detected. Astonishingly, the 1910 return of 1P/Halley again created apprehension: the spectroscopic detection of hydrogen cyanide in its tail which passed Earth made people fear that they would be poisoned.

1.2.3 The role and understanding of comets in modern astronomy

The idea of Whipple (1950) that comets consist of icy conglomerates revolutionised cometary research; for some historians, Whipple marks the beginning of the modern, or at least the contemporary era of cometary research. Whipple's theory delivered explanations

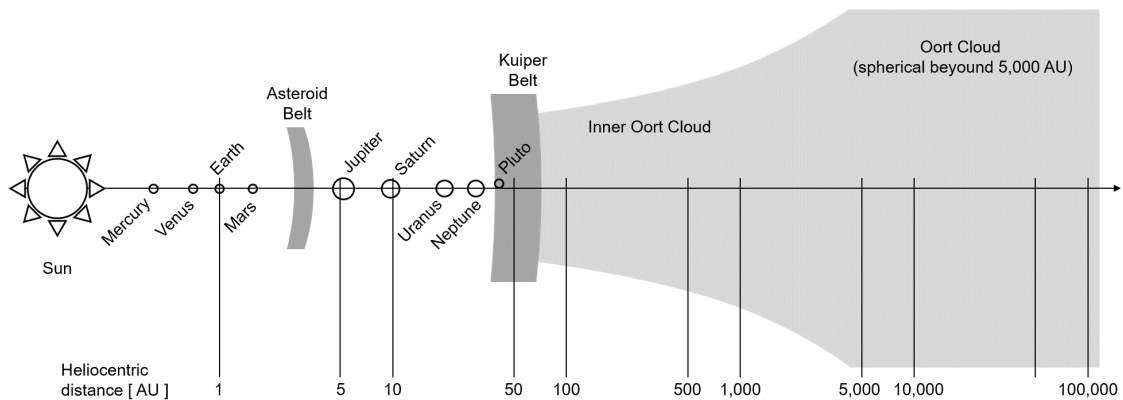


Figure 1.3: Kuiper belt and Oort cloud locations in the solar system, based on illustrations in Schwamb (2014)

for both, non-gravitational forces acting on comets, and the survival of many perihelion passages: The sublimation of volatiles, by definition chemical elements or compounds with a phase transition liquid-vapor at a generally low, e.g. room temperature and subsequent erosion of the nucleus surface creates a momentum that is capable to affect the orbit, due to the relatively small mass of the nucleus. The low heat conductivity prevents the nucleus to reach a thermodynamic equilibrium in its interior which would lead to its disintegration.

The study of comets contributed to various discoveries: The detection of the solar wind as a stream of charged particles originating from the solar corona had been forecast by the behaviour of ionized molecules in the gas tail of comets (Biermann 1951, Parker 1958). This so-called ion tail is directed in anti-solar direction, and deviates from neutral gas and dust tail directions. The space probe Luna 1 measured and confirmed the existence of the solar wind in 1959.

The classification of comets with respect to their orbital parameters, mainly semi-major axis and inclination, revealed new insights about the structure of the solar system. The key question was one about the origin of comets: Due to gravitational perturbations of the gas giants, especially Jupiter, highly elliptical orbits are temporarily unstable and orbital parameters of comets are altered, leading in the end to a removal of comets from the system by scattering them inwards and outwards. The second limiting factor is cometary activity. Erosive processes reduce the mass of comets and affect stability. Break-ups of comets under influence of gravitational field gradients and apparently internal sublimation pressure [e.g. comet C/2012 S1 ISON, Steckloff *et al.* (2015)] have been observed for the gravity field of the sun, but also for Jupiter [the most famous being D/1993 F2 Shoemaker-Levy 9 that collided with Jupiter in 1994, e.g. Solem (1995)] following close encounters. Some Centaur objects, detected in orbits between Jupiter and Neptune, develop a seasonal coma that resembles that of comets. The spectra of several extraordinary dark asteroids suggest they might be inactive former comets, now dead or dormant in activity.

The restricted lifetimes of comets in the inner solar system required the existence of a reservoir of comet replenishment. Three regions in the outer solar system were proposed as source and reservoirs of comets (see Figure 1.3):

1. Oort cloud: The proposal of the Oort cloud (Oort 1950), a region formed as a spher-

ical shell of objects up to 100.000 AU heliocentric distance, dates back to an analysis of the distribution of cometary semi-major axis lengths and orbit inclinations. The Oort cloud is likely the origin of long-period comets, as numerical simulations suggest (Kaib and Quinn 2009).

2. Edgeworth-Kuiper belt: The Kuiper belt (Kuiper 1951) was suggested to be the reservoir of short-period comets, whose orbital revolution times are less than 200 years and hence are unlikely to originate from the Oort cloud (Morbidelli 2005): Gas giants have low gravitational impact in this remote region of the solar system as Kuiper belt objects do not have high elliptical orbits and group around 40 to 55 AU from the sun. The argument in favor for a reservoir is that the orbital inclination of short period comets concentrate around the ecliptic. The assumption of the Kuiper belt as origin for short-period comets was abandoned, as the Kuiper belt is dynamically too stable for comet replenishment.
3. Scattered disk: The scattered disc, embracing more diverse eccentricities than the Kuiper belt and created through the outward motion of Neptune, forms a more suitable source (Duncan and Levison 1997) for short-period comets, and is currently considered as the reservoir from which the short-period comets derive.

Comets play a major role in the evolution of solar system formation models. Trustworthy scenarios need to explain the existence of these mentioned cometary reservoirs and the wealth of cometary orbits, as well as the physical and chemical composition of cometary nuclei. Compatible currently discussed explanatory approaches are the Grand Tack scenario (Walsh *et al.* 2011, Raymond and Morbidelli 2014), and the Nice model, e.g. (Gomes *et al.* 2005, Morbidelli *et al.* 2005, Tsiganis *et al.* 2005, Levison *et al.* 2008).

Due to the small geometric dimensions of cometary nuclei compared to their developed comae and tails, and in combination with the overpowering brightness of the latter, direct measurements by a visiting spacecraft are much more rewarding for the understanding of comets than remote observations: A new era began with the first space probes sent to comets that could resolve the source of all cometary phenomena: the nucleus.

1.3 Space missions to comets – an overview

The 1986 return of comet 1P/Halley offered a great chance for direct investigation of a cometary nucleus, and a fleet (the so-called Halley armada) of spacecraft from several space agencies was launched. The European Space Agency (ESA) mission Giotto, equipped with the Halley Multicolor Camera, obtained the first snapshot of a cometary nucleus (Figure 1.4). Among the peculiarities were the unexpected extremely low albedo of the nucleus (Greenberg 1986), and its apparently inhomogeneous activity: certain areas of the nucleus could be identified as sources of dust jets, while others appeared inert (Keller *et al.* 1986). The Soviet Union Vega programme returned thermal measurements.

Four NASA flyby missions in the early 2000s focused on the exploration of Jupiter-Family comets (JFCs), of which three were successful. The Contour mission which was designated to explore several comets, one of them famous 2P/Encke, experienced a launch failure. Deep Space 1, a technology demonstration mission, imaged 19P/Borelly, the darkest ever visited object of the solar system, with albedo variations between 0.01 and 0.03

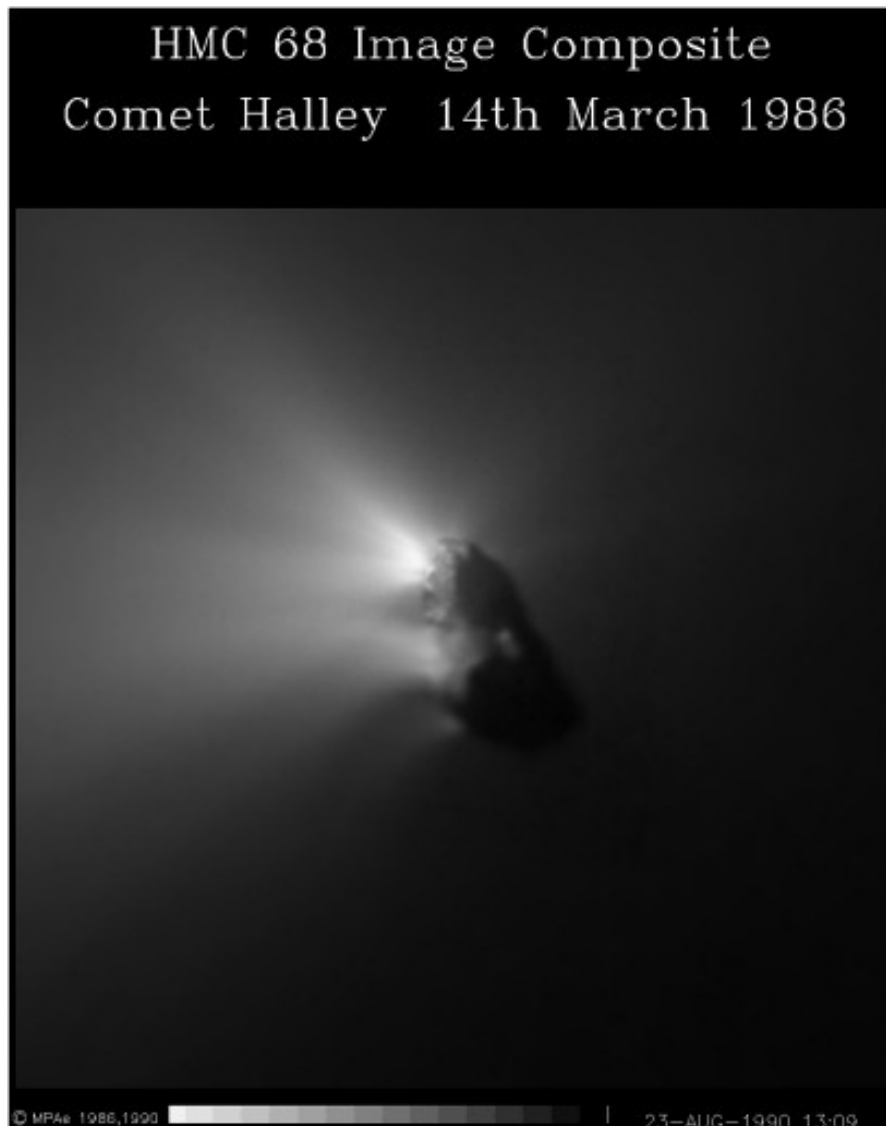


Figure 1.4: (a) Nucleus of comet 1P/Halley, imaged during flyby with the Halley Multi-color Camera. Image credits: ESA, MPAE

(Soderblom *et al.* 2002). The Stardust mission focused on sample return of collected cometary dust. It flew past comet 81P/Wild 2 at a distance of only 236 km and was able to detect coma particles and returned them to Earth in 2006 (Brownlee *et al.* 2004). Stardust images resolved a pitted, crater-like surface morphology that was interpreted to be typical for a comet that only recently (1974) entered the inner solar system.

The Deep Impact mission focused on investigating differences between surface and interior of comet 9P/Tempel 1. The space probe carried a designed penetrating impactor, and its collision with the nucleus of 9P proved the high porosity of the nucleus material (A'Hearn 2005). One orbital revolution later, comet Tempel 1 was visited by the Stardust probe in context of the Stardust-NEXT mission extension (Veverka *et al.* 2013). Image comparison revealed changes on the surface and thus proved surface erosion theories, as detailed in Figure 1.7. The second target of Deep Impact (after mission extension under

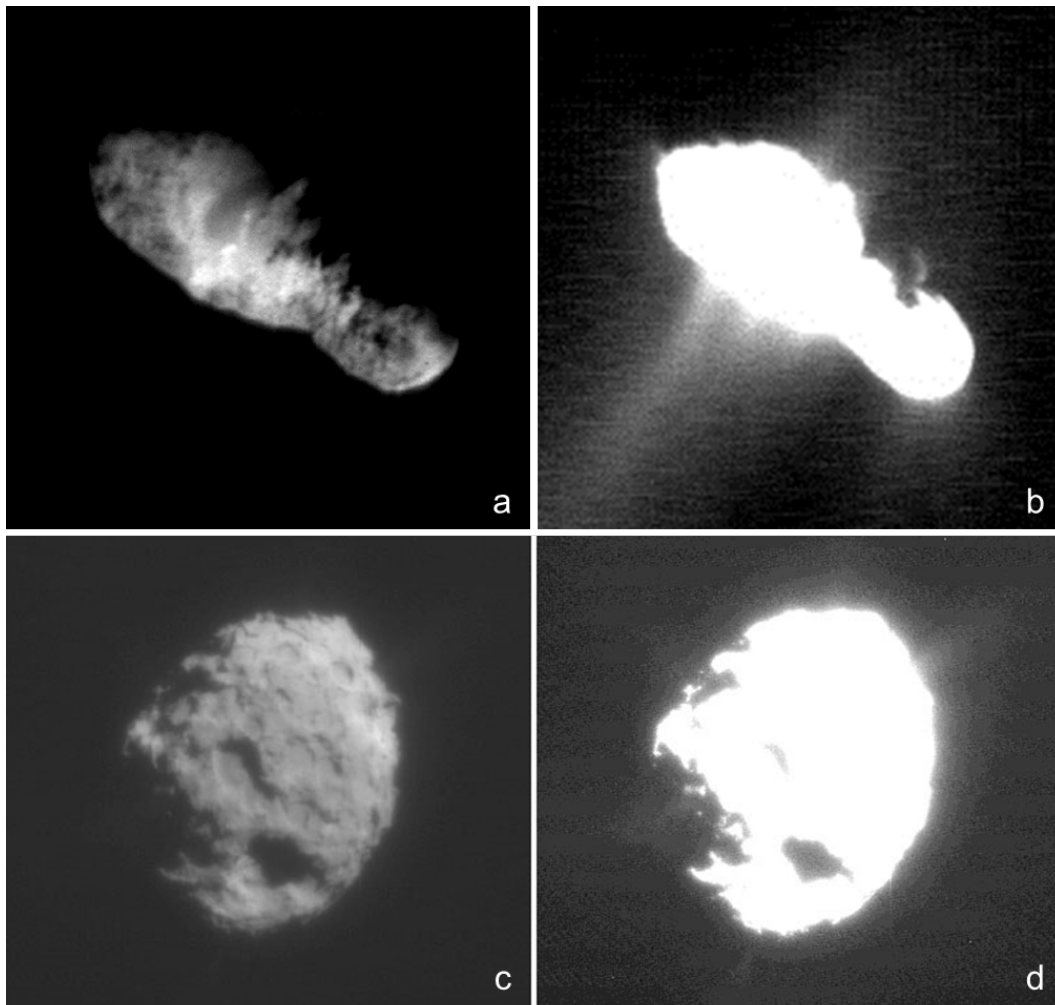


Figure 1.5: (a) Comet 19P/Borelly as imaged during the fly-by of Deep Space 1 (closest approach 2170 km) (b) Dust activity of 19P, visible through image stretching (c) Comet 81P/Wild 2, at a distance of 236 km with approximately 20 m resolution imaged from Stardust (d) Stretched image c to illustrate the presence of the coma. Image credits: NASA, JPL, Stardust team

the name Epoxi) was comet Hartley 2 (103P/Hartley), the smallest nucleus ever visited - and by far the most active. The fly-by at a distance of 700 km showed that the previously unexplainable high water production rate was partly created from icy chunks sublimating in the comet's coma initiated by CO_2 sublimation (A'Hearn *et al.* 2011). The Deep Impact probe observed highly resolved thermal emissions of the surface of both investigated nuclei, and derived temperatures much higher than the sublimation temperature of water ice.

Yet, large groups of comets have not yet been visited from spacecraft – long-period and irregular comets. The problem of investigating previously not detected long-period or comets that enter the inner solar system for the first time is that by the time observatories are able to detect them and constrain their orbit, preparing a space probe is generally too late. Historic observations, as already mentioned in the last sections, were not precise

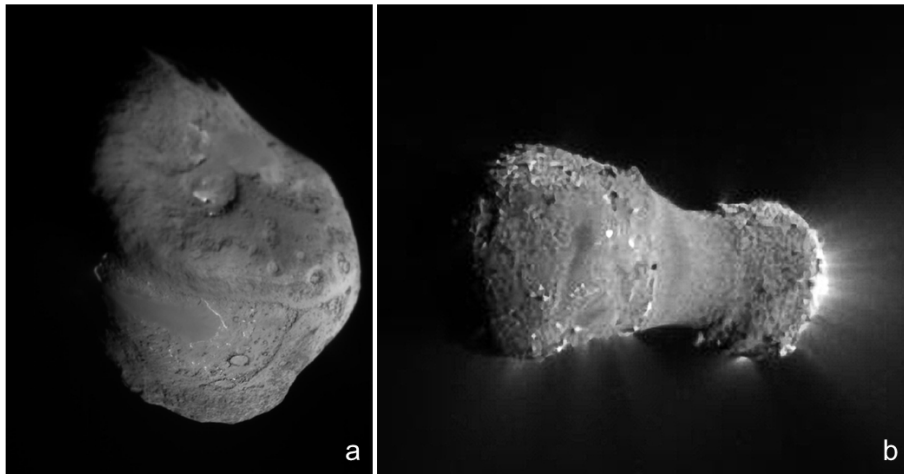


Figure 1.6: (a) Nucleus of comet 9P/Tempel 1, imaged from 3000 km (b) 103P/Hartley imaged from 700 km distance. Both images were acquired by the probe Deep Impact. Image credits: NASA, JPL-Caltech, UM

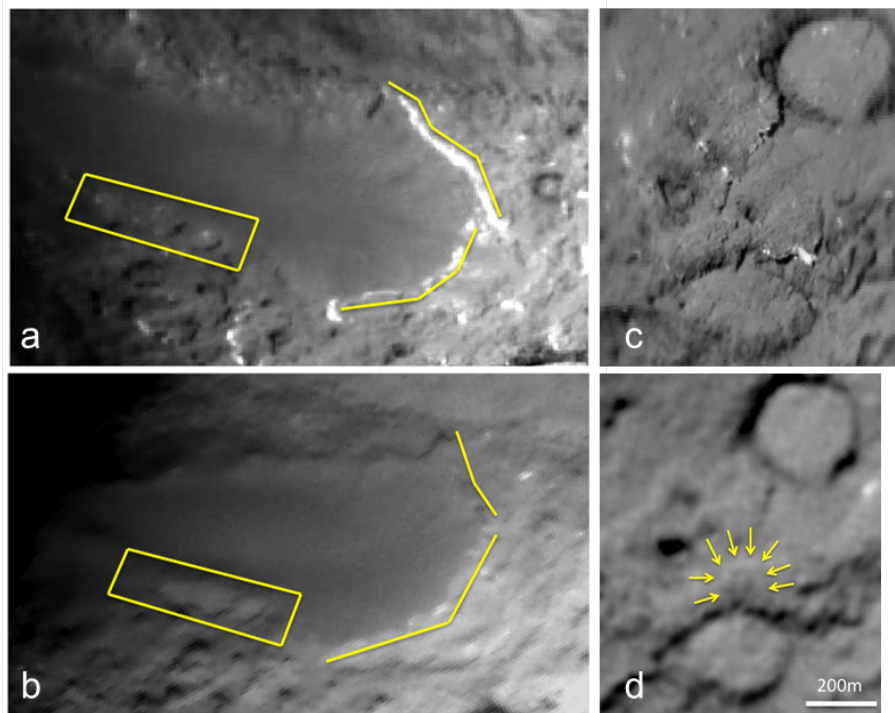


Figure 1.7: Surface changes on comet 9P/Tempel 1 between July 2005 and February 2011. Left: Scarp recession of an apparently smooth flow imaged by Deep Impact (a) and Stardust-NEXT (b). Right: 50 m depression at the impact site crater, seconds before (c) and 5.5 years after (d) the impactor of Deep Impact collided with the nucleus. Image Credits: NASA, JPL, Stardust team, Cornell

enough to derive orbits and reliable reappearance times of those comets. A new ESA mission under preparation, the Comet Interceptor to be launched in 2028, will address this: The mission plans to visit a yet to be newly detected comet, and for this purpose being parked at the Lagrange point L2 until a possible target is within range. With several new comets being detected every year, chances are high that one is within reach of the probe.

1.4 The ESA mission Rosetta to comet 67P/Churyumov-Gerasimenko

The ESA cornerstone mission Rosetta, named after an ancient Egyptian relic, the Rosetta stone that kept a key to decipher hieroglyphics, was a visionary project in several ways: technically, scientifically, and in respect to operations.

1.4.1 Challenges of a cometary mission

All previous missions to comets were high-speed fly-bys, and as such inherently unable to record evolutionary behaviour of the nucleus over more than the limited time of the encounter. Typical flyby velocities ranged between 6 km/s for Epoxi at 103P/Hartley and 70 km/s for Giotto at 1P/Halley. Even for comet 9P/Tempel 1, the single nucleus imaged by two probes, the short observation time allowed snap-shots only and hence revealed limited evidence of morphologic changes and the effect of activity of the nucleus surface.

Several technological challenges have been accepted by ESA, in order to, for the first time in human history, “catch a comet”. To reach the orbit of a comet with today’s launch capabilities, a complicated trajectory with three gravity-assist manoeuvres at Earth, one at Mars and fly-bys at two selected asteroids had to be engineered. Technical uncertainties after the failure of Europe’s top-notch rocket, the Ariane 5 ECA on its maiden flight led to a delay of the launch date of about a year, and forced a reorientation for a different comet. The original target 46P/Wirtanen was out of reach for the complex spacecraft trajectory, and the mission profile had to evolve to allow the encounter with a different comet. ESA then focused on the slightly larger but less active comet 67P; the successful launch took place on 26th of February 2004.

Prior to Rosetta, spacecraft which traveled farther than to the outer frontier of the asteroid belt at approximately 3.4 AU have mostly relied on energy source other than photovoltaics, as solar irradiation in the belt only attains levels between 120 and 280 Wm⁻², about less than one fifth of that in Earth orbital distance. To account for the cold conditions at higher heliocentric distances, the Rosetta probe was put into an hibernation mode, which required a challenging wake-up sequence.

Never before, a probe has been navigated in the vicinity of an active comet, which means low gravity but gas drag influence instead. The operation of Rosetta within a coma of reflecting dust particles confused star trackers that are fundamental for its altitude control. Climax of the mission was the release of the lander Philae, which disembarked towards 67P in November 2014. It touched the comet at the foreseen landing site, but bounced back to finally come to rest under an overhang with limited illumination conditions.

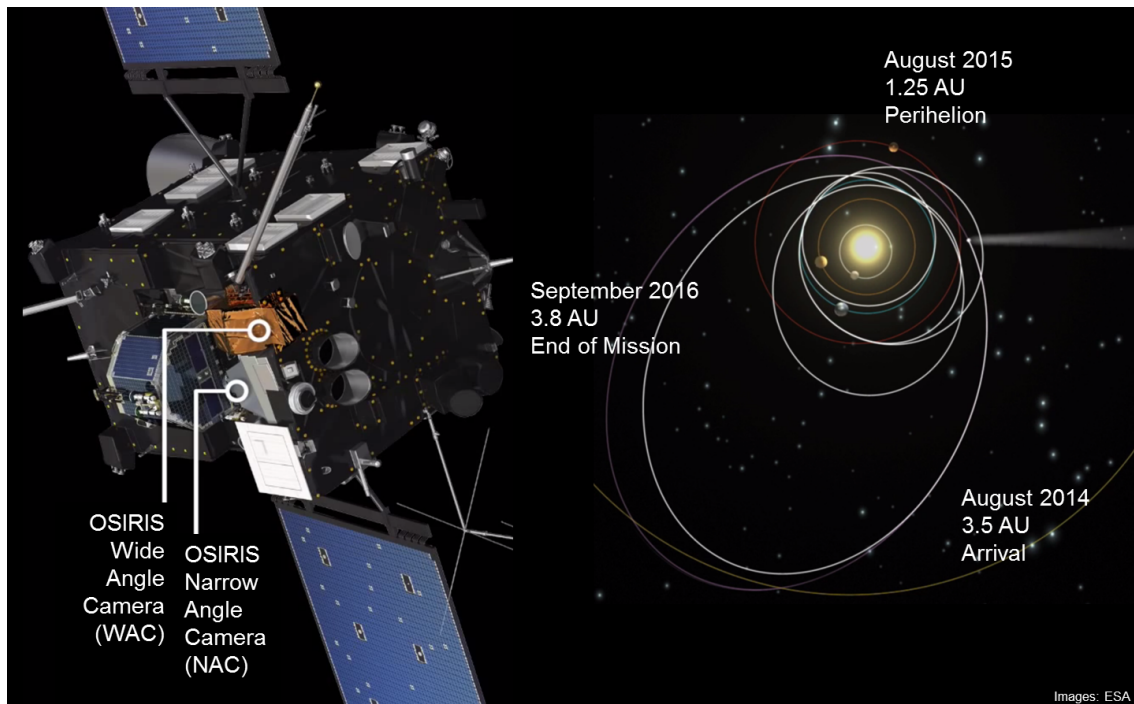


Figure 1.8: Left: Rosetta spacecraft with lander Philae and the location of OSIRIS cameras. Right: Trajectory of the Rosetta mission and the orbit of comet 67P/Churyumov-Gerasimenko. Image credits: ESA

On the way to the target, Rosetta passed the asteroid belt and became the first space mission to deliver resolved images of the asteroids 21 Lutetia and 2867 Steins.

1.4.2 The scientific goals of Rosetta

The scientific tasks of the Rosetta mission included the global characterisation of the cometary nucleus, morphologic diversity, geologic processes and formations, its detailed shape and the establishment of global and local digital terrain models. The physical, chemical and mineralogical properties and the composition of nucleus and coma were determined by orbiter and lander. Rosetta measured key attributes like mass, isotope ratios, and production rates of gases. All these data-intensive investigations were performed partly sequential, partly concurrent since the wake-up of the Rosetta probe in January 2014, arrival at 67P in August 2014, during the perihelion approach in its passage in August 2015 and until the end of the mission in September 2016. By interpreting the data, the scientific community tries to answer prior formulated major scientific questions:

1. Cometary nuclei as solar system formation remnants: Are comets primordial rubble piles (Weissman 1986), or collisional rubble piles (Stern 1988)? Did comets form in gravitational instability or by accretion (Blum *et al.* 2014, Weissman *et al.* 2020)?
2. What is the origin of 67P, under which environmental conditions did comets form (Rubin *et al.* 2015, 2020, Davidsson *et al.* 2016, Fulle *et al.* 2016)? Is our current

understanding of the solar system formation in line, or rather disagreeing with the findings at 67P?

3. What are the physical mechanisms of gas release and dust activity (Vincent *et al.* 2013, Gundlach *et al.* 2015, Blum *et al.* 2017, Vincent *et al.* 2019)? How does a comet 'work' to produce the observed patterns of its coma? Which forces act that particles are removed from the nucleus? What are the driving forces for the formation of dust jets?

Beyond the scientific community, some aspects are of special importance – questions that catch the interest of the general public: Did comets bring water to Earth, transforming it to the blue planet it is today? And did comets deliver building blocks of life, contributing to today's organic diversity?

Beside scientific questions, the Rosetta mission was a giant step for the European Space Agency in respect to its technical heritage.

1.4.3 Instrumentation on Rosetta

To achieve the ambitious scientific goals of the Rosetta mission, 11 instruments were selected, including the lander Philae. The high resolution scientific camera system OSIRIS (Optical, Spectroscopic, and Infrared Remote Imaging System) was the main scientific camera system. The imaging infrared spectrometer VIRTIS (Visible and Infrared Thermal Imaging Spectrometer), and the MIRO (Microwave Instrument for the Rosetta Orbiter) were capable to determine thermal properties. Two scientific camera systems were deployed on the lander Philae, CIVA and ROLIS. Several instruments were capable to collect and measure dust grains, their sizes and composition (GIADA, COSIMA, MIDAS on the orbiter, DIM on the lander). CONSERT (Comet Nucleus Sounding Experiment by Radiowave Transmission) uses a radar connection between orbiter and lander to constrain the nucleus interior. The objective of ALICE (an ultraviolet imaging spectrograph) was to find rare gases in the coma. ROSINA, the Rosetta mass spectrometer, determined the gas composition of the coma of 67P.

The total scientific payload added up to 165 kg on the orbiter. Beside the orbiter, a lander was part of the mission. Rosetta's navigation camera NAVCAM served navigation purposes. In comparison to 11 scientific instruments on Rosetta, the smaller Deep Impact mission comprised of three.

1.4.4 OSIRIS - the scientific camera system

The OSIRIS camera system, built by the Max Planck Institute for Solar System Research, scientific camera system on the orbiter (Keller *et al.* 2007), was a heavy contributor to the scientific payload with its total mass of 35 kg. The OSIRIS instrument consisted of two camera systems, the Wide Angle Camera (WAC) with a field of view (FOV) of 11.9 degrees, and the Narrow Angle Camera (NAC) for high resolution images with a FOV of 2.18 degrees. Both cameras had built-in filter wheels with a selection of bandpass filters. 14 WAC filters aimed mostly for the detection of gas emissions by using narrow bands, while the 11 NAC filters were designed to characterize the nucleus reflectance spectrum. The large focal plane array of OSIRIS of 2048 by 2048 pixels, combined

with a large dynamic range, led to images of unprecedented detail. The NAC angular resolution of $18 \mu\text{rad}/\text{px}^{-1}$ allowed images with a detection capability of around 15 cm at orbital distances of 10 km to the nucleus. The resolution was chosen, as the intended distance of Rosetta to its target aimed to be in the range of a few kilometers. In contrast, flyby cometary missions were restricted to tens of meters spatial resolution despite higher angular resolution properties e.g. Deep Impact (2 to $10 \mu\text{rad}/\text{px}^{-1}$), and mostly due to the higher flyby distances and velocities, strong limitations in data volume. As a consequence, OSIRIS images set a new standard for cometary research.

1.5 Cometary activity - the motivation for this thesis

The term ‘cometary activity’ has an observational background: the detection that the dust and gas coma is created and supplied by material which was removed from the nucleus. The areas with a removal of cometary material are considered active; a general overview of active region characteristics is given in Rickman (2018) and Vincent *et al.* (2019). Ground observations before Rosetta expected the nucleus to consist of areas that are more or less ‘active’, with the active parts being small volatile-rich spots (Lamy *et al.* 2004). Restricted areas of dust and gas emission helped to explain the peculiar features of the coma of a wide variety of comets (Sekanina 1987).

Dust jets are the prevailing image of cometary activity (Vincent *et al.* 2016, Shi *et al.* 2016). They tend to form after short illumination times and last throughout the day, some extend to night times. Outbursts, short-term events, could be constrained by OSIRIS images to exist for short periods in the order of minutes (Vincent *et al.* 2016).

The driving force is the sublimation of volatile components through solar illumination and induced thermal processes. A variety of volatile species have been discovered, with H_2O , CO and CO_2 being the most abundant. The physical mechanisms, especially the theory of sublimation pressure of volatiles overcoming the cohesion of agglomerates in the uppermost layers of a nucleus, do not adequately explain release of observed particle sizes in the dust coma and their patterns (Gundlach *et al.* 2015). The evolution of a cometary coma and sometimes a bright tail, the visibility of comets in the night sky even with naked eyes, created by forces on the level of the constituents of cometary agglomerates of grains - a puzzling quest demanding for its study. This fascination was the starting point for my research and this thesis.

The aim of the thesis is to contribute to a better understanding of the mechanisms of cometary activity, and to constrain conditions likely to lead to the release of dust from the cometary surface. The approach in this thesis is theoretical and focuses on modelling thermophysical processes in the uppermost layers of the cometary nucleus of 67P by specifically looking at topographic surface conditions.

A thermophysical model based on heat transfer in porous media (Gundlach and Blum 2012) is developed to fit to resolved geometries of comet 67P/Churyumov-Gerasimenko. As cometary nuclei have very low thermal inertia (Davidsson *et al.* 2013), radiative heat transfer dominates conduction, and the exposure to the sun in contrast to shadows reveal high temperature differences for topographic patterns on the surface of the nucleus. The OSIRIS cameras, while mapping the entire nucleus, discovered a wide variety of terrains, among them fractured cliffs and networks of furrows. When illuminated, these fractures

act as heat traps like depressions analysed by Colwell *et al.* (1990). The concave terrains accumulate and retain solar radiation and hinder thermal emission towards deep space, leading to higher temperatures than their surroundings. Higher temperatures will evoke higher sublimation rates, if volatiles are present beneath the surface. While this process is known and studied for planetary objects covered with regolith (Lagerros 1996, 1997), it has not been quantitatively derived for comet 67P.

Temperatures and heat fluxes of fractures and furrows on 67P shall be investigated in detail by setting up a geometrically variable, parameterized thermophysical model. The analysis includes self-heating effects through thermal infrared heat transfer, solar illumination patterns, internal conductive fluxes, and sublimation from water ice. By variations of parameters such as illumination angles, location of volatiles, and heliocentric distance, the typical diurnal thermophysical processes and cycles shall be determined, and possible favourable conditions for increased sublimation rates and potential activity shall be identified. The analysis is supported by correlations between observations and computational results, especially acquired from OSIRIS camera observations, and the nucleus properties constrained by several other Rosetta instruments.

Chapter 2 gives an overview on comet 67P and its morphology; it describes the setup of a thermophysical model, discusses its contents, and shows the derived diurnal and orbital thermal waves. Chapter 3 describes the wide range of parameters and cases that are applied to the fractured terrain, presents the findings and their implication, and compares the impact of the heat trap effect to flat topographies. Chapter 4 extends the derived small-scale analysis to a comet wide, full-scale thermophysical model of the nucleus and applies it to a cliff collapse event observed by Rosetta shortly before 67P's perihelion passage. Chapter 5 concludes the findings, emphasizes that there is a very robust heat trap effect that shall impact activity patterns, and gives an outlook.

2 A thermal model for the nucleus of comet 67P

2.1 The cometary nucleus - a portrait

2.1.1 67P - A member of the Jupiter Family Comets

The target comet of the Rosetta mission was discovered in 1969 by Klim Churyumov and Svetlana Gerasimenko and named after them 67P/Churyumov-Gerasimenko. Due to its orbital characteristics, including a moderate elliptical orbit with an eccentricity of 0.64, an orbital period of 6.44 years, and currently an aphelion distance slightly higher than that of Jupiter at 5.45 AU, 67P can be considered a typical Jupiter Family Comet (JFC) (Weissman and Lowry 2008). JFCs originate mostly from the scattered disc (Morbidelli 2005) which contains icy bodies that can be linked to the greater family of transneptunian objects. These relatively small bodies have been formed at distances between 25 and 35 AU; the interference of Neptune dispersed them to a scattered disc (see e.g. Duncan and Levison (1997)) with aphelion distances of up to 100 AU. Consecutive encounters with gas giants shortened the orbital pericenter distance towards the sun, and leading to intermediate stages like the centaur group with similar orbital elements (Tiscareno and Malhotra 2003). The orbital history of 67P can be traced back to the 1840s (Guzzo and Lega 2017), but the nucleus transformed into a JFC long before that. The perihelion of 67P approached the current 1.24 AU in 1959 (Guzzo and Lega 2017, Carusi *et al.* 1985) after a century beyond 2.7 AU. Ten years after the last significant change, 67P was discovered during its second perihelion passage near its closest proximity to the sun in its entire lifetime. In the near future, orbital predictions of 67P (Maquet 2015) indicate that the perihelion passage moves even closer to the sun. After the injection into the inner solar system, cometary evolution accelerates and timescales of changes significantly drop. However, cometary orbits are not stable and orbital perturbations especially by Jupiter induce changes to eccentricity on a regular basis (Maquet 2015).

2.1.2 Temporal evolution

Nucleus temperatures and their spatial, lateral and temporal distribution change significantly during a comet's lifetime. The variety of orbital characteristics define unique boundary conditions, such as rotation rates and insolation, for each comet.

Cometary nuclei undergo significant changes in short timescales during their sojourn in the inner parts of the solar system. Close to the sun, insolation is by far the ruling



Figure 2.1: Nucleus of 67P, taken on 12th of August 2015 at a distance of 331 km from Rosettas OSIRIS NAC. The image shows the famous outburst just before perihelion (Image NAC 2015-08-12T17.35.04.738Z ID20 1397549000 F22)

parameter for nucleus surface temperatures; yet their comparably longer history at high solar distances determines the conditions in the interior. The environment, far away from the sun and partly outside the heliopause, was constantly affected by the remote gravity fields of the solar system gas giants; today it is mostly neptune. The thermal environment at heliocentric distances beyond 40 AU leads to solar irradiation in the order of 1 Wm^{-2} , thus being a small source of energy among others. Surface changes are mostly due to space weathering and high energy particles (Stern 2003), while the effects of impact heating of larger bodies play a minor role due to low impact velocities (Huebner *et al.* 2006). It neither dominates cometary surface evolution nor triggers significant outgassing. Temperatures of small trans-neptunian objects (TNOs) do not deviate from formation temperatures for billions of years (Davidsson *et al.* 2016); the long timescales lead to thermal equilibrium even for low values of thermal conductivity that are expected for pristine material. Outgassing products of 67P include molecular oxygen (Bieler *et al.* 2015a, Mousis *et al.* 2016), nitrogen (Rubin *et al.* 2015) and Argon (Balsiger *et al.* 2015), they all possess low condensation temperatures. Thus, these gases can be trapped in clathrates (postulated to exist in cometary nuclei; highly volatile molecules included in a lattice of less volatile

matter) at very low formation temperatures only. Conclusively, the storage environmental temperature is derived to be below 30 K. In contrast, comets also incorporate elements that should have formed under high temperatures (Bridges *et al.* 2012).

2.1.3 Properties of the nucleus

Two lobes characterize the irregular shape of the nucleus, with its overall dimensions being approximately 4.3 km x 4.1 km x 1.8 km. The density of the nucleus was determined to $(535 \pm 35) \text{ kgm}^{-3}$ (Preusker *et al.* 2015). No abundance of icy areas in at least the upper millimeters of the nucleus could be detected (Gulakis *et al.* 2015). However, water ice is strewn in small localized patches mostly in shadowed areas under cliff structures (Filacchione *et al.* 2016, Pommerol *et al.* 2015), and water vapour forms the main constituent of the gas surrounding the cometary nucleus (Hässig *et al.* 2015).

The thermal inertia of a planetary object is determined by the square root of thermal conductivity, heat capacity and density, and described in detail by Equation 2.41. First MIRO measurements revealed a thermal inertia I of $10\text{-}50 \text{ Jm}^{-2}\text{K}^{-1}\text{s}^{-1/2}$ (Gulakis *et al.* 2015), more detailed and accurate analysis confined this value to $15\text{-}30 \text{ Jm}^{-2}\text{K}^{-1}\text{s}^{-1/2}$ (Schloerb *et al.* 2015). Also values of $120 \text{ Jm}^{-2}\text{K}^{-1}\text{s}^{-1/2}$ (Spohn *et al.* 2015) were found for specific terrain. Further investigations indicate the thermal inertia to be lower or equal to $80 \text{ Jm}^{-2}\text{K}^{-1}\text{s}^{-1/2}$ (Marshall *et al.* 2018). VIRTIS spectrometer data distinguished between the thermal inertia of local terrain morphologies, as dust layered areas exhibit values of $10\text{-}25 \text{ Jm}^{-2}\text{K}^{-1}\text{s}^{-1/2}$, while the rougher terrain revealed $I \geq 50 \text{ Jm}^{-2}\text{K}^{-1}\text{s}^{-1/2}$ (Leyrat *et al.* 2015).

Dust sample measurements by COSIMA (Schulz *et al.* 2015) and GIADA (Fulle *et al.* 2015) detected highly porous particles of sizes up to mm-scales. Large particles observed by VIRTIS (Filacchione *et al.* 2016) have sizes around 2 mm. An agglomerate consists of a compound of small grains, which are made of refractories (refractories are defined to be the opposite of volatiles, as they tend to condense at high temperatures) and silicates; at depths beyond the sublimation zone, there are ices of volatiles included. The ice-free part forms a dust mantle.

The albedo of comets is among the lowest investigated planetary bodies in the solar system. Measurements of all visited cometary nuclei revealed values of the geometric albedo (the fraction of light reflected from a celestial body, compared to a disk with diffuse scattering of light) in the range of 0.02-0.07 (Lamy *et al.* 2004, Buratti *et al.* 2016). Organic refractories themselves show a high degree of absorption, as the refractory material exhibits a high carbon content which has broad absorption bands. The high porosity of the surficial layers and the composition of small grains contribute to a small amount of backscattering in the dust mantle. C-type asteroids have a comparable albedo (0.06) despite being less porous than comets. Icy patches discovered on the surface of 67P (Pommerol *et al.* 2015, Fornasier *et al.* 2015) appear brighter, hence have higher albedos. However, these places are generally small and restricted to localized areas that receive less insolation, mostly due to shadowing of the ruptured surface. For thermophysical studies of the nucleus surface, the Bond albedo (strictly a value between 0 and 1, as it is defined to be the planetary albedo and denotes the fraction of all reflected light over all phase angles), is the decisive variable. It was determined by the use of OSIRIS images to be 0.06 (Fornasier *et al.* 2015). The surface emissivity ε of 67P was determined to be 0.97

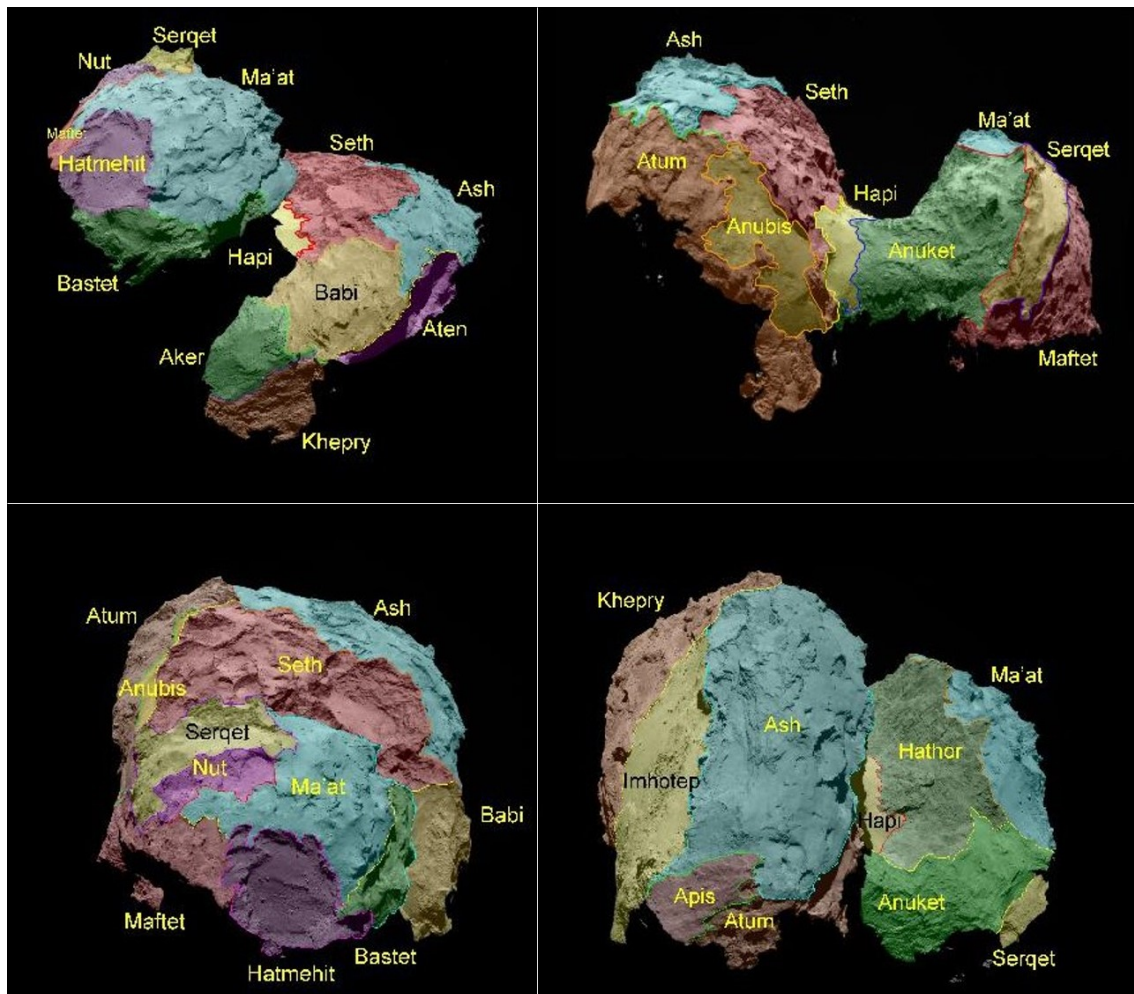


Figure 2.2: Regional mapping of 67P; image credits: El-Maarry *et al.* (2015b), Regional surface morphology of comet 67P / Churyumov-Gerasimenko from Rosetta / OSIRIS images, in *Astronomy & Astrophysics*, volume 583, A26, figure 2; reproduced with permission from *Astronomy & Astrophysics*, ©ESO.

in the Abydos area, near the final landing site of Philae (Kömler *et al.* 2017). This is close to unity, which is defined for a blackbody radiator with Lambertian emission characteristics; due to the small deviation from 1 the surface emission can be treated to be rather hemispherically uniform.

2.1.4 Topographic diversity of 67P

The OSIRIS cameras imaged a wealth of topographies, ranging from dust-covered plains, talusses covered with boulders, to terrains with a more rocky appearance. While earlier cometary missions found pits and scarps that partly also dominate the surface of 67P, the OSIRIS camera system was able to identify several different terrain types on smaller scales (Thomas *et al.* 2015b). Especially rough terrain shows a highly fragmented relief and appear to have comparably higher material strength. Hence, the term ‘consolidated terrain’ became accepted, in order to distinguish it from the more smooth, ocularly dusty

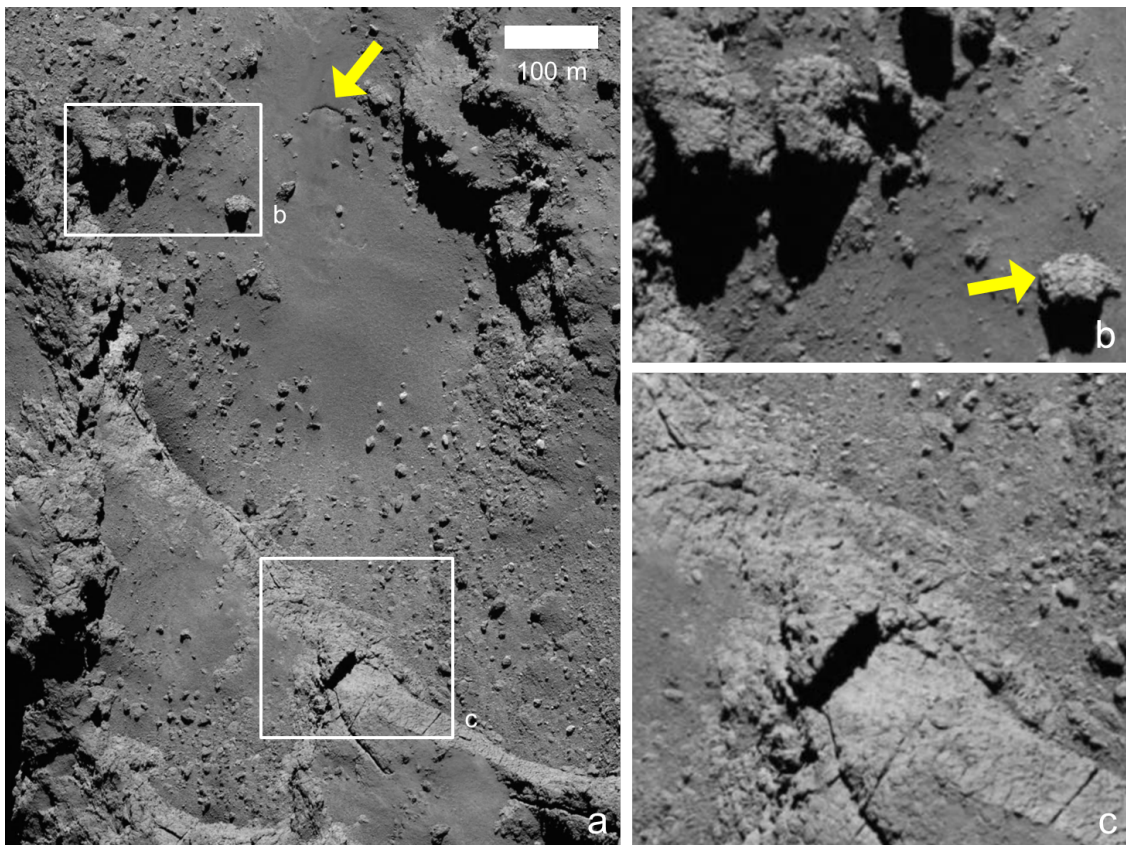


Figure 2.3: : a) Typical northern hemispherical landscape of 67P, the arrow points to an erosive depression; b) Morphologic features that bear fractures, located at the edge of the basin, are rocky outcrops and rocks or boulders (arrow) which could have been former parts of the rim structure; c) Steep fractured consolidated terrain with long fissures. (OSIRIS Image NAC_2015-03-28T15.24.03.101Z_ID30_1397549001_F24)

areas. The latter are likely to be products of mass-wasting and boulder fragmentation (Pajola *et al.* 2015), products of cometary activity through airfall (Thomas *et al.* 2015a), some even show aeolian features such as surface ripples due to dust mobilization (El-Maarry *et al.* 2015b). The great variety of terrains led to a geomorphologic mapping with quite unique regions on 67P as depicted in Figure 2.2; depending on characteristic morphologies, insolation and orientation of the gravity vector (El-Maarry *et al.* 2015b).

The term ‘consolidated’ might be misleading, as it implies material with a high absolute internal strength. Analysis showed that the tensile strength is in the order of up to hundreds of Pascals (Groussin *et al.* 2015a), such that the ratio of strength and gravity is similar to rocks on Earth. In this respect, ‘consolidated’ is meant in comparison to the apparently smooth dusty terrains found on flat plains. These consolidated terrains are characterized by a high degree of diversity and features of the size of meters. Consolidated terrain prevails on gravitational slopes (Groussin *et al.* 2015b), especially on the walls of the widespread cliffs and pits (Vincent *et al.* 2016) in the northern hemisphere. The latter is strewn with ruptures in the surficial layers, which resemble fractures or lineaments. A representative image of the variety of 67P’s surfaces is depicted in Figure 2.3. Especially

the fractured boulder (marked with an arrow in the right bottom corner of Figure 2.3b) is a good example of the fragmented surface relief. Directly in its vicinity, one can identify a depression in the smooth terrain (arrow in Figure 2.3a).

2.2 Thermophysical processes of nucleus surfaces

This section describes mechanisms of heat transfer and their relevance in thermophysical models of 67P and its nucleus upper layers.

Heat transfer mechanisms are distinguished by the physical processes and interactions of the matter involved. The main theorems of thermodynamics and the conservation laws of mass, energy and momentum have to be fulfilled; heat transport is a process that irreversibly raises the thermodynamic entropy of the system. Thus, all ways of heat transport fluxes (unit is energy per area and time) are guided in direction of the negative gradient of the thermodynamic temperature of the considered system. In a closed adiabatic system, considered after an infinite amount of time, all involved particle temperatures strive to reach an equilibrium, erasing any thermal gradient.

2.2.1 Conduction

The one-dimensional Fourier law states the phenomenologically derived correlation between conductive heat flux $\dot{q}_{\text{cond},z}$ normal to a surface A_{xy} , temperature gradient $d(T)/dz$ and thermal conductivity λ_z . The unit of a heat flux \dot{q} is Wm^{-2} .

$$\dot{q}_{\text{cond},z} = -\lambda_z \frac{dT}{dz} \quad (2.1)$$

Conductive heat transport is governed by diffusive processes within the material itself. Conduction occurs in all states of matter, and different physical phenomena drive the thermal exchange: While microscopic movements of molecules dominate in fluidic conditions, lattice oscillations are mostly responsible for solids. The geometrical organization of the particles influences the heat conductivity λ : electron gases in electrical conductors contribute to higher conductivities, while the amorphous organization of material in subcooled melts marks lower values than arranged grids. The thermal conductivity therefore is dependent on the material temperatures. Inherent anisotropic material organization results in an anisotropy of the thermal conductivity as well. For simplification of thermophysical analysis, convective and radiative processes (described in the next paragraphs) are often integrated in modeling isotropic thermal conduction; this comprehensive approach then is referred to as ‘effective thermal conductivity’ and denoted λ_{eff} .

2.2.2 Convection

Convective heat transfer is associated with the macroscopic length scales of an enthalpy flux, in contrast to the diffusive processes of conduction. Every volume element of a fluent phase (and in this respect, fluent can be all physical states, including multi-phase flows) transports a certain mass. Due to changes of the temperature T and consequently the enthalpy H of the flow, convective heat transport \dot{q}_{conv} is associated with an enthalpy

flux \dot{H} (constituted by a mass flux \dot{m} and its specific heat capacity c) across a surface A between times and points i and j :

$$\dot{q}_{\text{conv},ij} = \frac{1}{A}(\dot{H}_j - \dot{H}_i) = \frac{\dot{m}c}{A}(T_j - T_i) \quad (2.2)$$

Convective heat fluxes on planetary surfaces are not restricted to atmospheric processes, as soils often incorporate fluidic materials. Atmosphereless bodies that contain non-negligible amounts of volatiles might take into account convective processes mostly due to their interplay in phase-change processes. Cometary nuclei, rich in volatiles, show several types of convection-based phenomena: Outgassing of sublimating volatiles and their redeposition (Priyalnik 2020), and processes in the cometary gas coma. However, observed gas densities are in nearly all cases very low, such that one can assume Knudsen layer (defined as several mean free path lengths thin layer at the evaporation zone, with molecular interactions between gaseous and solid phases) flow characteristics as the molecular relative mean free path length is higher than spatial scales. Interactions between gas molecules are rare, as these particles are dispersed around the nucleus. Such flow characteristics do not reach a thermodynamic equilibrium of the particles, derivation of a characteristic temperature constrained by the statistics of thermodynamics of the gas remains a challenge.

2.2.3 Radiation

Radiative heat transfer, contrary to convection and conduction, does not include a medium of transport, as it propagates by electromagnetic radiation. Assuming radiative emissive areas in thermodynamic equilibrium, one can apply the Stefan-Boltzmann law for the emissive heat flux density \dot{q}_{rad} per area and time

$$\dot{q}_{\text{rad}} = \sigma T^4 \quad (2.3)$$

with T being the emissive temperature of a surface A . Assuming that surfaces in radiative contact are not perfect blackbodies but grey emitters, radiative heat transfer between surfaces respectively facets i and j (small, completely flat surface elements are denoted as facets), often referred to as self-heating, is given by the Stefan-Boltzmann-Law:

$$Q_{\text{rad},ij} = \varepsilon_i \varepsilon_j \sigma F_{ij} A_i (T_i^4 - T_j^4). \quad (2.4)$$

σ denotes the Stefan-Boltzmann-Constant, ε_i and ε_j the IR emissivity of facets i and j , T is the absolute temperature. F_{ij} describes the view factor between surfaces i and j that are in radiative contact (Davidsson and Rickman 2014):

$$F_{ij} = \frac{A_j \cos \theta_i \cos \theta_j}{\pi d_{ij}^2} \quad (2.5)$$

which is valid in case of the distance between facet barycenters i and j $d_{ij}^2 \gg A_i + A_j$. θ_i and θ_j describe angles between the surface element normal and the connecting vector between both surfaces. The sum of all view factors is one, thus the view factor of a surface i towards space $F_{i,\text{space}}$ is the difference of one and all factors between facets (with n being the number of all facets):

$$F_{i,\text{space}} = 1 - \sum_{j=1}^n F_{ij} \quad (2.6)$$

The maximum of radiative emission towards deep space lies within the infrared spectrum. According to Wiens displacement law, the wavelength with maximum intensity is (with T_{body} being the surface temperature)

$$\lambda_{\text{max}} = \frac{2897.8 \mu\text{m} \cdot K}{T_{\text{body}}}. \quad (2.7)$$

For planetary surface temperatures between 100 and 400 K, the wavelength with maximum intensity λ_{max} is in the range between 7 to 30 μm . The temperature T_{space} is given by the cosmic microwave background radiation (approximately 3 K), but can be higher if e.g. a cometary nucleus is shaded by a dense, partly absorbing coma. Radiative heat transport is the single dominant mechanism of thermal exchange between celestial bodies in the solar system; with an exception when matter is removed from surfaces e.g. by erosive processes on comets.

2.2.4 Insolation

The main heat source for planetary surfaces in the solar system is direct solar irradiation. The solar emission spectrum resembles that of a blackbody emitter with a temperature of 5770 K. The spectral emittance peak of solar irradiation lies within the visible light at 500 nm, while the infrared contributes significantly to the overall emission. Beside that, but negligible for most thermal analyses of planetary bodies, UV and radio emission deviate widely from this blackbody temperature.

A simple approach subsumes the total available spectrum of solar energy at a heliocentric distance of 1 AU under the solar constant of $S = (1367 \pm 0.5) \text{ W/m}^2$ (Kopp and Lean 2011). The absorbed heat flux density \dot{q}_{abs} is defined by the quotient of irradiation S and the quadratic distance R to the sun (in AU), the Bond albedo α and the inclination angle θ_i of the planetary surface:

$$\dot{q}_{\text{abs}} = (1 - \alpha) \frac{S}{R^2} \cos \theta_i \quad (2.8)$$

An idealized spherical planetary body with radius r_p , given the albedo α is constant, uniform and independent of the inclination angle (the deviation of the solar vector from the surface normal) θ , then receives the following heat flux:

$$\dot{Q}_{\text{abs}} = (1 - \alpha) \frac{S}{R^2} r_p^2 \pi \quad (2.9)$$

For irregular non-spherical shapes and rough surfaces, one has to account for additional view factors that are dealt with later in this work.

2.2.5 Dust mantle heat transport

Experimental findings (Huetter *et al.* 2008) suggest that the main constituents of heat transfer for porous media under low pressure and vacuum are conduction and radiation.

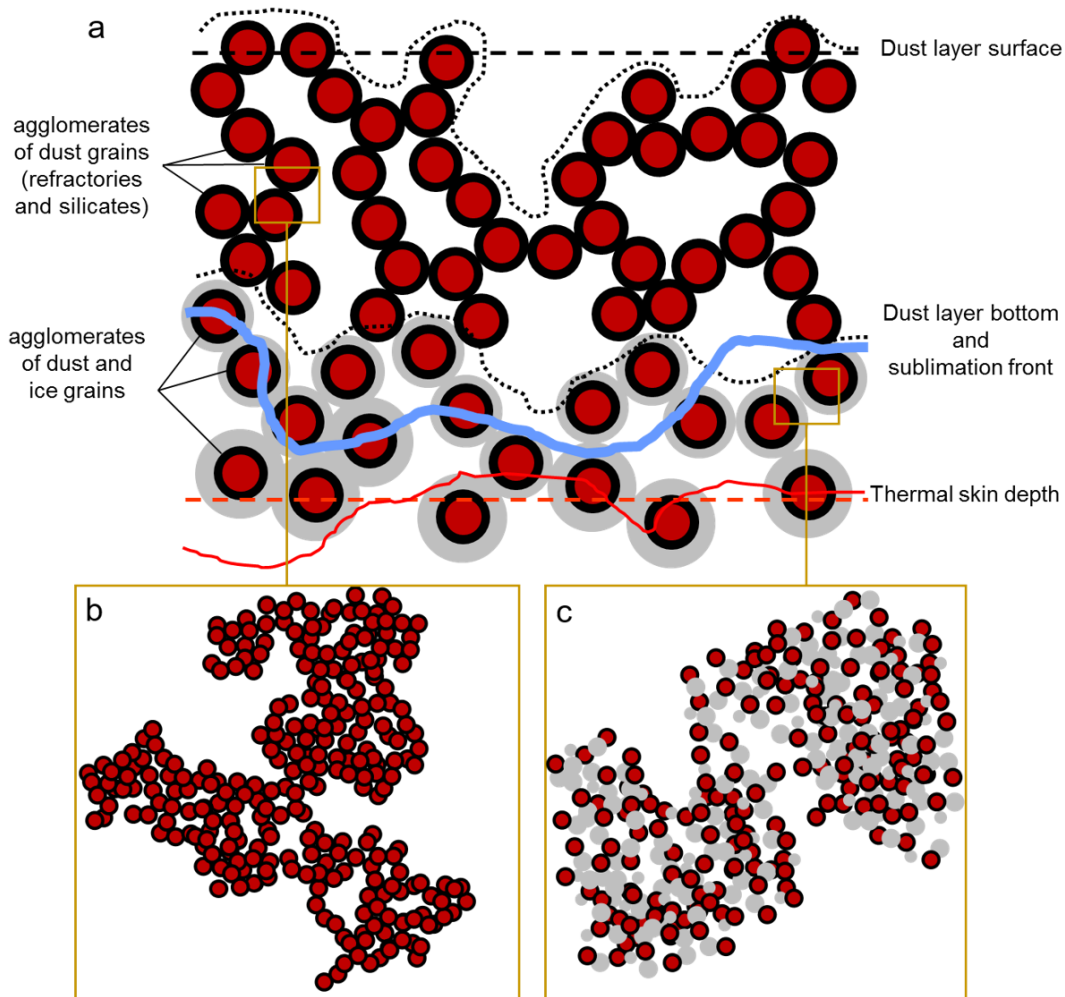


Figure 2.4: a: Cross-section of the model nucleus surficial layers, formed by agglomerates. Agglomerates consist of physically bonded monomers in a hierarchical structure. Dashed straight lines show the distance between surface (black dashed) and the penetration depth of the diurnal temperature variation (thermal skin depth – red dashed; explained in section 2.4.3). Curved lines visualize real surface (top dotted black line), zone of volatile-free agglomerates (bottom dotted black line), thermal skin depth (red line) and sublimation front (thick blue line); their distance from the surface varies based on agglomerate structure. The brown boxes detail the schematically depicted agglomerates: b) shows that volatile-free agglomerates are composed of inert grains, while agglomerates as in c) under the dust mantle also contain ices. Icy grains are represented as grey, inert (refractory) ones in red. The border between agglomerates is characterized by few coagulated grains, internally, grain connections are more numerous. Space between grains account for the high porosity of the material.

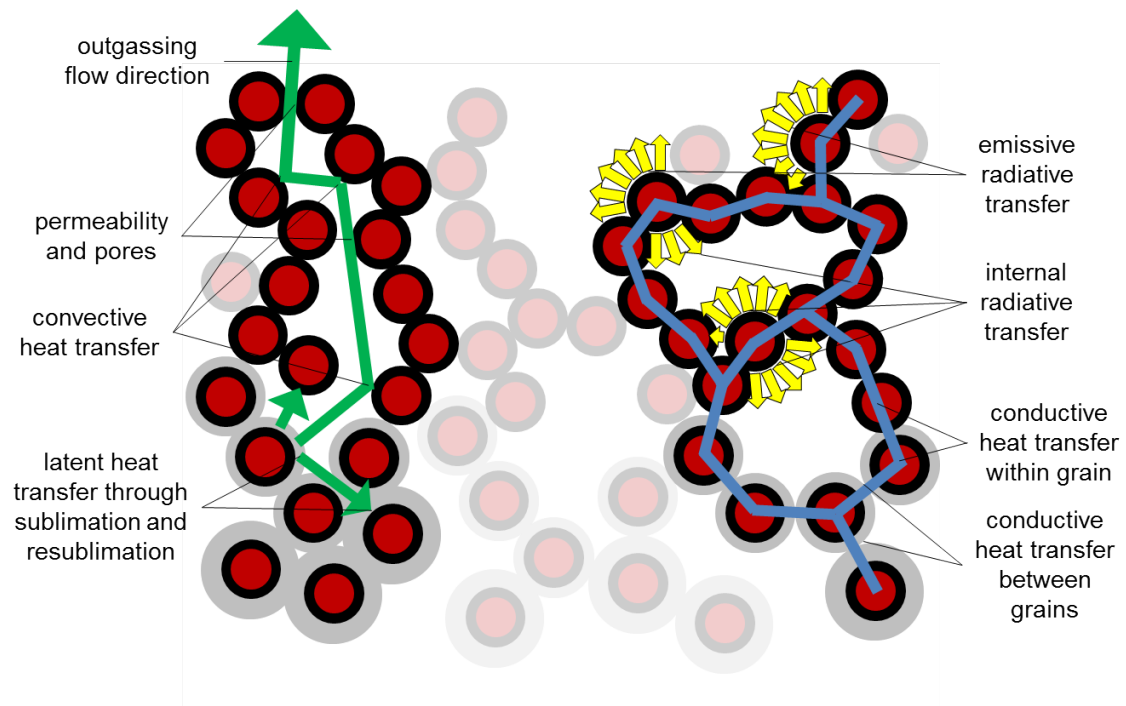


Figure 2.5: Schematics of relevant heat transport processes in the uppermost layers of cometary nuclei.

Their relative contribution strongly depends on the structural porosity and the sizes of the single grains. The thermodynamics of porous structures have been widely studied (Schotte 1960a, Krause *et al.* 2011) also for low fill factors (Arakawa, Sota *et al.* 2017)). Standard thermophysical models of porous media combine linear and radiative contributions in an effective thermal conductivity that is temperature-dependent. The radiative contribution is affected by the mean free path length (Gundlach and Blum 2012) – which depends on porosity and the granular matter size distribution.

In the following, the term agglomerates is used to describe the porous cometary nucleus material, as the interaction between the particles are weak. In contrast, aggregates describe structures with chemical bonds which have stronger interactions.

High porosities combined with large agglomerate sizes lead, according to the mentioned models, to a strong dominance of radiative transfer. However, it has to be noted that the model assumptions include isothermal agglomerates and large overall dimensions: These constraints are not fulfilled for dust mantle layers consisting of few layers of agglomerate with sizes beyond millimeters. Therefore, a layer model that separates the derivation of radiative and conductive contributions to heat transfer is proposed. Radiative exchange is modeled by accounting for a view factor between the cells of the numerical model. The view factor is influenced by the distribution of the free path lengths of the emitted thermal infrared radiation. A comprehensive scheme is shown in Figure 2.5.

Indicated by findings of the COSIMA instrument onboard Rosetta (Schulz *et al.* 2015), a hierarchical structure of porous media is assumed here. Particular spherical grains coagulate to form an agglomerates, and the agglomerates then compound to the layers of the cometary nucleus (Blum *et al.* 2014).

The transport of energy through these layers combines radiative and conductive heat fluxes - in case of present volatiles also the effects of gas diffusion and the transport of latent heat by phase changes, in our case sublimation/resublimation processes. Thus, all thermal processes within the porous cometary dust mantle are merged to a temperature- and porosity-dependent effective heat conductivity $\lambda_{L,\text{eff}}$.

$$\lambda_{L,\text{eff}} = \lambda_{\text{Con}} + \lambda_{\text{Rad}} + \lambda_{\text{Dif}} + \lambda_{\text{PhC}} \quad (2.10)$$

This effective conductivity is controlled by a wide field of parameters, including the structural and geometrical composition of both the monomers and their agglomerates, as well as the material properties. The contribution of diffusive gas processes λ_{Dif} and the impact of phase changes λ_{PhC} is neglected; these effects bring in a wide variety of additional parameters, while they tend to enhance the effective conductivity only.

The heat transport perpendicular to an agglomerate layer $A_{L,\text{eff}}$ is described by the Fourier law:

$$Q_{\text{con}} = \lambda_{L,\text{eff}}(T) A_L \frac{dT}{dx} \quad (2.11)$$

The approach to model the thermophysical behaviour of the comet nucleus upper layers is detailed in Gundlach and Blum (2012) and references therein. Parameters that determine the effective layer conductivity are detailed in Table 2.1; the subscripts distinguish between monomer (M), agglomerate (A) and cometary layer (C) level. The effective thermal conductivity of the cometary nucleus layer $\lambda_{C,\text{eff}}(T)$ then is (Equation 14, Gundlach and Blum (2012)):

$$\lambda_{C,\text{eff}}(T) = \lambda_A(T) \left(\frac{9(1 - \mu_A^2)}{4E_A} \pi \gamma_A(T) r_A^2 \right)^{\frac{1}{3}} \xi_C + \lambda_{\text{Rad}}(T) \quad (2.12)$$

with γ_A defined as (Equation 15, Gundlach and Blum (2012)):

$$\gamma_A(T) = \phi_A \gamma_M^{\frac{5}{3}}(T) \left(\frac{9(1 - \mu_A^2)}{r_M E_M} \right) \quad (2.13)$$

The effective thermal conductivity of a single agglomerate λ_A depends on the monomer properties (Equation 16, Gundlach and Blum (2012)):

$$\lambda_A(T) = \lambda_M(T) \left(\frac{9(1 - \mu_M^2)}{4E_M} \pi \gamma_M(T) r_M^2 \right)^{\frac{1}{3}} \xi_A \quad (2.14)$$

The bulk conductivity is (Equation 3, Gundlach and Blum (2012)) that of vitreous SiO_2 , which will be used in this model even though the composition of 67P comprises a large fraction of organic material the bulk conductivity of which is not determined and hard to be estimated:

$$\lambda_M(T) = b_1 T + b_2 \quad (2.15)$$

with b_1 and b_2 being fitted coefficients.

The radiative contribution λ_{Rad} (Equation 5, Gundlach and Blum (2012)) is neglected on monomer level, as the geometric dimensions imply $\lambda_{\text{Rad}} \ll \lambda_{\text{Con}}$. The radiative heat exchange between two separated agglomerates assumes isothermal behaviour of the individual agglomerate:

$$\lambda_{\text{Rad}}(T, \Lambda(r_A, \phi_C)) = \kappa T^3 \Lambda(r_A, \phi_C) \quad (2.16)$$

Table 2.1: Model parameters of monomers, agglomerates and dust layer for application in the effective thermal conductivity for porous dust layers composed of agglomerates

Property	Monomer	Agglomerate	Layer
Particle radius	r_M	r_A	
Filling factor		ϕ_A	ϕ_C
Poisson's ratio	μ_M	μ_A	
Specific surface energy	γ_M	γ_A	
Young's modulus	E_M	E_A	
Packing coefficient		ξ_A	ξ_C
Radiative coefficient			κ

with $\Lambda(r_A, \phi_C)$ being the mean free path length for the averaged radiative heat transfer (Equation 13, Gundlach and Blum (2012)):

$$\Lambda(r_A, \phi_C) = c_3 \frac{1 - \phi_C}{\phi_C} r_A \quad (2.17)$$

and c_3 a fitting coefficient.

2.2.6 Internal heat sinks and sources

Planetary bodies differ in mass and physical composition. Several internal mechanisms can act as both heat sources or sinks

- phase-changes between states of matter, especially sublimation, or even within the solid state (e.g. exogenic transformation from amorphous to hexagonal ice).
- nuclear reactions, such as the release of decay heat due to radioactive isotopes
- chemical reactions, both reversible and non-reversible

Nuclear reactions could have affected comet formation at times of solar system formation, especially Al-26 (Davidsson *et al.* 2016), but today long-lived isotopes have no decisive effect on the thermal evolution of comets (Guilbert-Lepoutre *et al.* 2015).

Chemical reactions on the surface, triggered by solar irradiation, might act among the organic refractories - their influence has yet not been investigated in detail, nor quantified in numbers.

Phase change processes however dominate the upper layers of cometary surfaces. The ruling process is the sublimation of different ices, including H₂O, CO₂ or CO. A subordinate process are solid-solid state changes, including the release of gases that were formerly trapped in clathrates. However, the existence of clathrates is not verified and still considered controversial.

The predominant sublimating volatile species in 67P is H₂O (Gulkis *et al.* 2015). The temperature-dependent sublimation rate $Z(T)$ is calculated using the classical Hertz-Knudsen approach and a sublimation coefficient α_{sub} as described in Gundlach *et al.*

(2011) and references therein:

$$Z(T) = \alpha_{\text{sub}} p_{\text{sub}}(T) \sqrt{\frac{m_{\text{H}_2\text{O}}}{2\pi kT}} \quad (2.18)$$

with p_{sub} being the sublimation pressure according to Clausius-Clapeyron, $m_{\text{H}_2\text{O}}$ the mass of the sublimating water molecule, and k the Boltzmann-constant. p_{sub} is approximated by the subsequent equation

$$p_{\text{sub}} = a_1 \exp\left(\frac{-a_2}{T}\right) \quad (2.19)$$

The coefficients $a_1 = 3.23 \cdot 10^{12}$ Pa and $a_2 = 6134.6$ K are proposed by Gundlach *et al.* (2011). The sublimation enthalpy H_{sub} then defines the heat sink $Q_{\text{sub},i}$ induced by the sublimation process $Z(T)$ of an area element A_i :

$$Q_{\text{sub},i} = Z(T)H_{\text{sub}}A_i. \quad (2.20)$$

This analysis focuses on the sublimation of water ice as governing heat sink; sublimation terms of other volatiles are considered relevant but not necessary for the goals of this work – they rather introduce higher levels of complexity. Sublimation processes in this modeling approach are restricted to take place in a small zone in the subsurface nucleus layers, as schematically depicted in Figure 2.6. Heat transport via sublimated gases is considered to be small.

A postulated, but not directly verified process is the transformation of amorphous to hexagonal ice - but there are hints that this process drives cometary outbursts (Prialnik and Bar-Nun 1992). These phase-change processes might even trigger further effects, such as release of former trapped molecules in clathrates and subsequent chemical reactions. Outbursts observed on 67P indicate some form of energy storage (Agarwal *et al.* 2017) in the subsurface terrain.

Beside the internal sources or sinks, physical processes on the surface might also influence the aforementioned heat transfer mechanisms. As an example, condensation of ices due to temperature drops might trigger higher albedos - while high temperatures can positively affect the thermal conductivity through sintering processes in dust layers.

2.3 The effect of surface roughness

2.3.1 Beaming effect on atmosphereless planetary bodies

Observations of the lunar surface, already performed in the first half of the 20th century, revealed an effect that became widely known as thermal infrared limb brightening (Pettit and Nicholson 1930): Towards the limb of the lunar disk, measured brightness temperatures were higher than predicted. This effect was later confirmed by Saari and Shorthill (1963), as they found that the emissive heat flux distribution over the elevation angles of the lunar disk cannot simply be approximated with the use of cosine law. It rather follows a function $Q_{\text{rad}} = a \cos^{3/2} \chi$, with a being a constant, and χ the emission angle between the local surface normal of a spherical body and the vector to Earth. Even at the subsolar point, retrieved brightness temperatures were above those expected from flat

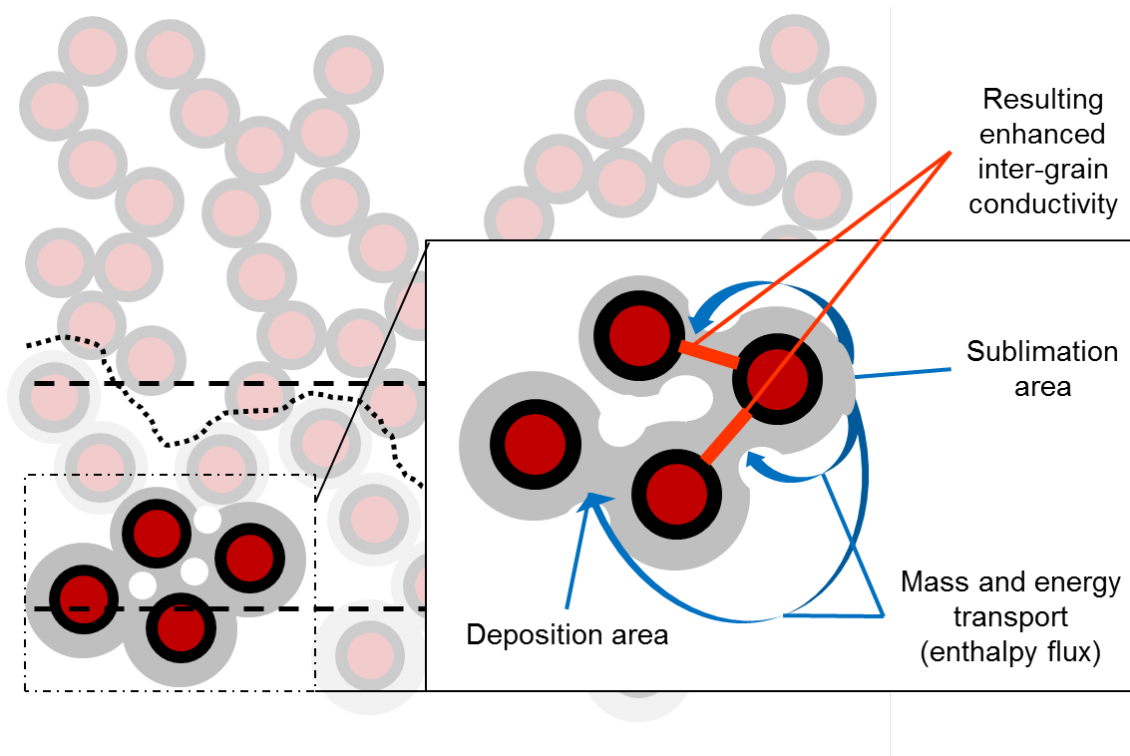


Figure 2.6: Scheme of sublimation processes in the nucleus uppermost layers. The highlighted agglomerates consist of dust and ice grains, sublimating ice grains remove contacts within some agglomerates, their deposits create additional contacts; both effects may change the effective conductivity of the porous layer structure. Temperature cycles will also lead to higher contact areas between the grains; this process, also known as sintering, increases the overall conductivity.

black-body surfaces in radiative equilibrium. Towards the limb, the brightness temperature differences increased, e.g. revealing temperature differences of 40 K at angles around 60 degrees from the subsolar point.

The thermal inertia of the lunar surface should interplay with these findings and lead to a varying specificity of the effect on morning and evening terminator. However, conductivity of lunar regolith is below 0.01 W/mK (e.g. see Urquhart and Jakosky (1997)), thus thermal inertia is low and its effects on this phenomenon could be neglected. Accordingly, morning and evening hemisphere of the moon do not show significant influence on the results – in addition to low thermal inertia, this is also attributed to the slow rotation rate of the moon. In comparison, the diurnal period of comet 67P/CG is about 50 times shorter.

Studying the thermal emissions of asteroids, Lagerros (1996) used non-spherical shapes and crater models to analyze their impact on radiative IR emissions. The analysis showed that under certain circumstances, local temperatures lie above the theoretical predictions for ideal flat, perpendicular illuminated blackbody conditions (Lagerros 1997). Shadowing and self-heating effects thus impact the original sinusoidal insolation function and alter it, revealing deviating thermal surface patterns.

Rosetta's encounter with asteroid 21 Lutetia confirmed other interplanetary missions

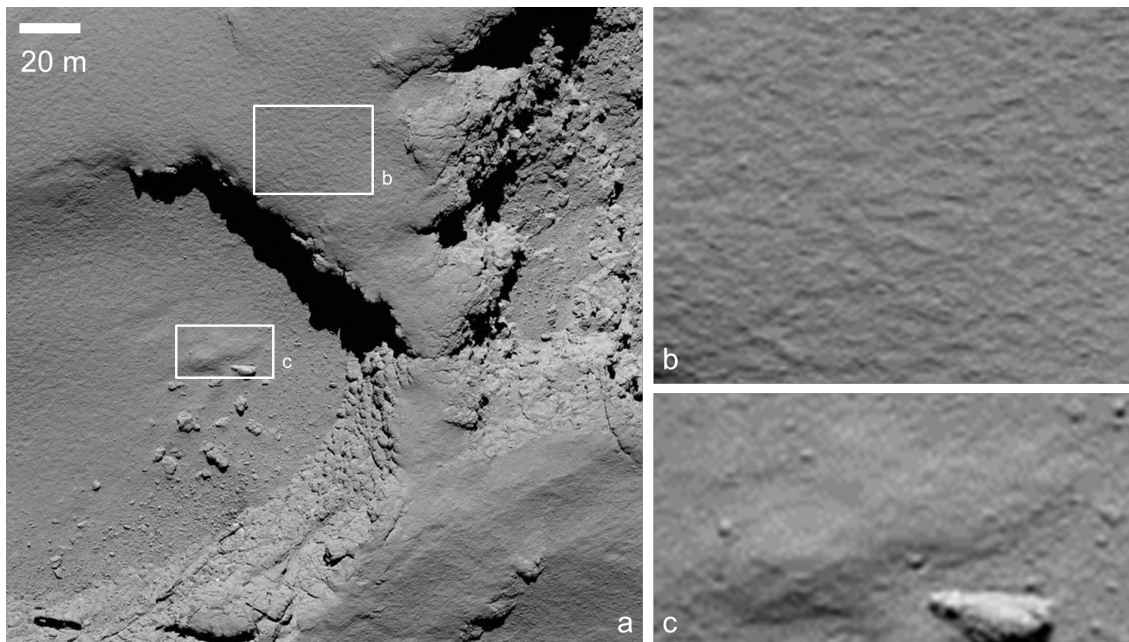


Figure 2.7: a) Image NAC_2016-09-30T08.18.33.740Z_ID10_1397549800_F22 near the final landing site of Rosetta. b) and c) Close-up views of the surface roughness of so-called smooth terrain. The terrain texture has a typical length scale of 1 m (b), while typical topographical features have larger scales.

that the effect can be also extended to asteroids (Keihm *et al.* 2011). The temperature measurements on the nuclei of 103P/Hartley 2 and 9P/Tempel 1, unveiled limb brightness patterns, (Groussin *et al.* 2013). The retrieved colour temperatures from spectrographic measurements showed persistently higher temperatures for 9P with a peak deviation for large incident angles, than the corresponding cosine function. The cause of the thermal limb brightening is widely explained with surface roughness.

2.3.2 Surface roughness of comet 67P

Planetary surfaces without atmospheres, regardless whether planets, minor bodies, or comets, lack aeolian or convection-driven mechanisms which can process and alter terrains and structures. Additionally, regolith-covered surfaces have very low thermal conductivities due to their fine-grained texture (Gundlach and Blum 2013). As such, the governing heat transport process is absorption of solar irradiation and thermal infrared emission. These two prerequisites lead to wide temperature differences on potentially small spatial scales, conduction then is relevant only in length scales of the thermal skin depth (Davidsson and Rickman 2014). Remote-sensing methods from spacecraft, even if they are designed as imaging spectrometers, have limited resolution capabilities and integrate radiation over an observed area. As such, small-scale temperature variations can hardly be resolved in full detail. This chapter discusses thermal effects of rough surfaces by investigating a specific, generated terrain feature from different observer positions.

The image sequence of the Rosetta spacecraft landing site enabled the OSIRIS camera to take a look at the nucleus surface in highest details and culminated in a resolution of

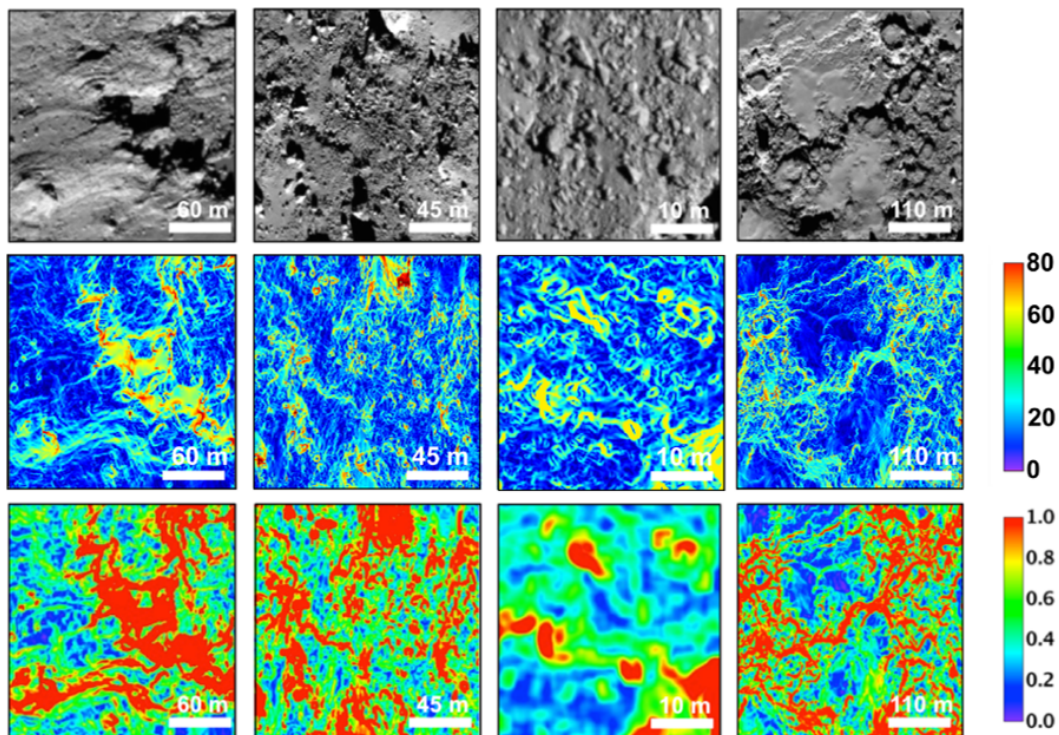


Figure 2.8: Several surface morphologies of 67P rough terrains (top), corresponding slope maps (middle) and the rms roughness (bottom). Image credits: Birch *et al.* (2017), Monthly Notices of the Royal Astronomical Society, Geomorphology of comet 67P/Churyumov-Gerasimenko, Volume 469, Issue Suppl2, Figure 8.

up to 2 mm per pixel. The images show that the previously smooth appearance of the terrain, created by airfall and given the illumination circumstances with a low elevation angle of the sun, unveiled a unique roughness patterns (Figures 2.7 b and c). Birch *et al.* (2017) analysed several terrain features and compared them in respect to slope angles and root-mean-squared roughness (see Figure 2.8).

Roughness exists on a wide variety of length scales, from constituent grain sizes up to the irregularity of whole cometary nuclei. Several approaches for roughness models that aim at thermophysical analysis have been detailed by Davidsson *et al.* (2015), among them spherical caps, trenches, or fractal surfaces. The beaming of irregularly shaped asteroids (Lagerros 1997) and surface roughness effects (Lagerros 1998) have significant impact on the thermal radiation emitted by small bodies. For cometary nuclei, comparable thermal inertia and body sizes implicate a similar approach.

2.3.3 Modeling surface roughness

The prerequisite for a stratified temperature map on any rough surface is the illumination condition. The surface appears different to the observer, depending on the viewing geometry. Thus, the corresponding angles need to be defined: The geometric setting for a surface element is characterised by the positions of the sun, the considered surface and the observer. The positions are described by three angles. The incidence angle ξ is defined by

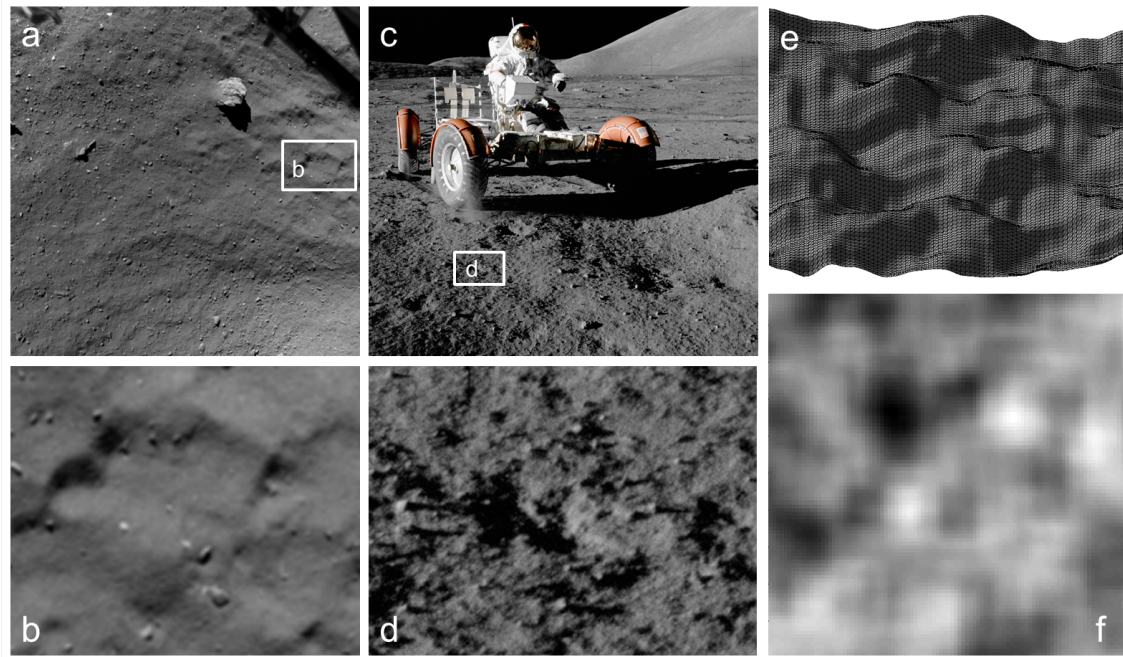


Figure 2.9: Rough surfaces on planetary bodies in reality and model: a) View from Rosetta lander Philae camera ROLIS (Boehnhardt *et al.* 2017) during its descent towards Agilkia landing site, Image credits: ESA/Rosetta/Philae/ROLIS/DLR; b) Close-up of b), showing the dust-covered surface of 67Ps Agilkia landing site, c) Lunar Roving Vehicle of Apollo 17 with lunar dust (image credits: NASA), d) Close-up of lunar regolith (image credits: NASA), e) A typical surface generated with Perlin noise, f) simulation of the Perlin noise generated surface under illumination conditions

the angle between incident irradiation (which is the negative solar vector) and the surface normal. The emission angle χ refers to the angle created by surface normal and observer vector. Both incidence and emission vector establish a plane, the angle between these vectors is the phase angle ϕ . By projecting this plane onto the surface plane, one obtains the azimuth angle ψ . The setting is visualized in Figure 2.10.

There are a number of ways to generate and specify a typical rough surface representative for airless planetary bodies. This work's approach uses a noise function method named Perlin Noise (Perlin 2002), based on a frequency-superpositioning method and widely used in computer graphics to create surface textures (Li *et al.* 2015), especially water or clouds. Perlin Noise is a noise function, which is based on gradient noise. The method is based on a two-dimensional mesh, and each point of the mesh is attributed a gradient value. Between those mesh points, the gradient values are interpolated, generating a smooth function that resembles rolling hills, as in Fig. 2.9a.

The detailed process of generating a cloud of coordinates by using the Perlin noise method can be found in <https://adrianb.io/2014/08/09/perlinnoise.html>. Surfaces generated with this method resemble regolith-covered terrains created by micro-impacts, ejecta or airfall (see Figure 2.9b, d and f).

Before creating a rough surface patch, the size of the terrain has to be determined as a number of vertices or points in both x and y direction, the points in a row being equidis-

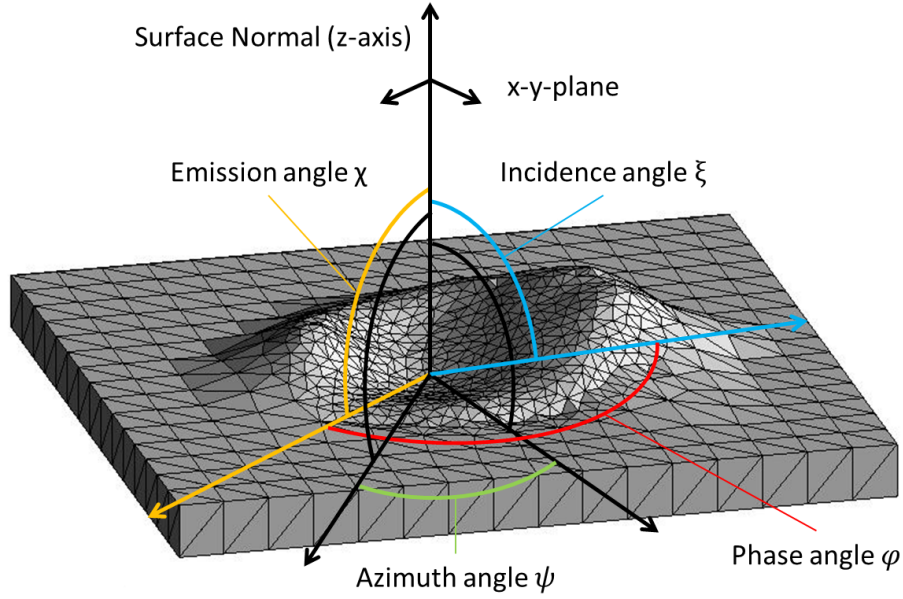


Figure 2.10: Geometrical definition of variables that describe the illumination and observer position for a rough surface, based on a surface feature: incidence angle ξ , emission angle χ , azimuth angle ψ and phase angle ϕ

tant in x respectively in y -direction. A typical rough terrain segment that is used in this work then consists of 21 by 21 points, in total 441. The z coordinate is generated by using algorithms of Perlin noise, dependent of the coordinates in x and y . The terrain is composed of triangular facets. Adjacent facets share two points; the example full terrain then consists of 800 facets. A terrain generated of 800 facets is on one hand small enough to be calculated in reasonable time for a wide variety of viewing angles, and on the other hand patterns like heights or furrows can be adequately resolved. It shall not be used to exactly quantify the effects of surface roughness, as there is a dependency of the distance to the edge of the terrain; and edges deform the results. The size is considered as good enough to qualitatively resolve the effects of the viewing geometry and to draw conclusions on the heat trap effect of cometary surfaces.

A criteria to rank the level of surface roughness is a prerequisite for analysis. There are different approaches to measure the degree of surface roughness. The Lagerros surface roughness x relates the area of a real surface A_r to the area that is obtained when this area is projected on a flat surface A_f (Lagerros 1997, 1998). Here, the real surface, respectively the rough surface is the sum of all facets $\sum A_r$ in the generated patch:

$$x = 1 - \frac{A_f}{\sum A_r} \quad (2.21)$$

Another way of determining the quantity of surface roughness is the mean slope angle θ that is averaged over all slope angles $\sum_{i=1}^m \theta_m$ of the m facets of the patch.

2.3.4 Heat balance of rough surface patches

The temperature of the patch surface i is considered to be in thermal equilibrium with its surrounding surface elements j and absorbed solar insolation $Q_{\text{abs},i}$. A thermal inertia of 0 is assumed, which is acceptable as it results in reasonable temperatures for illuminated areas (Groussin *et al.* 2013). The energy conservation equation for a facet i is:

$$Q_{\text{abs},i} + Q_{\text{emit},i} + \sum_j Q_{\text{rad},ij} = 0 \quad (2.22)$$

Solar absorption $Q_{\text{abs},i}$ is given by:

$$Q_{\text{abs},i} = (1 - \alpha) \frac{S}{R^2} A_i \cos \theta_i f_{\text{solar},i} \quad (2.23)$$

with $f_{\text{solar},i}$ being an indicator and linked to a view factor, representing if the respective surface is illuminated. During direct illumination, this value is 1, otherwise set to 0. Thermal infrared emission to space $Q_{\text{emit},i}$ is calculated

$$Q_{\text{emit},i} = F_{i,\text{space}} \varepsilon \sigma T^4 \quad (2.24)$$

with $F_{i,\text{space}}$ being the view factor of the facet towards deep space. The resulting radiative exchange $Q_{\text{rad},ij}$ then is:

$$Q_{\text{rad},ij} = \varepsilon_i \varepsilon_j \sigma A_i (T_i^4 - T_j^4) \frac{A_j \cos \theta_i \cos \theta_j}{\pi d_{ij}^2} f_{ij,\text{vis}} \quad (2.25)$$

σ denotes the Stefan-Boltzmann-Constant, ε_i and ε_j the IR emissivity of facets i and j , T_i and T_j the absolute temperature. $f_{ij,\text{vis}}$ is 1 if the barycenter of both surfaces are in direct radiative exchange. When direct contact is obstructed by third party facets k being directly in the line between both areas i and j , $f_{ij,\text{vis}}$ is 0. So, the potential direct connection between surface centers determines if there is self-heating or not.

Each facet temperature T_i is calculated by subsequent iterations l , until a stability criterion $\Delta T_{i,l} < 0.01\text{K}$ is reached.

The disadvantage of a zero-thermal-inertia method is that shadowed and not illuminated facets result in extremely low temperatures. Inclined edge elements might partially not even receive thermal emission (self heating) from adjacent facets. To mitigate these misleading results, a facet minimum temperature of 130 K is introduced, in line with the minimum temperatures expected for surfaces in long shadow.

A distant observer, looking at the described surface patch, notices a wide spectrum of surface temperatures. Each of the surfaces in radiative contact will contribute to the received signal. Depending on the geometric setting, the observer might receive diverging temperature signals, as some facets might be visible and others obscured (see Figure 2.11).

The observer receives the heat flux density \dot{q}_{obs} calculated by integrating over all surfaces of the patch visible to the observer:

$$\dot{q}_{\text{obs}} = \sum_i \varepsilon_i \sigma A_i T_i^4 \frac{A_{\text{obs}} \cos \theta_i \cos \theta_{\text{obs}}}{\pi d_{\text{obs}}^2} F_{j,\text{obs}} \quad (2.26)$$

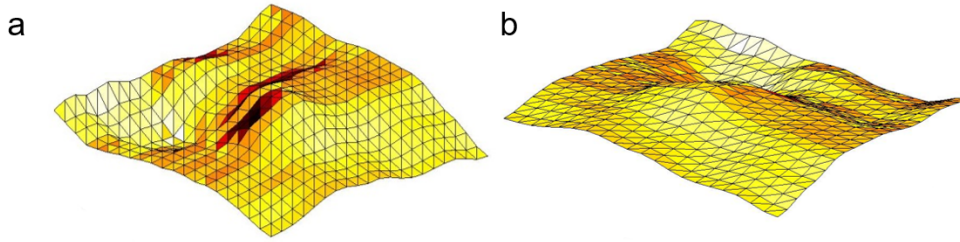


Figure 2.11: Radiative exchange on the faces of a generated rough surface patch for two rough surfaces: a) has a Lagerros surface roughness of 0.10, b) is smooth with 0.05. The patches show different viewing conditions, in a) the observers sees partly obstructed terrain (shown in dark red) with the solar irradiation coming from the right. In b) the solar vector is pointing in the direction of the reader.

The algorithm includes a visibility check between surfaces: If facet i is visible to the observer, $F_{j,obs}$ is 1; and 0 if there is no direct radiative exchange. The angle θ_{obs} is the angle between observer surface normal and the connecting line to facet barycenter i . The observed brightness temperature T_{obs} then is

$$T_{obs} = \left(\frac{\dot{q}_{obs}}{\sigma} \right)^{1/4} \quad (2.27)$$

Brightness temperatures for the surface patch can be calculated for any position in a half-sphere above the roughness element. The position is characterized by the angles of azimuth ψ and emission χ . The observer signal can vary for irregular surfaces, depending on the surface orientation. This effect is especially severe when the surface patch is composed of a small number of facets. Two possible solutions are suggested: The first one takes a large surface patch with a high number of facets. This is impractical due to the high computational efforts to calculate the large amount of view factors. The second approach takes the same surface patch and evaluates it from several different rotational angles. So, the surface patch is calculated from in total k positions, each of them with a rotation of 15 degrees compared to the previous position. The observed brightness temperature T_{obs} here is composed of an average of $k=24$ heat flux densities \dot{q}_{obs}

$$T_{obs} = \left(\frac{\frac{1}{k} \sum_k \dot{q}_{obs}}{\sigma} \right)^{1/4} \quad (2.28)$$

The obtained result is independent of the patch orientation and representative of an isotropic composition of surface normals for a typical nucleus morphology, for example representing airfall terrain.

2.3.5 Temperature maps for rough surfaces

In this analysis, four surface patches with increasing roughness levels are detailed. The parameters of the study are shown in Table 2.2. The surfaces are generated using the same Perlin noise generation parameters, solely the amplitude is adjusted. The topography

Table 2.2: Thermophysical parameters for surface roughness analysis

Property	Unit	all	a	b	c	d
Heliocentric distance R	[AU]	1.5				
Albedo α	[-]	0.05				
Emissivity ε	[-]	0.95				
Incidence angle ξ_1	[deg]	60				
Mean slope angle θ	[deg]	-	8.3	18.2	26.4	31.9
Lagerros roughness x	[-]	-	0.01	0.05	0.10	0.15
Incidence angle ξ_2	[deg]	75				
Mean slope angle θ	[deg]	-	8.3	18.2	26.4	31.9
Lagerros roughness x	[-]	-	0.01	0.05	0.10	0.15

pattern is the same for all four surfaces, with the z-coordinate stretched by a specific factor to match four given roughness levels.

A flat surface, illuminated under an incidence angle ξ_1 and parameters such as indicated in Table 2.2 results in a surface temperature of 272 K. This value is derived for any emission angle, thus independent of any observer location. For a rough surface that is composed of a patch of facets with different temperatures, an observer receives the integral over all facet emissive thermal radiation, weighted by the view factor to the observer. Some facets might be obstructed by others, blocking any emission from them, their contribution therefore being zero. As a result, each observational location receives a unique emission signal from the same patch of facets, and this signal translates to different obtained temperature results depending on position.

Calculation results are shown in Figure 2.12 for two different incidence angles. While for a relatively smooth surface (1a) at an incidence angle of 60 deg, the temperature range is small and comprises values from 260 to 280 K, more rough surfaces (1d) bridge 220 and 310 K. Especially for large emission angles, the observed temperatures are close to the maximum temperatures at a perpendicular illumination; this value is 323 K. For smaller emission angles, the bandwidth of observed temperatures decline and differences dissolve. The same trend can be observed for an incidence angle of 75 deg (Figure 2.12 2a to 2d). The main difference is the higher bandwidth of temperatures especially at the colder end of the spectrum.

Conclusively, the described surface roughness leads to two-dimensional radiative transfer patterns. The application of a single beaming factor, as described in previous models, e.g. in Rozitis and Green (2011), is considered as misleading for calculation of self-heating in resolved thermal models. Radiative fluxes, as observed by a distant spacecraft observer, contribute to resolved nucleus temperatures (Groussin *et al.* 2013). Similarly on smaller, not resolved scales, the radiative fluxes in topographic features potentially strengthen peculiar local effects, such as outgassing or surface processing. The effect turned out to be strongest for high roughness surfaces; morphologies with wide varieties of incidence angles are expected to represent this in their thermal behaviour.

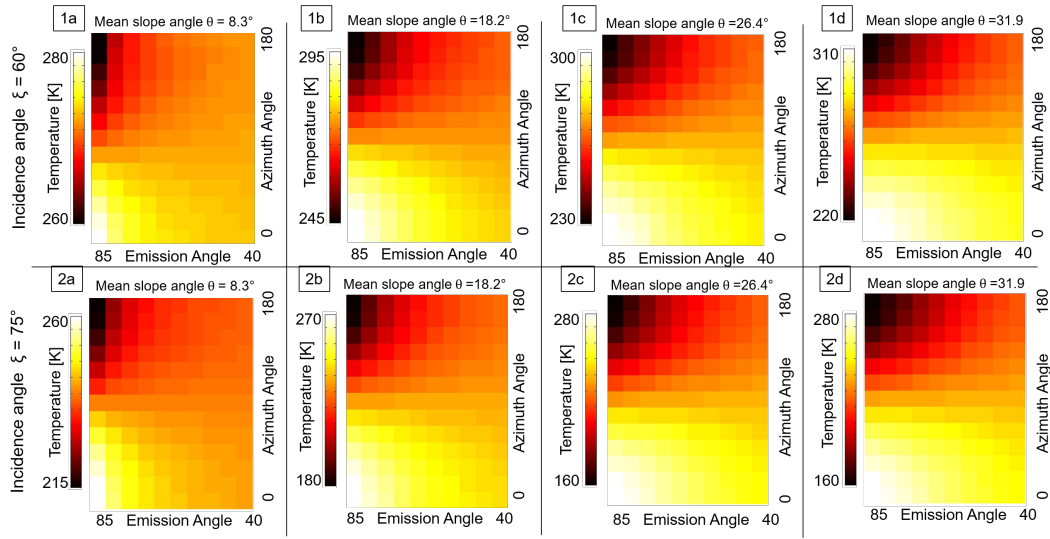


Figure 2.12: Brightness temperature, dependant on the position of the observer and the surface roughness of the patch representing a planetary body surface. The incidence angle ξ is 60 deg for all four top cases (1a–d), and 75 deg for all four bottom cases (2a–d). Each plot differs in roughness, given by the slope angle, in ascending roughness from a to d. The plot layout show the brightness temperature for emission angles χ between 85 and 40 degrees on the horizontal axis, against azimuth angles ψ between 0 and 180 degrees.

2.4 Simple models of surface temperatures

2.4.1 Radiative equilibrium model

The simplest thermal model of an idealized cometary, or more generalized, a planetary surface, is the energy balance between absorbed solar irradiation and the emission of thermal radiation according to the Stefan-Boltzmann-law (equations 2.4 and 2.8):

$$\varepsilon\sigma T^4 = (1 - \alpha) \frac{S}{R^2} \cos \theta \quad (2.29)$$

This approach neglects any thermo-physical processes of the surface, and is feasible only if one expects perfect isolation of the surface towards interiors of planetary bodies. The radiative equilibrium temperature of an area of the surface then is only dependent on its inclination angle θ_i towards the solar vector:

$$T = \left[(1 - \alpha) \frac{S}{R^2} \cos \theta_i \frac{1}{\varepsilon\sigma} \right]^{1/4} \quad (2.30)$$

This method already allows highly-resolved temperature maps of a planetary body or cometary nucleus. For an object that is covered with highly insulating regolith and shows long diurnal periods, this method can well reproduce temperatures on the surface. Thermal models used for exploration of Moon and Mercury with orbiters rely on this approach. However, calculated night side temperatures deviate from reality, as the assumption of perfect isolation of the surface does not apply here.

For the determination of the average surface temperature, one has to integrate over all incidence angles. The energy balance then is influenced by the ratio between the

illuminated circle of the dayside $A_c = r^2\pi$, and the total surface of the spherical object $A_p = 4r^2\pi$

$$\varepsilon\sigma T^4 = (1 - \alpha) \frac{S\pi}{4R^2} \quad (2.31)$$

The average planetary body surface temperature then is

$$T = \left[(1 - \alpha) \frac{S\pi}{4R^2\varepsilon\sigma} \right]^{1/4} \quad (2.32)$$

2.4.2 Standard thermal model for planetary bodies

The standard thermal model of planetary surfaces was introduced in the 1970s for the determination and reproduction of asteroid surface temperatures, after observations in the IR became feasible. The term 'Standard Thermal Model' (STM) was introduced for asteroids by Lebofsky *et al.* (1986). The STM focuses on the time-variable temperatures in the uppermost layers of a planetary surface. It takes into account the radiative heat balance, derived in the last paragraph, as a boundary condition on the surface. The application of the Fourier law to the heat balance of a closed system (in three spatial dimensions and time) yields

$$\frac{\partial}{\partial x} \left(\lambda \frac{\partial T}{\partial x} \right) + \frac{\partial}{\partial y} \left(\lambda \frac{\partial T}{\partial y} \right) + \frac{\partial}{\partial z} \left(\lambda \frac{\partial T}{\partial z} \right) + \dot{\omega}_{\text{int}} = \rho c \frac{\partial T}{\partial t} \quad (2.33)$$

with $\dot{\omega}_{\text{int}}$ being an internal heat source density, or sink density, with the unit W/m^3 . Considering the thermal conductivity λ of the planetary regolith to be directionally independent and invariant of temperature, one obtains a relation for the depth z of the nucleus while fluxes in directions x and y become zero:

$$\frac{\lambda}{\rho c} \frac{\partial^2 T}{\partial z^2} = \frac{\partial T}{\partial t} \quad (2.34)$$

Introducing the thermal inertia $I = \sqrt{\rho c \lambda}$ as a means to describe the ability of the surface to adopt to temperature changes of the environmental boundary conditions, one obtains

$$\frac{I^2}{(\rho c)^2} \frac{\partial^2 T}{\partial z^2} = \frac{\partial T}{\partial t} \quad (2.35)$$

with the boundary condition at the surface ($z=0$)

$$\varepsilon\sigma T^4 - (1 - \alpha) \frac{S}{R^2} \cos \theta_i = \lambda \left. \frac{\partial T}{\partial x} \right|_{z=0} \quad (2.36)$$

Weissman and Kieffer (1984) adopted this model for cometary nuclei, and they included the effects of surface sublimation and coma reflections. The intention was the model application to comet 1P/Halley for its perihelion in 1986.

Several thermophysical models of comets have been formulated, Brin and Mendis (1979), Cowan and A'Hearn (1979), or Weissman and Kieffer (1981), and the so-called standard thermal model (STM) for comets (Prialnik *et al.* 2004, Prialnik 2020) evolved as some sort of reference model. Subsequent studies based their models on the STM, and

these investigations derived temperature and heat flux profiles for the nucleus subsurface (Weissman and Kieffer 1984, Kömle and Dettleff 1991, Skorov *et al.* 2001, Rodionov *et al.* 2002, Davidsson and Skorov 2002, Capria 2002, Rosenberg and Prialnik 2010) and Klinger (1999).

2.4.3 Length and time scales of thermal waves

In the previous section, the thermal inertia I was derived, which indicates not only how fast the surface reacts to varying irradiation conditions, but also allows for the determination of the penetration of the thermal waves on both orbital and diurnal time scales. A solution to the Fourier differential equation by means of a Fourier transformation was proposed by Wesselink (1948), originally for the description of lunar material and exercised on comet 67P by Schloerb *et al.* (2015) for interpretation of MIRO data. The temperature of the nucleus as function of depth z and time t can be represented as a Fourier series, which yields

$$T(z, t) = T_0 + T_1 e^{-z/d_{\text{diu}}} \cos\left(2\pi t/P_{\text{diu}} - \tau_1 - \frac{z}{d_{\text{diu}}}\right) + T_2 e^{-\sqrt{2}z/d_{\text{diu}}} \cos\left(4\pi t/P_{\text{diu}} - \tau_2 - \sqrt{2}\frac{z}{d_{\text{diu}}}\right) + \dots \quad (2.37)$$

with d_{diu} being the thermal skin depth, P_{diu} the rotational period, T_n amplitude, and τ_n phase of the Fourier term n . Couching these mathematical findings, temperatures in deeper surfacial layers show a time shift compared to the sinusoidal illumination conditions. The diurnal variations get shallower with depth, and the thermal lag increases. At a distance of d_{diu} from the surface, referred to as diurnal skin depth, the variations are diminished by the logarithmic factor e :

$$d_{\text{diu}} = \left(\frac{P_{\text{diu}} \lambda}{\pi \rho c}\right)^{1/2} \quad (2.38)$$

If one applies the same boundary conditions for a Keplerian orbit with a being the semimajor axis, G the gravitational constant, and M_{\odot} the solar mass, this results in the orbital skin depth d_{orb} . The rotational period P_{diu} is replaced with the orbital period $P_{\text{orb}} = 2a^{3/2}\pi(GM_{\odot})^{-(1/2)}$:

$$d_{\text{orb}} = \left(\frac{2a^{3/2} \lambda}{(GM_{\odot})^{1/2} \rho c}\right)^{1/2} \quad (2.39)$$

Strictly speaking, the approach of a constant thermal skin depth also requires a constant heat conductivity. As one will see in the subsequent sections, the porous nature of the nucleus structure demands an approach that treats this heat conductivity to be temperature-dependent and therefore violates this statement. Additionally, the existence of heat sinks within the dimensions of the diurnal skin depth also affects the real thermal skin depth. Nevertheless, the above mentioned derivation of the thermal skin depth is an important indicator for analysis, as it provides the order of magnitude of the impact on nucleus layers near the surface.

2.5 Development of a one dimensional thermal model

2.5.1 The impact of orbital parameters

The local temperatures of irregular bodies show a much wider stratification than expected from ideal spherical shapes (Groussin *et al.* 2013); this is of special importance when analysing the thermophysical behaviour and activity of cometary nuclei. The orbital temperatures and characteristic heat fluxes of a representative 67P nucleus surface element and the underlying strata during its JFC phase are governed by insolation and activity (Priyalnik 2020), which can be seen as removal of material with higher enthalpy than the material remaining on the comet surface.

Any thermal analysis of an irregularly shaped cometary nucleus on a high eccentricity orbit is by far more complex than the previously dominating one-dimensional approaches. One needs to investigate dominant heat transfer mechanisms, and which ones can be rather ruled out or neglected; expected and measured temperature ranges and variations for a full cometary orbit, and depths of thermal penetration and alteration due to orbital and diurnal parameters. A typical cross-section of the uppermost surface layers of a cometary nucleus is schematically depicted in Figure 2.4. While the surface is expected to show a complex form, models are restricted to general assumptions. The spin axis orientation, combined with highly elliptical orbits, contributes to quite complex, partly even unique thermal behaviour over diurnal and orbital periods. The roughness of surfaces is worth a closer study.

The orbit defines the intensity of the solar irradiation, orbital parameters were derived by Mottola *et al.* (2014). Diurnal effects of the illumination to the orbital behaviour are taken into account by the model by superpositioning heliocentric distance and nucleus rotation. As a result, two thermal waves can be distinguished; one following one cometary revolution around the sun, the other a 12.4 hour revolution by comet rotation: So, one orbital period is comprised of about 4450 diurnal revolutions of the nucleus, hence diurnal and orbital effects happen on significantly different timescales.

2.5.2 Heat capacity of porous agglomerate layers

The heat capacity of each node i is denoted as source or sink term $Q_{\text{cap},i}$ and dependent of its temperature T_i , heat capacity c_C and mass $m_{C,i}$ - which itself constitutes from monomer bulk density ρ_M and both filling factors ϕ_C and ϕ_A of a single volume element $V_{C,i}$ of the layer.

$$Q_{\text{cap},i} = m_{C,i}c_C \frac{dT}{dt} = \rho_M \phi_C \phi_A c_C V_{C,i} \frac{dT}{dt} \quad (2.40)$$

The thermal inertia I

$$I = \sqrt{\rho_C c_C \lambda_{L,\text{eff}}} \quad (2.41)$$

then is a temperature-dependent variable that relies on the cometary layer properties density ρ_C , heat capacity c_C and the thermal conductivity $\lambda_{L,\text{eff}}$. The diurnal thermal skin depth L_{diu}

$$L_{\text{diu}} = \sqrt{P_{\text{diu}} \lambda_{\text{C,eff}} / (\rho_{\text{C}} c_{\text{C}} \pi)} \quad (2.42)$$

of a rotating surface element with diurnal period P_{diu} reveals the penetration depth of the thermal wave. In cases of low thermal inertia I which can be regarded as justified because of the low effective thermal conductivity, the diurnal thermal skin depth is small in comparison to the surface feature length scales. Thus, treating the heat transfer through the porous cometary layers with a simple 1D mesh geometry perpendicular to all surfaces of the local topography is considered a reasonable approach.

2.5.3 Heat fluxes of a 67P thermal model

A simple 1D numerical model approach consists of a strip of connected nodes perpendicular to the surface for simulation of the uppermost first ten meters of the cometary nucleus. Absorbed solar irradiation, denoted Q_{abs} , and thermal emission to space Q_{emit} is restricted to the surface node; there is no self-heating included as no surface element is radiatively coupled to other elements. The thermal equilibrium of 67P then results in the subsequent heat balance equation of each single node i :

$$Q_{\text{abs}} + Q_{\text{emit}} + Q_{\text{con,im}} + Q_{\text{con,in}} + Q_{\text{sub,i}} = Q_{\text{cap,i}} \quad (2.43)$$

Subsurface nodes have two neighbouring nodes (nodes m respectively n) in the vertical direction and share a conductive heat flux $Q_{\text{con,im}}$ and $Q_{\text{con,in}}$. Sublimation is restricted to the sublimation zone (which is either exactly one node, or left out in calculations with an inert nucleus), so $Q_{\text{sub,i}}$ characterizes the heat sink due to sublimation processes. The surface node is defined to receive perpendicular insolation at a latitude of the equator, i.e. the diurnal (local) maximum at on-site noon; at higher latitudes, the maximum insolation is smaller. $Q_{\text{cap,i}}$ denotes stored or released internal energy. There is no tilted axis taken into consideration, meaning seasonal changes are not accounted for. The solar absorption then depends on the time-dependent illumination angle and the heliocentric distance. During night times, the absorption $Q_{\text{abs,i}}$ is set to 0. The solar absorption $Q_{\text{abs,i}}$ during daytime then is:

$$Q_{\text{abs,i}} = (1 - \alpha) \frac{S}{R^2} A_i \cos \theta_i(t) \quad (2.44)$$

Including the previously described flux definitions, the obtained special thermal balance equation can be derived (i_{rad} is set to 1 for the surface node, i_{sub} for sublimation nodes):

$$\begin{aligned} i_{\text{rad}}(1 - \alpha) \frac{S}{R^2} A_i \cos \theta - i_{\text{rad}} \varepsilon_i \sigma A_i F_{ij} (T_i^4 - T_j^4) - (1 - i_{\text{rad}}) \lambda_{\text{L,eff}}(T_{i,m}) A_i \frac{T_i - T_m}{\Delta z_{i,m}} \\ - (1 - i_{\text{con}}) \lambda_{\text{L,eff}}(T_{i,n}) A_i \frac{T_i - T_n}{\Delta z_{i,n}} - i_{\text{sub}} Z(T_i) H_{\text{sub}} A_i = m_i c_i \frac{dT_i}{dt} \end{aligned} \quad (2.45)$$

The solar irradiation is calculated according to the distance to the sun given by Mottola *et al.* (2014). Parameters of the six analysis cases of the model are displayed in the

Table 2.3: Thermophysical fracture model parameters for 67P orbital analysis

Property	Unit	RadEqu	Sublim	A Flat	B Flat	A Crater	B Crater
Albedo α	[-]	0.06	0.06	0.05	0.05	0.05	0.05
Emissivity ε	[-]	0.97	0.97	0.90	0.90	0.90	0.90
Density ρ_S	[$\frac{\text{kg}}{\text{m}^3}$]	500.0	500.0	1348.0	808.8	2089.4	505.5
Capacity c_S	[$\frac{\text{kJ}}{\text{kgK}}$]	800.0	800.0	778.0	778.0	778.0	778.0
Enthalpy H_{sub}	[$\frac{\text{kJ}}{\text{kg}}$]	n.a.	2830.0	n.a.	n.a.	n.a.	n.a.
Period P_{diu}	[h]	12.4	12.4	12.4	12.4	12.4	12.4
Conductivity λ_M	[$\frac{\text{W}}{\text{mK}}$]	f(T)	f(T)	0.012	0.0017	0.069	0.0034
View factor F_M	[-]	1.0	1.0	0.9	0.9	0.67	0.33

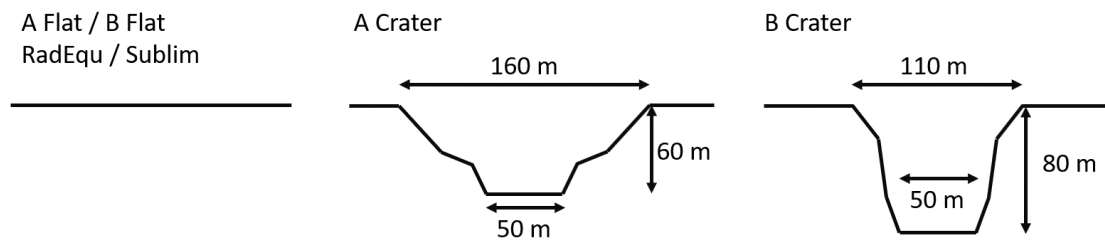


Figure 2.13: Geometrical representation of the model surface for the orbital analysis; the crater morphologies of *A Crater* and *B Crater* are results of impact simulation detailed in Vincent *et al.* (2015a). These A and B Crater cases assume compacted material at the impact area, therefore a higher thermal conductivity is calculated, and the view factor to deep space F_M is smaller.

Table 2.3. The cases *RadEqu* and *Sublim* evaluate differences between a volatile-free dust mantle and a sublimation front at 5mm depth. The four cases to the right of the table are restricted to a study of the effects of impact cratering, as discussed in Vincent *et al.* (2015a); their topography is shown in Figure 2.13 and thermal aspects are detailed in section 2.6.4. The thermal conductivity for these cases is assumed to be independent of temperature for simplicity reasons. Actually, a temperature-independent value can be considered as oversimplified for a cometary nucleus, as described in previous chapters. As this analysis mostly covers high heliocentric distances and aims at showing the difference between diurnal and orbital thermal lags, the assumption of a constant conductivity is justified.

The high eccentricity of a typical JFC orbit leads to significant differences in solar irradiation. While it takes 6.44 years to complete one cometary revolution around the sun, the solar irradiation varies by more than one order of magnitude. It actually covers a broad range of more than 800 Wm^{-2} difference, which comprises a factor of 15 between both extrema. For Earth, the variability is lower than 100 Wm^{-2} and the corresponding factor is smaller than 1.1.

Cases *RadEqu* and *Sublim* in Table 2.3 and Figure 2.14 depict temporal fluxes of the nucleus surface during two orbital revolutions. The diagram starts at perihelion position

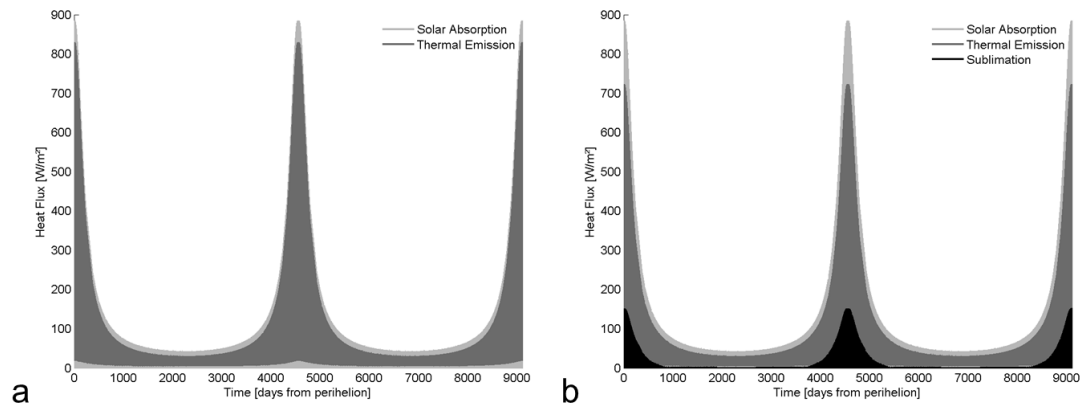


Figure 2.14: Thermal fluxes for two orbital revolutions of comet 67P. Left (a): Case *RadEqu*; radiative heat fluxes, restricted to the surface node of the nucleus for a volatile-depleted layer. The bright grey continuum denotes the varying solar irradiation, the dark grey continuum shows the thermal infrared reemission towards space. Right (b): Case *Sublim*; bright grey and dark grey continua are according to a. This case additionally takes into account sublimation at a sublimation zone at a depth of 5 mm. Sublimation is shown by the dark black continuum.

and depicts the range of a value at a certain time, as the diurnal changes are not resolved. The bright grey continuum illustrates solar absorbed irradiation, ranging from 0 Wm^{-2} during night times to 900 Wm^{-2} at perihelion. At aphelion, the range is between 0 and 60 Wm^{-2} . The short diurnal timescale of 12.4 h compared to the orbital one of 6.44 years make it obvious that only long term fluctuations are visible and distinguishable in the figures.

Reemission values, depending on the temperature of the surface, have a slightly smaller range in (a). Analysing the effect of an additional heat sink in the equation (b), the impact of sublimation on thermal emission is a significant reduction at perihelion. Given an entire orbital period, relevant magnitudes ($>1\%$) of sublimation are restricted to less than 20% of the time. Absolute values are small and never exceed 150 Wm^{-2} . Calculated heat sink values are highly dependent on the position of the sublimation front.

2.5.4 Orbital and diurnal thermal waves

The horizontal temperature distribution for an inert comet surface and layers below down to 3 m (case *RadEqu*); and for one with a sublimation front at 5 mm depth (case *Sublim*) are discussed in the following. While surface temperatures do not deviate between both models at distances $>3 \text{ AU}$, around perihelion maximum differences can approach up to 10 K. At increasing depths below the sublimation front, differences between both models become significant. Inert model *RadEqu* attains 200 K at 50 cm depth at perihelion, but these temperatures are high enough to trigger substantial sublimation in model *Sublim*. As an effect, the heatwave cannot penetrate further due to the inhibiting sublimation front. Diurnal fluctuations remain small even for depths of 5 cm.

Outgassing reduces the temperatures below the sublimation front to 160 K at 50 cm

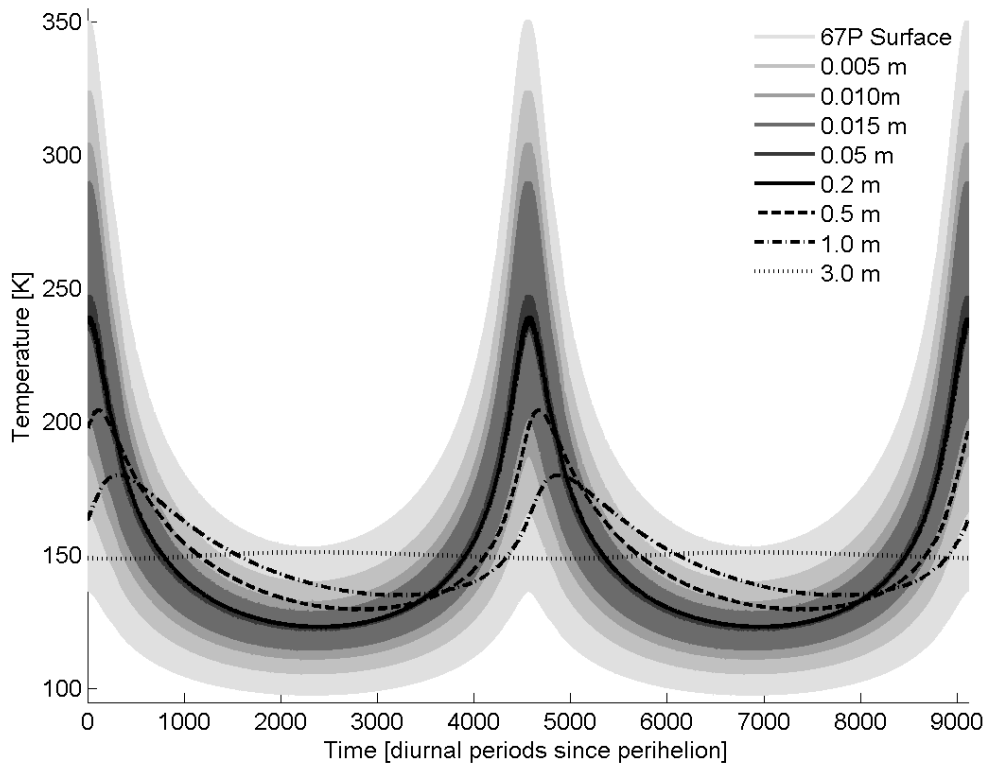


Figure 2.15: Temperatures at various depths for two orbital revolutions of 67P/CG for case *RadEqu* without sublimation fluxes

depth. This heat sink also has significant impact on the maximum of the thermal wave, and its penetration depth. At 3 m distance to the surface, both models outline small orbital variations and temperatures remain constant; the inert strata model is slightly warmer by about 10 K. The orbital heatwave for both models is depicted in Figure 2.15 and Figure 2.16.

The diurnal heatwave can be disentangled from the orbital one by resolving the orbit and selecting periods of e.g. 50 comet days. Generally, differences between adjacent diurnal periods are small and even for the nucleus surface less than one degree per revolution. To identify the changes, Figure 2.17 shows the differences of the temperature distribution close to perihelion; at a position where the insolation increase or decrease per diurnal revolution is at its climax. The maximum temperatures can be obtained slightly after local noon directly at the surface nodes. Surface temperature ranges outline an axially symmetric behaviour for pre and post perihelion, there is no thermal lag induced by the orbital thermal wave. Subsurface nodes show an increasing influence of the orbital heat wave, temperatures at 1 m depth rise by 30 K during 400 revolutions. At 3 m depth, the temperature remains stable and changes less than 1 K during one revolution of 6.44 years. While the pre-perihelion temperatures show a general increase at all depths, the post-perihelion trends diverge: Temperatures at depths >0.5 m still increase and show an orbital lag. The pre-perihelion temperature distribution in contrast is characterised by a

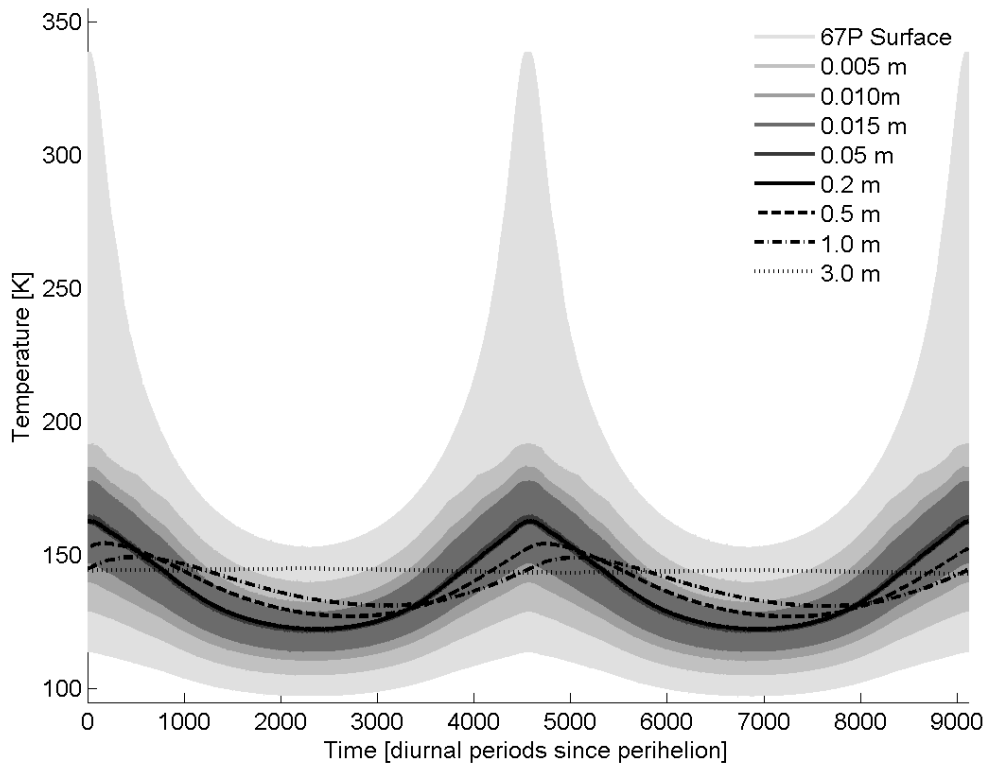


Figure 2.16: Temperatures at nucleus surface and eight different depths up to 3 meters for two orbital revolutions of 67P/CG for case *Sublim*, the sublimation front is at 0.005 m depth.

significant net heat transport to deeper layers.

The described effect is stronger if the thermal model does not include a heat sink by sublimation: Thermal lag, if compared pre- and post-perihelion, is stronger and leads to higher temperature differences in deeper layers of the comet. A comparison of the diurnal thermal waves for both models *RadEqu* and *Sublim* for perihelion and aphelion is detailed in Figure 2.18.

The existence of a temperature-dependent heat sink due to sublimation at a depth of 5 mm has a significant impact on the calculated temperatures, especially at perihelion: Subsurface average temperatures are up to 80 K lower; below the sublimation front, the bandwidth is tremendously reduced to 60 K. As the heat is removed from the nucleus by sublimation, the *Sublim* thermal model also reveals lower temperatures in depths that are not affected by the diurnal wave. The aphelion temperatures, far away from significant sublimation figures, show a negligible temperature at surface and layers until 20 cm depth. Nevertheless, beyond that there is an impact of the missing sublimation enthalpy for the *RadEqu* model, and hence higher temperatures. The history of 67P, as outlined in previous chapters, does indicate much lower temperatures at greater depths which this model approach does not show due to its limitations. Applying lower temperature boundary conditions at a depth of 5 m would be possible if there is material removal included in the

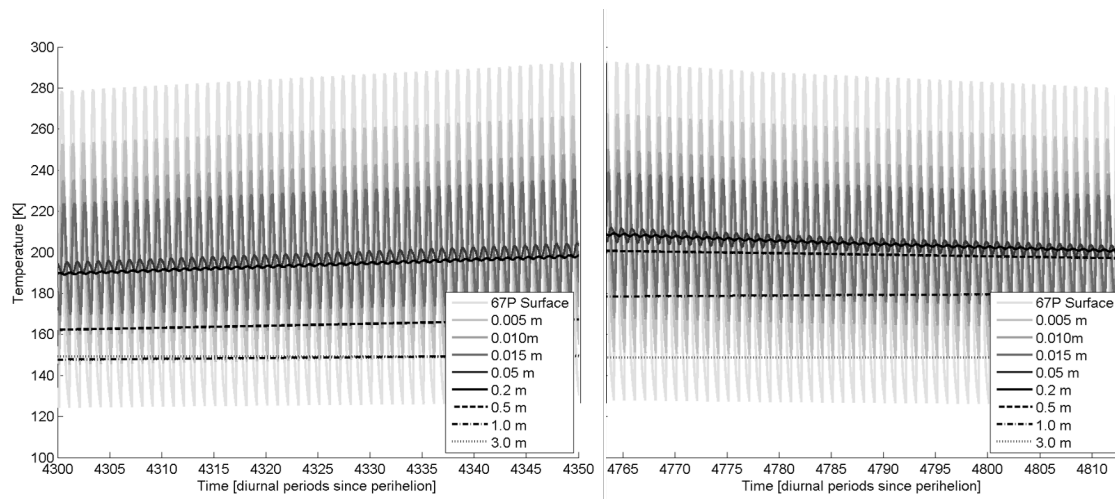


Figure 2.17: Case *RadEqu* diurnal thermal wave: 67P Temperatures at nucleus surface and eight different depths between 0.005 m and 3 m for a total of 50 diurnal revolutions before (left) and after (right) perihelium. Surface temperatures range between extremes of 122 and 294 K, internal nodes show smaller bandwidths. The diurnal thermal wave reaches values of <1 K at depths >0.02 m.

model, but this adds two more parameters to chose from to the analysis.

2.5.5 Surface property alteration by impacting objects

The physical properties of the cometary nucleus analysed in the previous chapter have been those of a primitive surface with no alteration of the agglomerate textures. Vincent *et al.* (2015a) suggested that impact events on cometary nuclei will alter the morphology of the surface by creating crater geometries depending on impact velocity, and locally reduce porosities: Material gets compacted through the impact, to a larger degree at the impact zone, but as well in the ejected and backfalling material. Two effects can be derived that affect the thermal behaviour: First, there is a formation of a crater topography with crater walls that shadow the influence of the sunlight and also reduce reemission of infrared emission towards space. Second, the compaction of material influences its thermal conductivity, as detailed in the approach of Krause *et al.* (2011) and shown in Table 2.3. The thermal conductivity of a highly porous nucleus will increase from values around $0.0017 \text{ Wm}^{-1}\text{K}^{-1}$ to $0.0034 \text{ Wm}^{-1}\text{K}^{-1}$. The gain is higher for moderate porosities; it changes from 0.012 to $0.069 \text{ Wm}^{-1}\text{K}^{-1}$.

Temperatures tend to be affected by these changes, as indicated by Figure 2.19. In all cases, higher porosity, hence lower thermal conductivity, correlate negatively with thermal skin depth. Average temperatures in subsurface layers tend to be warmer for lower porosities. The formation of a crater wall leads to warmer environmental conditions.

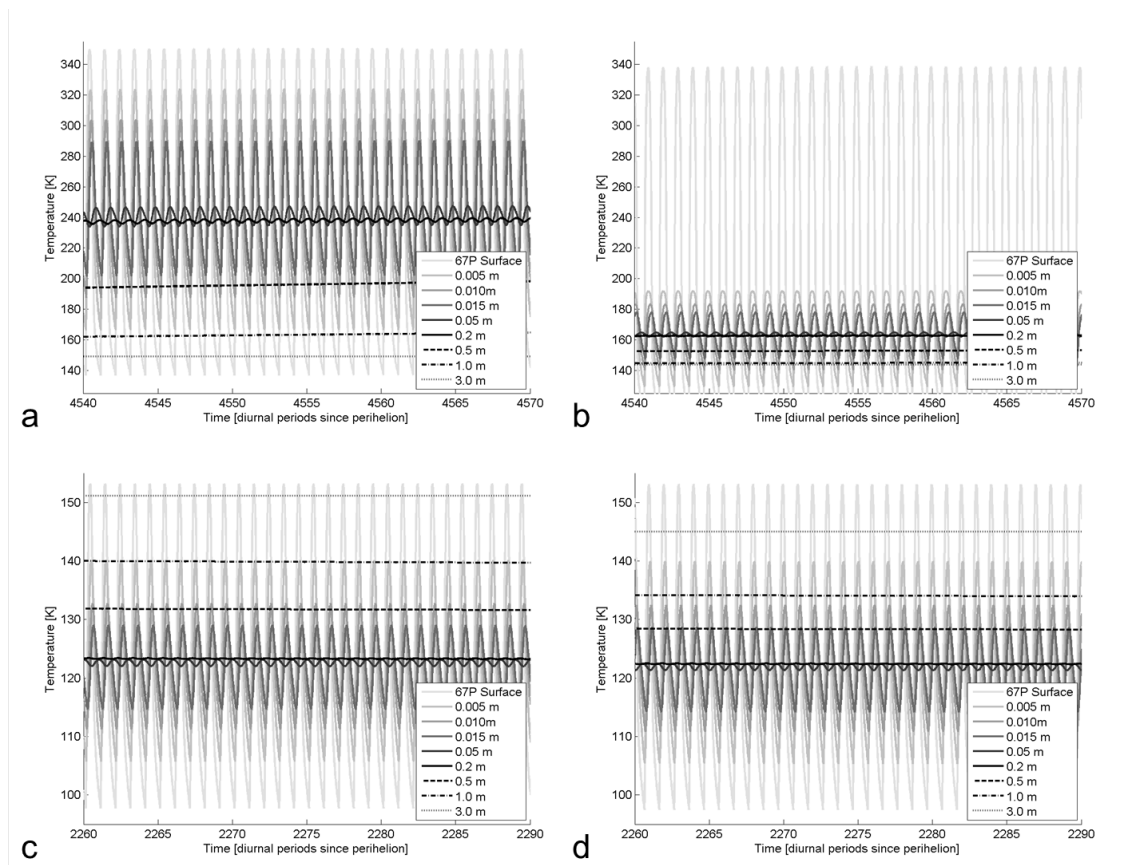


Figure 2.18: Cases *RadEqu* (both left, a and c) and *Sublim* (both right, b and d) at perihelion (both top, a and b) and aphelion (both bottom, c and d): Temperatures for 30 diurnal revolutions in nine depths between 5 mm and 3 m.

2.5.6 Model limitations and implications for resolved geometric thermophysical models

The presented analysis shows general trends and differences for a relatively simplified setting. Temperatures higher than 400 K should be taken with caution and are likely due to model constraints: In reality, crater walls receive emitted thermal radiation from the impact zone which results in a cooling effect of the crater floor. The effect of thermal self-heating is discussed in detail in following chapters, especially in the fracture analysis that considers fracture walls and their impact on the temperature patterns in great detail. Moreover, assumed thermal conductivities for low porosity cases are lower than derived by Rosetta instrumentation for the surface of 67P (Groussin *et al.* 2019). As the analysis focuses on distinguishing the two thermal waves, it ignores the fact that the interior of the nucleus may be significantly colder. Setting a temperature boundary condition at the interior, the erosive mass losses have to be known to give reasonable results.

Nevertheless, the generic 67P thermal model is able to show temperature variations over the orbital period and effects of diurnal thermal waves. Nevertheless, there is much more complexity that needs to be addressed: The tilted axis of 67P leads to short but intense southern summers during perihelion, while the northern hemisphere is mostly

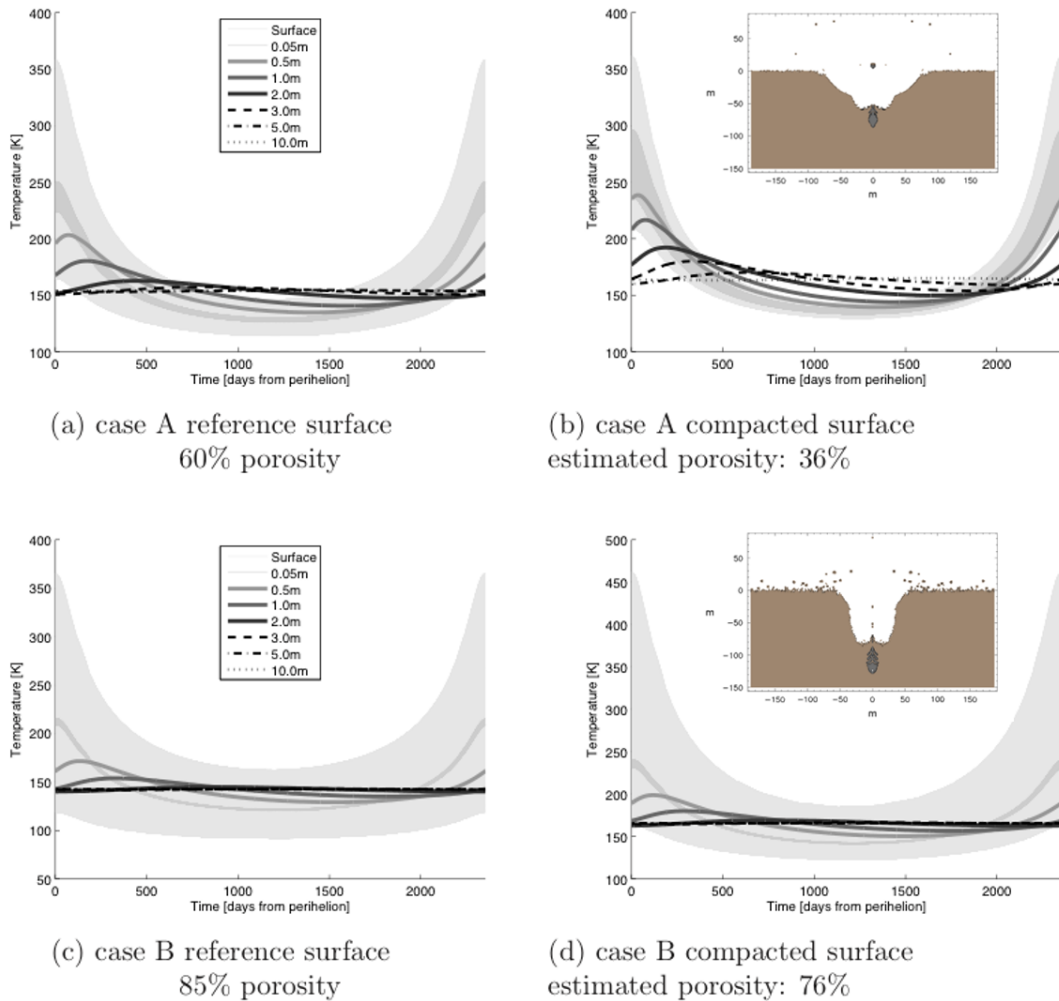


Figure 2.19: Four thermal wave simulations showing different temporal temperature behaviour and the effect of the compaction, as published in Vincent *et al.* (2015a). Image credits: Craters on comets, Planetary and Space Science, Volume 107, Figures 6 a,b and 8. The first row represents the surface used in our crater experiment A, before and after impact. The second row represents the surface used in crater experiment B before and after impact. All figures display the orbital variations of temperature, the area indicate the diurnal thermal wave variations. Diurnal variations become negligible at depths around 50 cm from the surface in all cases. Areas with high porosity show a rapid decline of the thermal wave with depth, while compacted material allows the wave to penetrate to deeper layers. Compaction also increases the equilibrium temperature at greater depths: (a) case A reference surface 60% porosity; (b) case A compacted surface estimated porosity: 36%; (c) case B reference surface 85% porosity; and (d) case B compacted surface estimated porosity: 76%. (b) and (d) show the cross-section of the crater morphology, derived from numerical simulations, in the small center window.

illuminated at higher distances from the sun. The bilobate shape of the nucleus, and the peculiar topography with numerous cliffs and sinkholes (Vincent *et al.* 2015b) lead to a great variety of insolation patterns. The temperature pattern of Figure 2.19 (d) is indicative of a shadowed crater floor. To constrain the thermal behaviour of 67P, the effect of terrain morphologies shall be studied. Topographies that differ from flat shapes, subsumed under the term of surface roughness, can be found on all scales – from the irregular shape of the nucleus itself, to the constituents of the single agglomerates.

3 Model application to fractured topographies

This section describes the application of the derived thermophysical model to the fracture topographies observed on 67P. The analysis and its results have been published as Hoefner et al, *Astronomy & Astrophysics*, Volume 608, A121. The contents are reproduced with permission ©ESO, fully consistent with the version published in A&A.

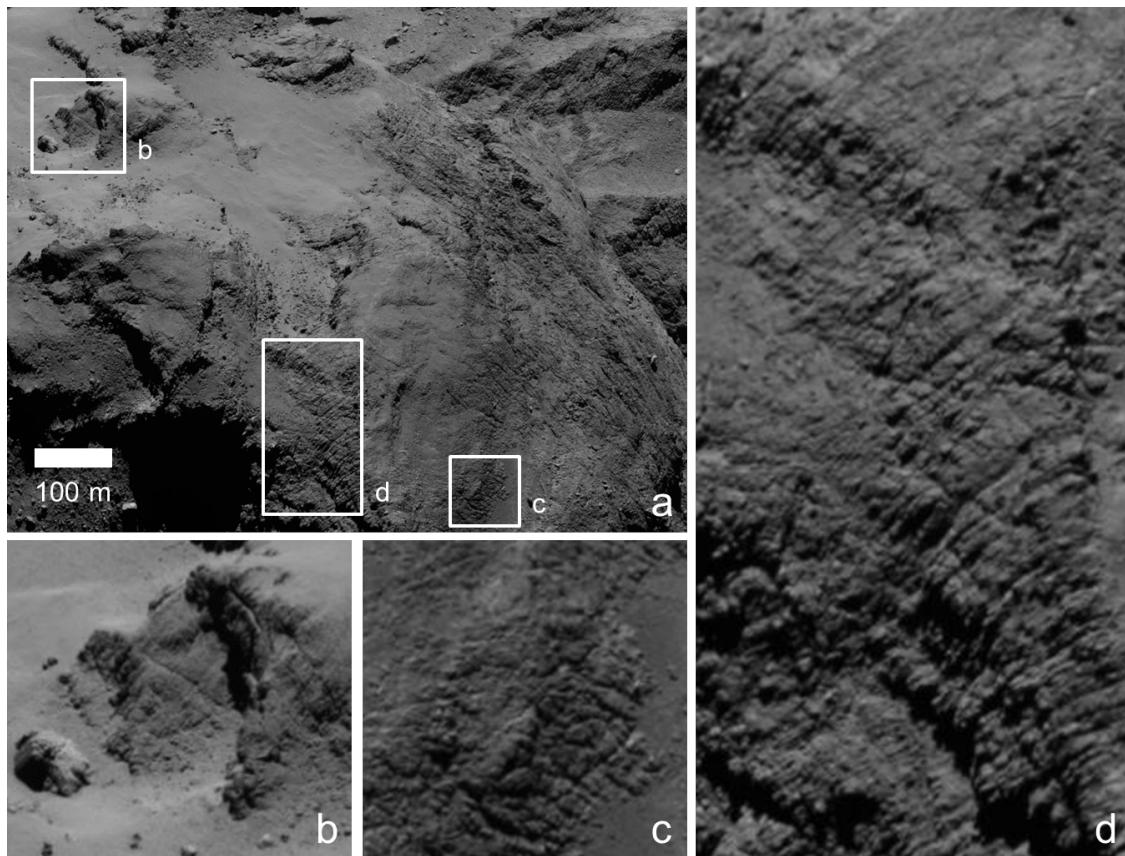


Figure 3.1: a) Fracture structure and their variety on the head of 67P, b) irregularly shaped fractures on a steep outcrop, c) complex fracture network surrounded by more smooth terrains, d) slope of consolidated terrain, strewn with fractures of similar size and all oriented in a predominant orientation (OSIRIS Image NAC_2014-09-14T16.21.40.802Z_ID30_1397549001_F41)

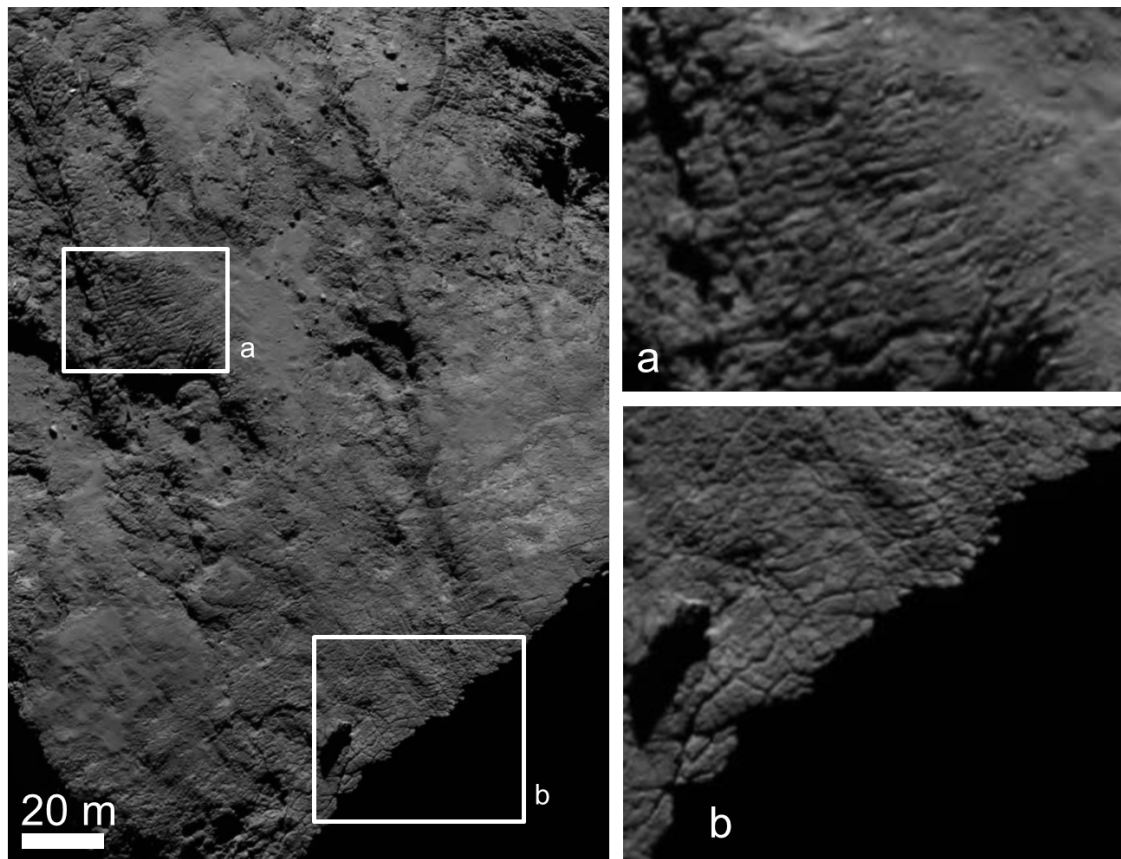


Figure 3.2: Fracture networks on 67P, in detail a) irregular fractures on top of a cliff, b) elongated polygonal fracture network (OSIRIS Image NAC_2014-09-15T11.32.07.326Z_ID30_1397549800_F22)

3.1 Observed fracture morphology and its variety

Morphological features like furrows and fractures dominate the consolidated terrains on 67P. Some areas show a coverage of mass-wasted material, leaving bare outcrops and fractured escarpments between smooth terrains, likely originating from low velocity air-fall (Thomas *et al.* 2015a). Beside the wealth in geomorphological variety, also the observed fractures come with great diversity. One example for the fracture variety is detailed in Figure 3.1: This area on the northern hemisphere of the head of 67P of less than one square kilometer (a) comprises irregular fractures at steep outcrop surfaces (b), a patch of complex fracture networks (c), and long linear fractures (d) with all of them in a predominant orientation. Nevertheless, there is no clear global predominant direction or pattern of the fractures and furrows; some can be attributed to layering (Ruzicka *et al.* 2018). Different locations of patches of consolidated terrain bear no obvious reason that this direction is driven by erosion, insolation, or layering of the comet.

El-Maarry *et al.* (2015a) give an overview and classification of fractures. There is a clear distinction between single and unique fractures, and those that appear in patches – mostly due to divergent formation mechanisms. The most common type of fractures has a width ≤ 1 m, the length embraces sizes from a few meters to several hundred. The

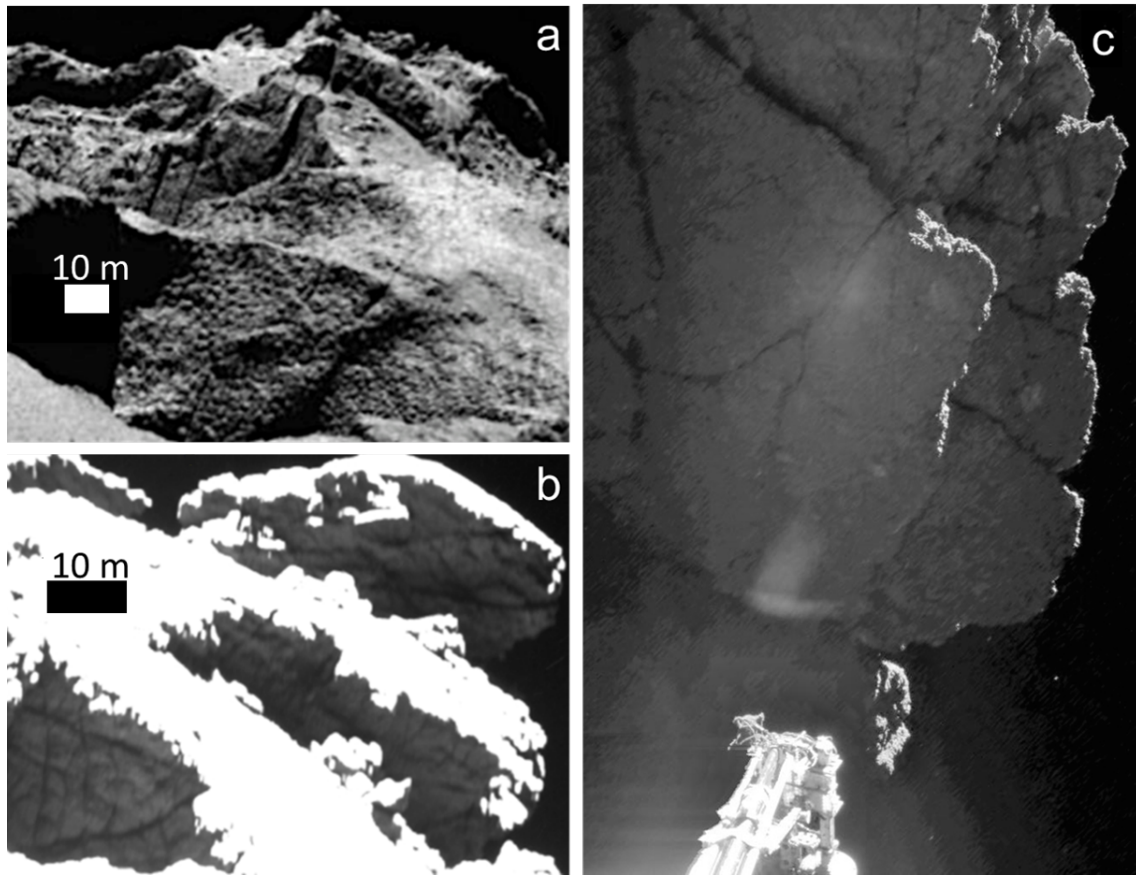


Figure 3.3: a) OSIRIS image NAC 2014-09-22T12.50.19: Polygonal structures formed due to thermal stresses (Auger *et al.* 2018) or clods that are cometary building blocks (Davidsson *et al.* 2016)? OSIRIS NAC revealed structures from the walls of a pit or sinkhole. b) NAC_2014-10-14T18.58.11.922Z_ID30_1397549400_F22: The shadowed rocky terrain is overexposed to reveal the hidden fracture network, secondary illuminated by reflections of the terrain directly in front of it. c) CIVA camera 1 showing a fractured block (Poulet *et al.* 2016) including retraced cracks in the surfacial texture; Image credits: ESA/Rosetta/Philae/CIVA

surrounding area can be flat or slided. Fractures show a tendency to appear grouped, but their intersection angles and distances vary, especially when comparing the topography of patches from two different locations. Outcrops of consolidated material sometimes show that fractures cut through strata (Giacomini *et al.* 2016) which can be seen as evidence for the existence of layers (Massironi *et al.* 2015). Especially boulders appear to be overrepresented among fractured terrains: most of the larger ones are fractured to a great extent. Beside fractures, patches of polygonal networks (Auger *et al.* 2018) are present on the nucleus. Two examples are detailed in Figure 3.2, one of them (b) shows a smooth transition between fractures and polygonal structures.

3.1.1 Cometary building blocks or polygonal contraction cracks?

The walls of large pits and several areas on the northern hemisphere of 67P showed structures nicknamed as “goosebumps” (Sierks *et al.* 2015, Davidsson *et al.* 2016) and clods that could pass as building blocks of the cometary formation period (Figure 3.3 a). Auger *et al.* (2018) identified a variety of differences among them, with the trough geometry being one of them. One possible explanation is an ageing process through surface erosion forces. The initial formation of these networked fractures might be cracking by thermal contraction; the loss of volatiles and the linked desiccation can form erosion patterns and play a role in this formation scenario.

The typical length of such a polygonal side is between one and five meters. Smaller fractures are hardly being observed, as the image resolution restricts the discovery of smaller structures. However, the rough appearance of the terrain beneath existing fractures due to the variations in small-scale illumination conditions keep small scale furrows within the realms of possibility. The Rosetta lander Philae hosted five CIVA cameras that imaged the landing site (Bibring *et al.* 2015, Poulet *et al.* 2016). The cameras detected fractured areas, but these fractures showed some differences to those detected by OSIRIS. As expected, these fractures have smaller dimensions than those resolved from orbit - CIVA found that these micro-fractures are not longer than 50 mm (Poulet *et al.* 2016), and likely to form along the texture of the surface material.

3.1.2 Illumination and implications on fracture topography

The illumination condition of the imaged area and the position of the remote sensing spacecraft impact the retrieved images of the nucleus surface. During the mapping phases of the Rosetta mission, the camera pointing was oriented towards nadir within a pointing range of a few degrees to image the entire nucleus. The minimum distance to the nucleus was around 20 km, interrupted by flyby manoeuvres which allowed for a closer encounter of about 1 km. In the final mission phase in September 2016, with the ultimaded descending trajectory and the targeted crash landing of the Rosetta orbiter on the surface of the nucleus, images from distances of hundreds of meters have been acquired.

Mapping phase images (which aimed at the setup of a three-dimensional map of the nucleus) were mostly taken during terminator orbits, orbital phase angle and likewise the solar illumination angle on the nadir point were large. Due to the irregular and bilobate shape of the nucleus and the local inclination of the terrain, this results in a wide range of illumination conditions. The local inclination of the fracture plane is a vital parameter to derive topography and cross-section of a typical fracture. For a better understanding of processes in the subsurface of comet 67P, it is also vital to have a good estimate of the fracture depth - at least how deep they are penetrating into the interior of the nucleus.

One can apply two ways to set limits to the parameters of observed fractures: First, comparing images from a flyby sequence with several consecutive illumination conditions of the nucleus surface (e.g. Masoumzadeh *et al.* (2017)). Figure 3.4 covers three different incidence angles ranging from roughly 15 degrees to direct opposition (with the sun being in line with the Rosetta spacecraft). During the sequence, the nucleus rotated around its z-axis for another 50 minutes, which is equal to about 25 degrees. Rosetta roughly kept its position and pointed nadir during the manoeuvre. The red boxes of Figure 3.4 a-c show

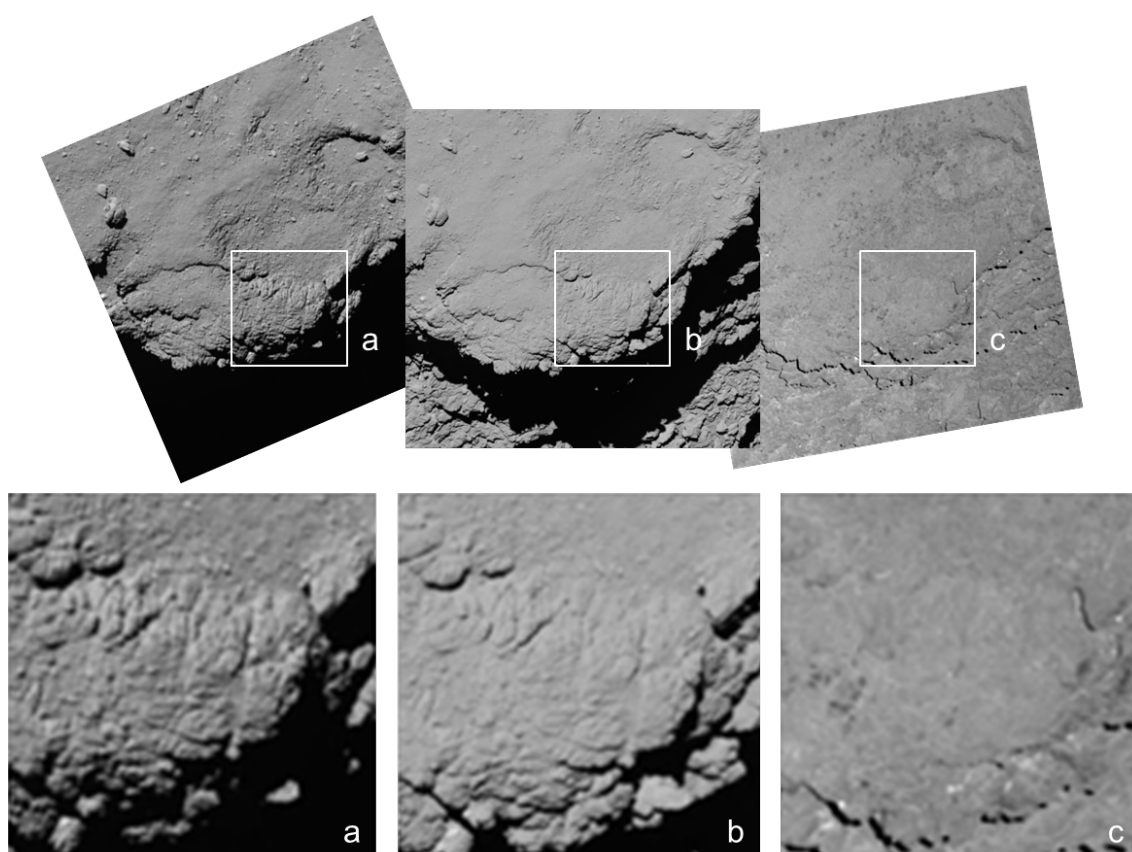


Figure 3.4: Fly-by sequence close-up images for three different phase angles reveal the fracture topography and depict the sequential evolution of the reflectivity of the fracture: a) NAC_2015-02-14T11.49.31.363Z_ID30_1397549000_F82 b) NAC_2015-02-14T12.21.58.746Z_ID30_1397549000_F82 c) NAC_2015-02-14T12.40.09.089Z_ID30_1397549001_F84

the sequential evolution of the reflectivity of the fracture sides. Even at an incidence angle of zero degrees, the fracture is slightly darker than the environment. At an incidence angle of 15 degrees, both walls are clearly distinguishable; the dark side might even be partly in shadows.

Secondly, choosing an outcrop for analysis that has been imaged well-resolved about more than three times, from several directions and by the help of various illumination conditions. The nicknamed ‘slingshot fracture’, depicted in Figure 3.5 can be treated as a good example. The solar incidence angle can be estimated through a combination of the orientation of the facets that form the outcrop, and its local illumination conditions. Therefore, one can apply a high-resolution 3D shape model of 67P (Preusker *et al.* 2015), shown in Figure 3.6 and derive the local inclination from the according facet.

The steep fracture wall creates a shadow on the opposite side walls or the bottom of the furrow. Its inclination angle can be estimated by interpreting the shadow in different illumination conditions: If a shadow exists under all circumstances, it indicates that the wall angle of the fracture side wall exceeds the incidence angle of insolation. The slingshot fracture wall angle for instance could be limited to values of ≤ 25 degrees. A

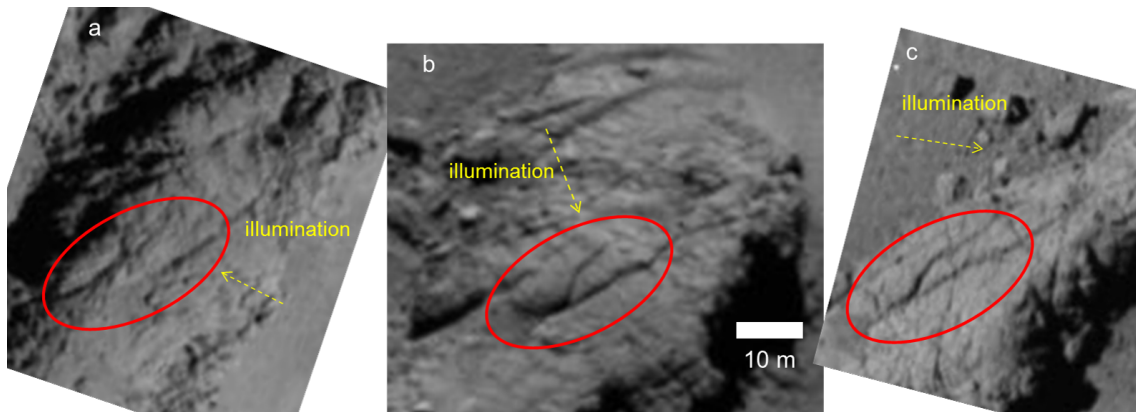


Figure 3.5: Three cutouts of a terrain feature on the head of 67P: the nicknamed ‘slingshot fracture’ highlighted in red in region Maat in three different illumination conditions in September 2014 (a,b) and March 2015 (c). The arrows roughly show the incident solar illumination. a) NAC_2014-09-14T03.51.26.800Z_ID10_1397549001_F41 b) NAC_2014-09-19T23.09.40.111Z_ID30_1397549000_F24 c) NAC_2015-03-28T16.12.49.393Z_ID30_1397549000_F82

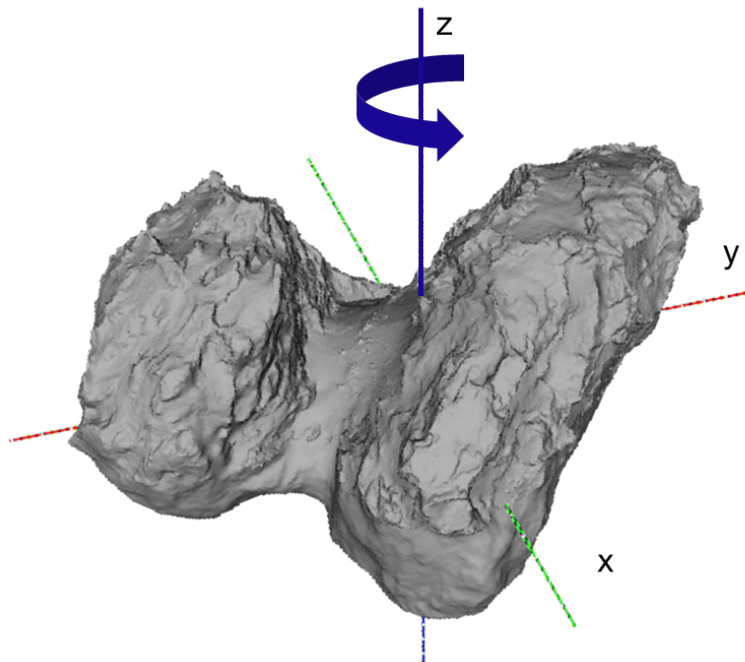


Figure 3.6: Shape model of 67P (Preusker *et al.* 2015): The geometry of 67P is represented with triangular facets; the z-axis is the rotational axis. The brightness of a facet depends on its orientation and produces the impression of illumination; shadowing is neglected.

Table 3.1: Model fracture parameter variations: Each fracture geometry is defined by bottom width w_b and top width w_t . Angles are described in Figure 3.9. The apex angle γ is given for a case where the solar plane and the fracture axis share an angle of 30 degrees.

Fracture Geometry	w_b [m]	w_t [m]	α [deg]	γ [deg] $\eta = 30$ deg
A1	0.1	0.1	0.0	11.4
A2	0.1	0.2	2.9	22.6
A3	0.1	0.3	5.7	33.4
A4	0.1	0.4	8.5	43.6
A5	0.1	0.5	11.3	53.1
A6	0.1	0.6	14.0	61.9
A7	0.1	0.8	19.3	77.3
A8	0.1	1.0	24.3	90.0
B1	0.2	0.3	2.9	33.4
B2	0.2	0.4	5.7	43.6
B3	0.2	0.6	11.3	61.9
B4	0.2	0.8	16.7	77.3
C1	0.4	0.6	5.7	61.9
C2	0.4	0.8	11.3	77.3
C3	0.4	1.2	21.8	100.4
C4	0.4	1.6	31.0	116.0

qualitative statement on the geometry of the bottom of the fracture cannot be retrieved from the data.

One must admit that there is limited confidence in the validity of this strategy. Local surface morphology was not resolved to meters. The texture of the consolidated terrains outlines a high roughness on a variety of length scales. Aside, there is no “typical” fracture topography, but a wide range of fracture types and morphologies.

From these constraints, a conclusion is that a consistent strategy to describe thermophysical patterns shall make use of a parametric geometrical model with a broad variation of different geometrical setups. A wealth of analysis respecting various geometries then will allow for condensing meaningful results.

3.2 Parametric fracture geometry and composition

The prerequisite of a thermophysical analysis is the definition of a typical fracture geometry and its physical structure.

Geometric model variations are based on the derived upper limit wall angle of roughly 25 degrees. The model fracture surface consists of a bottom surface, two inclined side walls, and two perpendicular end walls. A set of 16 different geometries was defined, varying in fracture bottom width w_b , and divided into three subgroups A, B and C (see

table 3.1). The A series consists of eight model fractures with a bottom width of 0.1 m, the top width varies between 0.1 and 1.0 m. Thus, the ratio w_t/w_b varies between 1 and 10, this leads to wall angles α between 0 and 24.3 degrees. The B and C series use a broader bottom width of 0.2 and 0.4 m and they cover w_t/w_b ratios between 1.5 and 4. The resulting wall angles cover 2.9 to 16.7 deg for B, and 5.7 to 31.0 deg for the C series. All model fractures share the same length l of 5 m and a height h of 1 m.

The location of volatiles determines the position of sublimation heat sinks within any model fracture. Formation history and fracture ageing might have led to different compositional textures and distribution of volatiles. This study takes four different compositional variants into account, depicted in Figure 3.7:

1. A fully inert fracture without volatiles, the composition is uniformly those of agglomerates of dust particles; no sublimation processes occur. A fully inert fracture can also be regarded an acceptable assumption if the volatiles have retreated beyond the thermal wave penetration depth.
2. In an icy-bottom fracture, dusty agglomerates which lost their volatiles form the side walls, while the bottom (still) consists of a dust-ice mixture. This compositional assumption partly applies to fractures whose side walls are split into an ice-free top part, and the lower areas (still) volatile-rich.
3. Fully icy fractures are composed of a dust-ice mixture in their entirety, similarly homogeneous as the fully inert fractures.
4. Icy layer fractures fill the gap between a fully inert fracture and the icy bottom fracture. Here, both side walls and the fracture bottom are covered by dusty agglomerates. While the sides are inert (respectively the volatiles are buried under thick dust layer such that they do not interfere in the local thermodynamics), the dust-ice mixture in the bottom of the fracture is located at depth of several mm. This depth is varied in the icy layer analysis.

The fracture geometry adds shadowing effects. Shadows move with the position of the sun, a high resolution of facets is required to resolve the spatial effects. The bottom area is represented by 40 facets, side walls are spatially resolved by 400 rectangular facets. Each facet is represented by a flat rectangular surface cell element. The perpendicular end wall is modelled by 20 trapezoid facets. In total, every model fracture contains 480 facets, designed to act as surface thermal nodes. Figure 3.8 depicts all 16 model fractures; table 3.1 describes the geometry model variations.

3.3 Insolation conditions of fractured terrain

Absorbed solar irradiation impinging on a model fracture is the only source of heat in the analysis, dominating the fracture temperature pattern. The absolute value of the irradiation vector varies with the distance to the sun, while the diurnal illumination is determined by the rotation rate and the solar exposure. The diurnal rotation period of 67P during its perihelion approach was determined to be 12.4 h (Mottola *et al.* 2014). Non-gravitational force modelling predicted that the spinning rate would speed up during the perihelion

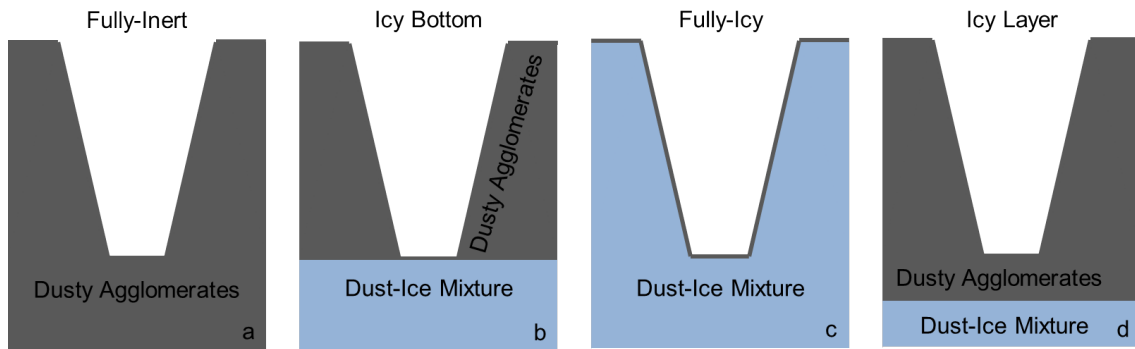


Figure 3.7: Cross section through four configurations of model fracture compositions: a) fully inert fracture without sublimating ices, b) icy bottom fracture distinguishes between a dust-ice mixture at the bottom and dusty agglomerates at the side walls, c) fully-icy fracture that consists of a dust-ice mixture, and d) an icy layer in a predominantly dusty fracture, the ice is restricted to the bottom of the fracture, and buried under a layer of dust.

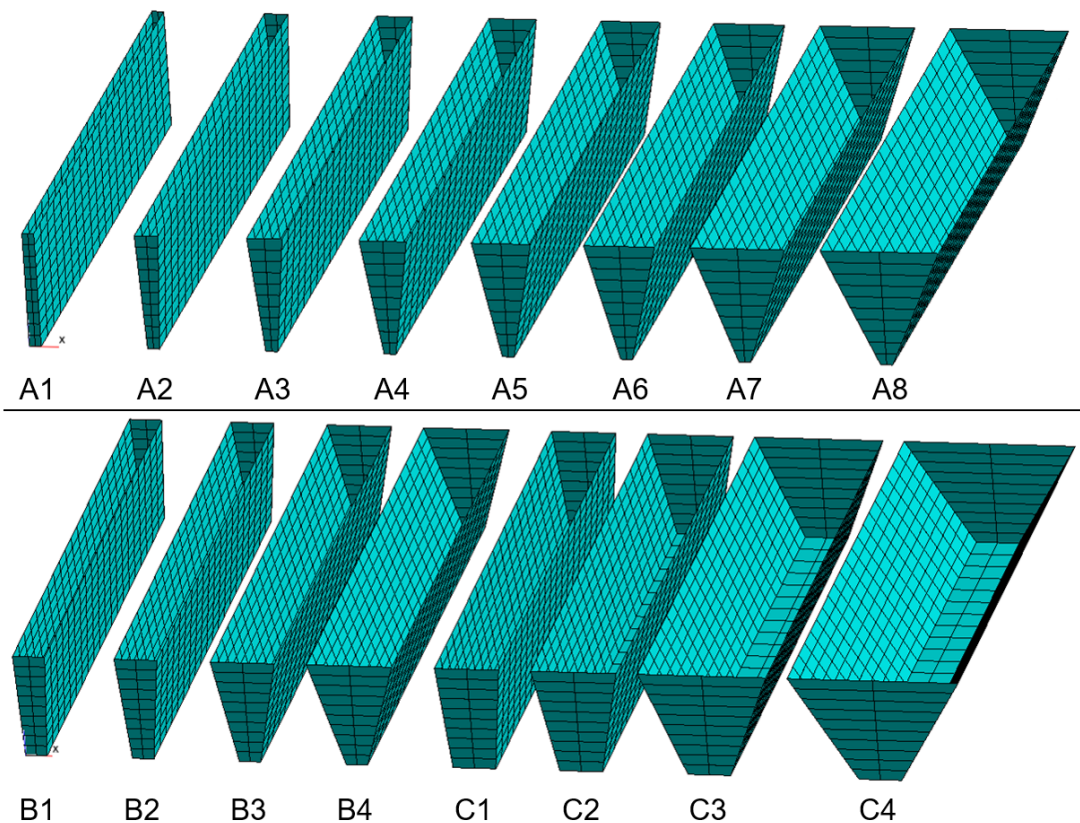


Figure 3.8: Definition of a model fracture geometry. Upper row: fracture geometries of the series A with A1 (first from left) to A8 (first from right) in ascending numeration; Lower row: B1 (left) to B4 (fourth from left side); C1 (fifth from left) to C4 (first from right)

passage, which was confirmed by observations (Keller *et al.* 2015). Earlier observations of the light curve of 67P had detected even longer rotation periods (Lowry *et al.* 2012), so this trend is not unanticipated. The analysis of an entire 67P model fracture rotation around the sun requires the setup of a solar vector plane that includes all solar vector orientations and their time-dependency.

The interaction between solar irradiation and fracture is described by the plane angle η . The plane angle itself is defined by solar plane and fracture plane. The fracture plane is set up by length and height vector of the respective model fracture and therefore independent of the fracture geometry. The basic assumption is that the solar plane is perpendicular to the fracture surface (which is formed by w_i and l), as illustrated in Figure 3.9.

The apex angle γ lies in the solar plane, and it takes into account the geometry of the fracture. To visualize this angle, one can describe a hypothetical observer located in the middle of the fracture floor. The solar irradiation vector virtually moves around the fracture, at some point it starts to illuminate this position, considered to be local “sunrise”. The cometary day passes on, with the sun (respectively the solar vector) moving on until the position of its apparent “sunset”. Local sunrise and sunset positions are in the solar plane. If one takes this observer position as angular point of view and define the vectors to sunrise and sunset positions as half-lines, the apex angle γ of that model fracture is obtained. It describes the span when the center of the fracture floor is illuminated directly. The time interval of solar irradiation, restricted to a diurnal period, can be determined to $T_{\text{irr}} = P_{\text{diu}}\gamma/2\pi$. The apex angle γ is depicted in Fig 3.9. The descriptions of fracture side walls and bottom are purely geometric and refer to the solar vector, while neither gravity vector nor the exact position on the nucleus are relevant.

The model insolation geometry requires the solar plane to be perpendicular to the rotation axis. Strictly speaking, these conditions are met for equinox only, which in the course of the Rosetta mission was reached on May 11th 2015 at a heliocentric distance of about 1.67 AU. The obliquity angle, the tilt of the rotation axis with respect to the orbital plane of 67P is 52 degrees. This means that the “solar plane” actually is a conical surface, with a varying cone angle that equals the current angle between rotation axis and solar vector. The maximum conical angle is reached at both solstices, the southern solstice was reached about a month later than the perihelion passage, on September 5th 2015. Such a complex solar plane combined with a highly elliptical orbit leads to strong variations in illumination conditions for a single fracture during one orbit. The inclination of the solar vector is addressed by the analysis (Figure 3.9). The “solar plane” can be tilted, with a model fracture illuminated under a tilting angle.

In contrast to equinox configuration, one considers an exemplary patch of fractures, located in the northern planes. This area is illuminated for a long time during perihelion approach between 4 and 2 AU. The diurnal variations are modest, as the area is in constant sunlight. Irradiation intensity increases with the approach to the sun, while the obliquity of the spin axis leads to shallower illumination angles and a decrease of illumination times. Conclusively, in the course of an orbit, the fracture illumination pattern drastically changes. Additionally, the irregular shape of 67P adds complexity to the real insolation condition: the bilobate shape, as well as large cliff structures and pits add nearly random shadowing to certain areas. Self heating from exposed illuminated areas also affect the thermal budget of the fracture surfaces. In consequence, the irradiation pattern for every fracture is close to being unique. Thus the analysis is restricted to variations of the plane

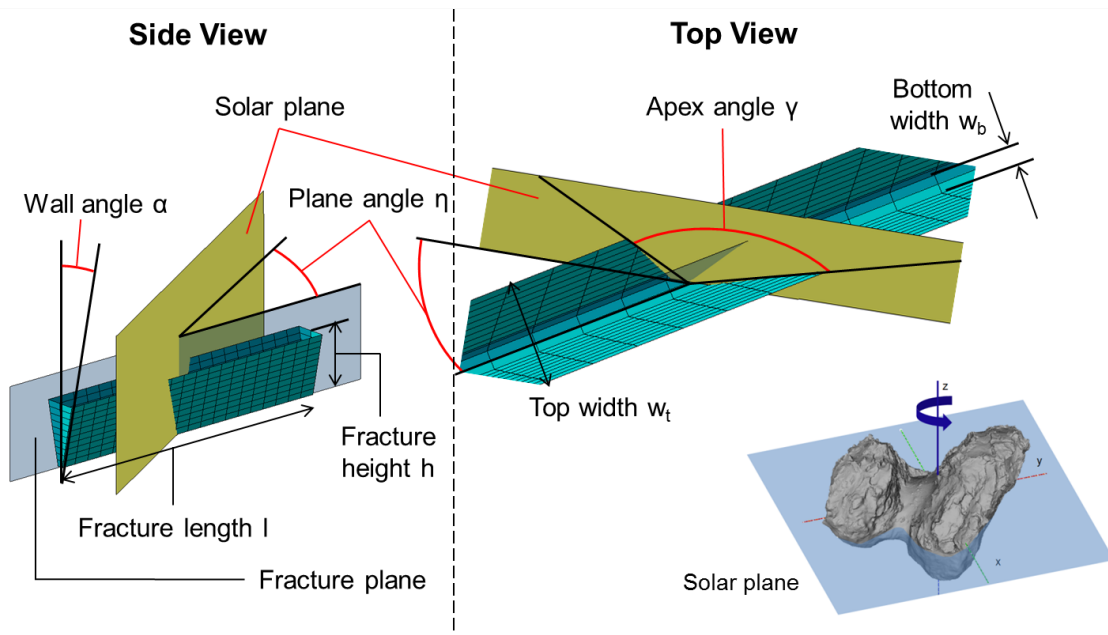


Figure 3.9: Parametric geometric model definition for a generic fracture, side view (left) and top view (right). The solar plane in respect to the nucleus rotation axis of 67P at equinox is depicted in the right bottom corner. The sun in its zenith position irradiates perpendicularly on the fractures.

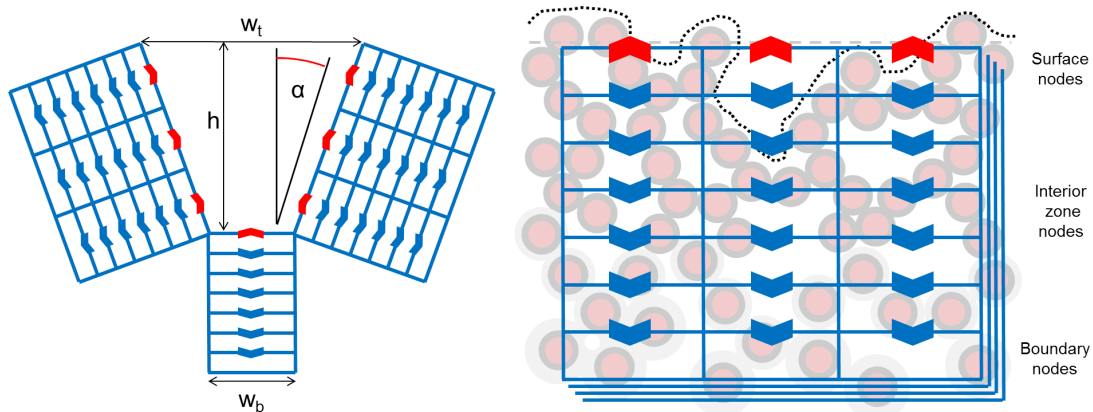


Figure 3.10: Nodal breakdown of a generic model fracture: cross section (left) and detailed nodal resolution of a typical fracture floor (right).

angle η , which leads to a widespread range of apex angles γ (Table 3.2). The maximum apex angle always is smaller than π , as the model fracture length is restricted to 5 m.

Table 3.2: Model fracture parameters: Apex angles γ for variations of the plane angle η

Fracture Geometry	γ [deg] $\eta = 0$ deg	γ [deg] $\eta = 30$ deg	γ [deg] $\eta = 60$ deg
A1	157.4	11.4	6.6
A2	157.4	22.6	13.2
A3	157.4	33.4	19.7
A4	157.4	43.6	26.0
A5	157.4	53.1	32.2
A6	157.4	61.9	38.2
A7	157.4	77.3	49.6
A8	157.4	90.0	60.0

3.4 Energy balance in a model fracture

3.4.1 Thermophysical model assumptions

The thermophysical analysis of the model fracture is based on a finite difference computation scheme. The data points are volume elements, each with an attributed heat capacity, and referred to as nodes. Facets are surface nodes and in radiative contact to other surface nodes. The fracture model takes radiative and conductive interactions into account. Sublimation of volatiles is restricted to H₂O. Deposition process, gas diffusion and gas-solid interaction are neglected. Processes in the coma of 67P are treated as not being relevant for the thermodynamics of fractures, radiative influence of the coma is excluded.

An overview on nodal dependencies is given in Figure 3.10. Red arrowheads indicate that the respective node is a facet and exchanges radiation with other facets, while blue ones describe conductive heat exchange including internal radiative processes.

The model fracture consists of a three-dimensional mesh of about 24,000 nodes, 480 of them surface nodes. These surface node facets are quadrilaterals with side walls in the order of tens of centimeters, well beyond the diurnal skin depth. Modeling the conductive heat transfer between adjacent facets would lead to very small thermal exchange rates, as thermal gradients are low and distances high. Therefore a full 3 D thermophysical model with heat exchange to all adjacent nodes is not required; thus conductive heat transfer is restricted to neighboring nodes perpendicular to the surface of fracture bottom and side walls, named columns. The general thermal balance equation of each single node i then is

$$Q_{\text{con},im} + Q_{\text{con},in} + \sum_j Q_{\text{rad},ij} + Q_{\text{rad},space} + Q_{\text{abs},i} + Q_{\text{sub},i} = Q_{\text{cap},i} \quad (3.1)$$

For a surface node with subscript i , all facets in radiative contact are denoted by j . The radiative thermal flux, emitted from node i and received by node j , is described by $Q_{\text{rad},ij}$. The emitted flux to space is characterized as $Q_{\text{rad},space}$. Neighbouring nodes (nodes i and m respectively n) perpendicular to the orientation of the respective surface of the fracture part (including floor and walls) share a conductive heat flux $Q_{\text{con},im}$, respectively $Q_{\text{con},in}$. The absorbed solar irradiation is denoted $Q_{\text{abs},i}$, $Q_{\text{sub},i}$ characterizes the heat sink

due to the sublimation processes. $Q_{\text{cap},i}$ denotes stored or released internal energy in the node. In the following subsection, the heat flux terms are described in detail.

3.4.2 Heat conductivity in subsurface fracture layers

The temperature-dependent effective thermal conductivity in the layer $\lambda_{\text{L,eff}}(T_{i,k})$ is based on the approach of single grains forming agglomerates and takes into account conductive and radiative processes; radiative heat transfer dominates the term. Q_{con} is modeled by taking the interpolated temperature of the adjacent nodes i and m (for conduction towards upper layers) respectively n (for conduction to lower layers) and applying equation 2.12:

$$T_{i,m} = \frac{T_i \Delta z_i + T_m \Delta z_m}{2 \Delta z_{i,m}} \quad (3.2)$$

The length of nodes in z-direction are given by Δz_i and Δz_m , distances between adjacent nodes then is denoted $\Delta z_{i,m}$ and $\Delta z_{i,n}$.

Thermal conductivity is widely affected by the texture and the porosity of the agglomerates that form the nucleus of 67P. The temperature-dependent effective thermal conductivity is depicted for four cases in Figure 3.11; the derivation of the conductivity is described in section 2.2.5.

3.4.3 Radiative transport between surfaces facets

The fracture geometry is particularly sensitive to the calculation of view factors. The classical approach to calculate view factors, $F_{ij} = (A_j \cos \theta_i \cos \theta_j) / (\pi d_{ij}^2)$, see equation 2.5 is not in all cases compliant with the requirement of $d_{ij}^2 \gg A_i + A_j$. In short, the aforementioned approach can lead to a view factor sum that is greater than one; this violates radiative flux laws and is therefore considered as not accurate enough (Davidsson and Rickman 2014, Davidsson *et al.* 2015). Model facets emit thermal radiation with a lambertian distribution and do not favor a specific vector. To account for this, radiative exchange factors F_{ij} are calculated by using a numerical approach with a Monte-Carlo ray-tracing algorithm. View factors are determined by emitting a total of 10000 rays from every facet i in random directions (randomized over the half sphere above the facet; the angle between emission vector and facet normal always is below 90 degrees). The amount of rays that reach facet j are then counted and weighted with the emissivity of the facet. The fraction $1-\varepsilon$ on facet j is reflected in a random direction (similarly determined as the emission vector for facet i) and might be reabsorbed by facet k . The relation between rays absorbed at facet j absorbed and emitted at facet i determine the view factor $F_{i,j}$ between both facets. In this way, facets i and k (which might not be in direct radiative contact) also share a view factor $F_{i,k}$. So, this algorithm includes multiple reflections through rays that are scattered from third party facets. Rays that do not reach any other facet contribute to the view factor $F_{i,\text{space}}$ to deep space.

3.4.4 Absorbed solar irradiation

Similarly to the radiative exchange between facets, the absorbed insolation term $Q_{\text{abs},i}$ is derived by using the same Monte-Carlo ray tracing method; the albedo α replaces the

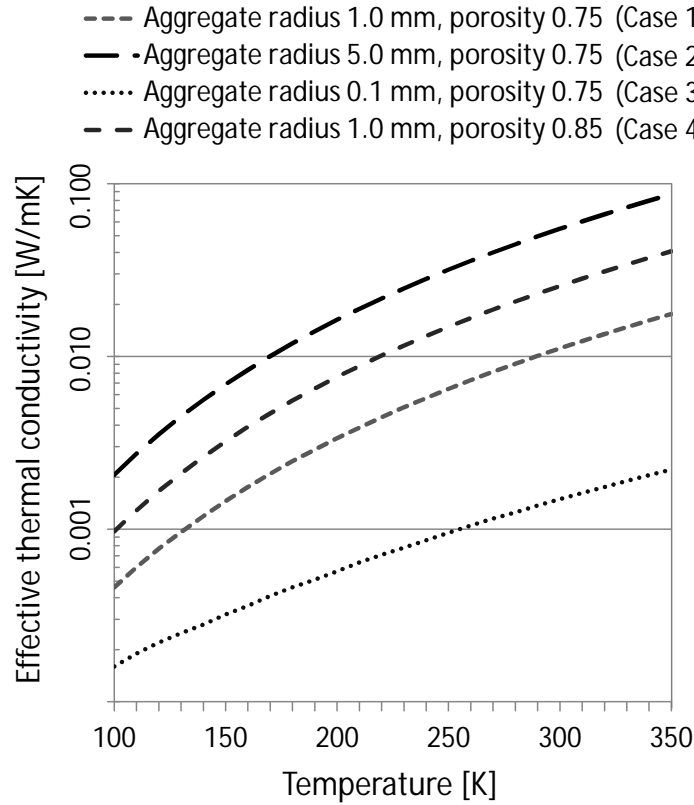


Figure 3.11: Temperature-dependent effective thermal conductivities for thermophysical parameter cases 1-4: R denotes the radius of the agglomerates according to R_A in Tab. 3.3, Case 4 assumes a high porosity of 85 % by lowering the fill factor of the agglomerate structure to 0.3. The derivation of the conductivity is described in section 2.2.5. These values are within the range constrained by a comparison between laboratory studies and Rosetta findings (Blum *et al.* 2017).

emissivity ε in the approach described in the last section. Solar irradiation is repetitively calculated for a step of 2 degrees of the solar plane, resulting in 90 values for the irradiation vector of a facet. Instead of a solar constant S , a time-dependent array $Q_{\text{abs,time},i}$ is used for each facet, replacing the standard approach of $Q_{\text{abs},i} = (1 - \alpha)S r^{-2} A_i \cos \theta$ with $S_{\text{abs,time},i}$. The absorbed solar heat flux then is time-dependent:

$$Q_{\text{abs,time},i}(t) = f_{\text{scaling}} S_{\text{abs,time},i}(t) \quad (3.3)$$

Irradiation patterns are independent of the heliocentric distance, total absorption values are not; thus a scaling factor f_{scaling} is introduced to transfer the 2.0 AU results to heliocentric distances between 1.25 and 5.0 AU. The corresponding time step is about four minutes, with linear interpolation to obtain values between these points.

Table 3.3: Thermophysical fracture model parameters for four compositions of the nucleus layers, denoted case 1 to 4. Cases differ in agglomerate size and layer porosity. Subscript explanations are given in Table 2.1.

Property	Unit	Case 1	Case 2	Case 3	Case 4
Flat surface albedo α	[-]	0.06			
Emissivity ε	[-]	0.97			
Density ρ_L	[$\frac{kg}{m^3}$]	500.0			
Specific heat capacity c_L	[$\frac{J}{kgK}$]	800.0			
Sublimation enthalpy H_{sub}	[$\frac{kJ}{kg}$]	2830			
Diurnal period P_{diu}	[h]	12.4			
Monomer radius r_M	[μm]	0.75			
Agglomerate radius r_A	[mm]	1.0	5.0	0.1	1.0
Layer fill factor ϕ_C	[-]	0.5	0.5	0.5	0.3
Agglomerate fill factor ϕ_A	[-]	0.5			

3.4.5 The sublimation front

Models with a dust-ice mixture include a term for sublimation, the sublimation front is restricted to one node per column. In the icy bottom and fully-icy model, this is identical to the surface node. The icy layer model assumes one nodal layer in the interior zone, at a depth of one to five millimeters. The sublimation heat sink is calculated using equation 2.20:

$$Q_{sub,i} = \alpha_{sub} p_{sub}(T) \sqrt{\frac{m_{H_2O}}{2\pi kT}} H_{sub} A_i \quad (3.4)$$

The mass loss dm_i/dt of node i due to the loss of volatiles is assumed to not change the nodal capacity and the material is removed from the interior without any further interaction (e.g. deposition) with the layers above the sublimation front. Layers located below the respective sublimation front nodes are considered inert.

3.4.6 The fracture thermophysical model

The thermophysical parameters of the analysis are detailed in Table 3.3. This analysis considers four cases that diversified agglomerate sizes and fill factors; case 1 is assumed to be the standard case.

Thermal skin depth and thermal inertia calculations are based on temperatures around 180 K. Above a temperature of 180 K, sublimation of water ice becomes an important heat sink in volatile-rich environments. The porous agglomerate radius R_A of 1 mm of Case 1 properties, combined with a porosity Φ of 0.75 result in an average thermal skin depth of about 10 mm at 180 K. The thermal inertia then is $31 \text{ Jm}^{-2}\text{K}^{-1}\text{s}^{-1/2}$. As temperatures vary from about 120 to 300 K, thermal inertia ranges between 10 and $20 \text{ Jm}^{-2}\text{K}^{-1}\text{s}^{-1/2}$ for $R_A = 0.1$ mm, and 40 to $150 \text{ Jm}^{-2}\text{K}^{-1}\text{s}^{-1/2}$ for $R_A = 5.0$ mm. The corresponding thermal skin depth for Case 2 $R_A = 0.1$ mm then is 0.4 mm; respectively 2.0 mm for Case 3

agglomerates of 5 mm size.

The thermal balance equation 3.1 then becomes:

$$\begin{aligned}
 i_{\text{rad}}(1 - \alpha) \frac{S}{r^2} A_i \cos \theta - i_{\text{rad}} \sum_j \varepsilon_i \varepsilon_j \sigma A_i F_{ij} (T_i^4 - T_j^4) \\
 - (1 - i_{\text{rad}}) \lambda_{\text{L, eff}}(T_{i,m}) A_i \frac{T_i - T_m}{\Delta z_{i,m}} - (1 - i_{\text{con}}) \lambda_{\text{L, eff}}(T_{i,n}) A_i \frac{T_i - T_n}{\Delta z_{i,n}} \\
 - i_{\text{sub}} Z(T_i) H_{\text{sub}} A_i = m_i c_i \frac{dT_i}{dt}
 \end{aligned} \tag{3.5}$$

The factors i are set to either 1 or 0 depending on location and role of its thermal node (see Figure 3.10). In detail:

1. i_{rad} is set to 1 for all 480 surface nodes - surface nodes exchange radiative fluxes with space and other surface nodes (respectively facets).
2. i_{con} is set to 1 for all 480 boundary nodes at the interior block of the modelled nucleus surface layers, i.e. in the lowest modelled stratum; otherwise it is set to zero. The adiabatic boundary condition restricts heat fluxes from diffusing to deeper zones of the nucleus. The boundary is set at a depth at which diurnal temperature differences are lower than 0.1 K.
3. i_{sub} is set to 1 at the sublimation front location, and 0 for all non-subliming nodal positions. The sublimation front is set to be at the uppermost layer of the dust-ice mixture. Nodes in deeper layers are considered to be inert and not sublimating.

Subsurface layers consist of 49 nodes per column; in total 23520 nodes constitute the interior layers of a model fracture.

A commercial solver, ESATAN TMS (www.esatan-tms.com), is considered to be an appropriate tool for the analysis of fractures. ESATAN TMS calculates view factors and thermal models; it is well appreciated as thermal analysis tool in space industry. The calculation uses a Crank-Nicholson forward-backward iteration method to solve the non-stationary energy balance equation.

The time step for the thermal analysis mainly depends on the sublimation term. This term is highly dependent on temperature, longer time steps can cause the computations to not converge. Therefore, the analysis time step varies between 1 s for 1.25 AU, and 60 s for distances greater of 3.5 AU.

Diurnal cycles are repeated until temperature differences reach values of less than 0.01 K between each revolution. For the plots, one data point of temperatures and heat fluxes is obtained for every 60 seconds.

3.5 Analysis of heat fluxes and temperatures

3.5.1 Range of parameter variations

This section describes the governing heat fluxes and temperatures of the previously described fracture geometries. The focus is on deriving the individual impact of variables identified as being both relevant for the results and revealed (within certain limits) by Rosetta measurements. The analysis details

- comparisons between fractured and flat terrains,
- variations of the heliocentric distance,
- effects of the fracture geometry variations,
- different illumination conditions,
- location of ice within the fracture parts and at different depths, and
- the influence of thermal conductivity due to agglomerate size and porosity.

To study the variation of parameters, it is suitable to define one fracture geometry type as a baseline. Geometry type A4 is chosen, as it is in the center of the spectrum of side wall angles (see Figure 3.8) and it serves as a good example of the observed heat trap effects of fractures. The other reference parameters include a distance chosen to be 2 AU, a plane angle η of 30 deg at a latitude of 0 deg are chosen as baseline environmental conditions. The standard thermophysical parameters are those of case 1 in Table 3.3.

3.5.2 Comparison of fractured and flat terrains

3.5.2.1 Heat flux characteristics

Idealized flat terrain is neither shadowed nor including view factors to its other facets (i.e. flat terrain does not radiatively interact with itself). Illumination conditions are characterized by a sinusoidal insolation pattern for half of its diurnal period, the second half (equivalent to night) receiving no radiative fluxes. The low thermal inertia of the nucleus uppermost layers leads to a surface temperature rise, at 2 AU heliocentric distance in the order of 2-3 K/min in the morning. Induced conductive fluxes to the interior are small compared to a growing surfacial emission. For a sublimating ice front located within the first millimeters below the subsurficial layers, it takes more than 30 minutes until a temperature of 180 K is reached. Considerable sublimation rates (more than 1 W/m²) are reached half an hour after the illumination started. After another hour, the sublimation is dominating the fluxes and higher than IR emission and conductive fluxes to deeper layers. Peak sublimation rates account for 72 % of the maximum of insolation values reached three minutes after passing the subsolar point. Sublimation enthalpy makes up 62 % of the total insolation for an entire diurnal period. The remaining 38 % is emitted through thermal infrared radiation to deep space. Sublimation characteristics of flat terrain in comparison to solar irradiation is detailed by the dash-dotted line in Figure 3.12.

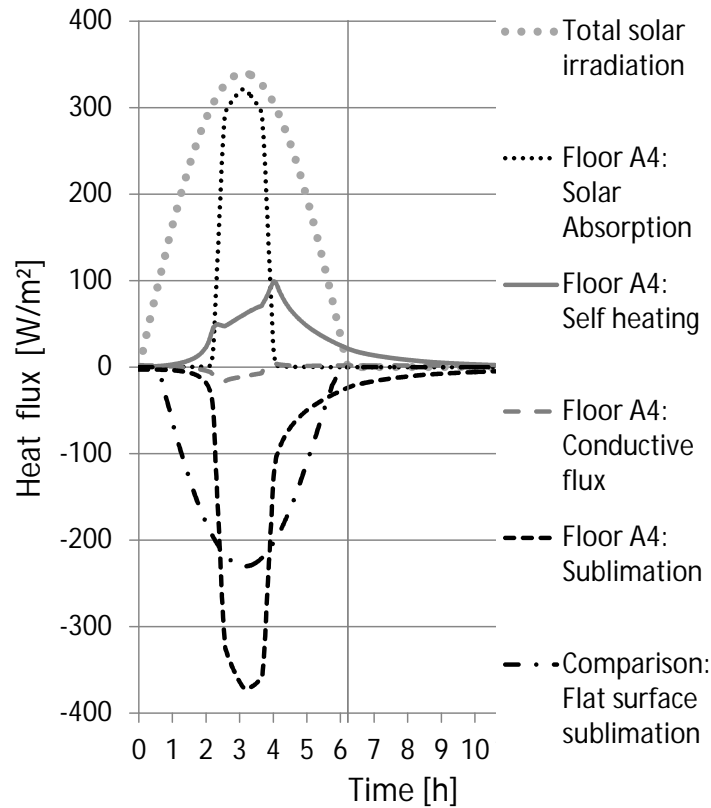


Figure 3.12: Heat flux patterns for fracture type A4 at a heliocentric distance of 2.0 AU and a plane angle $\eta = 30^\circ$ for one diurnal period of 12.4 h. The vertical lines at 0h and 6.2h indicate local morning and evening terminator. The coarse-dotted grey line denotes the incident total solar irradiation, while the smaller black dotted line outlines the absorbed heat flux by the fracture floor. The grey continuous line shows the self heating by infrared radiation, emitted from the fracture side walls, which impinges on the fracture floor: A positive value indicates a net heat flux direction towards the fracture floor. The grey dashed line illustrates the heat exchange with underlying nucleus layers through conductive and radiative transport. The black dashed line marks the local heat sink by sublimation phase change processes. For comparison, the dash-dotted line marks the sublimation pattern of a flat surface with identical thermophysical properties. The sublimation front is located directly at the surface of the fracture floor. Remarks: (1) The heat fluxes are related to 1 m² sublimating fracture floor. Due to the concave structure of geometry type A4 and the decreasing width with depth, the fracture top sums up to 4 m². (2) The fractured terrain absorbs about 4% more thermal energy than a flat surface due to absorption of scattered irradiation.

While the diurnal solar irradiation pattern for flat terrains and fracture geometries is identical, the behaviour of the evoked sublimation heat flux varies in both quantitative and temporal values. The relatively small apex angle of 43.6 deg induced by a solar plane angle of 30 deg results in a direct insolation of the fracture bottom, its total time adds up to 90 minutes per rotation. There is a significant difference in area: A typical class A4 fracture of type “Icy Bottom” consists of 95 % inert (non-subliming) walls, the active bottom constitutes a small fraction only. The total surface area is about 22.3 times of that of a flat area.

Analysing the fluxes of Figure 3.12, one finds that the conduction to deeper layers is small compared to all other fluxes (radiative and sublimative). Hence thermal energy storage in the small uppermost nodes is negligible. Incident solar irradiation is absorbed, and reemitted as infrared radiation. As there is a significant view factor to the fracture floor, this secondary radiation is absorbed by its dust-ice mixture surface, and thus consumed for sublimation. A fracture view factor towards open space is significantly smaller than for flat terrains. Thus, the sublimation term consists of mainly two constituents: direct solar illumination (which reaches its diurnal maximum only minutes after perpendicular illumination at the subsolar point after 3.1 h), and self-heating by the fracture walls. The wall infrared radiation creates a more irregular pattern, culminating when the floor moves into shadows. There is a constant IR flux during the whole diurnal period, even after the evening terminator, confirming a significant difference in the heat storage ability of inert parts of the fracture, and the active sublimating floor: As fracture walls contribute to 95 % of the entire fracture surface, their heat capacity is not negligible. Lacking heat sinks, they tend to be warmer than the fracture floor; as their view factor to space is much smaller than that of flat terrain, their cooling rates are lower.

The distribution of the sublimation pattern of the fracture floor (the black dashed line in Figure 3.12) shows a superposition of both incoming self-heating from other facets, and solar irradiation. As the wall infrared contribution result in its peak in 30% of the absorbed direct insolation, both integral sublimation and its maximum value are higher compared to flat terrain. Energy storage in fracture walls adds a tail of self-heating. While flat terrain sublimation dies out before the evening terminator, sublimation from an “Icy Bottom” fracture lasts during the entire shadow phase. Sublimation adds up to 6.5% of its peak three hours before, even when direct insolation on the fracture floor ended two hours earlier.

Another characteristic of fractured terrain is the shift of peak sublimation to a later time in the diurnal period: the sublimation tail moves the diurnal mean to early afternoon. In contrast, flat terrain sublimation gets negligible ($<1.0 \text{ W/m}^2$) minutes before local sunset.

3.5.2.2 Diurnal temperature patterns

Diurnal temperature patterns are shown in Figure 3.13. Flat terrain temperatures show a variation from peak 195 K at the subsolar point and an all-time minimum of 100 K shortly after the morning terminator. The surface temperature peak has a 3 minutes thermal lag to the peak irradiation. As long as the thermophysical processes are controlled by the sublimation directly within this surface layer, temperatures remain nearly stable on a quasi-flat plateau above 190 K. The sublimation term grows fast, nearly all additional

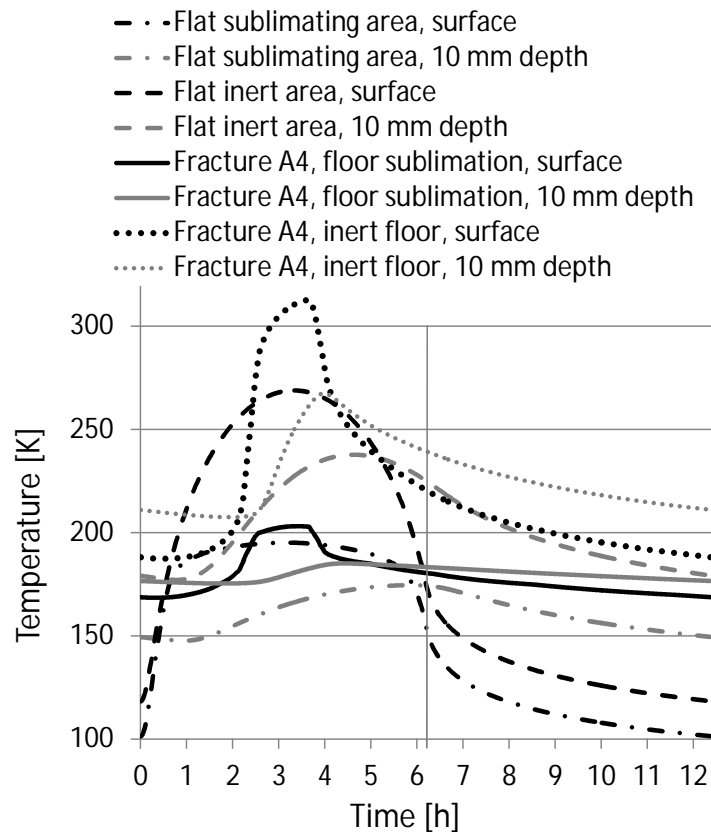


Figure 3.13: Modelled diurnal temperatures for flat terrain and for the bottom of fracture geometry A4. Heliocentric distance is 2.0 AU, plane angle $\eta = 30$ deg and the sublimation front is identical with the surface. The displayed fracture temperatures are averaged values over the four most central node positions at the fracture bottom, and 10 mm under it.

incoming fluxes are directly consumed for sublimation; and this effect dominates for about 3.5 hours. At a subsurface layer of 10 mm, which corresponds roughly to the diurnal thermal skin depth, the bandwidth has already declined to a range between 148 K and 175 K. In case of an absent heat sink (which happens on fully inert terrains without any water ice left) the general temperature level is higher: temperatures range between 120 and 270 K.

A typical fracture geometry like A4 results in a significantly higher temperature level, its bandwidth lies between 185 and 313 K for a fracture bare of volatiles. In icy composition, temperature differences to the even terrain are smaller with diurnal temperature variations between 168 and 203 K. Subsurface layers outline differences of 175 to 185 K between daily maximum and minimum in the shadow phase.

Integrating the sublimation for one diurnal period, pure ice erosion of a flat surface accounts for 1.0 kg/m^2 . Similar values have been derived by Colwell *et al.* (1990), whose assumptions included small deviations in albedo and diurnal period. Total erosion rates of 0.94 kg/m^2 were calculated for the geometry type A4 fracture floor, directly at the fracture bottom flat area. In contrast to these slightly lower values for an integrated diurnal period, maximum sublimation rates in fractures are significantly (61 %) higher. There are two

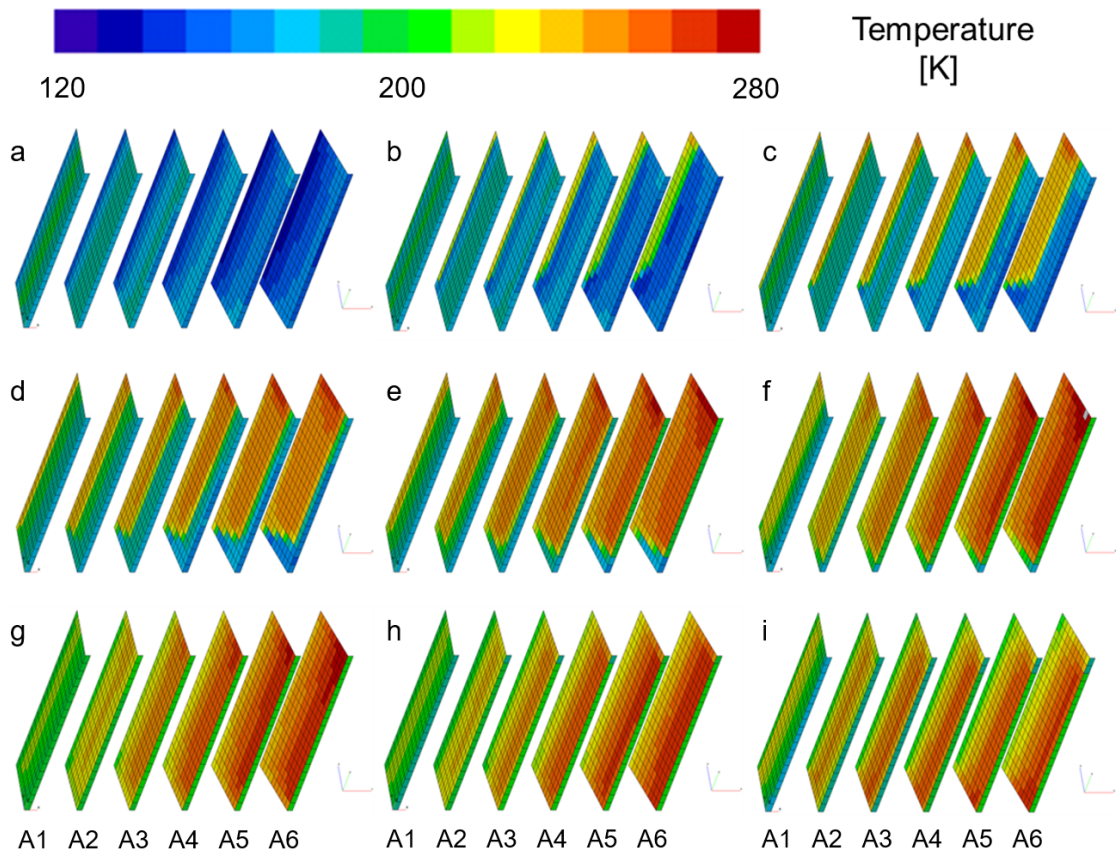


Figure 3.14: Resolved surface temperatures in [K] for subsequent illumination conditions in the course of a diurnal period. Six different fracture geometries have been chosen, from left to right: A1, A2, A3, A4, A5, A6. The fracture side wall (which is illuminated in the morning) and the fracture icy bottom are displayed in nine positions: morning terminator (top left) and the step between each group image is 15 deg (counted from top left to bottom right). Perpendicular illumination (zenith) is reached at the bottom left image.

reasons; the larger exposed area than the considered flat terrain, mostly because of the inclined walls; and only a small fraction of volatiles. As a result, integrated erosion rates, related per area are higher for flat terrain for these models. Figure 3.14 shows the resolved diurnal temperature patterns.

3.5.3 Resolved fracture geometries

The previous paragraph derived averaged overall values for the fracture floor. The temperatures of the side walls depend on the onset of absorbed insolation, and they differ due to local exposition. Detailed surface temperatures are depicted in Figure 3.14 for six different fracture geometries for the time between morning terminator and shortly after zenith.

At the morning terminator, narrow fractures show the highest temperatures of more than 200 K, with their maximum being between fracture top and bottom. Their ability to

reemit the absorbed solar energy is low, because their surface is barely exposed to space. In sharp contrast, the top facets of wider fractures (e.g. types A5 and A6) with larger view factors to space have cooled down to 130 K. In the course of the diurnal rotation, the uppermost nodes get insolated; in response, their temperatures rise. Additionally, there are edge effects at both ends of the fracture (the fracture side walls share a 90 degree angle with front and back wall); the shadowed front remains colder while the back side heats up more strongly.

At a solar elevation of 75 degrees, the wider fractures show the highest temperatures (280 K) at their walls, while their floor reached a plateau and sublimation dominates the heat budget. After zenith, wall temperatures decline, while surface temperatures show a maximum near the center of its walls: Nodes close to the bottom emit their heat mostly to the colder fracture floor, while the nodes that are closer to the top of the fractures are characterized with a higher emission towards deep space. The generally higher maximum temperatures of the wider fracture wall therefore also results from their better exposure to the sun. Direct illumination on the fracture floor is restricted by its walls; the fracture top width (w_t , see Tab. 3.1) hence drives the pattern of sublimation.

Diurnal heat flux patterns for sublimating surfaces are depicted in Figure 3.15. The incoming solar irradiation, denoted with a black dashed line and always a positive value, is restricted by the geometry; its pattern is symmetrical to the subsolar position. The sublimation heat sink follows insolation, for flat terrain and for wider fractures (e.g. the geometry types A7 and A8), it gets negligible during nights. The smaller the fracture, the more pronounced the peak, and the longer the tail of shadow-phase sublimation. Wall thermal emission accounts for up to one fourth of the sublimation, with its maximum for geometry types A5 and A6. The peak values here are similar for all observed fractures at the end of the direct illumination of the fracture floor. A minimum sublimation enthalpy flux of 9.0 W/m^2 was calculated during nights.

Fractured terrain that contains ices at their bottom, as displayed in Figure 3.16, show a general trend to higher temperatures than flat terrain. Smaller fractures show temperatures oscillating around 180 K in their subsurface layers, broader fractures around 170 K; flat surfaces are up to 20 K colder. Smaller fractures exhibit a brief peak of high temperatures (e.g. a peak around 200 K lasting for about 30 minutes in fracture model A2); while wider fracture reach slightly higher temperatures (the bottom of A7 peaks at 205 K). Temperatures close to the peak value last longer for wide fractures, as direct bottom insolation times are significantly longer: for fracture A8 this time is about three hours, equivalent to one quarter of a diurnal period. The lowest temperatures are derived for flat terrain, including their peak temperature of 195 K. In summary, the geometric types show a wide range of temperatures in the inert side walls, and these temperatures are highly dependent on the local illumination conditions. These differences lead to the spectrum of sublimation patterns, but they all have a pronounced heat trap effect in common.

3.5.4 Fracture floor size variation

Previous results concentrated on fractures of a depth-to-width ratio of 10 at the fracture floor; fracture floors that have a depth-to-width ratio of 5 and 2.5 are described in Table 3.1. The fractures denoted with letter B have a bottom surface width w_b of 0.2 m, type C fractures are assumed to be even broader with a fracture floor of 0.4 m.

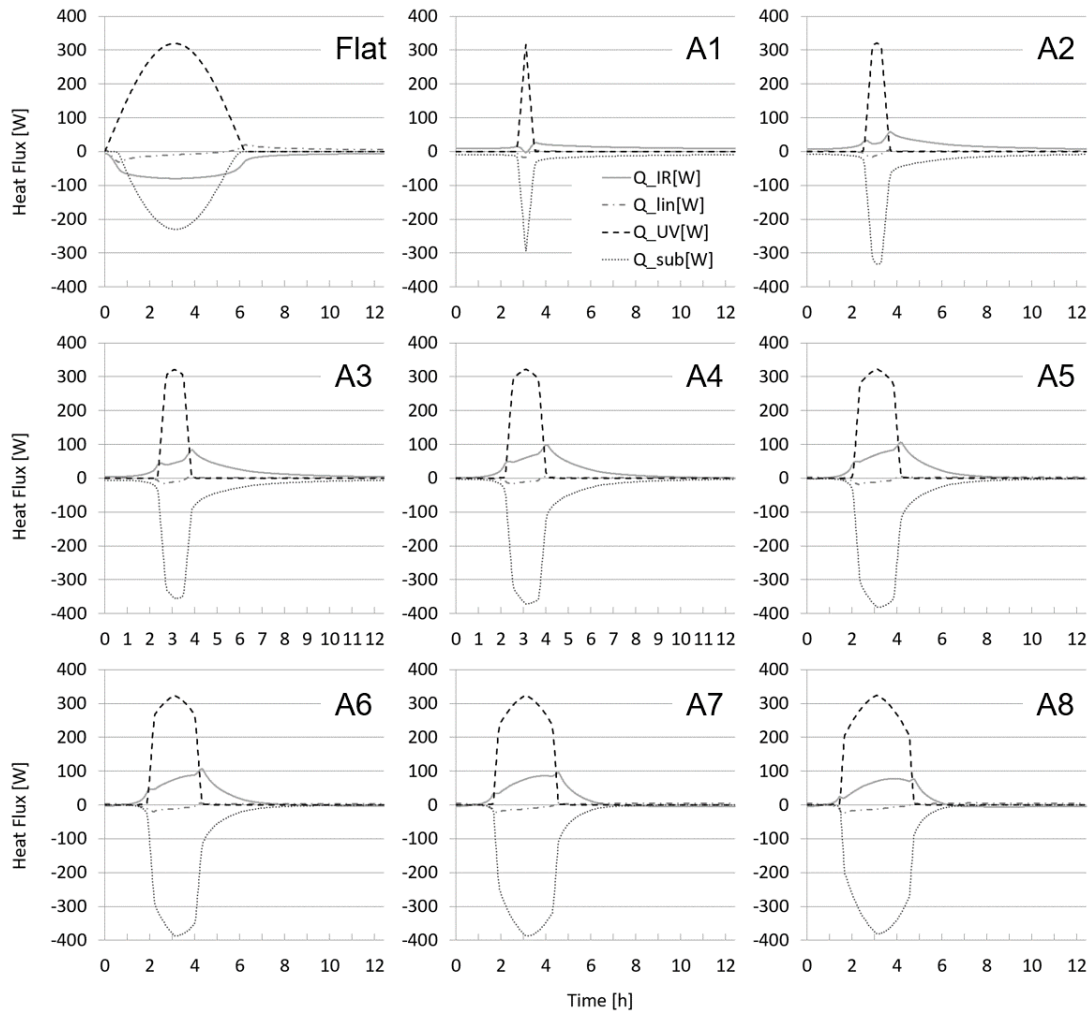


Figure 3.15: Diurnal heat fluxes in [W] for nine geometries, including flat terrain (top left) and fracture geometries A1 (top middle), A2 (top right), A3 (center left), A4 (center middle), A5 (center right), A6 (bottom left), A7 (bottom middle) and A8 (bottom right). The grey line shows the emitted IR (named Q_{IR} ; for flat terrain emission to deep space, for the fractures the heat flux from fracture walls to the floor). The dash-dotted line depicts the heat conduction to subsurficial nucleus layers (Q_{lin}), the dotted line the heat flux consumed for sublimation Q_{sub} of the fracture floor (respectively the entire surface for the flat terrain), and the dashed line the solar irradiation (denoted Q_{UV}). The y-axis denotes the flux (positive values are incoming fluxes, negative values describe fluxes that are outbound), the x-axis gives the time in [h]. All diagrams set the morning terminator as starting time. The model shows that the combined solar insolation and the self-heating via infrared fluxes from the side walls are consumed for sublimating the water ice in the fracture floor.

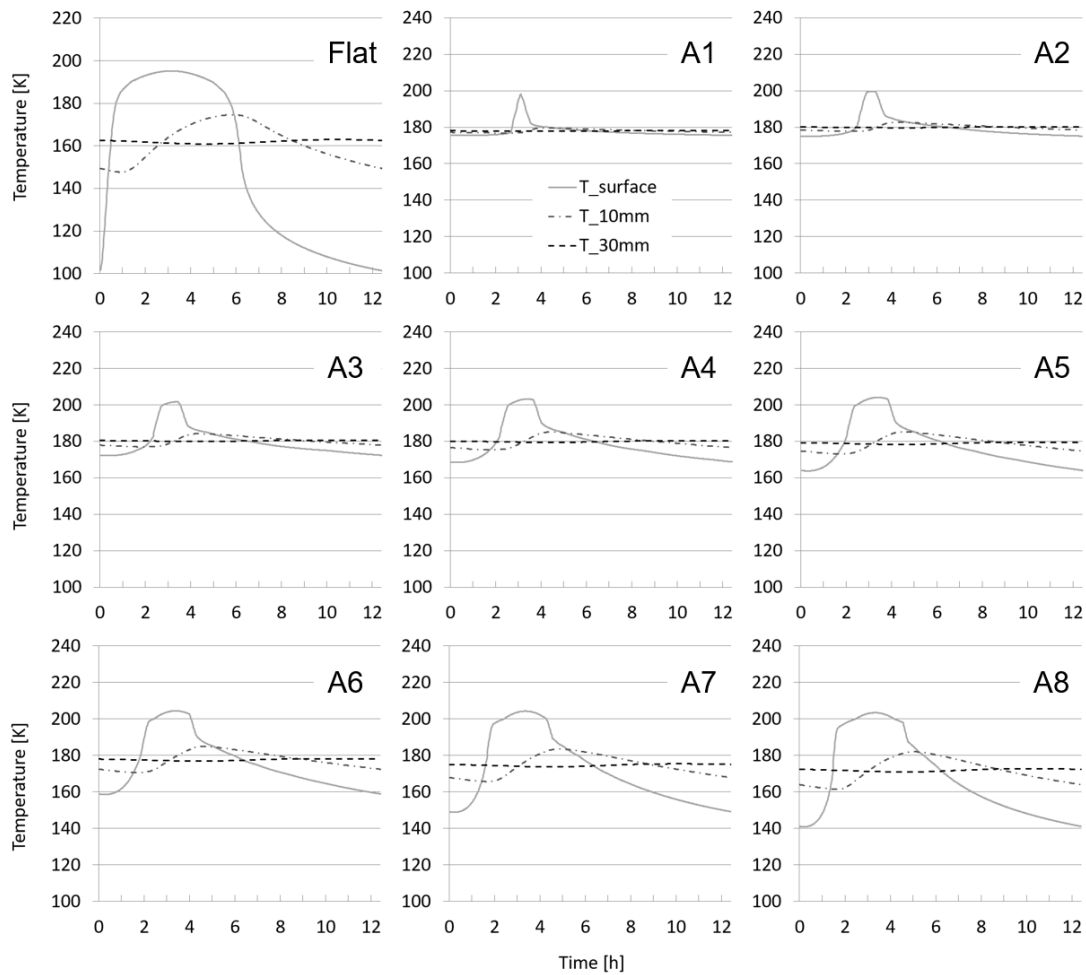


Figure 3.16: Diurnal temperatures, calculated for the fracture floors, in [K] for flat terrain (top left) and fracture geometries with icy floor A1 (top middle), A2 (top right), A3 (center left), A4 (center middle), A5 (center right), A6 (bottom left), A7 (bottom middle) and A8 (bottom right). The grey line shows the surface nodal temperature, the dash-dotted line temperatures at 10 mm below the surface, and the black dotted line at 30 mm below the surface. The y-axis denotes the temperature in K, the x-axis gives the time in [h]. All diagrams set the morning terminator as starting time. The temperatures in the fracture floor are generally higher than flat terrains in both peak and average values, and their bandwidth shows smaller variations for all fracture types.

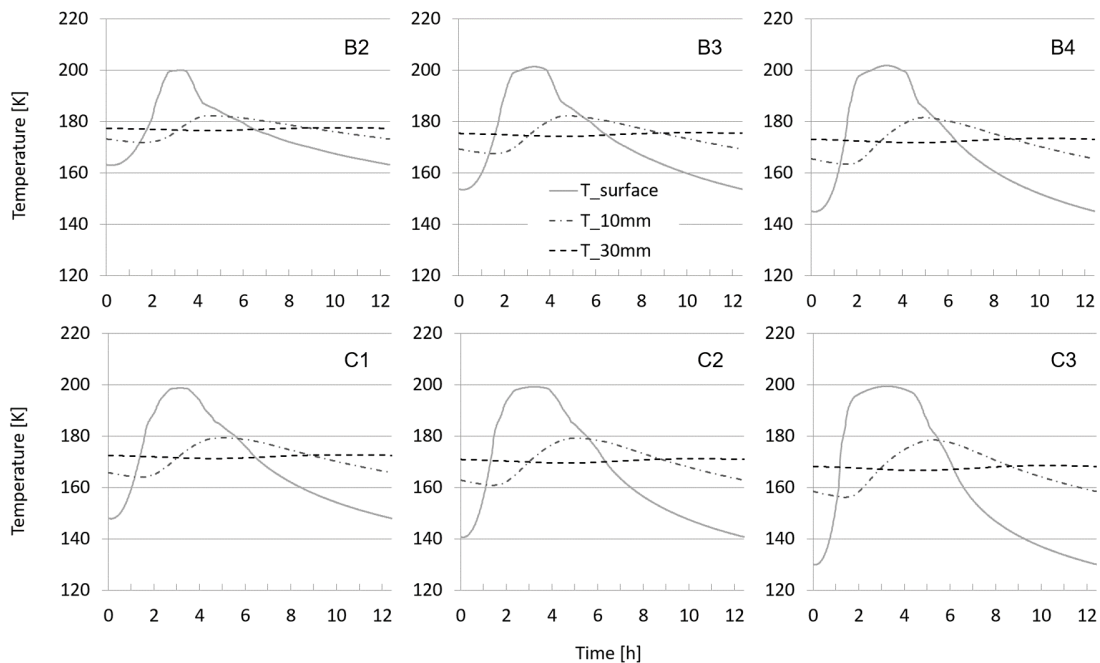


Figure 3.17: Diurnal temperatures, calculated for icy fracture floors, in [K] for geometries B2 (top left), B3 (top middle), B4 (top right), C1 (bottom left), C2 (bottom middle) and C3 (bottom right). The grey line shows the surface nodal temperature, the dash-dotted line temperatures at 10 mm below the surface, and the black dotted line at 30 mm below the surface. The y-axis denotes the temperature in K, the x-axis gives the time in [h]. All diagrams set the morning terminator as starting time. The B and C fracture types show slightly lower temperatures than the A types in Figure 3.16 and higher temperature variations.

The results in Figure 3.17 show similar trends to those of type A fractures: Wider fractures (with less steep side walls) result in higher fluctuations of temperatures in the subsurface layers, lower peak temperatures, and hence lower peak sublimation rates. However, the total amount of energy that accounts for the sublimation of volatiles, integrated over one diurnal rotation, increases with fracture width.

While thermal inertia is equivalent, thermal wave penetration depth is significantly reduced for small fractures. Night-time temperatures within fractures are higher, in any condition and for all analysed fractures if illuminated, than in flat terrain. Differences between 40 and 70 K were obtained, the highest deviations are observed for the smallest fracture geometry A1. If a fracture bottom is depleted in volatiles, this pattern will rise in significance, even enlarging the differences between fractured and flat nucleus terrain.

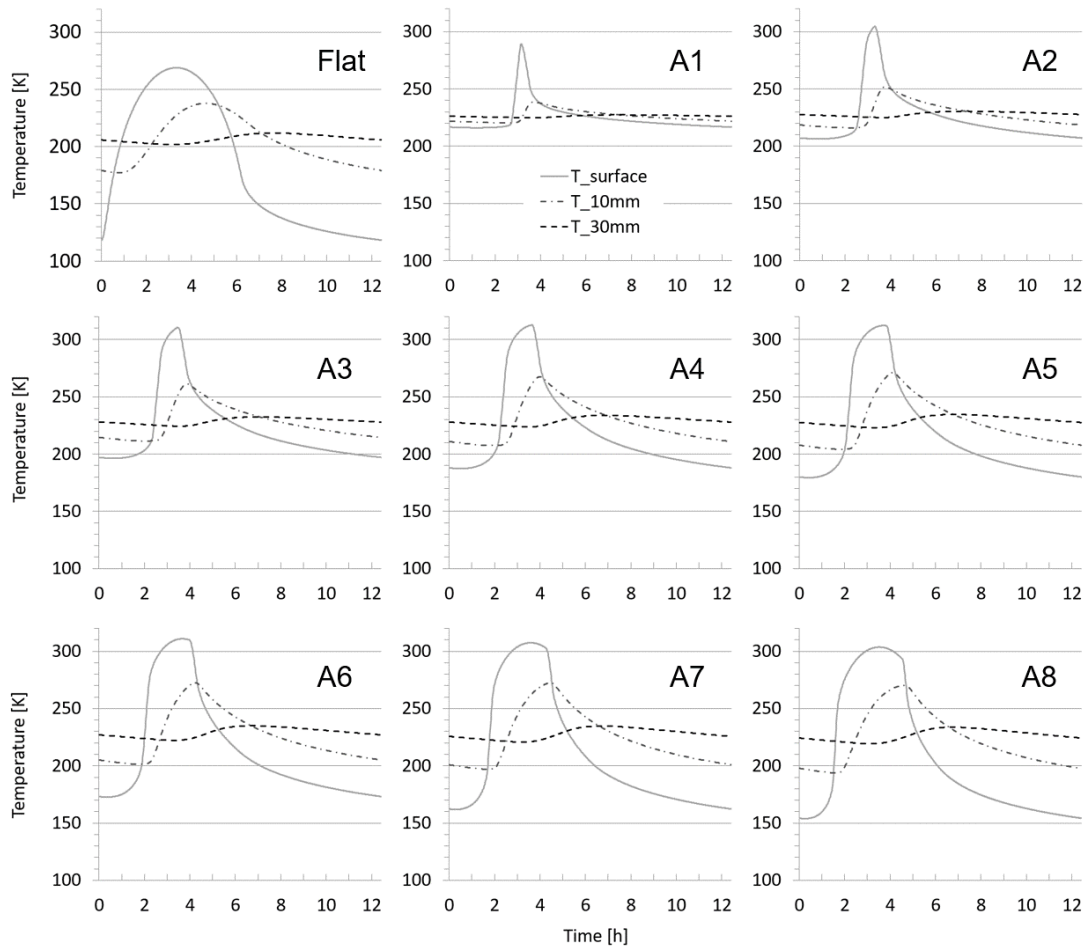


Figure 3.18: Diurnal temperatures, calculated for volatile-free fracture floors, in [K] against one diurnal period in [h] for flat terrain (top left) and fracture geometries A1 (top middle), A2 (top right), A3 (center left), A4 (center middle), A5 (center right), A6 (bottom left), A7 (bottom middle) and A8 (bottom right). The grey line shows the surface nodal temperature, the dash-dotted line temperatures at 10 mm below the surface, and the black dotted line at 30 mm below the surface. All diagrams set the morning terminator as starting time. These volatile-free model fractures all result in higher temperatures during an entire diurnal period than flat terrains in all depths, with peak values being 40 K above those in flat terrains.

3.5.5 Diurnal temperature patterns of ice-free fractures

Fractures with an icy bottom differ significantly in temperatures from their volatile-free counterparts. Diurnal temperature patterns and their comparison to flat terrain and detailed temperature curves are shown in Figure 3.18.

While temperature bandwidths of fracture geometries A1 to A8 differ significantly (see Table 3.2), overall patterns appear similar: The average temperature in both surface and subsurface layers lies between 220 and 240 K. The maximum temperature at the surface has a lag between 10 and 30 minutes with respect to the maximum insolation at 3.1 h.

The temperature increases instantly as the fracture floor is directly illuminated, and the rise shows higher values than the decline, which in contrast lasts longer. The smallest fracture A0 (with perpendicular walls) exhibits the longest time of temperature decline, but its range between maximum at 290 K and minimum (215 K) is small. The broader the fracture, the wider this range; fracture A8 spans a temperature range between 155 and 305 K.

3.5.6 Fracture orientation and solar plane angle

The shown conditions of fracture illumination have been restricted to a solar plane angle of 30 degrees. This results in wide variations of the apex angle between 11 and 90 degrees (see Table 3.1). Fracture topography on 67P clearly demonstrates a variety of fracture types in orientation and morphology (Auger *et al.* 2018). To be able to understand the role of the fracture orientation on the nucleus, one needs varied illumination patterns. The considered solar plane angles are 0, 30 and 60 deg (Table 3.2). Additionally, the analysis includes fractures not illuminated perpendicularly, but with a deviation of 30 degrees to the solar plane – this is a realistic case as the rotation axis is highly tilted towards its solar plane. This results in especially smaller fracture floors being not illuminated in their entire length due to shadowing from the side walls. The resulting temperature pattern is presented in Figure 3.19.

For a solar plane angle of 0 deg, illumination is not restricted by side walls but by fracture length – the longer a linear section of a fracture, the longer the direct illumination time. This increasing effect gets less and less significant with longer fractures and is finally restricted by the diurnal period. A small fracture geometry like A1 has its floor being illuminated for about 4.5 h, similar insolation periods are obtained for fractures A4 and A7 which have a larger opening angle. This also results in increasing variations and higher temperatures in the subsurface layers; fracture geometry A4 reaches 186 K in 30 mm depth – the highest value obtained for all “icy bottom” fractures at 2.0 AU. In contrast, a solar plane angle of 60 deg leads to shorter illumination times and lower temperatures in average. Peak temperatures, obtained for a zenith position, are similar to those with longer illumination times. The third row in Figure 3.19 does not show a deviating pattern: However, due to the insolation angle which is not perpendicular even at the subsolar point, maximum temperatures are slightly lower than the previously analysed illumination geometries. Comparing the fracture geometries A1, A4 and A7 under this variety of illumination conditions, the highest subsurface temperatures were obtained for fracture type A4, the highest fluctuations for type A7, the longest night-time sublimation for fracture type A1. These findings are robust towards the simulated variety of illumination conditions.

3.5.7 Fracture sublimation rates

Peak sublimation rate is defined as the calculated diurnal maximum of thermal energy consumed for sublimation. Compared to flat terrains, every single fracture geometry reveals higher peak sublimation rates; with a ratio of fractured/flat terrain between values of 1.28 and 1.68 (Figure 3.20). For fracture type A, the highest peak sublimation rates are calculated for 15 and 20 degrees wall angle. Interpolating all values with a least-square

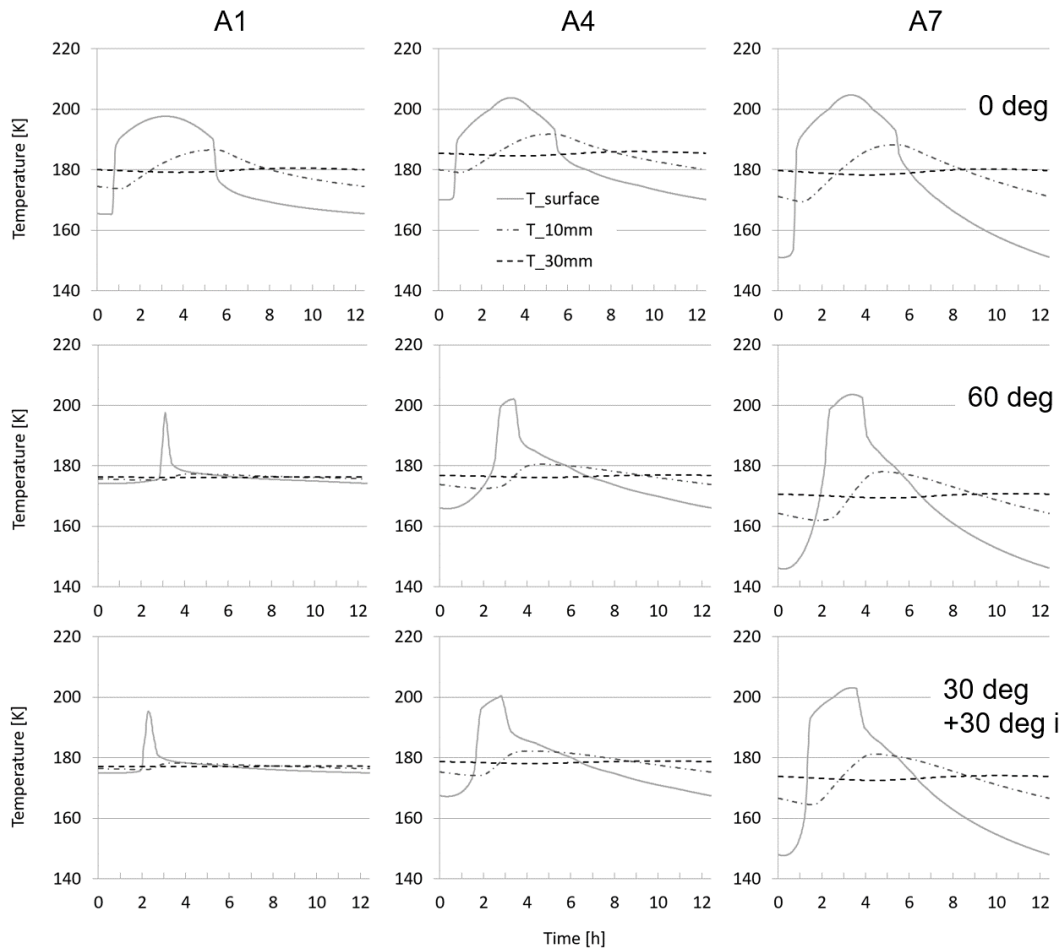


Figure 3.19: Diurnal temperatures in [K] for three fracture geometries and solar illumination condition. Fractures are grouped in columns: A1 (left column), A4 (center column) and A7 (right column). The illumination geometry is organised in rows: Solar plane angle of 0 deg (top row), 60 deg (center row), 30 deg and additional 30 deg inclination to the fracture bottom normal vector (bottom row). The grey line shows the surface nodal temperature, the dash-dotted line temperatures at 10 mm below the surface, and the black dotted line at 30 mm below the surface. The y-axis denotes the temperature in K, the x-axis gives the time in [h]. All diagrams set the morning terminator as starting time. The model results show that the illumination conditions alter the length of illumination times, but the overall pattern is similar and peak temperatures are all around 200 K. General average temperatures in all depths are highest for the A4 fracture type.

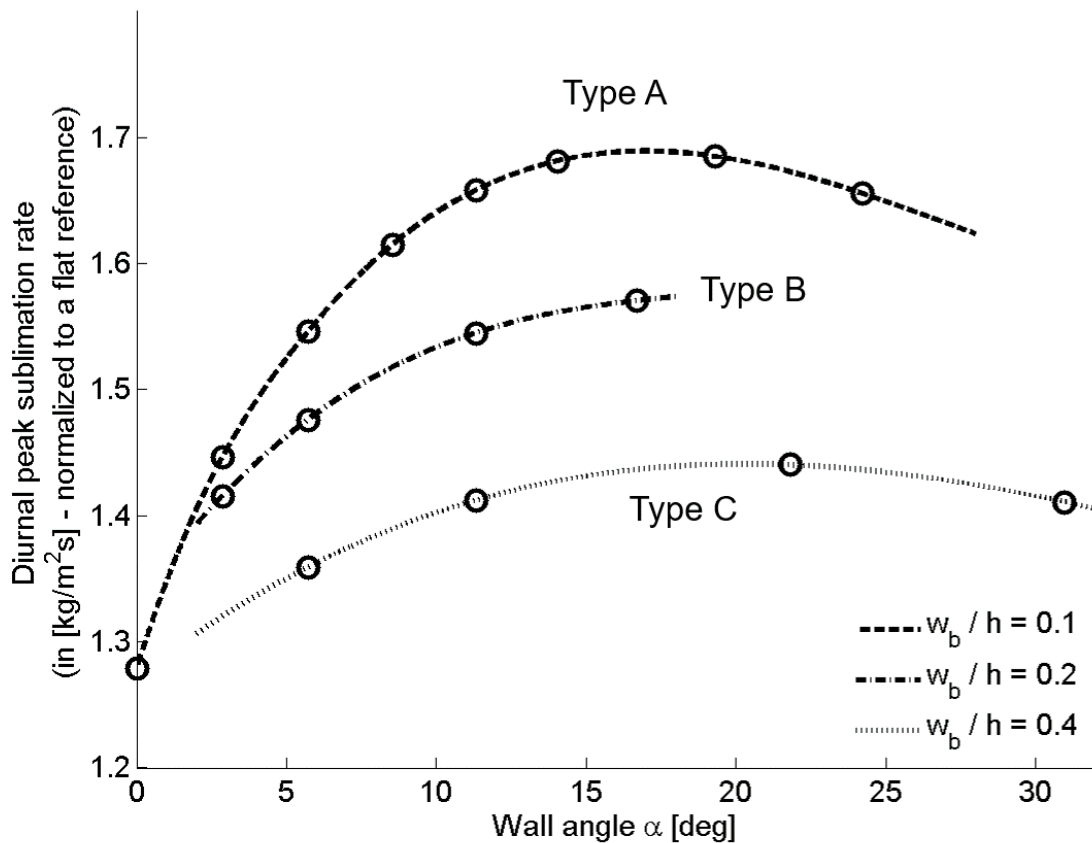


Figure 3.20: Normalized peak sublimation rate as a function of fracture wall angle, analysed for 16 fracture geometries. The diurnal peak sublimation rate is normalized to that of a flat surface with identical illumination and thermo-physical properties, and the same area as the fracture bottom. The circles denote calculated values, the lines show interpolating cubic functions. The dashed line depicts fracture geometries A1-A8 with a bottom width to height ratio of 0.1, the dashed-dotted line B1-4 and the dotted line C1-C4. All calculations were performed for 2.0 AU heliocentric distance, a plane angle of 30 deg, and a surficial sublimation front.

fit, a wall angle of 17.5 deg will have the highest ratio of 1.7 compared to flat terrain. Considering fracture geometries that have a larger fracture floor area, the calculated peak value shifts slightly to higher wall angles for broader fracture floors. Peak sublimation rates decrease to lower values: For fractures of type C, the peak sublimation rate is obtained for a 20 deg wall angle, but the ratio of fractured/flat terrain drops to a value of 1.44.

For all but the smallest fracture geometry, the peak sublimation rate shows higher absolute values than the incoming direct and reflected solar irradiation, as depicted for three model fractures (Figure 3.21).

In order to obtain the mass loss of fractured comet terrains, one has to include the non-volatile components of the uppermost fracture layers. Measurements showed a dust-to-ice ratio of 4 (Rotundi *et al.* 2015) and 6 (Fulle *et al.* 2016), some analysis even considers much higher values up to 100 for 67Ps perihelion passage (Fulle *et al.* 2016). The

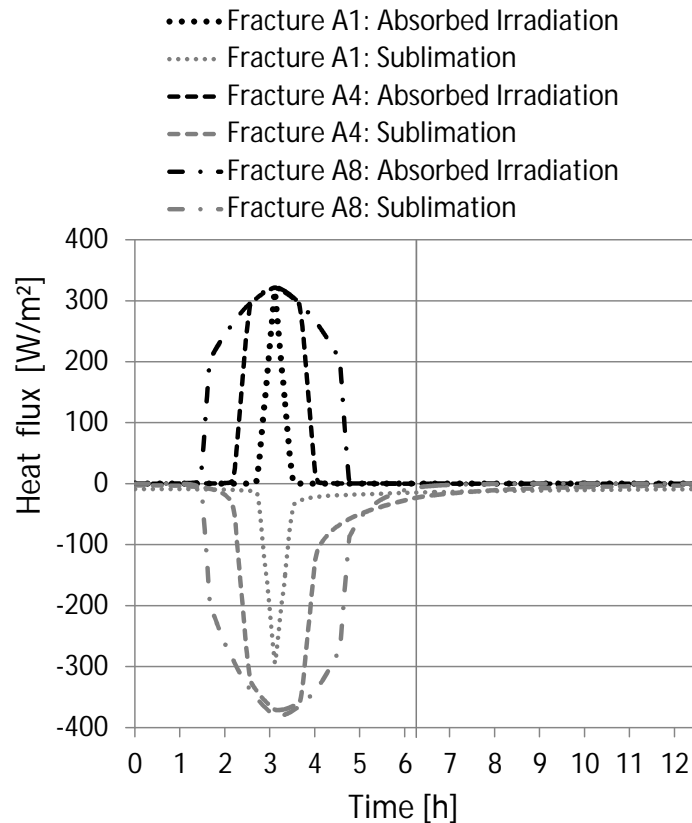


Figure 3.21: Absorbed solar irradiation and heat fluxes that are consumed for sublimation for three fracture geometries A1, A4 and A8, depicted for one diurnal period of comet 67. Values for the irradiation are shown as positive (black dotted line for A1, black dashed line for A4, and black dash-dotted line for A8). The sublimation is considered as a heat sink and given as negative lines (grey dotted line for A1, grey dashed line for A4, and grey dash-dotted line for A8). Peak sublimation rates are the global minima for each line, ranging between 298 and 382 W/m².

presented analysis assumes a dust-ice ratio of 4 to 6. For a heliocentric distance of 2.0 AU and calculated per diurnal period, the obtained accumulated retraction of the fracture floor would add up to 3-18 mm. In consequence, the resulting erosion and retreat of the uppermost layers of the fracture floor deepens icy fractures.

While obtained peak sublimation rates are significantly dependent on the fracture geometry, variations of the illumination conditions (such as different solar plane angles) have a much less pronounced effect. Considering total sublimation rates, the total exposure to insolation plays a significant role. Figure 3.22 shows the relative total sublimation energy for four different illumination conditions on a single fracture, normalized to the absorbed solar irradiation. The results are shown for fracture geometries A1 to A8 and in comparison to a flat surface which has a similar portion of its surface (a ratio of fracture bottom width to top width w_b/w_t) being inert and not sublimating. A general trend for all illumination conditions is that the normalised total sublimation enthalpy declines with the wall angle. One particular case can be singled out, as it shows a significant stronger total

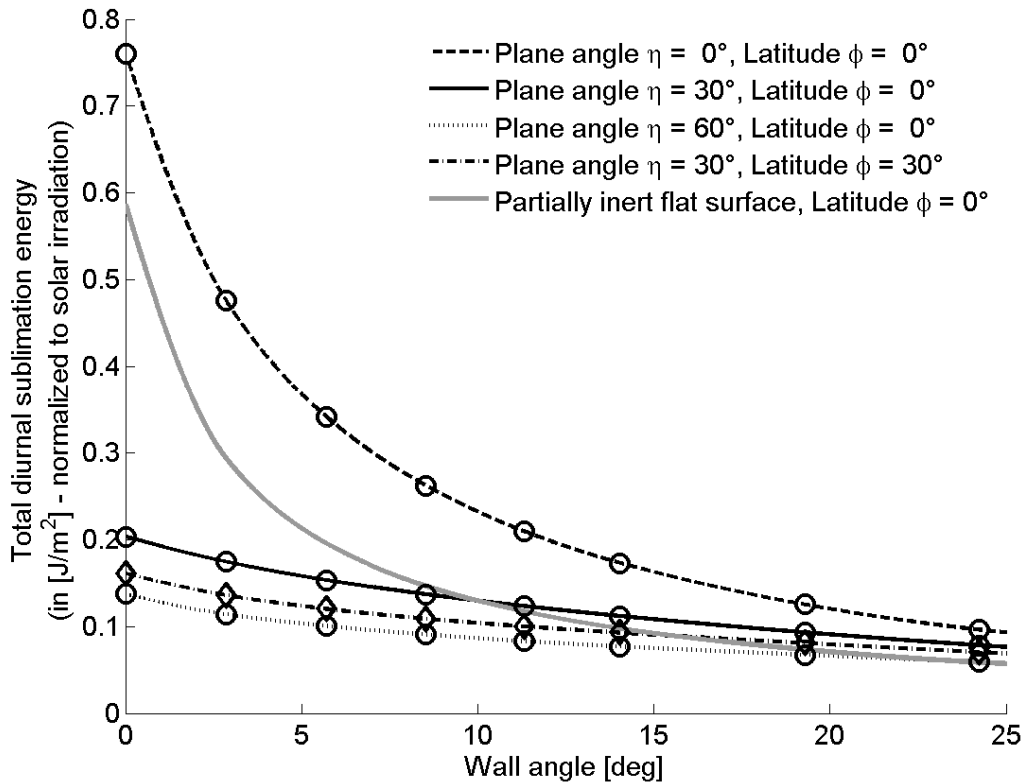


Figure 3.22: Normalized total diurnal sublimation energy, integrated over one diurnal period, displayed as a function of the fracture wall angle and analysed for four illumination scenarios. The sublimation energy is normalized to the total irradiated energy on all areas of the fracture. The circles denote calculated values, the lines shows the trend by cubic interpolation. All calculations were performed for 2.0 AU heliocentric distance and surface ice at the fracture floor. The grey line indicates the total sublimation energy for a flat surface, assuming that parts of the surface are inert: The sublimating area of the flat terrain equals the ratio between bottom and top width w_b/w_t .

sublimation than all the others, even those of flat terrain: the simulation run with a phase angle of 0 deg at a latitude of 0 deg. Here, the sun passes over a fracture in such a way that the fracture floor is illuminated nearly all day. This leads to a very pronounced heat trap effect and hence to high erosion rates. This illumination condition is restricted to very short time periods due to orbital parameters of 67P. Aside this finding, the presented analysis results in calculated diurnal sublimation rates of large top width w_t fractures being not highly dependent on the illumination conditions.

3.5.8 Variation of the sublimation front

Discussed previous analysis considered inert and sublimating areas in the fracture, while sublimating areas were expected to sublimate the exposed ice at the surface of a certain fracture area, in most cases the fracture floor. In this section, the focus is on the sublima-

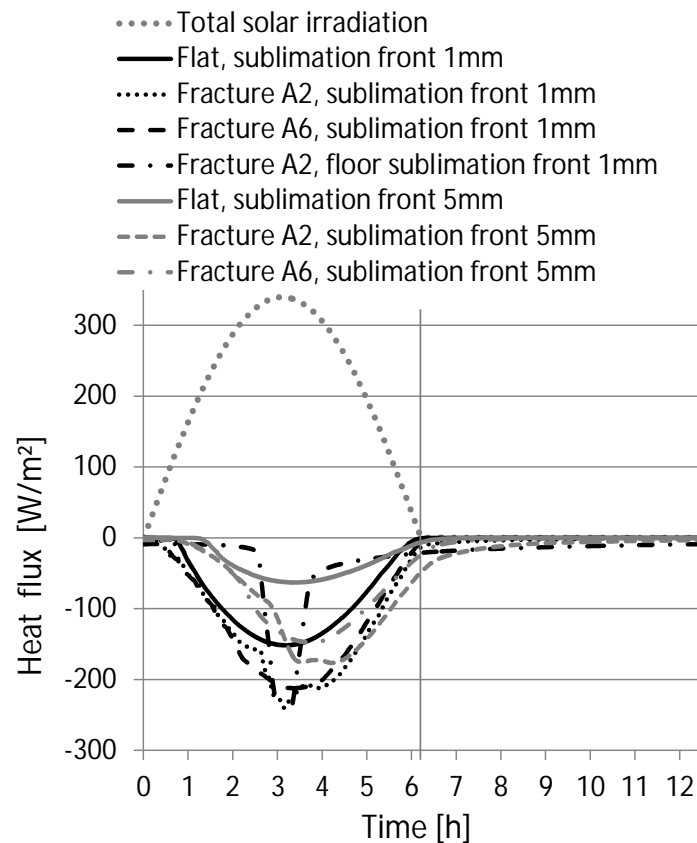


Figure 3.23: Diurnal irradiation and sublimation fluxes for fully subliming fractures A2 and A6. The grey dotted line show the solar irradiation for one diurnal revolution at 2 AU heliocentric distance as a positive heat source, the sublimation heat sinks are depicted for two sublimation fronts of 1mm and 5mm depth. The vertical line at 6.2 h denotes the terminator.

tion rates if the ice is buried under layers of non-volatile material.

The sublimation front is located at a depth between 1 and to 5 mm inside the porous nucleus layers. The fracture walls are considered inert or including ice (these fractures are named 'full-icy'), while the fracture bottom in all cases bears water ice.

Figure 3.23 shows the diurnal sublimation pattern for full-icy fractures in comparison to flat terrains and fracture floor ice only. There is a general trend to lower sublimation rates if the ice is buried deeper in the cometary layers. While flat terrains show a sinusoidal behaviour with a certain time delay after illumination of 1 to 2 hours, the curve of a full-icy fracture is stretched in time and appears irregular. Compared to flat terrain, the full-icy fracture shows a higher relative sublimation rate ratio for every single timestep. The difference is even higher if the ice is buried under deeper layers: Fully-icy fracture integrated diurnal sublimation surpasses that of flat surfaces by 44 % for a front at a depth of 1 mm and 130 % for a volatile reservoir in 5 mm depth only.

Towards the end of direct illumination on the fracture floor, the full-icy fractures show their highest diurnal peak sublimation rates. In absolute numbers, wall sublimation is dominating (due to large wall surfaces), while differences along the wall itself exist; with

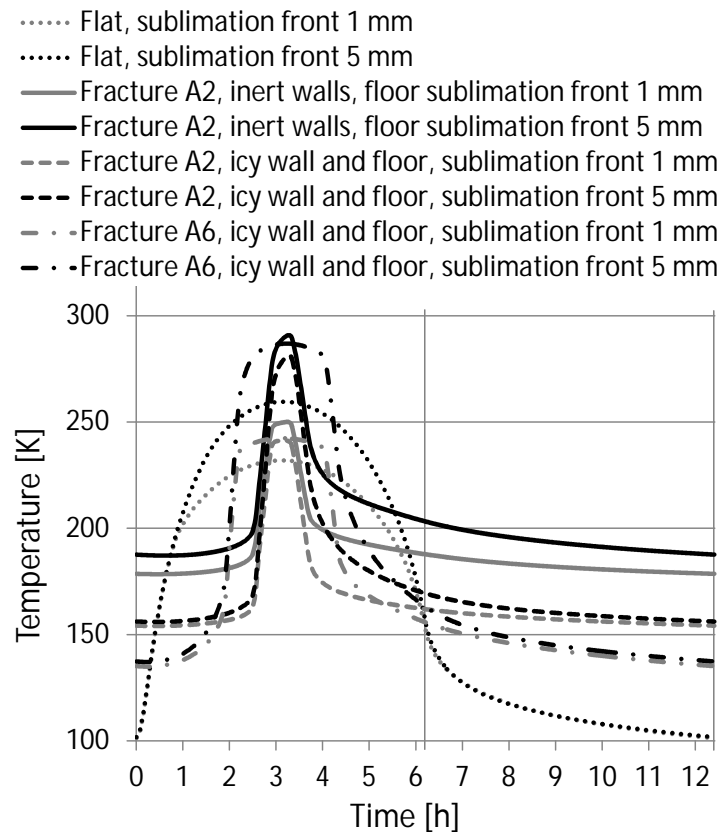


Figure 3.24: Diurnal temperatures for flat terrain (dashed) and for fracture geometry A4 (inert: continuous; icy floor: dotted). The sublimation front is located at a depth of 1 mm (grey) and 5 mm (black). Heliocentric distance is 2.0 AU, plane angle $\eta = 30$ deg and the sublimation front is identical to the surfacial node. Fracture temperatures are averaged over the four most central node positions at the fracture bottom.

the uppermost nodes contributing the least. Fractures whose ice content is restricted to the floors show 10 % higher peak sublimation rates, but in total less diurnal ice loss; i.e. their total sublimation of all icy fracture elements is higher than in icy floor fractures, as expected.

Independent of the fracture geometry, the results generally show higher temperatures for fracture floors than for their flat equivalent. Full-icy fractures result in 10-40 K lower temperatures than those with inert walls, as they consume the absorbed solar energy for sublimation directly without significantly heating up the fracture floor. This is the main reason for their higher sublimation rates during day, and their relatively quick decline once the fracture passes into shadows.

As worked out by Kührt and Keller (1994), surface sublimation leads to a devolatilization of the upper layers and hence a retreat of the sublimation front to the deeper cometary interior. The resulting higher surface temperatures (Kührt and Keller 1994) can be confirmed by the fracture floor temperature behaviour depicted in Figure 3.24: all displayed areas have their volatiles at depths of 1 and 5 mm with full-icy fractures ranging between flat surfaces and fractures with inert walls.

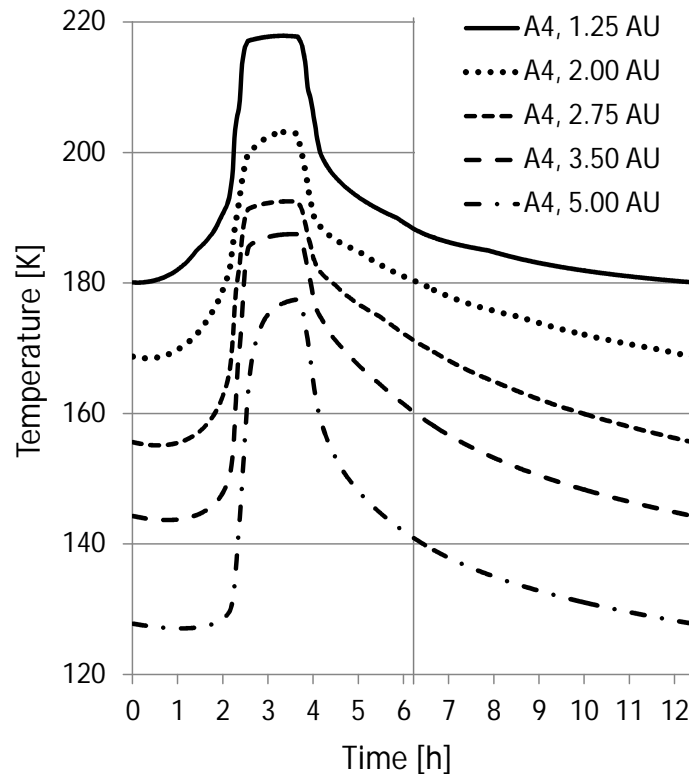


Figure 3.25: Fracture A4 floor temperatures for five heliocentric distance settings with surficial sublimation. The vertical line at 6.2h denotes the terminator.

3.5.9 The influence of heliocentric distance variations

The heliocentric distance of the comet has a significant influence on temperature and sublimation patterns. In total, five heliocentric distances during one comet orbit around the sun from 5.0 to 1.25 AU are considered.

Temperature patterns for all heliocentric distances are similar (Figure 3.25), and show diurnal variations between 35 and 50 K. A steep rise during direct illumination of the fracture floor is followed by a slower, longer lasting decline. At the time sublimation starts, the temperature rise is strongly decelerated, especially at temperatures higher than 180 K. At 2.75 AU and closer, the self heating from the surrounding fracture walls significantly (more than 10%) contributes to the total heat flux at the fracture floor.

Diurnal net infrared emission emanating from the fracture bottom outnumbers sublimation at higher heliocentric distances, at 5 AU by a factor of 4.8. Steep plateaus observed for 5.0 and 2.0 AU can be explained by differences in the composition of the thermal fluxes. Conduction through the layers, generally of minor importance, sums up to one third of the thermal balance at 5 AU.

Comparing flat and fractured terrain, sublimation rate ratios increase with heliocentric distance (Figure 3.26). The ratio varies from 1.6 at 1.25 AU to 14 at 5.0 AU. While 67P spends 2.5 years per orbital revolution at distances > 5.0 AU (which is typical for Jupiter-

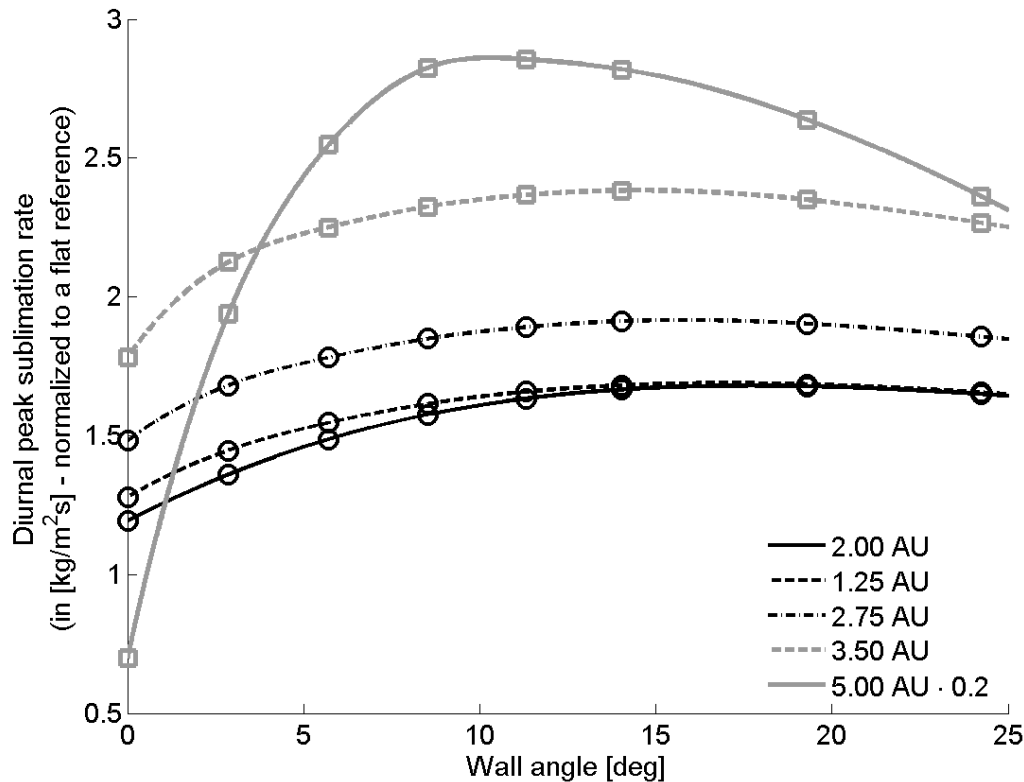


Figure 3.26: Peak sublimation rate as function of fracture wall angle for five heliocentric distance settings, normalized to an identical flat surface. The circles and rectangles denote calculated values, the lines show cubic interpolation. Calculations were performed for a solar plane angle of 30 deg and surface sublimation at the fracture bottom. The heliocentric distance of 5.0 AU reaches values of 14, to fit into the diagram, the line was multiplied with 0.2

family comets), peak sublimation rates at these distances are low: $4.7 \cdot 10^{-6} \text{ kg m}^{-2} \text{ s}^{-1}$. Close to perihelion at 1.243 AU, one obtains a maximum of $4.1 \cdot 10^{-2} \text{ kg m}^{-2} \text{ s}^{-1}$. This corresponds to an erosion of 16 mm of pure porous ice of 80 % total porosity). The fracture geometry with the highest peak sublimation rate also changes: it shifts from 10 deg at 5.0 AU to 18 deg at perihelion.

The analysis of fracture geometries A2 and A6 with a sublimation front at a depth of 3 mm below the fracture floor and inert walls, is depicted in Figure 3.27.

A comparison with flat terrain shows that its peak sublimation rate is 34 W m^{-2} , respectively $1.2 \cdot 10^{-5} \text{ kg m}^{-2} \text{ s}^{-1}$ for an icy surface. For a sublimation front depth of 3 mm, this value drops to $4.0 \cdot 10^{-6} \text{ kg m}^{-2} \text{ s}^{-1}$. The sublimation of a fracture floor is much higher, its rate peaks at 81 W m^{-2} ($2.9 \cdot 10^{-5} \text{ kg m}^{-2} \text{ s}^{-1}$). Additionally, significant high rates as 50 W m^{-2} (A6) and 72 W m^{-2} ($2.55 \cdot 10^{-5} \text{ kg m}^{-2} \text{ s}^{-1}$, A2) are kept for hours.

The ratio between fracture and flat terrain for 3.5 AU and 3 mm deep sublimation fronts is 2.4. Compared to the analysis of 2 AU, the tail of sublimation after direct illumination terminated is smaller and reaches values close to zero before sunset - due to colder

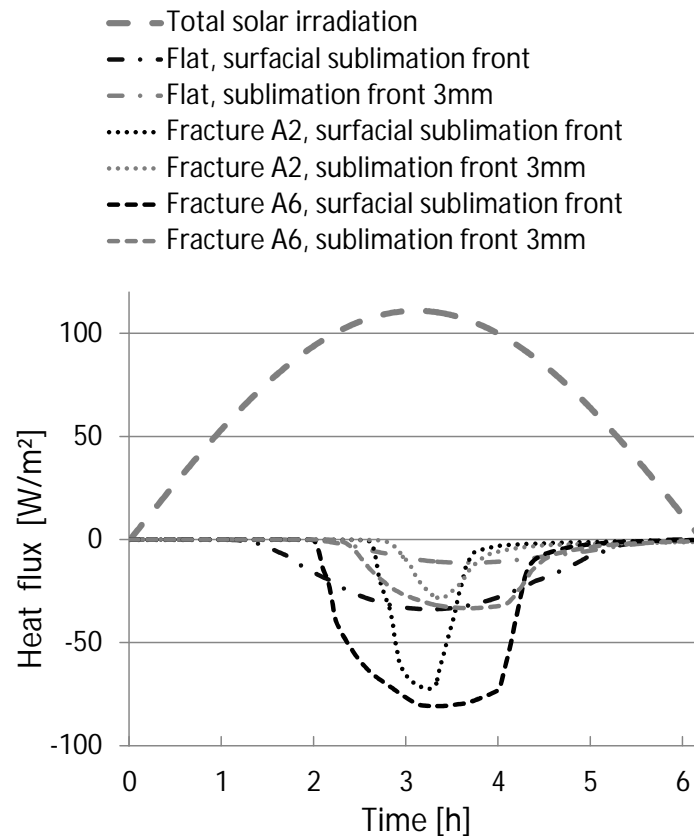


Figure 3.27: Diurnal sublimation rates for a sublimation front at the surface and at a depth of 3 mm calculated for a heliocentric distance of 3.5AU. The solar irradiation pattern for a flat surface is shown in comparison (large, dashed line); values are restricted to the 6.2 h in direct illumination conditions. Fractures A2 (dotted line) and A6 (dashed line) have sublimating floors. All calculations were performed for a solar plane angle of 30 deg and surface ice at the fracture bottom.

temperatures at this distance to the sun.

3.5.10 Temporal temperature fluctuations and gradients

This section compares temperature fluctuation rates in several model fractures and in unshadowed smooth flat terrain, focussing at inert model fractures to clearly identify trends.

Flat terrain reveals highest fluctuation rates (a global maximum) at their surface 20 minutes after sunrise, attaining up to 2 K/min. Subsequently, temperature changes drop and turn negative past the subsolar point. The global minimum is reached at sunset with a gradient of -1.7 K/min smaller in absolute numbers than the morning rise. Temperature changes in subsurface layers are up to 0.5 K/min two hours after sunset at a depth of 10 mm.

In contrast, the steep temperature rise in fracture floors coincides with direct illumination; hence this process starts several hours later. The minimum is reached earlier, the entire fluctuation process is reduced in time. Fracture floors outline stronger temperature

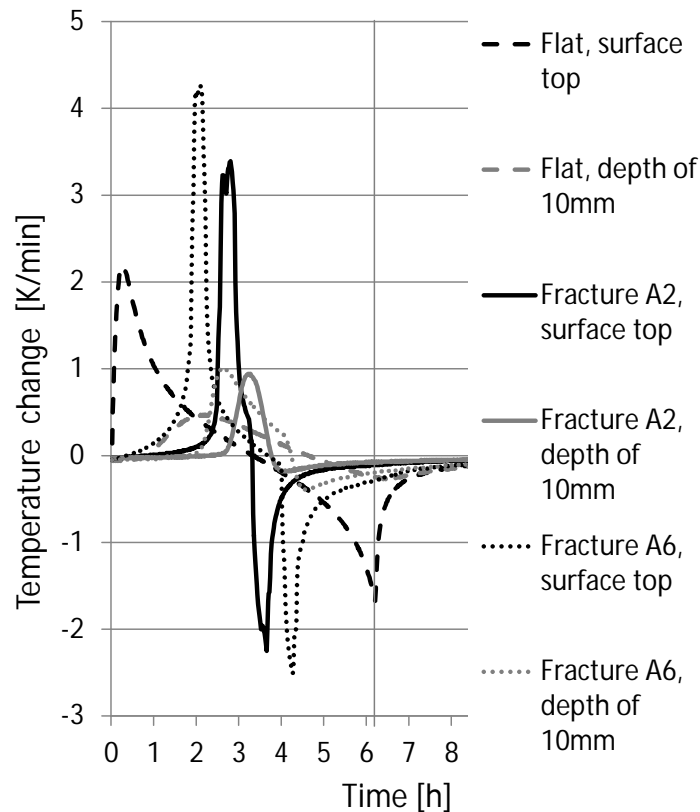


Figure 3.28: Diurnal temperature changes for fractures floors A2, A6 and flat surface topographies, calculated for surface layers and 10 mm depth. The analysis is performed for 2.0 AU heliocentric distance. The analysed fracture is considered fully inert without any sublimation front. The vertical line at 6.2h denotes the terminator.

changes, fracture A2 maximum values are 3.3 K/min, A6 shows even higher heating rates of 4.2 K/min. Diurnal cooling is significantly lower (2.5 K/min for fracture A6). In depths of 10 mm, the fluctuation rates significantly drop; however they are still double than those in flat terrains at similar depths.

Strongest thermal fluxes can be identified close to the nucleus surface, they rapidly decrease towards the interior. In the dust mantle of fracture floors, gradients attain 50 K/mm – significantly higher than in flat terrains (maximum 35 K/mm). Fracture A2 displays 250 K as surface temperature (see Figure 3.24), the temperature at the sublimation front 1 mm below is calculated to be 200 K. Small scale temperature gradients will be even higher, as effective thermal conductivity bridges values between 3.4 and 6.5 $\text{mWm}^{-1}\text{K}^{-1}$.

3.5.11 Modeling influence of surface erosion

The analysed model fractures neglected erosion effects: sublimation of volatiles dragging dust mantle particles with them. Extending the analysis to account for the effect of dust lift-off inherently requires a few more assumptions in the model:

1. Removal of material by erosion is equivalent to an outbound (negative) enthalpy

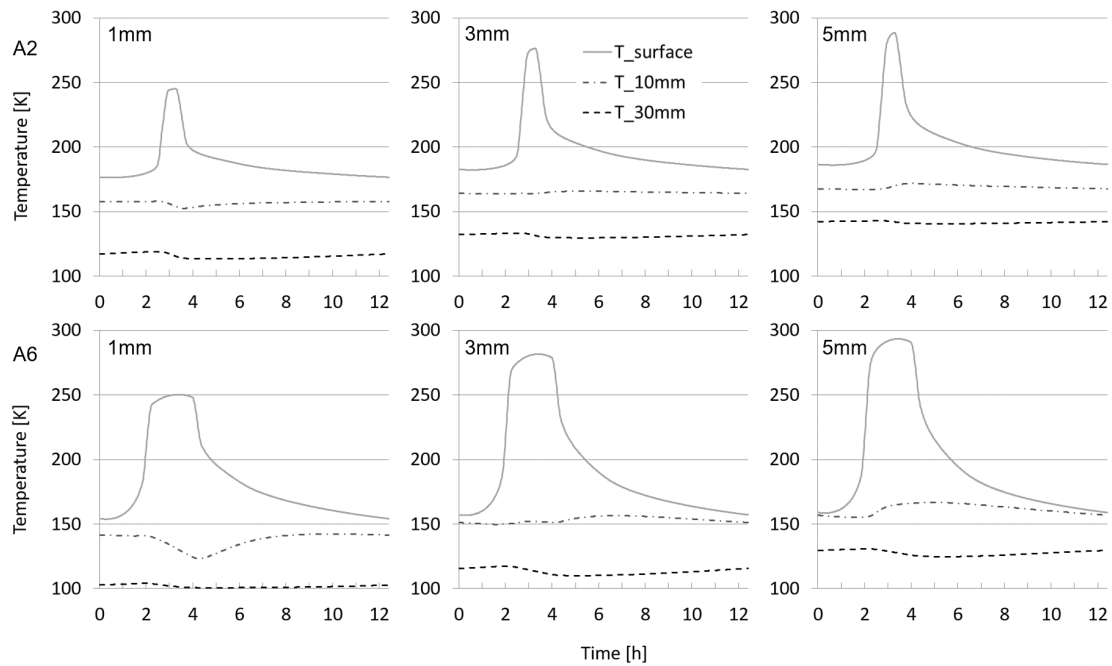


Figure 3.29: Model including dust erosion: Diurnal temperatures (in K on vertical axis, against h on horizontal axis) on its icy floor of fracture geometries A2 (top) and A6 (bottom) for three different sublimation and erosive front depths, from left to right: 1 mm, 3 mm and 5 mm. Heliocentric distance is 2.0 AU, solar plane angle η is 30 deg. The continuous line depicts the top layer (surface) temperatures, the dash-dotted line at 10 mm depth, the dashed line at 30 mm depth. The simulation uses a moving boundary approach and the interior temperature is 100 K.

flux in the total heat balance. To show the temperature evolution of the uppermost model layers in the fracture over time, the considered slice volume of the comet nucleus fractures shall be constant. As a consequence, sublimating and eroded material of the top layers has to be replaced at the bottom. To account for this, and by balancing out the mass that has been lost, this is equivalent to an inbound (i.e. positive) enthalpy flux.

2. Uppermost nodes will be depleted in mass, while lower stratum nodes will gain. The sublimation and erosion front migrates downwards, an elegant solution would be to include enthalpy balances in all neighbouring nodes. Similarly, one could integrate moving nodal boundaries into the model (Gortsas *et al.* 2011).
3. The pristine material is expected to have a boundary temperature in the simulation which lies in between formation and orbital equilibrium temperatures. This work assumed 100 K in this analysis, measurements indicate that this assumption might be too warm (Rubin *et al.* 2015).
4. The removed amount of dust, in comparison to the produced gas, has been estimated from Rosetta and modelling (Rotundi *et al.* 2015, Fulle *et al.* 2016), the value taken here is a dust/gas ratio of 4. This means that the total mass loss combined at the

nodes of the sublimation front (and hence the mass at the lower end of the model) and the surface layer is five times the sublimation mass loss, given similar densities.

The nodal energy balance of a node i is modified from Eq. 5.1 to include enthalpy fluxes \dot{H} :

$$Q_{\text{abs},i} + \sum_j Q_{\text{rad},ij} + Q_{\text{rad},\text{space}} + Q_{\text{con},im} + Q_{\text{con},in} + Q_{\text{sub},i} + \dot{H}_i = Q_{\text{cap},i} \quad (3.6)$$

The enthalpy flux \dot{H} is simplified to the alteration in heat capacity of the node, dependent on the volume flux $\dot{V}_{C,i}$:

$$\dot{H}_i = Q_{\text{cap},i} = \rho_M \phi_C \phi_{ACC} \dot{V}_{C,i} T \quad (3.7)$$

Negative enthalpy fluxes occur in the surface layer node where dust is lifted off, and in the sublimation front node. Positive fluxes are restricted to the boundary bottom node. Neighbouring nodal fluxes equal out.

The analysis uses two model fractures A2 and A6, both with an icy floor but inert walls, and varies the depth of the sublimation front. Analysed fracture floors illustrate a negative temperature gradient in its layers below the sublimation front (Figure 3.29) that is not reversed during a diurnal cycle. This finding is exclusive for simulations that include erosion. The temperature gradient is relatively large in (1) upper layers if the sublimation front is at deeper (e.g. 5 mm) depths, or (2): for surfacial sublimation fronts higher gradients are observed at deeper strata.

3.6 Conclusions of the parametric fracture analysis

This study varied illumination and fracture geometries, structural parameters of the surface, volatile-rich and inert, dusty fractures which led in total to more than 120 evaluated fracture models and corresponding datasets. While some results show a high robustness to varying parameters (the prevailing heat trap mechanism of fractures discussed in the subsequent sections being the most significant example), other findings are not dependent on a single variable alone: Here, results could be similar with different sets of input parameters (e.g. inert wide fractures resulted in similar surface temperatures than smaller ones with deep sublimation zones). This challenges the adjustment and correlation of complex thermal models with a wide variety of input parameters to observational facts.

The remote-sensing imaging capabilities of the OSIRIS camera system in spatial resolution and phase angle in the end depend on the trajectory of the spacecraft around comet 67P. Despite revealing fractured terrains all over its nucleus on various scales, their morphological characteristics and diversity (Sierks *et al.* 2015, Thomas *et al.* 2015b, Mottola *et al.* 2015, Bibring *et al.* 2015) leave free parameters for thermophysical modeling. One has to vary and parametrize a wide variety of influencing factors. As such, this approach varied illumination conditions, fracture geometry variety, physical parameters, and a set of different ice fractions in fractured terrain.

3.6.1 Heat trap mechanism of fractures

A clear trend is revealed - and none of the model variations showed a deviant result: Fractures and especially their floors invariably reveal higher average temperatures, smaller temperature variations per diurnal period, and higher peak sublimation rates than flat terrains.

This actually shows that a general heat trap mechanism exists which distinguishes fractured terrain from flat smooth surfaces.

1. Exposure towards space is smaller for fractures than for flat terrains with an open horizon; this applies invariably for all fracture facets including floor, walls, sides. Extremely sharp fractures have a low ability to emit thermal radiation to space.
2. Radiative heat transfer within the fractures dominates over emission to space. Flat fractures increase their time of illumination and show larger temperature fluctuations.
3. Solar illumination impinges the fracture floor for relatively short time periods. Due to the sinusoidal characteristics of the illumination function, higher insolation values can be found close to perpendicularity. The view factor, a simple factor of the emission function, applies in contrary to a full diurnal cycle. Thus, temperatures in the depths of fractured terrain is in all cases higher than in flat areas.
4. While flat terrain needs to warm up to reach significant sublimation rates, a fracture reaches this threshold faster. Larger fractions of received solar energy are transformed into volatile sublimation instead of reemission. Consequently, onset of activity, dust liftoff and outgassing in model fractures appear significantly earlier after illumination, than on flat terrain.

This heat trap mechanism for concavities of atmosphereless planetary bodies, first investigated for the case of lunar craters during eclipse (Saari and Shorthill 1963) and studied in theory for several types of rough terrain (Lagerros 1998, Colwell *et al.* 1990, Ivanova and Shulman 2002) here is confirmed and extended to a rotating cometary nucleus.

3.6.2 Diffusion and phase-change in porous media

The analysis found enhanced water sublimation rates and therefore production of water volatiles in fracture floors, compared to smooth terrain. While the analysis is restricted to water ice sublimation, the effect can be extended to other volatiles like CO₂ and CO.

1. The analysis resulted in high sublimation rates concurrent to strong heat fluxes to deeper nucleus layers through the porous strata. The conductivity of the porous layers reduces the thermal energy available for sublimation, and increases the observed thermal inertia. The stored energy can shift or extend the sublimation period or increase surface temperatures during the cooling phase at night.
2. The cooling phase is extended for fractured terrains, but its decreasing rate is lower than in flat terrain. Subsurface temperature profiles reverse during this time. Until

negligible sublimation rates are achieved at the sublimation front, the effective conductivity is enhanced through deposition effects. This effect was not modelled in the analysis, but frost was found in shadowed areas (De Sanctis *et al.* 2015) shortly after local sunrise and as a periodic diurnal water cycle phenomenon.

3. The mechanism applies to all volatile species in the cometary nucleus upper layers, thus several of these zones should exist at related depths; the more volatile the species, the deeper the sublimation zone. They should be affected by both diurnal and orbital skin depths.

Consecutive phase changes, i.e. the process of subsequent sublimation and resublimation at short distances, as well as heat transport through gas diffusion impact thermal conductivity but have been neglected in the analysis. Both mechanisms enhance heat transfer in a local effect close to the sublimation front: Sublimation and subsequent deposition especially at close distances can be considered as an extremely effective heat transport mechanism. Solid-to-gas phase change latent heat of H₂O, but also for CO and CO₂ outnumbers the specific heat for small (<10 K) temperature ranges by several orders of magnitudes.

Granular matter experiments conducted by Huetter *et al.* (2008) found that even close to water vapour saturation pressure levels at 200 K, measured thermal conductivity did not see a significant increase. This supports the neglect until heliocentric distances of about 2 AU. The KOSI experiments (Benkhoff and Spohn 1991) found a significant, partly dominant role of resublimation close to the sublimation front. However, the front dimension is small: The gas molecule mean free path length in the Knudsen regime of porous surface layers defines the typical length scale. This length scale is restricted by the stratum characteristics of the uppermost nucleus layers, as defined in previous chapters: the macro-porosity ϕ_S and the agglomerate radius r_A (Skorov *et al.* 2011).

The heat capacity of gases is negligible, and convective heat transfer lengths are comparable to the mean free path. Taken into consideration that $r_A = 1$ mm, the zone of sublimation and deposition comprises a few millimeters. As a consequence, the zone of locally enhanced thermal conductivity by phase change is extended to several mm as well. At temperatures well below 200 K, the thermal conductivity assumptions shall not significantly be altered by phase-change effects.

Energy conserved in fractures can lead to surface temperatures still comparably high in early shadow phases, extending the sublimation period. As the shadow-cooling phase is lasting significantly longer in fracture floors than in flat terrains, a reversed temperature profile can be noticed for longer times. Fracture parts that are colder than the sublimation front might experience a more pronounced recondensation process.

3.6.3 Porous agglomerate textures and effective thermal conductivity

Small cohesive forces between agglomerates (model assumptions take radii between 0.1 and 1 mm) result in a domination of radiative heat transfer over solid conduction through the porous strata. The assumption of isothermal agglomerates allows to integrate radiative heat transfer into an effective thermal conductivity. Larger agglomerates cannot fulfill this prerequisite. Porous agglomerates transform into a sintered structure (Grün *et al.* 1993) through alternating sublimation and deposition phases. Restructured layer textures change

the agglomerate sizes and their distribution and macro-porosity. As a consequence, diffusive transport is reduced (Gundlach and Blum 2012), and conductive heat transfer gains a more important role against the previously dominating radiation.

3.6.4 Thermal inertia of fractured terrains

VIRTIS and MIRO measurements on Rosetta and constitutive interpretation and analysis determined the thermal inertia of 67P to be between 15 and 120 $\text{Jm}^{-2}\text{K}^{-1}\text{s}^{-1/2}$ (Lowry *et al.* 2012, Schloerb *et al.* 2015, Spohn *et al.* 2015, Marshall *et al.* 2018), and varying over the regions of 67P (Leyrat *et al.* 2015). Areas on 67P with consolidated terrain, which bears most fractures, resulted in higher thermal inertia (Leyrat *et al.* 2015) than smooth topographies. The smooth neck region Hapi with its higher peak temperatures than the surrounding (due to its location between the two lobes, similar to the fracture geometric heat trap effect) revealed a higher thermal inertia than other smooth areas, which is explained with the effect of volatiles (Groussin *et al.* 2019) and also discussed in previous sections. The illumination conditions, interplay of sublimation heat sinks, and especially the surface roughness which includes fractured terrain topographies, all lead to uncertainties in thermal inertia determination.

3.6.4.1 Thermal infrared emissions

The surface thermal emission heat flux can be integrated to represent a hemispherical brightness temperature, according to the Stephan-Boltzmann law. This method can identify fractured terrains by IR-sensitive cameras; future comet missions will surely carry thermal mappers. In case an imaginable thermal mapper is not able to resolve the fracture geometry, the signal of the received thermal pattern can be interpreted as an integral brightness temperature. Following this thermal signal over time and ruling out the position of the observer in orbit (Davidsson *et al.* 2015), it can be interpreted as depicted in Figure 3.30.

3.6.4.2 Brightness temperature patterns

Figure 3.30 shows brightness temperatures of six different fracture topographies by integrating over the thermal emission signal. In general, they follow diurnal sinusoidal irradiation patterns. In comparison, a flat surface, characterised through a general low thermal inertia of $31 \text{ J m}^{-2} \text{ K}^{-1} \text{ s}^{-1/2}$ shows its temperature maximum a few minutes after the subsolar point: it lags 1 deg for a sublimating and 6 deg for an inert surface, measured in the deviation of the local hour. For all analysed fractures, the lag is larger: an inert fracture A2 with a wall angle $\alpha_{A2}=14.0$ deg accounts for 20.3 degrees, A6 with $\alpha_{A6}=2.9$ deg even results in a lag of 45.5 degrees after peak irradiation.

Temperature patterns get more complex if the fracture has a sublimating floor (marked as bottom sublimation in Figure 3.30). Due to the higher temperatures of fracture walls, a signal that has two peaks (fracture type A2) is obtained, respectively a continuous rise until late afternoon (A6). Full-icy fractures, compared to full-icy flat terrain, shows significantly smaller temperature fluctuations.

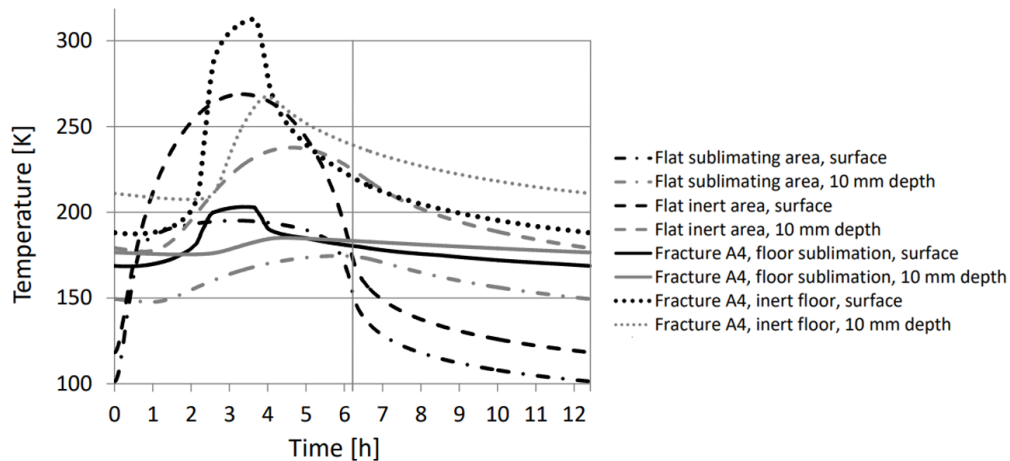


Figure 3.30: Diurnal hemispherical brightness temperatures of flat and fracture geometries A2 and A6 for different sublimation patterns. The heliocentric distance is 2.0 AU, the plane angle is $\eta = 30$ deg, and the sublimation front is identical to the surficial node. The dotted line shows the brightness temperature for flat terrains (sublimating and inert), while fracture geometries A2 (grey) and A6 (black) in three different configurations are displayed: for completely inert (dashed), sublimation of both bottom and walls (dash-dotted), and pure fracture floor/bottom sublimation.

Generally it can be observed from this, as previously noted, that fractures show slower heating and cooling, and higher night-time brightness temperatures. Substituting measurements by distant observers with the derived synthetic brightness temperatures from fractured terrains and comparing it to the temperature calculated solely for the fracture floors, as shown in Figure 3.24, the observer cannot resolve the full temperature bandwidth. As the terrain reaction to insolation and shadowing appears much slower than for flat terrain, thermal inertia derivations might be misleading: observed patterns appear similar to higher thermal inertia areas. In conclusion, fractured and consolidated terrain on 67P might have similar surface properties than flat, airfall areas - but thermal inertia from observations might indicate that they differ.

3.6.4.3 Thermal inertia of Philae landing site Abydos

MUPUS onboard the Rosetta lander Philae recorded temperatures in the vicinity of the final landing site, a depression beneath fractured cliffs named Abydos (Bibring *et al.* 2015, Lucchetti *et al.* 2016). Radiometer data (Figure 2 in Spohn *et al.* (2015)) revealed a dichotomy in the temperature decline during obscuration times. Their approach to determine the local thermal inertia resulted in relatively high values with a huge uncertainty of $(85 \pm 35) \text{ J m}^{-2} \text{ K}^{-1} \text{ s}^{-1/2}$. Fractured terrains shows some similarities: While both heliocentric distance and the effective latitude during Philae's measurements (3.0 AU) deviate widely, measured temperature patterns resemble calculated data depicted in Figure 3.24 (especially fracture A2).

Apparently, when the entire landing site passed into shadows, there is a cooling trend of all areas. The cliff next to the lander obscures fast cooling similarly as fracture walls do.

The proposed thermal inertia fitting is unable to resolve the underlying effects properly (Spohn *et al.* 2015). As such, the MUPUS data gives a good hint that the heat trap effect of fractures terrain is observed for a comet nucleus. An alternative explanation of the local thermal inertia in Abydos is an enhanced sintering of the surface layers (Groussin *et al.* 2019).

3.6.4.4 A solid-state greenhouse effect?

The thermal inertia discrepancies for flat and smooth airfall terrain, compared to the more fractured and consolidated terrain, can be attributed to the roughness variation (Gulkis *et al.* 2015, Leyrat *et al.* 2015). A second interpretation to explain discrepancies between modelled and observed temperatures on comet Tempel 1 (Groussin *et al.* 2013) might be the temperature-dependent heat conductivity: As porous dust models, composed of agglomerates, include radiation in the effective heat conductivity, heat fluxes directed inwards are enhanced and outbound fluxes are impeded. Combined with the impact of heat trapping of fractures, a solid-state greenhouse effect is feasible: The nucleus rough and fractured terrain is slightly warmer than heat balance analysis would suggest. Furthermore, this effect camouflages the small amount of active, sublimating surfaces (that shall have lower temperatures due to their internal heat sink) and makes them even harder to be estimated from multi-instrument parametric analysis of Rosetta data and future investigations.

3.6.4.5 Influence of illumination on fracture morphology

One of the parametric results is that the fracture geometry with the highest relative sublimation rates clearly depends on the illumination conditions. One of the consequences of this finding would be a diversity of fracture morphology between 67P's northern and southern hemisphere.

Three months before perihelion in August (Mottola *et al.* 2014), 67P passed its equinox in May 2015. With an axial tilt of 52 deg and due to the high eccentricity, southern summer is short but close to perihelion (Keller *et al.* 2015). Northern summer lasts much longer, but some areas never see higher irradiation than 400 Wm^{-2} , about half of the maximum at perihelion. High solar irradiance angles and isochronal low irradiation due to the distance then should characterize northern fractures. The relative sublimation rate of heat traps increases with higher heliocentric distances (see Figure 3.26). One would expect a gradual change of fracture topography from north to south, which observations could not detect. Fractures tend to broaden more quickly in the south as well.

The analysis found that fracture geometries aligned with the solar path around the comet evolve faster and broaden more quickly if erosive losses drive the evolution of fractures; one would expect a difference in dimensions to those that are perpendicular. Geomorphologic mapping showed in contrast to this analytical finding that fractures are not specifically aligned with the solar path around the nucleus (La Forgia *et al.* 2015, Basilevsky *et al.* 2018). Ideal conditions should lead to a fracture growth of about one meter per perihelion passage.

3.6.5 A scenario of fracture evolution

The devolatilisation of subsurface layers affects even deeper layers in fractures. Desiccated material is undergoing more rapid temperature changes and weakens cohesive structures in agglomerates. The funneling geometry of fractures enhances possible dust removal by gas drag. As a consequence, fractures grow in width and depth. Cliff walls with their gravity vector being perpendicular to the normal, can influence this by supporting material removal through collapse and erosion.

The fracture growth mechanism can be distinguished in sublimation mostly at the bottom, and erosive dust release from the side walls. The model calculations revealed diurnal water ice mass losses due to sublimation of 0.02 to 0.1 kg/m² for surfacial ice on the fracture floor and in fracture floor erosion rates of 0.4 to 2.4 mm per 12.4 h diurnal period at 3.5 AU. Near perihelion (1.25 AU), the diurnal erosion rate rises up to 1-4 cm. Buried water ice would result in lower rates, but these numbers are not orders of magnitude lower. Thus, if sublimation drives the fracture evolution, and the illumination conditions during perihelion passage were fair, OSIRIS images should have been able to detect fracture changes. So far, this could not be confirmed, as the observed neck crack broadening between both lobes is not likely to be driven by thermal forces.

The comparison of fractures with inert versus those with sublimating side walls resulted in the finding that the highest sublimation rates can be expected at the bottom of a fracture - restricted only when the fracture apex angle γ gets too small for significant illumination times. Assuming that dust activity is the predominant evolution mechanism, fractures are likely to grow in directions that are subject to direct illumination conditions. Dust-ice matrix heterogeneities influence this evolutionary growth direction. During the fracture evolution towards inner cometary layers, the thermal wave reaches yet unexploited volatile-rich areas.

The sublimated gases initiate a channel flow in the fracture that exerts a fluid flow pressure on fracture wall particles, and the resulting tensile and shear stresses excavate these particles from its neighboring agglomerates. Lifted dust particles in the fracture are likely to interact with wall dust and collisions might trigger to further dust-liftoff, with gravitational slope effects supporting this process.

4 Model application to a cliff collapse

The collapse of a large overhanging cliff is the most manifest cause of an outburst event on July 10th 2015 (Vincent *et al.* 2016). This chapter discusses the thermophysical processes in the cliff wall and possible explanations of the trigger mechanics of its collapse. The study has been published, co-lead by Höfner as Pajola *et al.* (2017) in Nature Astronomy, contents in this chapter are reproduced with permission from Nature Portfolio.

4.1 Outburst characteristics

One month prior to 67P's perihelion passage, at a heliocentric distance of 1.31 AU, the navigation camera on board of Rosetta imaged a bright dust plume that was categorised as outburst event (Figure 4.1, right). The observation plan of the OSIRIS cameras did not capture the event itself, but contributed to limit time interval and length of the outburst. The outburst morphology analysis concluded a type B outburst event, characterized by a broad plume and a wide dust fan (Vincent *et al.* 2016), that show a rather lateral than radial expansion. The outburst happened during local night in the northern hemisphere, which distinguished this event from all other outbursts catalogued by Vincent

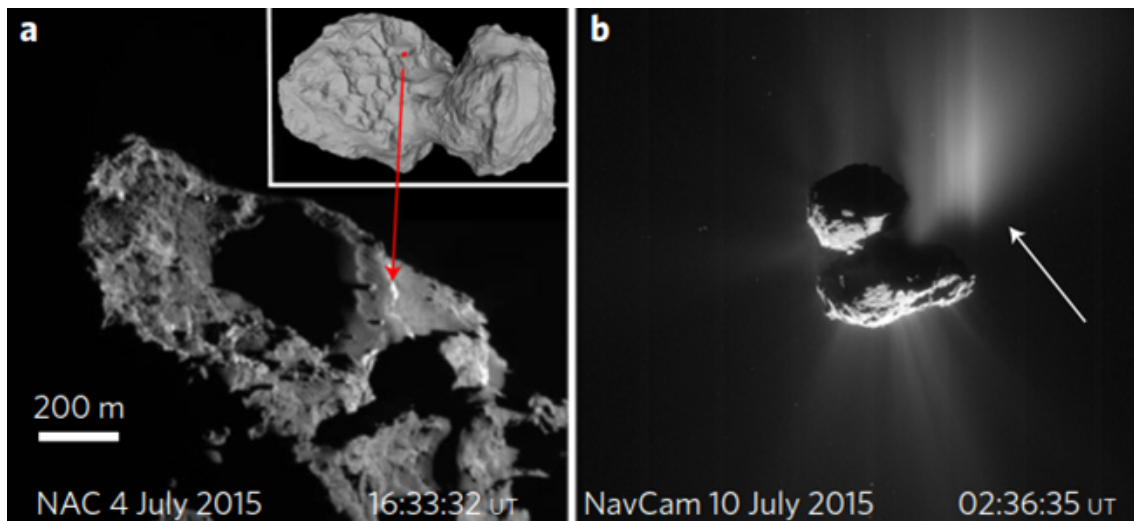


Figure 4.1: Image taken from Pajola *et al.* (2017), parts of figure 1: a) OSIRIS image NAC_2015-07-04T16.33.32 shows the poorly illuminated top view of the cliff, the location on 67P is visualized by the red dot. b) NAVCAM imaged the outburst plume, which is originating from the shadowed part on July 10th 2015.

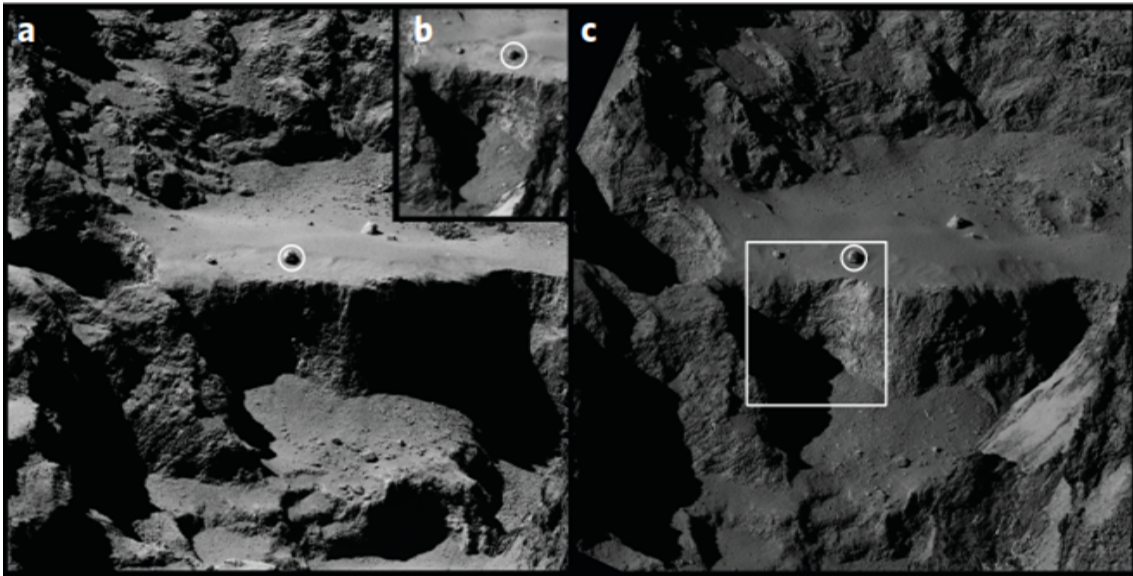


Figure 4.2: High resolution images of the Aswan cliff before (a,b) and after (c) the outburst event. The encircled boulder acts as a reference. 22000 m^2 of material was removed (Pajola *et al.* (2017), parts of figure 2)

et al. (2016). Roughly 10^6 kg of cometary material was ejected. Figure 4.1 (left) shows OSIRIS images of the cliff before the collapse.

4.2 Topography and evolution of the cliff

The collapsed cliff is located in a highly fractured area just above the neck on the larger of 67P's lobes in the northern hemisphere of the nucleus, in close vicinity to the northern pole in the Aswan region at the border to Seth; the naming is according to the regional mapping in Figure 2.2 by El-Maarry *et al.* (2015b). Due to the bilobate nucleus shape, this point is surrounded by terraces and cliffs and widely understood as layered structure (Massironi *et al.* 2015, Matonti *et al.* 2019). The cliff itself is partly an overhanging structure, as its surface normal and the local effective acceleration vector of combined gravity and centrifugal force form an angle of more than 90 degrees. From the total cliff height of 134 m, about 70 m crumbled, at a front between 57 and 81 m wide and with an average thickness of 12 m. This refers to a total volume of 22,000 cubic meters that collapsed. A large fracture on the terrace above the cliff was already imaged by OSIRIS shortly after arrival at the comet in August 2014. This fracture, appearing similar to glacier crevasses on Earth, disappeared in the course of the outburst event and assisted in estimating morphological processes. High-resolution images of the cliff structure, taken at better viewing conditions more than 3 AU heliocentric distances to the sun, are shown in Figure 4.2.

On July 15th 2015, five days after the outburst, OSIRIS imaged a fresh surface at the cliff, exposing the pristine interior of the nucleus. The interior structure captivates through a bright normal albedo of more than 0.4, in strong contrast to the dark comet surface around. Five months after the collapse, the albedo of the newly exposed surface

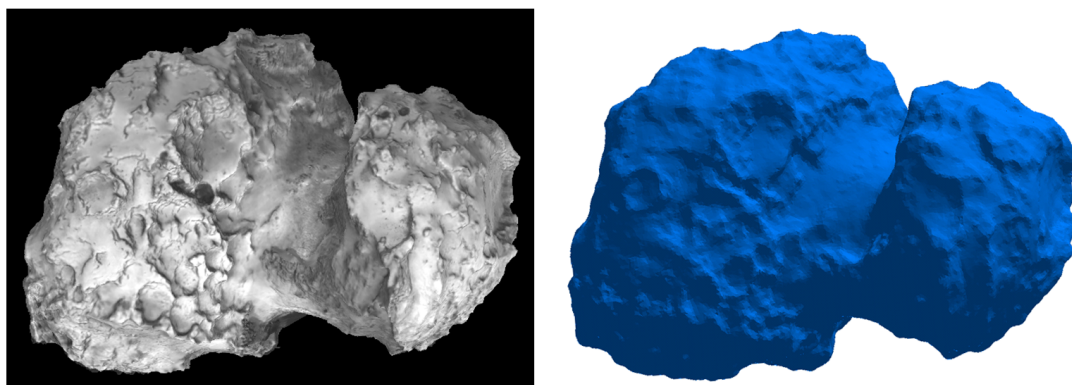


Figure 4.3: Shape model with 10^7 facets (left) and reduced geometry model with 100,000 facets (right) used for thermophysical analysis

has declined to 0.2; spectral analysis showed that the water ice content still was significantly higher than in the surrounding fractured and smooth terrains. Apart from an icy block that still stands out in respect of reflectivity, a year after collapse the cliff structure resembles the darker global surface values again. Local illumination conditions led to extremely short direct solar irradiance times and few possibilities to catch images for OSIRIS cameras.

4.3 Thermophysical analysis of the cliff structure

In order to contribute to a better understanding of the cliff state and to establish possible collapse scenarios, a thermophysical analysis of the region and its surroundings is performed. Pointed out in the chapter on thermophysical analysis of fractures and surface roughness, the detailed topography of the area governs local temperature distribution patterns, and these patterns are independent of the scales as long as they are larger than the characteristic thermal length scales. Due to the complex illumination geometry, the analysis considers the whole nucleus geometry and is not restricted to a regional cutout – also self-heating interactions with the opposite lobe of the nucleus and the imposed shadowing need to be accounted for.

4.3.1 Model of the cliff

The SHAP4S digital terrain model of 67P (Preusker *et al.* 2015), consisting of millions of triangular facets, is reduced to less than 100,000 surface elements by using Meshlab[®]. This reduction is considered to be reasonable and subject to trade geometric accuracy against the computational and convergence times of the model.

The thermophysical modeling approach is based on the fracture thermal models with small differences. The nucleus facets are divided into two groups; one group of nodes that will be investigated in detail in their column depth, and one group that forms the radiative environment. The first group includes all surfaces that are located along a cut through the cliff and adjacent on the terrace above it. These facets are supported with a one

dimensional column of thermal nodes that form the subsurface. Heat transfer is restricted to the conductive and radiative transfer in agglomerates, sublimation is neglected –mostly due to the wide range of parameters that add a lot of distracting complexity in this specific situation, as shown in the chapter before. The thermal model takes into account direct and scattered insolation, shadowing, and radiative exchange with all other facets of the nucleus. The thermal balance equation also accounts for lateral conduction:

$$Q_{\text{abs},i} + \sum_j Q_{\text{rad},ij} + \sum_j Q_{\text{rad},space} + Q_{\text{con},im} + Q_{\text{con},in} = Q_{\text{cap},i} \quad (4.1)$$

The single constituents then are

$$\begin{aligned} i_{\text{rad}}(1 - \alpha) \frac{S}{r^2} A_i \cos \theta - i_{\text{rad}} \sum_j \varepsilon_i \varepsilon_j \sigma A_i F_{ij} (T_i^4 - T_j^4) \\ - (1 - i_{\text{rad}}) \lambda_{\text{L, eff}}(T_{i,m}) A_i \frac{T_i - T_m}{\Delta z_{i,m}} - (1 - i_{\text{con}}) \lambda_{\text{L, eff}}(T_{i,n}) A_i \frac{T_i - T_n}{\Delta z_{i,n}} = m_i c_i \frac{dT_i}{dt} \end{aligned} \quad (4.2)$$

Parameters are the same as assumed in the standard model of the fracture analysis: i_{rad} is set to 1 for facets on the nucleus surface, and 0 for internal nodes. i_{con} is by default 0, but set to 1 for all boundary nodes at the bottom. Temperature variations fade out at depths of several centimeters. An adiabatic boundary at a depth of 0.35 m is assumed.

$$\left(\frac{dT}{dx} \right)_{x=0.35} = 0 \quad (4.3)$$

The subsurface temperature distribution is broken down to consist of in total 20 nodes for every surface element. The layer thickness ranges from 1 mm underneath the surface to 70 mm at the bottom.

The second group of nodes consist of all facets not part of the cliff. This group accumulates more than 99 % of all facets on the nucleus model, their purpose is to

1. form the radiative environment by determining a surface temperature that is in exchange with the cliff facets to model self-heating,
2. restrict cooling rates of the cliff nodes by reducing the view factor towards cold deep space,
3. ensure an accurate shadowing of the impinging solar rays and to limit the insolation times with sharp transitions.

These nodes exclude conduction to subsurface layers but retain an internal heat capacity to represent the thermal inertia of the surface. Their heat balance equation then is:

$$i_{\text{rad}}(1 - \alpha) \frac{S}{r^2} A_i \cos \theta - i_{\text{rad}} \sum_j \varepsilon_i \varepsilon_j \sigma A_i F_{ij} (T_i^4 - T_j^4) = m_i c_i \frac{dT_i}{dt} \quad (4.4)$$

This approach is only defensible for environmental nodes. With heat capacity neglected, cold environmental temperatures would be lower than observed, while temperature rises are overestimated. This was already found by comparison of thermal analysis and remote sensing measurements as discussed in Groussin *et al.* (2013). Analysis which use models with flat surface facets in combination without thermal inertia like in Davidson *et al.* (2015) receive huge modelling deviations for rough terrains.

4.3.2 Cliff illumination

The diurnal illumination pattern drives the changing thermophysical conditions at the cliff. Two different radiative environments for May 10th and July 10th 2015 are described in Table 4.1. Irradiation is calculated for every 5 degrees of the nucleus rotation, resulting in 72 positions per nucleus revolution. Times between those positions are linearly interpolated. Accurate sunrise modelling is crucial for the results, as it highly affects the accuracy of the temperature rise of the cliff surface due to shadowing of the opposite lobe of the nucleus.

The high obliquity of 67P's rotation axis resulted in a solar zenith elevation perpendicular over a latitude of 30.3 deg on July 10th 2015. This peculiar situation leads to short illumination times on the steep elevation surfaces on the northern hemisphere: Especially at overhangs like the Aswan cliff, the maximum irradiation angle is close to perpendicular. On the other hand, direct cliff illumination is restricted to about 90 minutes for one diurnal rotation. The smaller lobe of 67P led to a continuous shadowing during the morning hours, hence the illumination starts at local noon nearly perpendicularly on the cliff wall. The edge of the small nucleus lobe created a sharp contrast on the already illuminated part in the terraced region above the neck, as depicted in Figure 4.4 1-6. The cliff is directly illuminated between images 2 and 4 by a steep rise from shadow to about nearly 800 W/m². No other large, resolved structure on the northern hemisphere of the nucleus is that highly strained by solar irradiation. The decline of the local irradiation is slower than the instantaneous rise, and finally terminated by the shadow of the big lobe's rim (Figure 4.4 7-12).

The investigation of the temporal development of the illumination conditions focuses on a characteristic facet on the cliff, and comparing it to a typical facet of the plane above. The location of these facets with respect to the nucleus and the cliff are depicted in (Figure 4.5). These facets can be treated as good examples for the whole range of thermal behaviour of the cliff structures. The left side of Fig. 4.6 shows irradiation patterns for 1.5 diurnal revolutions, for the collapse date and the equinox exactly two months earlier.

Due to the highly elliptical orbit of 67P, the cliff illumination conditions change rapidly during perihelion approach; relevant properties for the thermodynamic analysis during perihelion approach and its implications on the illumination pattern are detailed in Table 4.1.

During equinox, the entire neck area in the northern hemisphere was illuminated for about three hours, the difference in insolation between cliff wall and plateau being low. Due to the bilobate character of the nucleus, a small fraction of illumination reached the Aswan region from the other side. A complex shadowing pattern evolved that changed quickly, as the months around equinox saw a change of the solar elevation of 0.30 to 0.57 degrees per day, with the highest change rates being around the time of the cliff col-

Table 4.1: 67P orbital data and its implications on the Aswan cliff during 67P perihelion approach, listed from the beginning of the Rosetta mapping phase until perihelion. The solar latitude describes the angle between the rotation axis and the orbital plane. The diurnal latitude change rate describes the shift of the solar position and strongly impacts the change of the qualitative illumination pattern; the peak irradiation gives the maximum possible direct insolation on the Aswan cliff. The maximum diurnal change rate describes the shift of the peak irradiation on the cliff for an Earth day.

Date	Solar latitude [deg]	Diurnal latitude change rate [deg/day]	Solar distance [AU]	Peak irradiation [W/m ²]	Max. diurnal change rate [W/m ² day]
10-Sep-2014	42.41	-0.068	3.395	64	0.3
10-Mar-2015	18.96	-0.235	2.137	248	2.5
10-Apr-2015	10.67	-0.306	1.898	342	3.7
11-Apr-2015	10.36	-0.309	1.890	346	3.7
25-Apr-2015	5.78	-0.349	1.784	402	4.3
Equinox					
10-May-2015	0.21	0.398	1.673	471	5.0
11-May-2015	-0.19	0.402	1.666	476	5.0
26-May-2015	-6.59	0.456	1.560	555	5.48
Maximum diurnal irradiation rate change					
01-Jun-2015	-9.38	0.478	1.521	588	5.54
10-Jun-2015	-13.81	0.510	1.464	638	5.41
25-Jun-2015	-21.80	0.555	1.379	714	4.4
10-Jul-2015	-30.31	0.574	1.311	767	2.3
11-Jul-2015	-30.88	0.574	1.308	769	2.1
Peak irradiation at cliff					
22-Jul-2015	-37.11	0.551	1.273	782	0.0
23-Jul-2015	-37.67	0.547	1.270	782	-0.1
26-Jul-2015	-39.29	0.533	1.263	780	-0.7
10-Aug-2015	-46.50	0.403	1.244	753	-2.4
Perihelion passage					
13-Aug-2015	-47.67	0.364	1.243	744	-3.1
05-Sep-2015	-52.04	-0.013	1.275	671	-2.8

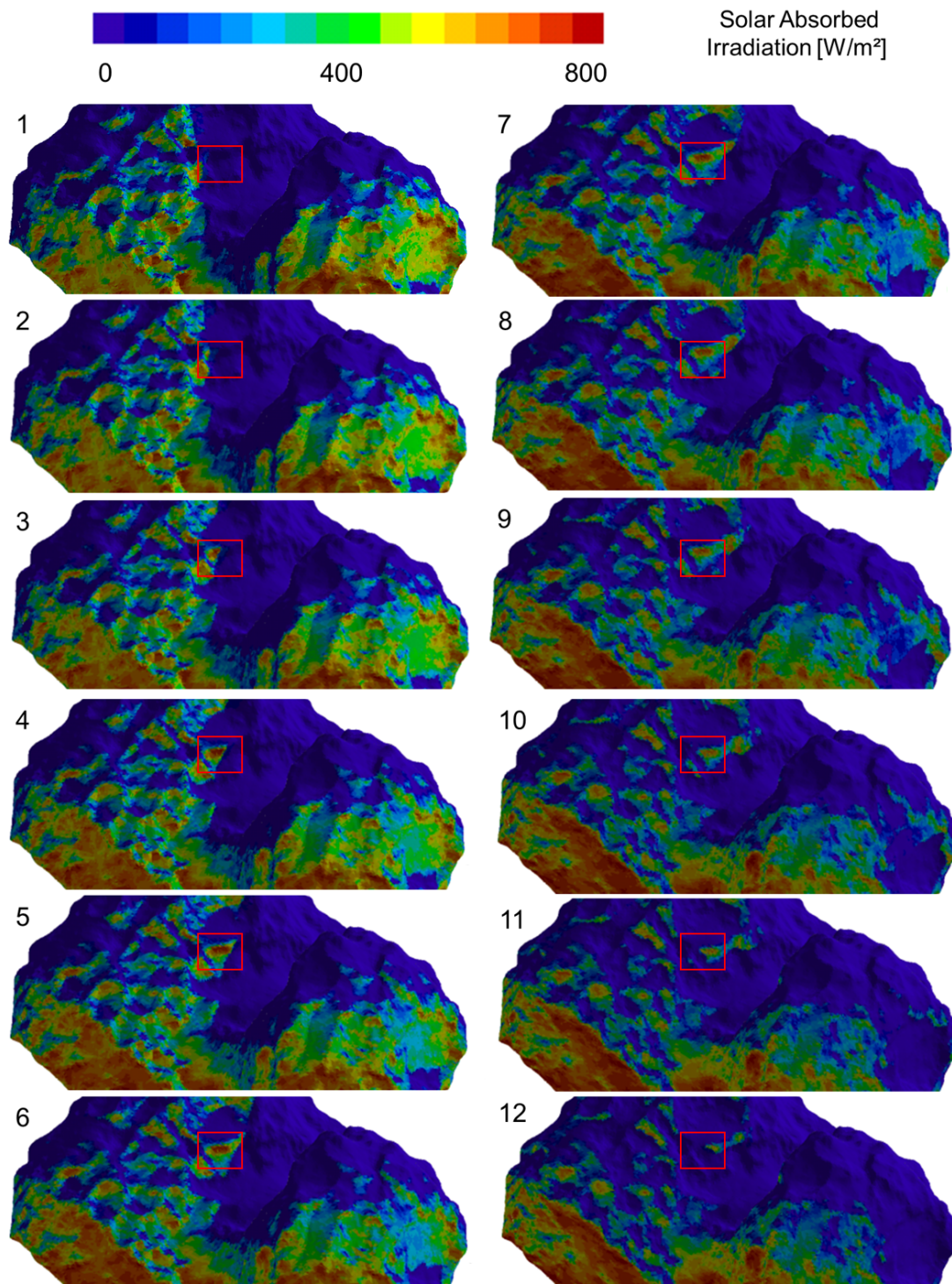


Figure 4.4: Solar irradiation pattern and values on the Aswan cliff and the surrounding as a sequence of 12 positions in intervals of 10 minutes

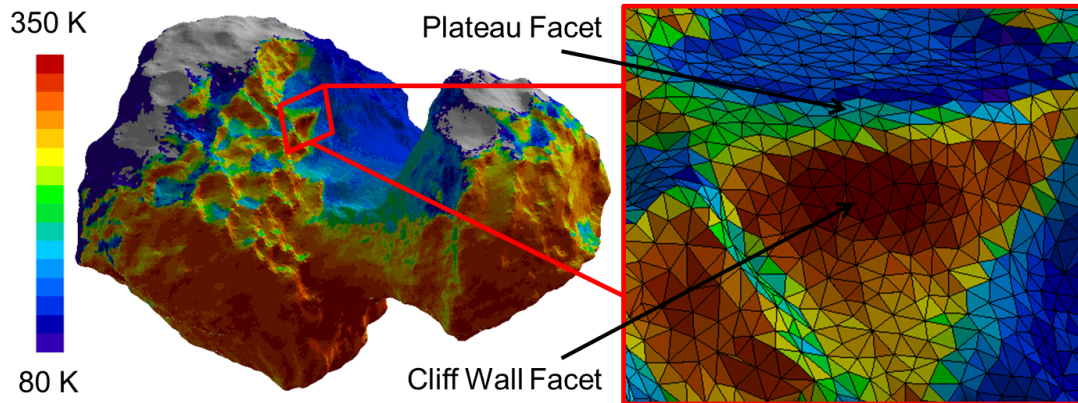


Figure 4.5: Location and maximum temperatures of the Aswan cliff wall and terrace (plateau) facets in respect to the cliff (right) and the whole nucleus (left)

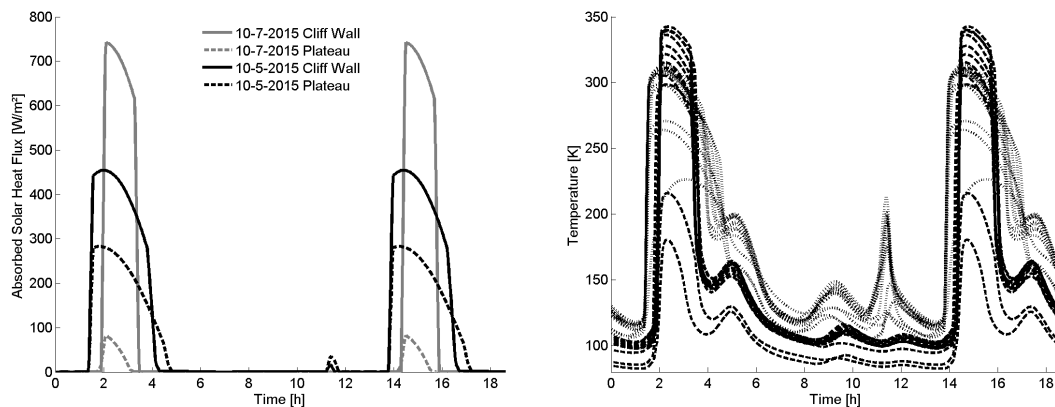


Figure 4.6: Irradiation on a typical facet of the Aswan cliff for equinox at May 10th 2015 (black, left) and date of the cliff collapse on July 10th 2015 (grey, left). Temperature distribution of the group of 12 facets of Aswan cliff and plateau (right), grouped into temperatures at May 10th 2015 (dotted) and July 10th 2015 (dashed).

lapse (see Table 4.1, column 3). Additionally, peak irradiation shifted from 470 W/m^2 to 770 W/m^2 , every new rotation increased the irradiation by 2.5 W/m^2 . The peak irradiation at the cliff at the day of collapse was only 15 W/m^2 lower than the seasonal maximum 12 days later.

Comparing the average insolation by integrating the time resolved values over one diurnal period, Figure 4.7 depicts the average solar irradiation of each facet at the equinox to the equivalent situation two months later at the cliff collapse date.

Generally, there is a widespread decline of irradiation values in the northern hemisphere; especially terraces covered with dust deposits and taluses are not illuminated any longer and will receive sunlight as late as early 2016 again. The Aswan cliff and the nearby areas with overhangs stick out in this image – they retain their average irradiation values despite illumination time drops. The Aswan cliff remains stable at values of about

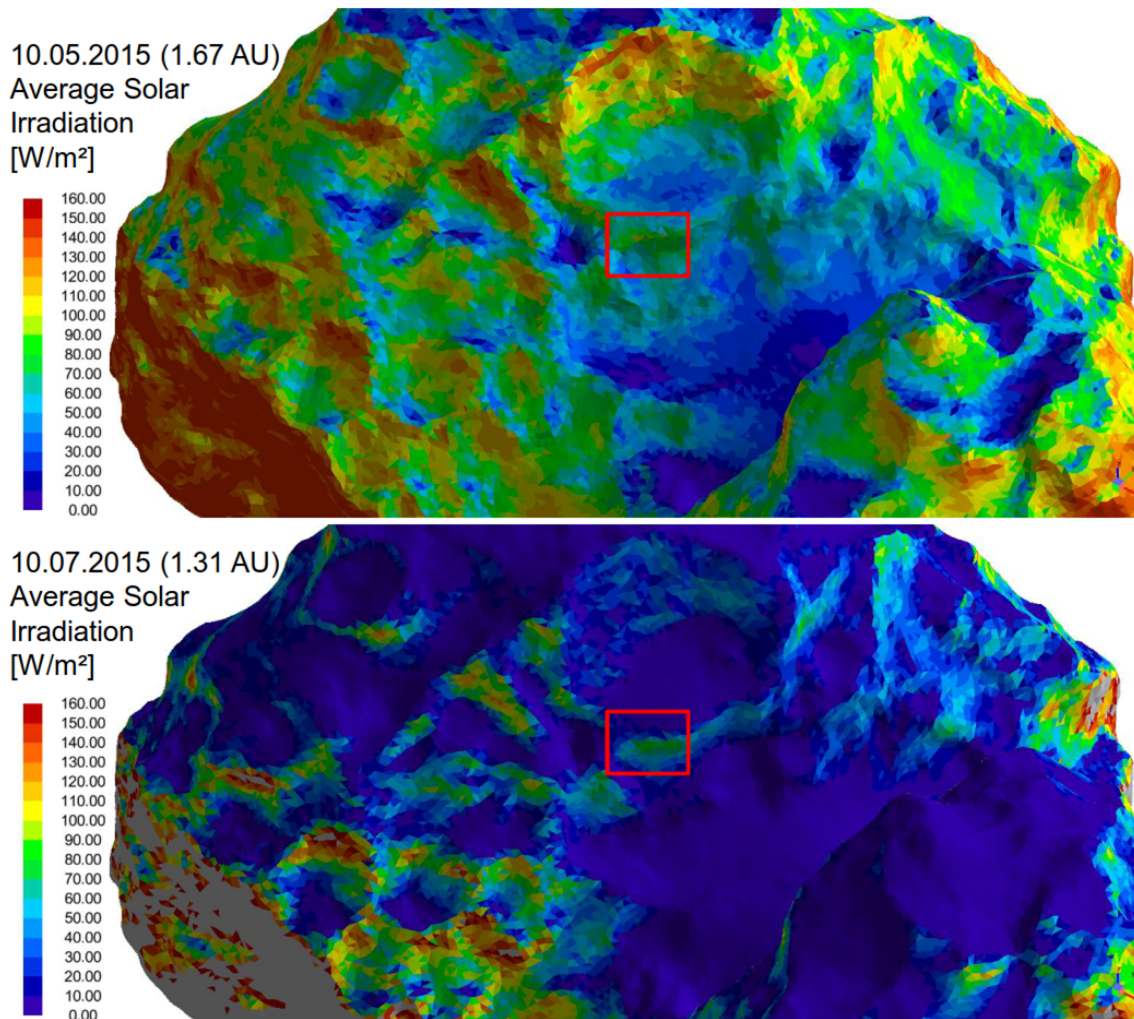


Figure 4.7: Average solar irradiation pattern for two different orbital positions: Equinox on May 10th 2015 (top) and date of the cliff collapse on July 10th 2015 (bottom)

80 W/m^2 . Most of the other fractures and steep terrains have their average insolation values dropped. In contrary, there is a significant rise in areas that are exposed to more southern facet normals. Beside the direct illumination pattern changes, secondary effects like scattered light and thermal emission even more pronounce this irradiation scheme.

4.3.3 Temperatures of the cliff

Figure 4.8 depicts the temperatures along the cliff surface, including facets of the terraced plateau, the cliff wall, and the border to the talus on 10th of July. At the moment of local sunrise, the smaller lobe of the nucleus casts shadows over the cliff. Shortly after local noon (with the peak potential irradiation already passed), the illumination starts sharply. At this moment, the temperatures at the cliff surface are at 100 K or slightly above. Ten minutes later, the cliff facet temperatures have risen to more than 250 K, reaching the maximum of 345 K another ten minutes later. Talus temperatures are slightly (310 K), plateau temperature significantly lower.

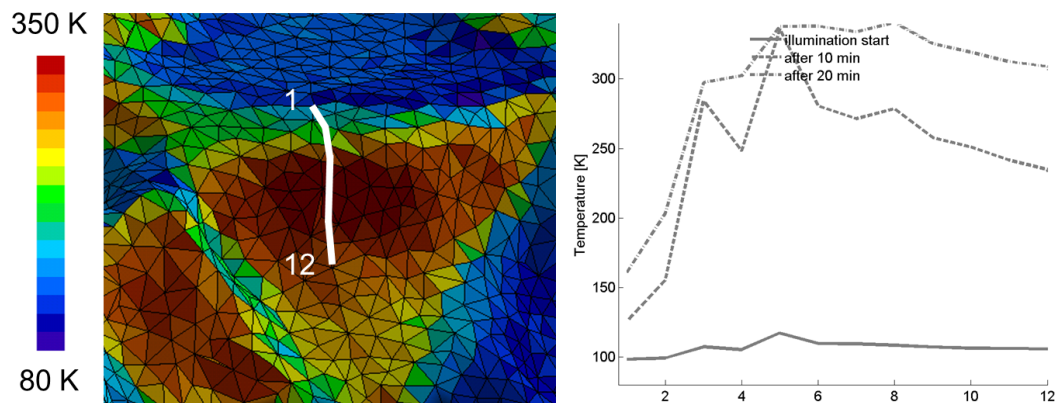


Figure 4.8: Cross-section through the Aswan cliff facets (left side – colours denote the maximum temperatures at these facets); Temperatures along the facets of the cliff thermophysical model (right side) for sunrise and ten minutes / twenty minutes later.

Figure 4.6 (right) shows the temporal evolution of all facets; the dotted lines correspond to equinox, the dashed lines to the cliff collapse date. One can distinguish three general patterns:

1. For the period that was analysed (two months and more than 100 nucleus revolutions), the maximum temperature is achieved within less than one hour of the minimum temperature, generating high fluctuations and material gradients.
2. Peak temperatures show higher values and a broader spread between maximum and minimum close to perihelion (on 13th of August 2015).
3. The facet pattern becomes more patchy on the collapse date, peak temperature ranges from 180 to 345 K.

Subsurface temperature curves of the cliff (see Figure 4.9 top left) show a steep rise due to the real sunrise and sunset position, whose pattern is similar for both analysed diurnal rotations. The deeper layers are significantly colder (about 20 to 50 K) at the time of collapse, and their diurnal temperature variation drops.

Temperature fluctuations, evoked by thermal self-heating and scattered light and relevant for the surface temperature, are dampened out at 5 mm depth below the surface. Subsurface layers show temperature fluctuations up to 12 K/min (at 1 mm depth). The low thermal conductivity leads to high temperature gradients in the cliff face upper layers. The maximum is 155 K/mm and 40 K/mm is surpassed for about an hour. At the plateau, lower gradients (95 K/mm for May and 55 K/mm in July) are calculated. Deeper nucleus layers maintain gradients around 10 K/mm for roughly an hour.

4.3.4 Consequences of sublimation and fracture geometry

This analysis neglected sublimation effects, while the high albedo of the freshly exposed surface clearly indicates that there are volatiles. From the knowledge accumulated in the fracture analysis, one can qualitatively describe what effects can be expected from

4.3 Thermophysical analysis of the cliff structure

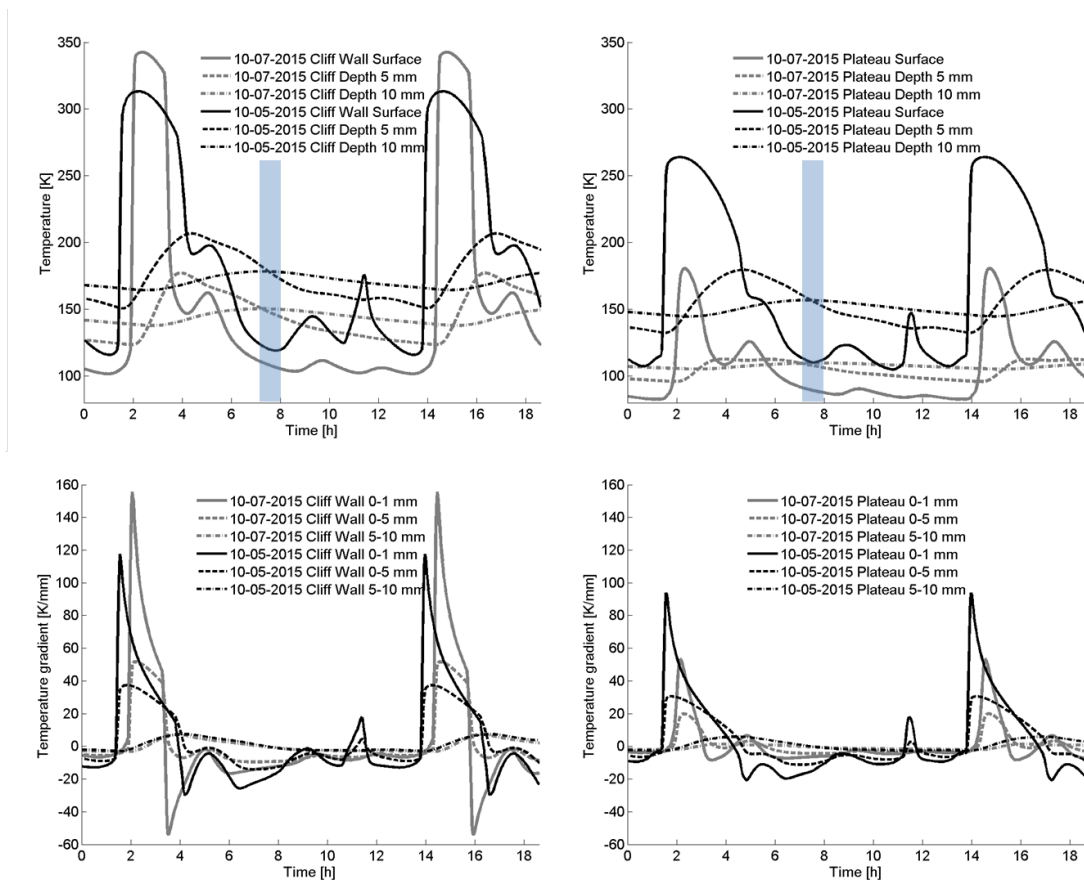


Figure 4.9: Calculated temperatures at the Aswan cliff for equinox at May 10th 2015 (top, left) and date of the cliff collapse on July 10th, 2015 (top, right) for surface, 5 and 10 mm depth, Temperature gradients for the uppermost 5 and 10 mm calculated May 10th 2015 Equinox (bottom, left) and July 10th, 2015 (bottom, right)

sublimation in the subsurface layers: Significant outgassing rates will start at temperatures of about 180 K, these will slow down the further temperature rise. Outgassing will further be restricted to the short time of direct solar irradiation. The volatile-rich layer has to be present within the first few mm: the thermal wave which leads to temperature above 180 K does not penetrate to deeper subsurface layers.

High local thermal gradients are expected due to the wide range of illumination conditions in these fractured walls. As the daytime solar irradiation at local noon around the orbital position of 67P at the cliff collapse is approximately perpendicular onto the cliff, deep thermal penetration of the fractures is plausible. Solar illumination might reach the interior of the wall and hence lead to high local absorption and local temperatures well beyond those expected from a flat facet.

4.4 Cliff collapse scenarios

OSIRIS and NAVCAM images restrict the event to a temporal window of 7:20 to 8:00 h, local midnight (see blue bar in Figure 4.9). Images taken months before the collapse that imaged the cliff from short distances showed that the cliff was already partly separated by a fracture.

Several potential mechanisms can have triggered the collapse:

- High cometary activity due to the perihelion approach leads to higher amounts of mass transportation around 67P (Keller *et al.* 2017). Ejected material not escaping the gravitational field is prone to impact on the cliff or the terrace above it.
- The rotation period of the nucleus increased by 18 minutes during the perihelion passage (Keller *et al.* 2015), leading to a change in the centrifugal force applied on the free standing cliff – however, most of the change in spin rate happened well after the collapse.
- Thermal gradients across the cliff were negative and small at the time of the collapse, and the temperatures were too low to account for significant sublimation and outgassing of water ice.

Backfalling material is likely the best explanation to have triggered the collapse; requiring the Aswan cliff being unstable already. This involves that the structure should have been more fragile compared to the previous perihelion passage 6.4 years before.

Diurnal thermal cycles, leading to thermal stress and thus fissuring rocks and regolith have been observed on Earth and on asteroid surfaces (Molaro and Byrne 2012, El-Maarry *et al.* 2015a). Even on 67P, studies suggest that thermal stress drives observed surface changes (Pajola *et al.* 2015) and led to early activity especially in the neck area with its unique illumination conditions at higher solar distances (Ali-Lagoa *et al.* 2015).

The cohesive strength of the nucleus material is in the order of 1 Pa (Attree *et al.* 2018a, O'Rourke *et al.* 2020); such a low value makes thermal fatigue effects difficult to explain. Depletion of volatile components could affect the layer cohesion inside of cliffs and trigger the collapse.

Observed fractures, from how they were formed, open channels into the deeper layers and enhance heat and mass transfer. This transfer leads to destabilizing effects: thermal gradients contribute to fracture creation by inducing thermal stresses. Sublimation and outgassing deepen and widen these fissures, predisposing the cliff to subsequent collapse (Skorov *et al.* 2016). Lower temperatures, especially of the terrace above the cliff, lead to local material contraction and the crack on top of the cliff likely widens and loses cohesive strength. Finally, it is the weak gravity that drives the collapse and crumbling of the wall.

4.5 Conclusions about the cliff collapse

The Aswan cliff collapse and subsequent outburst offered a great opportunity to check models about the behaviour of cometary nuclei. This event, witnessed for the first time in cometary history, allowed an insight into the pristine cometary material, once the overlying exposed layer had been removed. There are hints that the event is at least partly driven by solar irradiation on the cometary nucleus:

- The collapse occurred shortly before the maximum peak solar irradiation, integrated over one cometary orbit on the Aswan cliff, was reached. The cliff received the highest peak irradiation values of the entire northern hemisphere at the day of collapse.
- In the months before the collapse, the terraces cooled down significantly due to shadowing. While the cliff wall received rather constant, diurnal averaged irradiation, the pattern drastically changed to higher peak and shorter illumination times, as the solar elevation and the heliocentric distance shifted.
- The bilobate shape leads to nearly perpendicular irradiation on the cliff after sunrise due to the shadowing smaller lobe; causing a strong temperature rise unique to this location.
- The Aswan cliff is heavily fractured, thus allowing solar illumination to penetrate into the structures, and potentially causing large temperature differences and gradients on small spatial scales.

5 Conclusion and Outlook

Highly-resolved images of the OSIRIS camera system, never made by any cometary mission before the arrival of Rosetta at 67P, allowed for the setup of detailed thermophysical models. Based on the instruments on board, the surface of the comet was mapped in high detail, revealing a wealth of different landscapes and morphological patterns, and determining the comet physical properties. This thesis focuses on applying these properties in thermophysical models that contribute to understanding cometary activity.

5.1 Main results of thermophysical modelling

As OSIRIS images revealed the widespread fractured terrains on 67P, this work focused mainly on the analysis of the role of fractures as heat traps; in order to contribute to the quest what drives the activity of comets. Does fractured terrain show a specific behaviour with respect to outgassing patterns or activity with an abundance of dust jets?

This thesis presented a theoretical approach in deriving temperature distributions and evoked water sublimation rates in the uppermost nucleus layers of comet 67P/Churyumov-Gerasimenko. The main findings are:

- Significant water sublimation is restricted to the two years centered around perihelion, and there is a clear difference of the scales of rotational and orbital thermal lag.
- Small-scale terrain roughness evokes high temperature gradients at small spatial scales and has a significant impact on radiative flux vectors. This impact is significant for steeper average surface inclinations, and for larger emission angles. Distant observers may misinterpret temperatures derived from these surfaces based on their position to the object and the viewing geometry.
- Fractured terrain acts as heat traps for the absorbed insolation. Fractures are warmer and show increased peak sublimation rates compared to flat terrains, and keep outgassing into night times. Onset of outgassing is reached early, if compared to direct illumination on flat or smooth terrains. These findings are robust against a wide set of fracture shapes, different location of ices, and a great variety of illumination geometries and heliocentric distances.
- The bi-lobate shape of the nucleus, together with the elliptical orbit and the obliquity of the rotation axis, creates very unique insolation patterns. The collapse of a large cliff on 67P was observed at local night, but the area was exposed earlier to the highest local insolation rates during the entire revolution around the sun.

5.2 Observation of dust jets, activity and erosion

In July 2014 at 3.7 AU heliocentric distance, ROSETTA imaged the first resolved dust jets and linked them to the neck area on 67P (Lara *et al.* 2015). The small filament-like structures (Vincent *et al.* 2016) originated mostly from consolidated and fractured terrain. Observers, especially those at large distances, get the impression of a large jet from a single source. Due to shadowing structures, localised faint dust jet activity was imaged in late August at 3.5 AU heliocentric distance (Sierks *et al.* 2015); the source of activity could be localized as a highly structured and fractured sink hole wall.

Fine-scaled thermal models (Keller *et al.* 2015) based on retrieved nucleus shape models (e.g. Preusker *et al.* (2015)) investigated local illumination conditions and calculated expected surface erosion rates based on an dust-to-ice ratio of 4 (Rotundi *et al.* 2015). Most of the erosion takes place in the southern hemisphere, which becomes insolated only during the months of the perihelion passage. For the northern hemisphere, self-heating was predicted (Keller *et al.* 2015) and confirmed by VIRTIS measurements (Tosi *et al.* 2019). It significantly contributes to the neck activity at high heliocentric distances, and orbital erosion rates up to several meters can be expected (Keller *et al.* 2015), in a range detectable by OSIRIS.

Integrated over the whole perihelion passage of 67P, dust jets could not be restricted to specific terrains or types (Lai *et al.* 2019). They emerged shortly after sunrise and last throughout the day, with some even detected during early night (Shi *et al.* 2016) originating from smooth plains. Outbursts of different types offer a great variety of formation scenarios (Vincent *et al.* 2016, Agarwal *et al.* 2017). Coma reconstruction models created by outgassing patterns came to the conclusion that activity is not necessarily restricted to certain active regions or areas on the comet (Shi *et al.* 2018). A method with a simple uniform outgassing assumption also fitted to the morphology of the coma (Kramer and Noack 2016). Cambianica *et al.* (2021) showed that northern hemisphere dust deposits are partially restored during perihelion passage, when the southern hemisphere is exposed to higher values of insolation.

ROSETTA discovered patches of surface water-ice on specific barely illuminated spots (Pommerol *et al.* 2015, Filacchione *et al.* 2016) shortly after local sunrise, while most of the upper nucleus layers are void of water ice (De Sanctis *et al.* 2015). Frost from recondensation, originating from deeper layers of the cometary nucleus and coma gas, is quickly removed when insolation starts (Mottola *et al.* 2015).

During the perihelion approach of 67P, sublimation of water ice created water production rates that doubled within a month; from 0.6 kg/s in July 2014 to values of 1.2 kg/s in August and at heliocentric distances between 3.7 and 3.5 AU (Gulkis *et al.* 2015). A production rate of 1.2 kg/s at 3.5 AU is achieved in perpendicularly oriented and fully illuminated area of about 1 km² in fractured and flat terrains, according to the thermal model presented.

At higher solar distances, peak outgassing rates of H₂O were detected in the neck area (Biver *et al.* 2015, Bockelée-Morvan *et al.* 2015). Topographically comparable to a wide fracture and well illuminated during 67P's solar approach, the concavity apparently contributed to focus the observed expanding gas. On the night side, despite low temperatures (<120 K), 10% of the overall H₂O production (Biver *et al.* 2015) was registered. Numerical coma models that used a non-uniform H₂O source area approach (Fougere

et al. 2016) found the best correlation to observations (Bockelée-Morvan *et al.* 2015) for increased outgassing from the neck region Hapi at higher heliocentric distances.

At a heliocentric distance of 3.5 AU and a sublimation front depth of 5 mm, sublimation rates are low according to the thermophysical analysis; but increased by factor 2-3 if compared to flat terrain.

The thermal energy storage capability of fractured terrain keeps small outgassing rates even ongoing during night. Calculated values range between $9.2 \cdot 10^{-8} \text{ kg m}^{-2} \text{ s}^{-1}$ for narrow fractured terrain and a sublimation front depth of 3 mm, and $5.9 \cdot 10^{-10} \text{ kg m}^{-2} \text{ s}^{-1}$ for bottom surface ice in shallow fractures. These values were obtained for local midnight. Theoretically, an area of 1 km^2 is enough to reproduce the night-side outgassing observed by MIRO (Biver *et al.* 2015) (at local midnight). A fraction of 5 % active sublimating areas on 67Ps surface can reproduce the observed outgassing patterns on both night and day sides.

5.3 Fractures and cometary activity

One of the most imminent problems to explaining activity, a dust lift-off able to overcome particle cohesion, gravity, or both (Kührt and Keller 1994, Skorov *et al.* 2011, Blum *et al.* 2014, Gundlach *et al.* 2015) need high sublimation pressure levels. In order to describe dust jet activity being evoked by water ice alone, water production rates must be exceptionally high; this requires strong insolation possible only at close proximity to the sun.

According to Davidsson *et al.* (2010), the maximum size of liftable grains at 3.5 AU are dust particles of $4 \mu\text{m}$. Gundlach *et al.* (2015) concluded that water-ice sublimation alone cannot overcome cohesion if the considered objects are dust agglomerates, up to a certain size and compressive strength (Gundlach and Blum 2016). OSIRIS observed particles of millimeter to centimeter sizes in the coma of 67P - already at 3.5 AU heliocentric distance. Dust jet activity was found over all sorts of terrains on 67P (Fornasier *et al.* 2019) and not restricted to cliffs or fractured areas, but some of the observed jets are very short-lived that can well be explained with an origin in a narrow fracture.

In fractured or rough terrains, local peak sublimation rates are significantly higher than for standard flat models; this was shown for all fractures. Thus, assuming two terrain types, a flat and a rough, fractured one, and applying the same composition and physical properties: local peak water sublimation rates are higher in the latter. This effect is more pronounced for large heliocentric distances, and can be transferred to other volatile species as well.

The determined low thermal inertia of the nucleus surface physically allows heat trap mechanisms to have size dimensions below OSIRIS image resolution. Concave structures might exist on the surface of the nucleus that outline a similar behaviour like the reported fracture thermophysics. One example are 'honeycomb-like structures' initially reported to be embedded in several flat terrain morphologies of dust-covered airfall areas, but which most likely act as sources of jets that were observed near the evening terminator (Shi *et al.* 2016). The roughness analysis in this thesis also showed that wide temperature differences exist on other terrain types; effects found for fractures can be partly extended to morphologies that have higher average slope angles.

While fractured areas provide favorable conditions for the production of volatiles, they are likely not the unique source for dust jet activity (Fornasier *et al.* 2019). Nevertheless, fracture sublimation rates do not close the existing gap to explain dust lift-off. So, the heat trap effect of fractures still would need additional physical mechanisms to lift the grains.

Thermal cracking (as modelled for the neck region, Ali-Lagoa *et al.* (2015)) or gas drag in nozzle-like features (which could be fractures) can add to the likelihood of emerging dust jets (Vincent *et al.* 2016). Correlating observations to our modelling results that an energy consumption for sublimation of $>50 \text{ Wm}^{-2}$ triggers dust jet activity (Figure 3.27). This corresponds to a sublimation rate of $1.8 \cdot 10^{-5} \text{ kg m}^{-2} \text{ s}^{-1}$.

A considerable source for regolith formation on near-Earth asteroids (Delbo *et al.* 2014) is thermal fatigue. Temperature variations are suggested to drive the formation process of fractured terrain also on cometary nuclei, as maximum temperature changes of 15 K/min for flat terrain under favorable conditions have been predicted (El-Maarry *et al.* 2015a). Early activity in the neck region of 67P has been attributed to frequent temperature variations due to more heating and cooling cycles Ali-Lagoa *et al.* (2015). These lead to higher degrees of thermal cracking in these specific areas. MIRO (Gulkis *et al.* 2015) reported that the diurnal water production rate cycle coincides with direct illumination of the neck region. Thus, thermal cracking is a likely process.

5.4 Fracture formation and evolution

Several scenarios for the formation of fracture morphologies have been proposed. Fractured terrain resembles desiccated areas on Earth (Auger *et al.* 2018), and the appearance of the terrain can be distinguished into different maturity stages. The possible formation of a sintered crust due to recondensation processes can induce high thermal stresses in the subsurface layers on comets (Attree *et al.* 2018b), while in other areas, the lower material strength (Attree *et al.* 2018a) indicate rather the absence of sintering processes. The Philae lander touchdown process also indicates a lower material strength (O'Rourke *et al.* 2020).

An uneven distribution of ices and refractories in the nucleus layers could lead to different erosion rates; but there is currently no evidence that simple surface erosion by outgassing creates depressions that grow to fractures. A potential fracture growing mechanism is proposed: Desiccated, inert fractures without outgassing resulted in the highest temperatures and subsurface thermal gradients. In contrary, surface ice sublimating in thin cracks leads to medium temperature levels and small diurnal variations. So, thermal cracking is more realistic to the first. The heat trap effect allows for deeper penetration of the thermal wave when surfacial layers lost their volatiles and as a consequence establishing a sublimation zone at greater depths, again leading to higher desiccation rates of fractures compared to its direct environment. The fracture, as an effect, can grow in depth and width, allowing the thermal wave to travel even to deeper layers.

5.5 Outlook

The heat trap mechanism of fractures on comets is worth being investigated further, both experimentally and theoretically. For the improvement of thermo-physical models, taking characteristic networks of fractures as imaged by OSIRIS as a base model is proposed as a next step: These fractures and their orientation can be exposed to realistic, varying illumination conditions of a full comet orbit. Based on the sublimation patterns, expected surface changes in the fracture network can be calculated, and presented as a resulting geometry of an ageing fractures. The model solutions finally can be compared to OSIRIS images of fractured terrain. Iteratively, by adjusting the parameters used and studied in this thesis, one can derive more and more realistic and representative fracture models.

Another proposed improvement is adding more volatile species to the model: While this study is restricted to water ice, other volatile constituents also play a vital role in the activity of comets. These volatiles exist at deeper layers in the nucleus, and their sublimation starts at generally lower temperatures; comets that enter the inner solar system for the first time are more driven by the sublimation of CO and CO₂. The thermophysical modeling then adds quite some complexity, but the general approach would be similar to model several sublimation fronts in deeper nucleus layers.

Experimentally, setting up fracture models and illuminating them can be difficult, and cometary realities are hard to be rebuild on Earth. Future scientific missions shall be able to monitor cometary nucleus terrain with more variety in observation conditions, such as illumination angles and distances. The remote sensing instrumentation shall include a hyperspectral thermal infrared imager that is able to deliver highly resolved temperature maps from the surface. And, space instrumentation shall be built more robust to survive the harsh conditions in a cometary orbit.

The struggle for unveiling cometary activity continues, as a lot of questions are still open and awaiten further investigations. The rich amount of data still allows for new results, and recent studies get closer to the explanation how comets work (Gundlach *et al.* 2020, Fulle *et al.* 2020). The Rosetta mission to comet 67P delivered a lot of new insights to a cometary nucleus and enriched the scientific community with spectacular results. The OSIRIS images showed an amazing small member of the solar system in such level of detail, that the fascination impacted the general public and, beyond others, triggered young people to study natural sciences. And there are more adventures to come: Future scientific interplanetary missions shall go the next step, and focus on returning samples of a cometary nucleus to Earth, as well as preparing for comets that enter the solar system for the first time.

Bibliography

- Agarwal, J., Della Corte, V., Feldman, P. D., Geiger, B., Merouane, S., Bertini, I., Bodewits, D., Fornasier, S., Grün, E., Hasselmann, P., Hilchenbach, M., Höfner, S., Ivanovski, S., Kolokolova, L., Pajola, M., Rotundi, A., Sierks, H., Steffl, A. J., Thomas, N., A'Hearn, M. F., Barbieri, C., Barucci, M. A., Bertaux, J.-L., Boudreault, S., Cremonese, G., Da Deppo, V., Davidsson, B., Debei, S., De Cecco, M., Deller, J. F., Feaga, L. M., Fischer, H., Fulle, M., Gicquel, A., Groussin, O., Güttler, C., Gutierrez, P. J., Hofmann, M., Hornung, K., Hviid, S. F., Ip, W.-H., Jorda, L., Keller, H. U., Kissel, J., Knollenberg, J., Koch, A., Koschny, D., Kramm, J.-R., Kührt, E., Küppers, M., Lamy, P. L., Langevin, Y., Lara, L. M., Lazzarin, M., Lin, Z.-Y., Lopez Moreno, J. J., Lowry, S. C., Marzari, F., Mottola, S., Naletto, G., Oklay, N., Parker, J. W., Rodrigo, R., Rynö, J., Shi, X., Stenzel, O., Tubiana, C., Vincent, J.-B., Weaver, H. A., and Zaprudin, B. (2017). Evidence of sub-surface energy storage in comet 67P from the outburst of 2016 July 03. *Monthly Notices of the Royal Astronomical Society*, **469**(Suppl2), s606–s625.
- A'Hearn, M. F. (2005). Deep Impact: Excavating Comet Tempel 1. *Science*, **310**(5746), 258–264.
- A'Hearn, M. F. (2008). Deep impact and the origin and evolution of cometary nuclei. *Space Science Reviews*, **138**(1-4), 237–246.
- A'Hearn, M. F., Belton, M. J. S., Delamere, W. A., Feaga, L. M., Hampton, D., Kissel, J., Klaasen, K. P., McFadden, L. A., Meech, K. J., Melosh, H. J., Schultz, P. H., Sunshine, J. M., Thomas, P. C., Veverka, J., Wellnitz, D. D., Yeomans, D. K., Besse, S., Bodewits, D., Bowling, T. J., Carcich, B. T., Collins, S. M., Farnham, T. L., Groussin, O., Hermany, B., Kelley, M. S., Kelley, M. S., Li, J.-Y., Lindler, D. J., Lisse, C. M., McLaughlin, S. A., Merlin, F., Protopapa, S., Richardson, J. E., and Williams, J. L. (2011). EPOXI at Comet Hartley 2. *Science*, **332**(6036), 1396–1400.
- Ali-Lagoa, V., Delbo, M., and Libourel, G. (2015). Rapid temperature changes and the early activity on comet 67P/Churyumov-Gerasimenko. *Astrophysical Journal*, **810**(2), 5p.
- Arakawa, Sota, Tanaka, Hidekazu, Kataoka, Akimasa, and Nakamoto, Taishi (2017). Thermal conductivity of porous aggregates. *Astronomy & Astrophysics*, **608**, L7.
- Attree, N., Groussin, O., Jorda, L., Nébouy, D., Thomas, N., Brouet, Y., Kührt, E., Preusker, F., Scholten, F., Knollenberg, J., Hartogh, P., Sierks, H., Barbieri, C., Lamy, P., Rodrigo, R., Koschny, D., Rickman, H., Keller, H. U., A'Hearn, M. F., Auger, A.-T., Barucci, M. A., Bertaux, J.-L., Bertini, I., Bodewits, D., Boudreault, S., Cremonese,

- G., Da Deppo, V., Davidsson, B., Debei, S., De Cecco, M., Deller, J., El-Maarry, M. R., Fornasier, S., Fulle, M., Gutiérrez, P. J., Güttler, C., Hviid, S., Ip, W.-H., Kovacs, G., Kramm, J. R., Küppers, M., Lara, L. M., Lazzarin, M., Lopez Moreno, J. J., Lowry, S., Marchi, S., Marzari, F., Mottola, S., Naletto, G., Oklay, N., Pajola, M., Toth, I., Tubiana, C., Vincent, J.-B., and Shi, X. (2018a). Tensile strength of 67P/Churyumov-Gerasimenko nucleus material from overhangs. *Astronomy & Astrophysics*, **611**, A33.
- Attree, N., Groussin, O., Jorda, L., Rodionov, S., Auger, A.-T., Thomas, N., Brouet, Y., Poch, O., Kührt, E., Knapmeyer, M., Preusker, F., Scholten, F., Knollenberg, J., Hviid, S., and Hartogh, P. (2018b). Thermal fracturing on comets – Applications to 67P/Churyumov-Gerasimenko. *Astronomy & Astrophysics*, **610**, A76.
- Auger, A.-T., Groussin, O., Jorda, L., El-Maarry, M., Bouley, S., Sejourne, A., Gaskell, R., Capanna, C., Davidsson, B., Marchi, S., Höfner, S., Lamy, P., Sierks, H., Barbieri, C., Rodrigo, R., Koschny, D., Rickman, H., Keller, H., Agarwal, J., Hearn, M. A., Barucci, M., Bertaux, J.-L., Bertini, I., Cremonese, G., Da Deppo, V., Debei, S., De Cecco, M., Fornasier, S., Fulle, M., Gutierrez, P., Güttler, C., Hviid, S., Ip, W.-H., Knollenberg, J., Kramm, J.-R., Kührt, E., Küppers, M., Lara, L., Lazzarin, M., Lopez Moreno, J., Marzari, F., Massironi, M., Michalik, H., Naletto, G., Oklay, N., Pommerol, A., Sabau, L., Thomas, N., Tubiana, C., Vincent, J.-B., and Wenzel, K.-P. (2018). Meter-scale thermal contraction crack polygons on the nucleus of comet 67P/Churyumov-Gerasimenko. *Icarus*, **301**, 173 – 188.
- Balsiger, H., Altwegg, K., Bar-Nun, A., Berthelier, J.-J., Bieler, A., Bochsler, P., Briois, C., Calmonte, U., Combi, M., De Keyser, J., Eberhardt, P., Fiethe, B., Fuselier, S. A., Gasc, S., Gombosi, T. I., Hansen, K. C., Hässig, M., Jäckel, A., Kopp, E., Korth, A., Le Roy, L., Mall, U., Marty, B., Mousis, O., Owen, T., Rème, H., Rubin, M., Sémon, T., Tzou, C.-Y., Waite, J. H., and Wurz, P. (2015). Detection of argon in the coma of comet 67P/Churyumov-Gerasimenko. *Science Advances*, **1**(8).
- Basilevsky, A., Skorov, Y., Hviid, S., Krasilnikov, S., Mall, U., and Keller, H. U. (2018). Lineaments on the Surface of the Consolidated Material of the Comet 67P/Churyumov-Gerasimenko Nucleus. *Solar System Research*, **52**(6), 505–517.
- Belton, M. J. S. (2010). Cometary activity, active areas, and a mechanism for collimated outflows on 1P, 9P, 19P, and 81P. *Icarus*, **210**(2), 881–897.
- Benkhoff, J. and Spohn, T. (1991). Thermal histories of the KOSI samples. *Geophysical Research Letters*, **18**(2), 261–264.
- Bibring, J.-P., Langevin, Y., Carter, J., Eng, P., Gondet, B., Jorda, L., Le Mouelic, S., Mottola, S., Pilorget, C., Poulet, F., and Vincendon, M. (2015). 67P/Churyumov-Gerasimenko surface properties as derived from CIVA panoramic images. *Science*, **349**(6247), 671–1 – 671–3.
- Bieler, A., Altwegg, K., Balsiger, H., Bar-Nun, A., Berthelier, J.-J., Bochsler, P., Briois, C., Calmonte, U., Combi, M., De Keyser, J., van Dishoeck, E. F., Fiethe, B., Fuselier, S. A., Gasc, S., Gombosi, T. I., Hansen, K. C., Hässig, M., Jäckel, A., Kopp, E., Korth, A., Le Roy, L., Mall, U., Maggiolo, R., Marty, B., Mousis, O., Owen, T., Rème,

- H., Rubin, M., Semon, T., Tzou, C.-Y., Waite, J. H., Walsh, C., and Wurz, P. (2015a). Abundant molecular oxygen in the coma of comet 67P/Churyumov-Gerasimenko. *Nature*, **526**, 678–681.
- Bieler, A., Altwegg, K., Balsiger, H., Berthelier, J.-j., Calmonte, U., Combi, M., Keyser, J. D., Fiethe, B., Fougere, N., Fuselier, S., Gasc, S., Gombosi, T., Hansen, K., Hässig, M., Huang, Z., Jäckel, A., Jia, X., Roy, L. L., Mall, U. A., Rème, H., Rubin, M., Tenishev, V., Tóth, G., Tzou, C.-y., and Wurz, P. (2015b). Comparison of 3D kinetic and hydrodynamic models to ROSINA-COPS measurements of the neutral coma of 67P / Churyumov-Gerasimenko. *Astronomy & Astrophysics*, **583**(A7), 1–10.
- Biermann, L. (1951). Kometenschweife und solare Korpuskularstrahlung. *Zeitschrift für Astrophysik*, **29**, 274.
- Birch, S. P. D., Tang, Y., Hayes, A. G., Kirk, R. L., Bodewits, D., Campins, H., Fernandez, Y., de Freitas Bart, R., Kutsop, N. W., Sierks, H., Soderblom, J. M., Squyres, S. W., and Vincent, J.-B. (2017). Geomorphology of comet 67P/Churyumov-Gerasimenko. *Monthly Notices of the Royal Astronomical Society*, **469**(Suppl2), 50–67.
- Biver, N., Hofstadter, M., Gulkis, S., Bockelée-Morvan, D., Choukroun, M., Lellouch, E., Schloerb, F. P., and Rezac, L. (2015). Distribution of water around the nucleus of comet 67P / Churyumov-Gerasimenko at 3 . 4 AU from the Sun as seen by the MIRO instrument on Rosetta. *Astronomy & Astrophysics*, **583**(A3), 1–7.
- Blum, J., Gundlach, B., Mühle, S., and Trigo-Rodriguez, J. M. (2014). Comets formed in solar-nebula instabilities! - An experimental and modeling attempt to relate the activity of comets to their formation process. *Icarus*, **235**, 156–169.
- Blum, J., Gundlach, B., Krause, M., Fulle, M., Johansen, A., Agarwal, J., von Borsstel, I., Shi, X., Hu, X., Bentley, M. S., Capaccioni, F., Colangeli, L., Della Corte, V., Fougere, N., Green, S. F., Ivanovski, S., Mannel, T., Merouane, S., Migliorini, A., Rotundi, A., Schmied, R., and Snodgrass, C. (2017). Evidence for the formation of comet 67P/Churyumov-Gerasimenko through gravitational collapse of a bound clump of pebbles. *Monthly Notices of the Royal Astronomical Society*, **469**(Suppl2), S755–S773.
- Bockelée-Morvan, D., Debout, V., Erard, S., Leyrat, C., Capaccioni, F., Filacchione, G., Fougere, N., Drossart, P., Arnold, G., Combi, M., Schmitt, B., Crovisier, J., de Sanctis, M.-C., Encrenaz, T., Kührt, E., Palomba, E., Taylor, F. W., Tosi, F., Piccioni, G., Fink, U., Tozzi, G., Barucci, A., Biver, N., Capria, M.-T., Combes, M., Ip, W., Blecka, M., Henry, F., Jacquiod, S., Reess, J.-M., Semery, A., and Tiphene, D. (2015). First observations of H₂O and CO₂ vapor in comet 67P/Churyumov-Gerasimenko made by VIRTIS onboard Rosetta. *Astronomy & Astrophysics*, **583**, A6.
- Boehnhardt, H., Bibring, J.-P., Apathy, I., Auster, H., Finzi, A., Goesmann, F., Klingelhofer, G., Knapmeyer, M., Kofman, W., Krüger, H., Mottola, S., Schmidt, W., Seidensticker, K., Spohn, T., and Wright, I. (2017). The Philae lander mission and science overview. *Philosophical Transactions of The Royal Society A Mathematical Physical and Engineering Sciences*, **375**, 20160248.

- Bridges, J., Changela, H., Nayakshin, S., Starkey, N., and Franchi, I. (2012). Chondrule fragments from Comet Wild2: Evidence for high temperature processing in the outer Solar System. *Earth and Planetary Science Letters*, **341-344**, 186–194.
- Brin, G. and Mendis, D. (1979). Dust release and mantle development in comets. *Astrophysical Journal*, **229**, 402–408.
- Brownlee, D. E., Horz, F., Newburn, R. L., Zolensky, M., Duxbury, T. C., Sandford, S., Sekanina, Z., Tsou, P., Hanner, M. S., Clark, B. C., Green, S. F., and Kissel, J. (2004). Surface of Young Jupiter Family Comet 81P/Wild 2: View from the Stardust Spacecraft. *Science*, **304**(5678), 1764–1769.
- Bruck Syal, M., Schultz, P. H., Sunshine, J. M., Hearn, M. F. A., Farnham, T. L., and Dearborn, D. S. P. (2013). Geologic control of jet formation on Comet 103P / Hartley 2. *Icarus*, **222**, 610–624.
- Buratti, B. J., Choukroun, M., and Bauer, J. M. (2016). The Low Albedo of Comets. In *AGU Fall Meeting Abstracts*, pages P43A–2083.
- Cambianica, P., Cremonese, G., Fulle, M., Simioni, E., Naletto, G., Pajola, M., Lucchetti, A., Penasa, L., Massironi, M., Frattin, E., Güttler, C., Sierks, H., and Tubiana, C. (2021). Long-term measurements of the erosion and accretion of dust deposits on comet 67P/Churyumov-Gerasimenko with the OSIRIS instrument. *Monthly Notices of the Royal Astronomical Society*, **504**(2), 2895–2910.
- Capaccioni, F., Coradini, A., Erard, S., Arnold, G., Drossart, P., Sanctis, M. C. D., Capria, M. T., Tosi, F., Leyrat, C., Schmitt, B., Quirico, E., Cerroni, P., Mennella, V., Raponi, A., Ciarniello, M., Mccord, T., Moroz, L., Palomba, E., Ammannito, E., Barucci, M. A., Bellucci, G., Benkhoff, J., Bibring, J. P., Blanco, A., Blecka, M., Carlson, R., Carsenty, U., Colangeli, L., Combes, M., Combi, M., Crovisier, J., Encrenaz, T., Federico, C., Fink, U., Fonti, S., Ip, W. H., Irwin, P., Jaumann, R., Kuehrt, E., Langevin, Y., Magni, G., Mottola, S., Orofino, V., Palumbo, P., Piccioni, G., Schade, U., Taylor, F., Tiphene, D., Tozzi, G. P., Beck, P., Biver, N., Bonal, L., Despan, D., Flamini, E., Fornasier, S., Frigeri, A., Grassi, D., Gudipati, M., Longobardo, A., Markus, K., Merlin, F., Orosei, R., Rinaldi, G., Stephan, K., Cartacci, M., Cicchetti, A., Giuppi, S., Hello, Y., Henry, F., Jacquino, S., Noschese, R., Peter, G., Politi, R., Reess, J. M., and Semery, A. (2014). The organic-rich surface of comet 67P/Churyumov-Gerasimenko as seen by VIRTIS/Rosetta. *Science*, **347**(6220), 628.
- Capria, M. T. (2002). Sublimation mechanisms of comet nuclei. *Earth, Moon and Planets*, **89**(April), 161–177.
- Capria, M. T., Capaccioni, F., Filacchione, G., Tosi, F., De Sanctis, M. C., Mottola, S., Ciarniello, M., Formisano, M., Longobardo, A., Migliorini, A., Palomba, E., Raponi, A., Kuehrt, E., Bockelee-Morvan, D., Erard, S., Leyrat, C., and Zinzi, A. (2017). How pristine is the interior of the comet 67P/Churyumov-Gerasimenko? *Monthly Notices of the Royal Astronomical Society*, **469**(Suppl2), 685–694.

- Carusi, A., Kresak, L., Perozzi, E., and Valsecchi, G. B. (1985). *Long-term evolution of short-period comets*.
- Colangeli, L., Brucato, J. R., Hudson, R. L., and Moore, M. H. (2004). Laboratory Experiments on Cometary Materials. In *Comets II*, number 1, pages 695–718.
- Colwell, J. E., Jakowsky, B. M., Sandor, B. J., and Stern, S. (1990). Evolution of Topography on Comets II. Icy Craters and Trenches. *Icarus*, **5**(85), 205–215.
- Cowan, J. and A'Hearn, M. (1979). Vaporization of comet nuclei - Light curves and life times. *Moon and Planets*, **21**, 155–171.
- Davidsson, B. J. and Rickman, H. (2014). Surface roughness and three-dimensional heat conduction in thermophysical models. *Icarus*, **243**, 58–77.
- Davidsson, B. J. and Skorov, Y. V. (2002). On the Light-Absorbing Surface Layer of Cometary Nuclei II Thermal Modeling. *Icarus*, **159**(1), 239–258.
- Davidsson, B. J. R., Gulkis, S., Alexander, C., Allmen, P. V., Kamp, L., Lee, S., and Warell, J. (2010). Gas kinetics and dust dynamics in low-density comet comae. *Icarus*, **210**, 455–471.
- Davidsson, B. J. R., Gutiérrez, P. J., Groussin, O., A'Hearn, M. F., Farnham, T., Feaga, L. M., Kelley, M. S., Klaasen, K. P., Merlin, F., Protopapa, S., Rickman, H., Sunshine, J. M., and Thomas, P. C. (2013). Thermal inertia and surface roughness of Comet 9P/Tempel 1. *Icarus*, **224**(1), 154–171.
- Davidsson, B. J. R., Rickman, H., Bandfield, J. L., Groussin, O., Gutiérrez, P. J., Wilska, M., Teresa, M., Emery, J. P., Helbert, J., Jorda, L., Maturilli, A., and Mueller, T. G. (2015). Interpretation of thermal emission . I . The effect of roughness for spatially resolved atmosphereless bodies. *Icarus*, **252**, 1–21.
- Davidsson, B. J. R., Sierks, H., Güttler, C., Marzari, F., Pajola, M., Rickman, H., A'Hearn, M. F., Auger, A.-T., El-Maarry, M. R., Fornasier, S., Gutiérrez, P. J., Keller, H. U., Massironi, M., Snodgrass, C., Vincent, J.-B., Barbieri, C., Lamy, P. L., Rodrigo, R., Koschny, D., Barucci, M. A., Bertaux, J.-L., Bertini, I., Cremonese, G., Da Deppo, V., Debei, S., De Cecco, M., Feller, C., Fulle, M., Groussin, O., Hviid, S. F., Höfner, S., Ip, W.-H., Jorda, L., Knollenberg, J., Kovacs, G., Kramm, J.-R., Kührt, E., Küppers, M., La Forgia, F., Lara, L. M., Lazzarin, M., Lopez Moreno, J. J., Moissl-Fraund, R., Mottola, S., Naletto, G., Oklay, N., Thomas, N., and Tubiana, C. (2016). The primordial nucleus of comet 67P/Churyumov-Gerasimenko. *Astronomy & Astrophysics*, **592**, A63.
- De Sanctis, C. M., Capaccioni, F., Ciarniello, M., Filacchione, G., Formisano, M., Mottola, S., Raponi, A., Tosi, F., Bockelee-Morvan, D., Erard, S., Leyrat, C., Schmitt, B., Ammannito, E., Arnold, G., Barucci, M. A., Combi, M., Capria, M. T., Cerroni, P., Ip, W. H., Kuehrt, E., McCord, T. B., Palomba, E., Beck, P., and Quirico, E. (2015). The diurnal cycle of water ice on comet 67P/Churyumov-Gerasimenko. *Science*, **525**(300), 500–503.

- De Sanctis, M. C., Capria, M. T., and Coradini, A. (2005). Thermal evolution model of 67P/Churyumov-Gerasimenko, the new Rosetta target. *Astronomy & Astrophysics*, **444**(2), 605–614.
- Delbo, M., Libourel, G., Wilkerson, J., Murdoch, N., Michel, P., Ramesh, K. T., Ganino, C., Verati, C., and Marchi, S. (2014). Thermal fatigue as the origin of regolith on small asteroids. *Nature*, **508**(7495), 233–6.
- Duncan, M. and Levison, H. (1997). A scattered comet disk and the origin of Jupiter family comets. *Science*, **276**, 1670–1672.
- El-Maarry, M. R., Thomas, N., Marschall, R., Auger, A., Groussin, O., Mottola, S., Pajola, M., Massironi, M., Marchi, S., Höfner, S., Preusker, F., Scholten, F., Jorda, L., Kürt, E., Keller, H. U., Sierks, H., Hearn, M. F. A., Barbieri, C., Barucci, M. A., Bertaux, J., Bertini, I., Cremonese, G., Deppo, V. D., Davidsson, B., Debei, S., Cecco, M. D., Deller, J., Güttler, C., Fornasier, S., Fulle, M., Gutierrez, P. J., Hofmann, M., Knollenberg, J., Koschny, D., Kovacs, G., Kramm, J., Küppers, M., Lamy, P. L., Lara, L. M., Lazzarin, M., Moreno, J. J. L., Marzari, F., Michalik, H., Naletto, G., Oklay, N., Pommerol, A., Rickman, H., Rodrigo, R., Tubiana, C., and Vincent, J. (2015a). Fractures on comet 67P/Churyumov-Gerasimenko observed by Rosetta/OSIRIS. *Geophysical Research Letters*, **42**, 5170–5178.
- El-Maarry, M. R., Thomas, N., Giacomini, L., Massironi, M., Pajola, M., and Marschall, R. (2015b). Regional surface morphology of comet 67P / Churyumov-Gerasimenko from Rosetta / OSIRIS images. *Astronomy & Astrophysics*, **583**(A26), 1–28.
- Farnham, T. L., Bodewits, D., Li, J. Y., Veverka, J., Thomas, P., and Belton, M. J. S. (2013). Connections between the jet activity and surface features on Comet 9P/Tempel 1. *Icarus*, **222**(2), 540–549.
- Feistel, R. and Wagner, W. (2007). Sublimation pressure and sublimation enthalpy of H₂O ice Ih between 0 and 273.16K. *Geochimica et Cosmochimica Acta*, **71**(1), 36–45.
- Filacchione, G., De Sanctis, M. C., Capaccioni, F., Raponi, A., Tosi, F., and Cianiello, M. (2016). Exposed water ice on the nucleus of comet 67P/Churyumov-Gerasimenko. *Nature*.
- Fornasier, S., Hasselmann, P. H., Barucci, M. A., Feller, C., Besse, S., Leyrat, C., Lara, L., Gutierrez, P. J., Oklay, N., Tubiana, C., Scholten, F., Sierks, H., Barbieri, C., Lamy, P. L., Rodrigo, R., Koschny, D., Rickman, H., Keller, H. U., Agarwal, J., A'Hearn, M. F., Bertaux, J.-L., Bertini, I., Cremonese, G., Da Deppo, V., Davidsson, B., Debei, S., De Cecco, M., Fulle, M., Groussin, O., Güttler, C., Hviid, S. F., Ip, W., Jorda, L., Knollenberg, J., Kovacs, G., Kramm, R., Kürt, E., Küppers, M., La Forgia, F., Lazzarin, M., Lopez Moreno, J. J., Marzari, F., Matz, K.-D., Michalik, H., Moreno, F., Mottola, S., Naletto, G., Pajola, M., Pommerol, A., Preusker, F., Shi, X., Snodgrass, C., Thomas, N., and Vincent, J.-B. (2015). Spectrophotometric properties of the nucleus of comet 67P/Churyumov-Gerasimenko from the OSIRIS instrument onboard the ROSETTA spacecraft. *Astronomy & Astrophysics*, **583**, A30.

- Fornasier, S., Hoang, V. H., Hasselmann, P. H., Feller, C., Barucci, M. A., Deshapriya, J. D. P., Sierks, H., Naletto, G., Lamy, P. L., Rodrigo, R., Koschny, D., Davidsson, B., Agarwal, J., Barbieri, C., Bertaux, J.-L., Bertini, I., Bodewits, D., Cremonese, G., Da Deppo, V., Debei, S., De Cecco, M., Deller, J., Ferrari, S., Fulle, M., Gutierrez, P. J., Güttler, C., Ip, W.-H., Keller, H. U., Küppers, M., La Forgia, F., Lara, M. L., Lazzarin, M., Lin, Z.-Y., Lopez Moreno, J. J., Marzari, F., Mottola, S., Pajola, M., Shi, X., Toth, I., and Tubiana, C. (2019). Linking surface morphology, composition, and activity on the nucleus of 67P/Churyumov-Gerasimenko. *Astronomy & Astrophysics*, **630**, A7.
- Fougere, N., Altwegg, K., Berthelier, J.-J., Bieler, A., Bockelée-Morvan, D., Calmonte, U., Capaccioni, F., Combi, M. R., De Keyser, J., Debout, V., Erard, S., Fiethe, B., Filacchione, G., Fink, U., Fuselier, S. A., Gombosi, T. I., Hansen, K. C., Hässig, M., Huang, Z., Le Roy, L., Leyrat, C., Migliorini, A., Piccioni, G., Rinaldi, G., Rubin, M., Shou, Y., Tennishev, V., Toth, G., Tzou, C.-Y., the VIRTIS team, and the ROSINA team (2016). Three-dimensional direct simulation Monte-Carlo modeling of the coma of comet 67P/Churyumov-Gerasimenko observed by the VIRTIS and ROSINA instruments on board Rosetta. *Astronomy & Astrophysics*, **588**, A134.
- Fulle, M., Corte, V. D., Rotundi, A., Weissman, P., Juhasz, A., Szego, K., Sordini, R., Ferrari, M., Ivanovski, S., Lucarelli, F., Accolla, M., Merouane, S., Zakharov, V., Epifani, E. M., Moreno, J. J. L., Rodríguez, J., Colangeli, L., Palumbo, P., Grün, E., Hilchenbach, M., Bussoletti, E., Esposito, F., Green, S. F., Lamy, P. L., McDonnell, J. A. M., Mennella, V., Molina, A., Morales, R., Moreno, F., Ortiz, J. L., Palomba, E., Rodrigo, R., Zarnecki, J. C., Cosi, M., Giovane, F., Gustafson, B., Herranz, M. L., Jerónimo, J. M., Leese, M. R., Jiménez, A. C. L., and Altobelli, N. (2015). Density and charge of pristine fluffy particles from comet 67P Churyumov-Gerasimenko. *The Astrophysical Journal Letters*, **802**(1), L12.
- Fulle, M., Della Corte, V., Rotundi, A., Rietmeijer, F. J. M., Green, S. F., Weissman, P., Accolla, M., Colangeli, L., Ferrari, M., Ivanovski, S., Lopez-Moreno, J. J., Epifani, E. M., Morales, R., Ortiz, J. L., Palomba, E., Palumbo, P., Rodriguez, J., Sordini, R., and Zakharov, V. (2016). Comet 67P/Churyumov-Gerasimenko preserved the pebbles that formed planetesimals. *Monthly Notices of the Royal Astronomical Society*, **462**(Suppl1), S132–S137.
- Fulle, M., Blum, J., Rotundi, A., Gundlach, B., Güttler, C., and Zakharov, V. (2020). How comets work: nucleus erosion versus dehydration. *Monthly Notices of the Royal Astronomical Society*, **493**(3), 4039–4044.
- Giacomini, L., Massironi, M., El-Maarry, M. R., Penasa, L., Pajola, M., Thomas, N., Lowry, S. C., Barbieri, C., Cremonese, G., Ferri, F., Naletto, G., Bertini, I., La Forgia, F., Lazzarin, M., Marzari, F., Sierks, H., Lamy, P. L., Rodrigo, R., Rickman, H., Koschny, D., Keller, H. U., Agarwal, J., A’Hearn, M. F., Auger, A.-T., Barucci, M. A., Bertaux, J.-L., Besse, S., Bodewits, D., Da Deppo, V., Davidsson, B., De Cecco, M., Debei, S., Fornasier, S., Fulle, M., Groussin, O., Gutierrez, P. J., Güttler, C., Hviid, S. F., Ip, W.-H., Jorda, L., Knollenberg, J., Kovacs, G., Kramm, J.-R., Kührt, E., Küppers, M., Lara, L. M., Moreno, J. J. L., Magrin, S., Michalik, H., Oklay, N., Pommerol, A., Preusker, F., Scholten, F., Tubiana, C., and Vincent, J.-B. (2016). Geologic mapping

- of the Comet 67P/Churyumov-Gerasimenko's Northern hemisphere. *Monthly Notices of the Royal Astronomical Society*, **462**(Suppl1), S352–S367.
- Gomes, R., Levison, H., Tsiganis, K., and Morbidelli, A. (2005). Origin of the cataclysmic Late Heavy Bombardment period of the terrestrial planets. *Nature*, **435**, 466–469.
- Gortsas, N., Kührt, E., Motschmann, U., and Keller, H. (2011). Thermal model of water and CO activity of Comet C/1995 O1 (Hale-Bopp). *Icarus*, **212**(2), 858 – 866.
- Greenberg, J. (1986). Predicting that comet Halley is dark. *Nature*, **321**, 385.
- Groussin, O., A'Hearn, M. F., Li, J. Y., Thomas, P. C., Sunshine, J. M., Lisse, C. M., Meech, K. J., Farnham, T. L., Feaga, L. M., and Delamere, W. a. (2007). Surface temperature of the nucleus of Comet 9P/Tempel 1. *Icarus*, **191**(2 SUPPL.), 63–72.
- Groussin, O., Sunshine, J. M., Feaga, L. M., Jorda, L., Thomas, P. C., Li, J. Y., A'Hearn, M. F., Belton, M. J. S., Besse, S., Carcich, B., Farnham, T. L., Hampton, D., Klaasen, K., Lisse, C., Merlin, F., and Protopapa, S. (2013). The temperature, thermal inertia, roughness and color of the nuclei of Comets 103P/Hartley 2 and 9P/Tempel 1. *Icarus*, **222**(2), 580–594.
- Groussin, O., Sierks, H., Barbieri, C., Lamy, P., Rodrigo, R., Koschny, D., Rickman, H., Keller, H. U., Hearn, A. M. F., Auger, A., Barucci, M. A., Bertaux, J., Bertini, I., Besse, S., Cremonese, G., V. D. D., Davidsson, B., Debei, S., M. D. C., Fornasier, S., Fulle, M., Gutiérrez, P. J., Güttler, C., Hviid, S., Ip, W., Jorda, L., Knollenberg, J., Kovacs, G., Kramm, J. R., Kührt, E., Küppers, M., Lara, L. M., Lazzarin, M., J. L. M. J., Lowry, S., Marchi, S., Marzari, F., Massironi, M., Mottola, S., Naletto, G., Oklay, N., Pajola, M., Pommerol, A., Thomas, N., Toth, I., Tubiana, C., and Vincent, J. (2015a). Astrophysics Special feature Temporal morphological changes in the Imhotep region of comet. *Astronomy & Astrophysics*, **583**(A36), 1–4.
- Groussin, O., Jorda, L., Auger, A., Kührt, E., Gaskell, R., Capanna, C., Scholten, F., Preusker, F., and Lamy, P. (2015b). Gravitational slopes , geomorphology and material strengths of the nucleus of comet 67P / Churyumov-Gerasimenko from OSIRIS observations. *Astronomy & Astrophysics*, **583**(A32), 1–12.
- Groussin, O., Attree, N., Brouet, Y., Ciarletti, V., Davidsson, B., Filacchione, G., Fischer, H.-H., Gundlach, B., Knapmeyer, M., Knollenberg, J., Kokotanekova, R., Kührt, E., Leyrat, C., Marshall, D., Pelivan, I., Skorov, Y., Snodgrass, C., Spohn, T., and Tosi, F. (2019). The Thermal, Mechanical, Structural, and Dielectric Properties of Cometary Nuclei After Rosetta. *Space Science Reviews*, **215**, 29 – 80.
- Grün, E., Gebhard, J., Bar-Nun, A., Benkhoff, J., Düren, H., Eich, G., Hische, R., Huebner, W. F., Keller, H. U., Klees, G., and Kochan, H. (1993). Development of a dust mantle on the surface of an insolated ice-dust mixture: results from the KOSI-9 experiment. *Journal of Geophysical Research: Planets*, **98**(E8), 15091–15104.
- Guilbert-Lepoutre, A., Besse, S., Mousis, O., Ali-Dib, M., Höfner, S., Koschny, D., and Hager, P. (2015). On the Evolution of Comets. *Space Science Reviews*, **197**, 271–296.

- Gulkis, S., Allen, M., von Allmen, P., Beaudin, G., Biver, N., Bockelée-Morvan, D., Choukroun, M., Crovisier, J., Davidsson, B., Encrenaz, P., Encrenaz, T., Frerking, M., Hartogh, P., Hofstadter, M., Ip, W.-H., Janssen, M., Jarchow, C., Keihm, S., Lee, S., Lellouch, E., Leyrat, C., Rezac, L., Schloerb, F., and Spilker, T. (2015). Subsurface properties and early activity of comet 67P/Churyumov-Gerasimenko. *Science*, **347**, 709.
- Gundlach, B. and Blum, J. (2012). Outgassing of icy bodies in the Solar System - II: Heat transport in dry, porous surface dust layers. *Icarus*, **219**(2), 618–629.
- Gundlach, B. and Blum, J. (2013). A new method to determine the grain size of planetary regolith. *Icarus*, **223**(1), 479–492.
- Gundlach, B., Skorov, Y. V., and Blum, J. (2011). Outgassing of icy bodies in the Solar System - I. The sublimation of hexagonal water ice through dust layers. *Icarus*, **213**(2), 710–719.
- Gundlach, B., Blum, J., Keller, H. U., and Skorov, Y. V. (2015). What drives the dust activity of comet 67P/churyumov-Gerasimenko. *Astronomy & Astrophysics*, **583**(A12), 1–8.
- Gundlach, B., Fulle, M., and Blum, J. (2020). On the activity of comets: understanding the gas and dust emission from comet 67P/Churyumov-Gerasimenko's south-pole region during perihelion. *Monthly Notices of the Royal Astronomical Society*, **493**, 3690–3715.
- Gundlach, B. and Blum, J. (2016). Why are Jupiter-family comets active and asteroids in cometary-like orbits inactive? – How hydrostatic compression leads to inactivity. *Astronomy & Astrophysics*, **589**, A111.
- Guzzo, M. and Lega, E. (2017). Scenarios for the dynamics of comet 67P/Churyumov-Gerasimenko over the past 500 kyr. *Monthly Notices of the Royal Astronomical Society*, **469**, S321–S328.
- Hässig, M., Altwegg, K., Balsiger, H., Berthelier, J. J., Bieler, A., Bochsler, P., Briois, C., Calmonte, U., Combi, M., Keyser, J. D., Eberhardt, P., Fiethe, B., Fuselier, S. A., Galand, M., Gasc, S., Gombosi, T. I., Hansen, K. C., Keller, H. U., Kopp, E., Korth, A., Roy, L. L., Mall, U., Marty, B., Mouis, O., Neefs, E., Owen, T., Rubin, M., Tornow, C., Waite, J. H., and Wurz, P. (2015). Time variability and heterogeneity in the coma of 67P/Churyumov-Gerasimenko. *Science*, **347**(6220), 2–5.
- Huebner, W., Benkhoff, J., Capria, M.-T., Coradini, A., De Sanctis, M. C., Orosei, R., and Prialnik, D. (2006). Heat and Gas Diffusion in Comet Nuclei.
- Huetter, E. S., Koemle, N. I., Kargl, G., and Kaufmann, E. (2008). Determination of the effective thermal conductivity of granular materials under varying pressure conditions. *Journal of Geophysical Research*, **113**(E12), E12004.
- Ivanova, A. and Shulman, L. (2002). A model of an active region on the surface of a cometary nucleus. *Earth, Moon and Planets*, **90**, 249–257.

- Kaib, N. A. and Quinn, T. (2009). Reassessing the Source of Long-Period Comets. *Science*, **325**(5945), 1234–1236.
- Keihm, S. J., Tosi, F., Kamp, L., Capaccioni, F., Gulikis, S., Hofstadter, M. D., and Coradini, A. (2011). A Model for the Self-Heating of Asteroid Surfaces: Application to the Interpretation of Combined MIRO-VIRTIS Data During the Rosetta Fly-by of 21 Lutetia. In *AGU Fall Meeting Abstracts*, volume 2011, pages P23C–1722.
- Keller, H. U., Arpigny, C., Barbieri, C., Bonnet, R. M., Cazes, S., and Coradini, M. (1986). First Halley Multicolour camera imaging results from Giotto. *Nature*, **321**, 320–326.
- Keller, H. U., Barbieri, C., Lamy, P., Rickman, H., Rodrigo, R., Wenzel, K., Sierks, H., Hearn, M. F. A., Angrilli, F., Angulo, M., Bailey, M. E., Barthol, P., Barucci, M. A., and Bertaux, J. (2007). OSIRIS – The scientific camera system onboard ROSETTA. *Space Science Reviews*, (Figure 1), 433–506.
- Keller, H. U., Mottola, S., Davidsson, B., Skorov, Y., Groussin, O., Pajola, M., Hviid, S. F., Preusker, F., Scholten, F., Hearn, M. F. A., Angrilli, F., Barbieri, C., Barucci, M. A., Bertini, I., Cremonese, G., Debei, S., Cecco, D., Fornasier, S., Fulle, M., Jorda, L., Knollenberg, J., Koschny, D., Kramm, J. R., Lamy, P., Lazzarin, M., Moreno, J. J. L., Marzari, F., Michalik, H., Naletto, G., Rickman, H., Rodrigo, R., Sabau, L., Sierks, H., Thomas, N., Vincent, J. B., and Wenzel, K.-P. (2015). Insolation, Erosion, and Morphology of Comet 67P/Churyumov-Gerasimenko. *Astronomy & Astrophysics*, **583**(A34), 1–16.
- Keller, H. U., Mottola, S., Hviid, S. F., Agarwal, J., Kührt, E., Skorov, Y., Otto, K., Vincent, J.-B., Oklay, N., Schröder, S. E., Davidsson, B., Pajola, M., Shi, X., Bodewits, D., Toth, I., Preusker, F., Scholten, F., Sierks, H., Barbieri, C., Lamy, P., Rodrigo, R., Koschny, D., Rickman, H., A'Hearn, M. F., Barucci, M. A., Bertaux, J.-L., Bertini, I., Cremonese, G., Da Deppo, V., Debei, S., De Cecco, M., Deller, J., Fornasier, S., Fulle, M., Groussin, O., Gutierrez, P. J., Güttler, C., Hofmann, M., Ip, W.-H., Jorda, L., Knollenberg, J., Kramm, J. R., Küppers, M., Lara, L.-M., Lazzarin, M., Lopez-Moreno, J. J., Marzari, F., Naletto, G., Tübiana, C., and Thomas, N. (2017). Seasonal mass transfer on the nucleus of comet 67P/Churyumov-Gerasimenko. *Monthly Notices of the Royal Astronomical Society*, **469**(Suppl2), S357–S371.
- Keller, H. U., Mottola, S., Skorov, Y., and Jorda, L. (2015). The changing rotation period of comet 67P/Churyumov-Gerasimenko controlled by its activity. *Astronomy & Astrophysics*, **579**, L5.
- Klinger, J. (1999). Thermal evolution of comet nuclei. *Advances in Space Research*, **23**(7), 1309–1318.
- Kömler, N., Macher, W., Tiefenbacher, P., Kargl, G., Pelivan, I., Knollenberg, J., Spohn, T., Jorda, L., Capanna, C., Lommatsch, V., Cozzoni, B., and Finke, F. (2017). Three-dimensional illumination and thermal model of the abydos region on comet 67p/churyumov-gerasimenko. *Monthly Notices of the Royal Astronomical Society*, **469**, 2–19.

- Kömle, N. I. and Dettleff, G. (1991). Mass and Energy Transport in Sublimating Cometary Ice Cracks. *Icarus*, **89**, 73–84.
- Kopp, G. and Lean, J. L. (2011). A new , lower value of total solar irradiance : Evidence and climate significance. *Geophysical Research Letters*, **38**(January), 1–7.
- Kramer, T. and Noack, M. (2016). On the origin of inner coma structures observed by Rosetta during a diurnal rotation of comet 67P/Churyumov-Gerasimenko. *The Astrophysical Journal Letters*, **823**(1), L11.
- Krause, M., Blum, J., Skorov, Y., and Trieloff, M. (2011). Thermal conductivity measurements of porous dust aggregates: I. Technique, model and first results. *Icarus*, **214**(1), 286 – 296.
- Krebl, B. L. and Kömle, N. I. (2014). A two-dimensional model of crevasses formed by cometary activity. *Planetary and Space Science*, **87**(2013), 46–65.
- Kührt, E. and Keller, H. U. (1994). The formation of cometary surface crusts. *Icarus*, (109), 121–132.
- Kuiper, G. P. (1951). On the Origin of the Solar System. *Proceedings of the National Academy of Science*, **37**(1), 1–14.
- La Forgia, F., Giacomini, L., Lazzarin, M., Massironi, M., Oklay, N., Scholten, F., Pajola, M., and Bertini, I. (2015). Geomorphology and spectrophotometry of Philae s landing site on comet 67P / Churyumov-Gerasimenko. *Astronomy & Astrophysics*, **583**(A41), 1–18.
- Lagerros, J. S. V. (1996). Thermal physics of asteroids. I. Effects of shape, heat conduction and beaming. *Astronomy and Astrophysics*, **310**, 1011–1020.
- Lagerros, J. S. V. (1997). Thermal physics of asteroids. III. Irregular shapes and albedo variegations. *A&A*, **325**, 1226–1236.
- Lagerros, J. S. V. (1998). Thermal physics of asteroids IV . Thermal infrared beaming. *Astronomy and Astrophysics*, **332**, 1123–1132.
- Lai, I.-L., Ip, W.-H., Lee, J.-C., Lin, Z.-Y., Vincent, J.-B., Oklay, N., Sierks, H., Barberi, C., Lamy, P., Rodrigo, R., Koschny, D., Rickman, H., Keller, H. U., Agarwal, J., Barucci, M. A., Bertaux, J.-L., Bertini, I., Bodewits, D., Boudreault, S., Cremonese, G., Da Deppo, V., Davidsson, B., Debei, S., De Cecco, M., Deller, J., Fornasier, S., Fulle, M., Groussin, O., Gutiérrez, P. J., Güttler, C., Hofmann, M., Hviid, S. F., Jorda, L., Knollenberg, J., Kovacs, G., Kramm, J.-R., Kührt, E., Küppers, M., Lara, L. M., Lazzarin, M., López-Moreno, J. J., Marzari, F., Naletto, G., Shi, X., Tubiana, C., and Thomas, N. (2019). Seasonal variations in source regions of the dust jets on comet 67P/Churyumov-Gerasimenko. *Astronomy & Astrophysics*, **630**, A17.
- Lamy, P. L., Toth, I., Fernandez, Y. R., and Weaver, H. A. (2004). *The sizes, shapes, albedos, and colors of cometary nuclei*, page 223.

- Lara, L. M., Lowry, S., Vincent, J., Gutiérrez, P. J., Ro, A., Forgia, F. L., Oklay, N., Sierks, H., and Barbieri, C. (2015). Large-scale dust jets in the coma of 67P / Churyumov-Gerasimenko as seen by the OSIRIS instrument onboard Rosetta. *Astronomy & Astrophysics*, **583**(A9), 1–11.
- Lebofsky, L. A., Sykes, M. V., Tedesco, E. F., Veeder, G. J., Matson, D. L., Brown, R. H., Gradie, J. C., Feierberg, M. A., and Rudy, R. J. (1986). A refined “standard” thermal model for asteroids based on observations of 1 Ceres and 2 Pallas. *Icarus*, **68**(2), 239 – 251.
- Levison, H., Morbidelli, A., Van Laerhoven, C., Gomes, R., and Tsiganis, K. (2008). Origin of the structure of the Kuiper belt during a dynamical instability in the orbits of Uranus and Neptune. *Icarus*, **196**, 258–273.
- Leyrat, C., Erard, S., Capaccioni, F., Tosi, F., and Filacchione, G. (2015). Surface thermal properties of 67 / P inferred by VIRTIS / Rosetta. In *EGU 2015*, volume 17, page 9767.
- Li, H., Tuo, X., Liu, Y., and Jiang, X. (2015). A Parallel Algorithm Using Perlin Noise Superposition Method for Terrain Generation Based on CUDA architecture. In *Proceedings of the 2015 International Conference on Materials Engineering and Information Technology Applications*, pages 967–974. Atlantis Press.
- Lowry, S., Duddy, S. R., Rozitis, B., Green, S. F., Fitzsimmons, A., Snodgrass, C., Hsieh, H. H., and Hainaut, O. (2012). Astrophysics The nucleus of Comet 67P / Churyumov-Gerasimenko A new shape model and thermophysical analysis. *Astronomy & Astrophysics*, **548**(A12), 1–15.
- Lucchetti, A., Cremonese, G., Jorda, L., Poulet, F., Bibring, J.-P., Pajola, M., La Forgia, F., Massironi, M., El-Maarry, M. R., Oklay, N., Sierks, H., Barbieri, C., Lamy, P., Rodrigo, R., Koschny, D., Rickman, H., Keller, H. U., Agarwal, J., A’Hearn, M. F., Barucci, M. A., Bertaux, J.-L., Bertini, I., Da Deppo, V., Davidsson, B., Debei, S., De Cecco, M., Fornasier, S., Fulle, M., Groussin, O., Gutierrez, P. J., Güttler, C., Hviid, S. F., Ip, W.-H., Knollenberg, J., Kramm, J.-R., Kührt, E., Küppers, M., Lara, L. M., Lazzarin, M., Lopez Moreno, J. J., Marzari, F., Mottola, S., Naletto, G., Preusker, F., Scholten, F., Thomas, N., Tubiana, C., and Vincent, J.-B. (2016). Characterization of the Abydos region through OSIRIS high-resolution images in support of CIVA measurements. *Astronomy & Astrophysics*, **585**, L1.
- Maquet, L. (2015). The recent dynamical history of comet 67P/Churyumov-Gerasimenko. *Astronomy & Astrophysics*, **579**, A78.
- Marshall, D., Groussin, O., Vincent, J.-B., Brouet, Y., Kappel, D., Arnold, G., Capria, M. T., Filacchione, G., Hartogh, P., Hofstadter, M., Ip, W.-H., Jorda, L., Kührt, E., Lellouch, E., Mottola, S., Rezac, L., Rodrigo, R., Rodionov, S., Schloerb, P., and Thomas, N. (2018). Thermal inertia and roughness of the nucleus of comet 67P/Churyumov-Gerasimenko from MIRO and VIRTIS observations. *Astronomy & Astrophysics*, **616**, A122.

- Masoumzadeh, N., Oklay, N., Kolokolova, L., Sierks, H., Fornasier, S., Barucci, M. A., Vincent, J. B., Tubiana, C., Güttler, C., Preusker, F., Scholten, F., Mottola, S., Hasselmann, P. H., Feller, C., Barbieri, C., Lamy, P. L., Rodrigo, R., Koschny, D., Rickman, H., A'Hearn, M. F., Bertaux, J. L., Bertini, I., Cremonese, G., Da Deppo, V., Davidsson, B. J. R., Debei, S., De Cecco, M., Fulle, M., Gicquel, A., Groussin, O., Gutiérrez, P. J., Hall, I., Hofmann, M., Hviid, S. F., Ip, W. H., Jorda, L., Keller, H. U., Knollenberg, J., Kovacs, G., Kramm, J. R., Kührt, E., Küppers, M., Lara, L. M., Lazzarin, M., Lopez Moreno, J. J., Marzari, F., Naletto, G., Shi, X., and Thomas, N. (2017). Opposition effect on comet 67P/Churyumov-Gerasimenko using Rosetta-OSIRIS images. *A&A*, **599**, A11.
- Massironi, M., Simioni, E., Marzari, F., Cremonese, G., Giacomini, L., Pajola, M., Jorda, L., Naletto, G., Lowry, S., El-Maarry, M. R., Preusker, F., Scholten, F., Sierks, H., Barbieri, C., Lamy, P., Rodrigo, R., Koschny, D., Rickman, H., Keller, H. U., A'Hearn, M. F., Agarwal, J., Auger, A.-T., Barucci, M. A., Bertaux, J.-L., Bertini, I., Besse, S., Bodewits, D., Capanna, C., da Deppo, V., Davidsson, B., Debei, S., de Cecco, M., Ferri, F., Fornasier, S., Fulle, M., Gaskell, R., Groussin, O., Gutiérrez, P. J., Güttler, C., Hviid, S. F., Ip, W.-H., Knollenberg, J., Kovacs, G., Kramm, R., Kührt, E., Küppers, M., La Forgia, F., Lara, L. M., Lazzarin, M., Lin, Z.-Y., Lopez Moreno, J. J., Magrin, S., Michalik, H., Mottola, S., Oklay, N., Pommerol, A., Thomas, N., Tubiana, C., and Vincent, J.-B. (2015). Two independent and primitive envelopes of the bilobate nucleus of comet 67P. *Nature*, **526**(7573), 402–405.
- Matonti, C., Attree, N., Groussin, O., Jorda, L., Viseur, S., Hviid, S. F., Bouley, S., Nebouy, D., Auger, A.-T., Lamy, P. L., Sierks, H., Naletto, G., Rodrigo, R., Koschny, D., Davidsson, B., Barucci, M. A., Bertaux, J.-L., Bertini, I., Bodewits, D., Cremonese, G., Da Deppo, V., Debei, S., De Cecco, M., Deller, J., Fornasier, S., Fulle, M., Gutierrez, P. J., Güttler, C., Ip, W.-H., Keller, H. U., Lara, L. M., La Forgia, F., Lazzarin, M., Lucchetti, A., LÁşpez-Moreno, J. J., Marzari, F., Massironi, M., Mottola, S., Oklay, N., Pajola, M., Penasa, L., Preusker, F., Rickman, H., Scholten, F., Shi, X., Toth, I., Tubiana, C., and Vincent, J.-B. (2019). Bilobate comet morphology and internal structure controlled by shear deformation. *Nature Geoscience*, **12**, 157–162.
- Merrill, R. B. (1969). Thermal conduction through an evacuated idealized powder over the temperature range of 100 to 500 K. Technical report, NASA.
- Molaro, J. and Byrne, S. (2012). Rates of temperature change of airless landscapes and implications for thermal stress weathering. *Journal of Geophysical Research: Planets*, **117**(E10).
- Morbidelli, A. (2005). Origin and Dynamical Evolution of Comets and their Reservoirs. *ArXiv Astrophysics e-prints*.
- Morbidelli, A., Levison, H., Tsiganis, K., and Gomes, R. (2005). Chaotic capture of Jupiter's Trojan asteroids in the early Solar System. *Nature*, **435**, 462–465.
- Mottola, S., Lowry, S., Snodgrass, C., Lamy, P. L., Toth, I., Sierks, H., Angrilli, F., Barbieri, C., Barucci, M. a., Cremonese, G., Davidsson, B., Cecco, M. D., Debei, S.,

- Fornasier, S., Fulle, M., Groussin, O., Hviid, S. F., Ip, W., Jorda, L., Keller, H. U., Knollenberg, J., Koschny, D., Kramm, R., Lara, L., Lazzarin, M., Moreno, J. J. L., Marzari, F., Michalik, H., Naletto, G., Rickman, H., Rodrigo, R., Sabau, L., Thomas, N., Agarwal, J., Bertini, I., Ferri, F., Magrin, S., Oklay, N., Tubiana, C., RoÅijek, A., A´ Hearn, M. F., Bertaux, J.-L., Da Deppo, V., De Cecco, M., Guti rrez, P., K hrt, E., K ppers, M., Lopez Moreno, J. J., Wenzel, K.-P., G ttler, C., and Vincent, J.-B. (2014). The rotation state of 67P/Churyumov-Gerasimenko from approach observations with the OSIRIS cameras on Rosetta. *Astronomy and Astrophysics*, **569**(L2), 1–5.
- Mottola, S., Arnold, G., Jaumann, R., Michaelis, H., Neukum, G., Hamm, M., Otto, K. A., Pelivan, I., Proffe, G., Scholten, F., Tirsch, D., Kreslavsky, M., Remetean, E., Souvanavong, F., and Dolives, B. (2015). The structure of the regolith on 67P/Churyumov-Gerasimenko from ROLIS descent imaging. *Science*, **349**(6247), 1–4.
- Mousis, O., Ronnet, T., Brugger, B., Ozgurel, O., Pauzat, F., Ellinger, Y., Maggiolo, R., Wurz, P., Vernazza, P., Lunine, J. I., Lusp y-Kuti, A., Mandt, K. E., Altwegg, K., Bieler, A., Markovits, A., and Rubin, M. (2016). Origin of molecular oxygen in comet 67P/Churyumov-Gerasimenko. *The Astrophysical Journal*, **823**(2), L41.
- Oort, J. (1950). The structure of the cloud of comets surrounding the Solar System and a hypothesis concerning its origin. *Bulletin of the Astronomical Institutes of the Netherlands*, **11**, 91–110.
- O’Rourke, L., Heinisch, P., Blum, J., Fornasier, S., Filacchione, G., Van Hoang, H., Ciarniello, M., Raponi, A., Gundlach, B., Blasco, R. A., Grieger, B., Glassmeier, K.-H., K ppers, M., Rotundi, A., Groussin, O., Bockelee-Morvan, D., Auster, H.-U., Oklay, N., Paar, G., Perucha, M. d. P. C., Kovacs, G., Jorda, L., Vincent, J.-B., Capaccioni, F., Biver, N., Parker, J. W., Tubiana, C., and Sierks, H. (2020). The Philae lander reveals low-strength primitive ice inside cometary boulders. *Nature*, **586**(7831), 697–701.
- Pajola, M., Vincent, J.-b., G ttler, C., Lee, J.-c., Bertini, I., Massironi, M., Simioni, E., Marzari, F., Giacomini, L., Lucchetti, A., Barbieri, C., Cremonese, G., Naletto, G., Pommerol, A., El-maarry, M. R., Besse, S., K ppers, M., Forgia, F. L., Lazzarin, M., Thomas, N., Auger, A.-t., Groussin, O., Gutierrez, P. J., Hviid, S. F., Ip, W.-h., Jorda, L., Knollenberg, J., Marchi, S., Michalik, H., Moissl, R., Mottola, S., and Oklay, N. (2015). Size-frequency distribution of boulders ≥ 7 m on comet 67P / Churyumov-Gerasimenko. *Astronomy & Astrophysics*, **583**(A37), 1–17.
- Pajola, M., H fner, S., Vincent, J. B., Oklay, N., Scholten, F., Preusker, F., Mottola, S., Naletto, G., Fornasier, S., Lowry, S., Feller, C., Hasselmann, P. H., G ttler, C., Tubiana, C., Sierks, H., Barbieri, C., Lamy, P., Rodrigo, R., Koschny, D., Rickman, H., Keller, H. U., Agarwal, J., A´ Hearn, M. F., Barucci, M. A., Bertaux, J.-L., Bertini, I., Besse, S., Boudreault, S., Cremonese, G., Da Deppo, V., Davidsson, B., Debei, S., De Cecco, M., Deller, J., Deshapriya, J. D. P., El-Maarry, M. R., Ferrari, S., Ferri, F., Fulle, M., Groussin, O., Gutierrez, P., Hofmann, M., Hviid, S. F., Ip, W.-H., Jorda, L., Knollenberg, J., Kovacs, G., Kramm, J. R., K hrt, E., K ppers, M., Lara, L. M., Lin, Z.-Y., Lazzarin, M., Lucchetti, A., Lopez Moreno, J. J., Marzari, F., Massironi, M., Michalik, H., Penasa, L., Pommerol, A., Simioni, E., Thomas, N., Toth, I., and Baratti,

- E. (2017). The pristine interior of comet 67P revealed by the combined Aswan outburst and cliff collapse. *Nature Astronomy*, **1**, 0092.
- Parker, E. (1958). Dynamics of the Interplanetary Gas and Magnetic Fields. *Astrophysical Journal*, **128**, 664.
- Perlin, K. (2002). Improving Noise. *ACM Trans. Graph.*, **21**(3), 681-682.
- Pettit, E. and Nicholson, S. B. (1930). Lunar radiation and temperatures. *ApJ*, **71**, 102–135.
- Pommerol, A., Thomas, N., El-Maarry, M. R., Pajola, M., Groussin, O., Auger, A., Ockay, N., and Fornasier, S. (2015). OSIRIS observations of meter-sized exposures of H₂O ice at the surface of 67P / Churyumov-Gerasimenko and interpretation using laboratory experiments. *Astronomy & Astrophysics*, **583**(A25), 1–16.
- Poulet, F., Lucchetti, A., Bibring, J.-P., Carter, J., Gondet, B., Jorda, L., Langevin, Y., Pilorget, C., Capanna, C., and Cremonese, G. (2016). Origin of the local structures at the Philae landing site and possible implications on the formation and evolution of 67P/Churyumov-Gerasimenko. *Monthly Notices of the Royal Astronomical Society*, **462**(Suppl1), 23–32.
- Preusker, F., Scholten, F., Matz, K., Roatsch, T., Willner, K., Hviid, S. F., Knollenberg, J., and Jorda, L. (2015). Astrophysics Special feature Shape model, reference system definition, and cartographic mapping standards for comet 67P / Churyumov-Gerasimenko – Stereo-photogrammetric analysis of Rosetta / OSIRIS image data. *Astronomy & Astrophysics*, **583**(A33), 1–19.
- Prialnik, D. (1989). Thermal Evolution of Cometary Nuclei. *Advances in Space Research*, **9**(3), 25–40.
- Prialnik, D. (2002). Application to Comet C / 1995 O1 Hale – Bopp. *Earth, Moon and Planets*, pages 27–52.
- Prialnik, D. (2020). Thermal Physics of Cometary Nuclei.
- Prialnik, D. and Bar-Nun, A. (1992). Crystallization of amorphous ice as the cause of comet P/Halley's outburst at 14 AU. *Astronomy and astrophysics*, **258**, L9–12.
- Prialnik, D., Benkhoff, J., and Podolak, M. (2004). Modeling the structure and activity of comet nuclei. *Comets II*, **1**(1961), 359–387.
- Raymond, S. and Morbidelli, A. (2014). The Grand Tack model: a critical review. In *IAU Symposium*, volume 310 of *IAU Symposium*, pages 194–203.
- Rickman, H. (2018). *Origin and Evolution of Comets: Ten Years After the Nice Model and One Year After Rosetta*. Advances in planetary science. World Scientific Publishing Company Pte. Limited.

- Rinaldi, G., Formisano, M., Kappel, D., Capaccioni, F., Bockelée-Morvan, D., Cheng, Y. C., Vincent, J. B., Deshapriya, P., Arnold, G., Capria, M. T., Ciarniello, M., D'Aversa, E., De Sanctis, M. C., Doose, L., Erard, S., Federico, C., Filacchione, G., Fink, U., Leyrat, C., Longobardo, A., Magni, G., Migliorini, A., Mottola, S., Naletto, G., Raponi, A., Taylor, F., Tosi, F., Tozzi, G. P., and Salatti, M. (2019). Analysis of night-side dust activity on comet 67P observed by VIRTIS-M: a new method to constrain the thermal inertia on the surface. *A&A*, **630**, A21.
- Rodionov, A., Crifo, J.-F., Szego, K., Lagerros, J., and Fulle, M. (2002). An advanced physical model of cometary activity. *Planetary and Space Science*, **50**(10-11), 983–1024.
- Rosenberg, E. D. and Prrialnik, D. (2009). Fully 3-dimensional calculations of dust mantle formation for a model of Comet 67P / Churyumov-Gerasimenko. *Icarus*, **201**(2), 740–749.
- Rosenberg, E. D. and Prrialnik, D. (2010). The effect of internal inhomogeneity on the activity of comet nuclei - Application to Comet 67P/Churyumov-Gerasimenko. *Icarus*, **209**(2), 753–765.
- Rotundi, A., Sierks, H., Della Corte, V., Fulle, M., Gutierrez, P., Lara, L., Barbieri, C., Lamy, P., Rodrigo, R., Koschny, D., Rickman, H., Keller, H., López-Moreno, J., Accolla, M., Agarwal, J., A'Hearn, M., Altobelli, N., Angrilli, F., Barucci, M., Bertaux, J.-L., Bertini, I., Bodewits, D., Bussoletti, E., Colangeli, L., Cosi, M., Cremonese, G., Crifo, J.-F., Da Deppo, V., Davidsson, B., Debei, S., De Cecco, M., Esposito, F., Ferrari, M., Fornasier, S., Giovane, F., Gustafson, B., Green, S., Groussin, O., Grün, E., Güttler, C., Herranz, M., Hviid, S., Ip, W., Ivanovski, S., Jerónimo, J., Jorda, L., Knollenberg, J., Kramm, R., Kührt, E., Küppers, M., Lazzarin, M., Leese, M., López-Jiménez, A., Lucarelli, F., Lowry, S., Marzari, F., Epifani, E., McDonnell, J., Mennella, V., Michalik, H., Molina, A., Morales, R., Moreno, F., Mottola, S., Naletto, G., Oklay, N., Ortiz, J., Palomba, E., Palumbo, P., Perrin, J.-M., Rodríguez, J., Sabau, L., Snodgrass, C., Sordini, R., Thomas, N., Tubiana, C., Vincent, J.-B., Weissman, P., Wenzel, K.-P., Zakharov, V., and Zarnecki, J. (2015). Dust measurements in the coma of comet 67P/Churyumov-Gerasimenko inbound to the Sun. *Science*, **347**, 3905.
- Rozitis, B. and Green, S. F. (2011). Directional characteristics of thermal-infrared beaming from atmosphereless planetary surfaces - a new thermophysical model. *Monthly Notices of the Royal Astronomical Society*, **415**(3), 2042–2062.
- Rubin, M., Altwegg, K., Balsiger, H., Bar-Nun, A., Berthelier, J.-J., Bieler, A., Bochsler, P., Briois, C., Calmonte, U., Combi, M., De Keyser, J., Dhooghe, F., Eberhardt, P., Fiethe, B., Fuselier, S. A., Gasc, S., Gombosi, T. I., Hansen, K. C., Hässig, M., Jäckel, A., Kopp, E., Korth, A., Le Roy, L., Mall, U., Marty, B., Mousis, O., Owen, T., Rème, H., Sémon, T., Tzou, C.-Y., Waite, J. H., and Wurz, P. (2015). Molecular nitrogen in comet 67P/Churyumov-Gerasimenko indicates a low formation temperature. *Science*, **348**(6231), 232–235.

- Rubin, M., Engrand, C., Snodgrass, C., Weissman, P., Altwegg, K., Busemann, H., Morbidelli, A., and Mumma, M. (2020). On the Origin and Evolution of the Material in 67P/Churyumov-Gerasimenko. *Space Science Reviews*, **216**(102).
- Ruzicka, B.-K., Penasa, L., Boehnhardt, H., Pack, A., Dolives, B., Souvannavong, F., and Remetean, E. (2018). Analysis of layering-related linear features on comet 67P/Churyumov-Gerasimenko. *Monthly Notices of the Royal Astronomical Society*, **482**(4), 5007–5011.
- Saari, J. M. and Shorthill, R. W. (1963). Isotherms of Crater Regions on the Illuminated and Eclipsed Moon. *Icarus*, **136**(2), 115–136.
- Schloerb, F. P., Keihm, S., Allmen, P. V., Choukroun, M., Lellouch, E., Leyrat, C., Beaudin, G., Biver, N., Bockelée-morvan, D., Crovisier, J., Encrenaz, P., Gaskell, R., Gulkis, S., Hartogh, P., Hofstadter, M., Ip, W.-h., Janssen, M., Jarchow, C., Jorda, L., Keller, H. U., Lee, S., Rezac, L., and Sierks, H. (2015). Astrophysics Special feature MIRO observations of subsurface temperatures of the nucleus of 67P / Churyumov-Gerasimenko. *Astronomy & Astrophysics*, **583**(A29), 1–11.
- Schotte, W. (1960a). Thermal conductivity of packed beds. *AIChE Journal*, **6**(1), 63–67.
- Schulz, R., Hilchenbach, M., Langevin, Y., Kissel, J., Silen, J., Briois, C., Engrand, C., Hornung, K., Baklouti, D., Bardyn, A., Cottin, H., Fischer, H., Fray, N., Godard, M., Lehto, H., Le Roy, L., Merouane, S., Orthous-Daunay, F.-R., Paquette, J., Rynö, J., Siljeström, S., Stenzel, O., Thirkell, L., Varmuza, K., and Zaprudin, B. (2015). Comet 67P/Churyumov-Gerasimenko sheds dust coat accumulated over the past four years. *Nature*, **518**(7538), 216–218.
- Schwamb, M. (2014). Solar System: Stranded in no-man’s-land. *Nature*, **507**, 435–436.
- Seargent, D. A. J. (2009). Broom Stars and Celestial Scimitars.
- Sekanina, Z. (1987). Anisotropic emission from comets: fans versus jets. I. Concept and modeling. In E. J. Rolfe, B. Battrock, M. Ackerman, M. Scherer, and R. Reinhard, editors, *Diversity and Similarity of Comets*, volume 278 of *ESA Special Publication*, pages 315–322.
- Sekanina, Z. (2004). Modeling the Nucleus and Jets of Comet 81P/Wild 2 Based on the Stardust Encounter Data. *Science*, **304**(5678), 1769–1774.
- Shi, X., Hu, X., Güttler, C., Hearn, M. A., Blum, J., El-Maarry, M., Kührt, E., Mottola, S., and Pajola, M. (2016). Sunset jets observed on comet 67P / Churyumov-Gerasimenko sustained by subsurface thermal lag. *Astronomy & Astrophysics*, **586**(A7), 1–13.
- Shi, X., Hu, X., Mottola, S., Sierks, H., Keller, H. U., Rose, M., Güttler, C., Fulle, M., Fornasier, S., Agarwal, J., Pajola, M., Tubiana, C., Bodewits, D., Barbieri, C., Lamy, P. L., Rodrigo, R., Koschny, D., Barucci, M. A., Bertaux, J.-L., Bertini, I., Boudreault, S., Cremonese, G., Da Deppo, V., Davidsson, B., Debei, S., De Cecco, M., Deller, J., Groussin, O., Gutierrez, P. J., Hviid, S. F., Ip, W.-H., Jorda, L., Knollenberg, J.,

- Kovacs, G., Kramm, J.-R., Kührt, E., Küppers, M., Lara, L. M., Lazzarin, M., Lopez-Moreno, J. J., Marzari, F., Naletto, G., Oklay, N., Toth, I., and Vincent, J.-B. (2018). Coma morphology of comet 67P controlled by insolation over irregular nucleus. *Nature Astronomy*, **2**, 562–567.
- Sierks, H., Rickman, H., Keller, H. U., Agarwal, J., and Hearn, M. F. A. (2015). On the nucleus structure and activity of comet 67P/Churyumov-Gerasimenko. *Science*, **347**, aaa1044–1.
- Skorov, Y., Kömle, N. I., Keller, H. U., Kargl, G., and Markiewicz, W. J. (2001). A Model of Heat and Mass Transfer in a Porous Cometary Nucleus Based on a Kinetic Treatment of Mass Flow. *Icarus*, **153**(1), 180–196.
- Skorov, Y. V., Lieshout, R. V., Blum, J., and Keller, H. U. (2011). Activity of comets: Gas transport in the near-surface porous layers of a cometary nucleus. *Icarus*, **212**(2), 867–876.
- Skorov, Yu. V., Rezac, L., Hartogh, P., Bazilevsky, A. T., and Keller, H. U. (2016). A model of short-lived outbursts on the 67P from fractured terrains. *Astronomy & Astrophysics*, **593**, A76.
- Soderblom, L. A., Becker, T. L., Bennett, G., Boice, D. C., Britt, D. T., Brown, R. H., Buratti, B. J., Isbell, C., Giese, B., Hare, T., Hicks, M. D., Howington-Kraus, E., Kirk, R. L., Lee, M., Nelson, R. M., Oberst, J., Owen, T. C., Rayman, M. D., Sandel, B. R., Stern, S. A., Thomas, N., and Yelle, R. V. (2002). Observations of Comet 19P/Borrelly by the Miniature Integrated Camera and Spectrometer Aboard Deep Space 1. *Science*, **296**(5570), 1087–1091.
- Solem, J. (1995). Cometary breakup calculations based on a gravitationally-bound agglomeration model: the density and size of Shoemaker-Levy 9. *Astronomy & Astrophysics*, **302**, 596.
- Spohn, T., Knollenberg, J., Ball, A. J., Banaszkiwicz, M., Benkhoff, J., Grott, M., Grygorczuk, J., Huttig, C., Hagermann, A., Kargl, G., Kaufmann, E., Kömle, N., Kührt, E., Kossacki, K. J., Marczewski, W., Pelivan, I., Schrodter, R., and Seiferlin, K. (2015). Thermal and mechanical properties of the near-surface layers of comet 67P/Churyumov-Gerasimenko. *Science*, **349**(6247), aab0464–aab0464.
- Steckloff, J. K., Johnson, B. C., Bowling, T., Melosh, H. J., Minton, D., Lisse, C. M., and Battams, K. (2015). Dynamic sublimation pressure and the catastrophic breakup of Comet ISON. *Icarus*, **258**, 430–437.
- Stern, A. S. (2003). The evolution of comets in the Oort cloud and Kuiper belt. *Nature*, **424**, 639–642.
- Stern, S. (1988). Collisions in the Oort Cloud. *Icarus*, **73**, 499–507.
- Thomas, N., Davidsson, B., Fornasier, S., Giacomini, L., Hviid, S. F., Ip, W., Jorda, L., Keller, H. U., Knollenberg, J., Kührt, E., F. L. F., Lai, I. L., Liao, Y., Marschall, R., Massironi, M., Mottola, S., Pajola, M., Poch, O., Pommerol, A., Preusker, F., Scholten,

- F., Su, C. C., Wu, J. S., Vincent, J., Sierks, H., Barbieri, C., Lamy, P. L., Rodrigo, R., Koschny, D., Rickman, H., Hearn, A. M. F., Barucci, M. A., Bertaux, J., Bertini, I., Cremonese, G., V. D. D., Debei, S., M. D. C., Fulle, M., Groussin, O., Gutierrez, P. J., Kramm, J., Küppers, M., Lara, L. M., Lazzarin, M., J. L. M. J., Marzari, F., Michalik, H., Naletto, G., Agarwal, J., Güttler, C., Oklay, N., and Tubiana, C. (2015a). Redistribution of particles across the nucleus of comet 67P/Churyumov-Gerasimenko. *Astronomy & Astrophysics*, **583**(A17), 1–18.
- Thomas, N., Sierks, H., Barbieri, C., Lamy, P. L., Rodrigo, R., Rickman, H., Koschny, D., Keller, H. U., Agarwal, J., Hearn, M. F. A., Angrilli, F., Auger, A.-t., Barucci, M. A., Kramm, J., Kührt, E., Küppers, M., and Forgia, F. L. (2015b). The morphological diversity of comet 67P/Churyumov-Gerasimenko. *Science*, **347**(6220), 1–6.
- Tiscareno, M. S. and Malhotra, R. (2003). The Dynamics of Known Centaurs. *The Astronomical Journal*, **126**(6), 3122–3131.
- Tosi, F., Capaccioni, F., Capria, M. T., Mottola, S., Zinzi, A., Ciarniello, M., Filacchione, G., Hofstadter, M., Fonti, S., Formisano, M., Kappel, D., Kührt, E., Leyrat, C., Vincent, J.-B., Arnold, G., De Sanctis, M. C., Longobardo, A., Palomba, E., Raponi, A., Rousseau, B., Schmitt, B., Barucci, M. A., Bellucci, G., Benkhoff, J., Bockelee-Morvan, D., Cerroni, P., Combe, J.-P., Despan, D., Erard, S., Mancarella, F., McCord, T. B., Migliorini, A., Orofino, V., and Piccioni, G. (2019). The changing temperature of the nucleus of comet 67P induced by morphological and seasonal effects. *Nature Astronomy*, **3**, 649–658.
- Tsiganis, K., Gomes, R., Morbidelli, A., and Levison, H. (2005). Origin of the orbital architecture of the giant planets of the Solar System. *Nature*, **435**, 459–461.
- Urquhart, M. L. and Jakosky, B. M. (1997). Lunar thermal emission and remote determination of surface properties. *Journal of Geophysical Research: Planets*, **102**(E5), 10959–10969.
- Veverka, J., Klaasen, K., A' Hearn, M., Belton, M., Brownlee, D., Chesley, S., Clark, B., Economou, T., Farquhar, R., Green, S. F., Groussin, O., Harris, A., Kissel, J., Li, J.-Y., Meech, K., Melosh, J., Richardson, J., Schultz, P., Silen, J., Sunshine, J., Thomas, P., Bhaskaran, S., Bodewits, D., Carcich, B., Chevront, A., Farnham, T., Sackett, S., Wellnitz, D., and Wolf, A. (2013). Return to Comet Tempel 1: Overview of Stardust-NExT results. *Icarus*, **222**(2), 424–435.
- Vincent, J., Bönhardt, H., and Lara, L. M. (2010). Astrophysics A numerical model of cometary dust coma structures Application to comet 9P / Tempel 1. *Astronomy & Astrophysics*, **512**(A60), 1–8.
- Vincent, J., Oklay, N., Pajola, M., Höfner, S., Sierks, H., Hu, X., Barbieri, C., Lamy, P. L., and Rodrigo, R. (2016). Are fractured cliffs the sources of cometary dust jets ? Insights from OSIRIS / Rosetta at 67P. *Astronomy & Astrophysics*, **587**(A14).
- Vincent, J.-B., Lara, L. M., Tozzi, G. P., Lin, Z.-Y., and Sierks, H. (2013). Spin and activity of comet 67P/Churyumov-Gerasimenko. *Astronomy & Astrophysics*, **549**, A121.

- Vincent, J.-B., Oklay, N., Marchi, S., Höfner, S., and Sierks, H. (2015a). Craters on comets. *Planetary and Space Science*, **107**, 53 – 63.
- Vincent, J.-B., Bodewits, D., Besse, S., and Sierks, H. (2015b). Large heterogeneities in comet 67P as revealed by active pits from sinkhole collapse. *Nature*, **523**, 63–66.
- Vincent, J. B., A’Hearn, M. F., Lin, Z. Y., El-Maarry, M. R., Pajola, M., Sierks, H., Barbieri, C., Lamy, P. L., Rodrigo, R., Koschny, D., Rickman, H., Keller, H. U., Agarwal, J., Barucci, M. A., Bertaux, J. L., Bertini, I., Besse, S., Bodewits, D., Cremonese, G., Da Deppo, V., Davidsson, B., Debei, S., De Cecco, M., Deller, J., Fornasier, S., Fulle, M., Gicquel, A., Groussin, O., Gutiérrez, P. J., Gutiérrez-Marquez, P., Güttler, C., Höfner, S., Hofmann, M., Hviid, S. F., Ip, W. H., Jorda, L., Knollenberg, J., Kovacs, G., Kramm, J. R., Kührt, E., Küppers, M., Lara, L. M., Lazzarin, M., Lopez Moreno, J. J., Marzari, F., Massironi, M., Mottola, S., Naletto, G., Oklay, N., Preusker, F., Scholten, F., Shi, X., Thomas, N., Toth, I., and Tubiana, C. (2016). Summer fireworks on comet 67P. *Monthly Notices of the Royal Astronomical Society*, **462**, S184–S194.
- Vincent, J.-B., Farnham, T., Kührt, E., Skorov, Y., Marschall, R., Oklay, N., El-Maarry, M. R., and Keller, H. U. (2019). Local Manifestations of Cometary Activity. *Space Science Reviews*, **215**(30).
- Vincent, J.-B., Oklay, N., Pajola, M., Höfner, S., Sierks, H., Hu, X., Barbieri, C., Lamy, P. L., Rodrigo, R., Koschny, D., Rickman, H., Keller, H. U., A’Hearn, M. F., Barucci, M. A., Bertaux, J.-L., Bertini, I., Besse, S., Bodewits, D., Cremonese, G., Da Deppo, V., Davidsson, B., Debei, S., De Cecco, M., El-Maarry, M. R., Fornasier, S., Fulle, M., Groussin, O., Gutiérrez, P. J., Gutiérrez-Marquez, P., Güttler, C., Hofmann, M., Hviid, S. F., Ip, W.-H., Jorda, L., Knollenberg, J., Kovacs, G., Kramm, J.-R., Kührt, E., Küppers, M., Lara, L. M., Lazzarin, M., Lin, Z.-Y., Lopez Moreno, J. J., Lowry, S., Marzari, F., Massironi, M., Moreno, F., Mottola, S., Naletto, G., Preusker, F., Scholten, F., Shi, X., Thomas, N., Toth, I., and Tubiana, C. (2016). Are fractured cliffs the source of cometary dust jets? Insights from OSIRIS/Rosetta at 67P/Churyumov-Gerasimenko. *Astronomy & Astrophysics*, **587**, A14.
- Walsh, K., Morbidelli, A., Raymond, S., O’Brien, D., and Mandell, A. (2011). A low mass for Mars from Jupiter’s early gas-driven migration. *Nature*, **475**, 206–209.
- Weissman, P. (1986). Are cometary nuclei primordial rubble piles? *Nature*, **320**, 242–244.
- Weissman, P. and Kieffer, H. (1981). Thermal modeling of cometary nuclei. *Icarus*, **47**, 302–311.
- Weissman, P. and Kieffer, H. (1984). An Improved Thermal Model for Cometary Nuclei. *Journal of Geophysical Research*, pages 358–364.
- Weissman, P., Morbidelli, A., Davidsson, B., and Blum, J. (2020). Origin and Evolution of Cometary Nuclei. *Space Science Reviews*, **216**(6).
- Weissman, P. R. (2004). Structure and Density of Cometary Nuclei.

- Weissman, P. R. and Lowry, S. C. (2008). Structure and density of cometary nuclei. *Meteoritics and Planetary Science*, **43**(6), 1033–1047.
- Wesselink, A. J. (1948). Heat conductivity and nature of the lunar surface material. *Bulletin of the Astronomical Institutes of the Netherlands*, **10**, 351–363.
- Whipple, F. L. (1950). A comet model. I. The acceleration of Comet Encke. *Astrophysical Journal*, **111**, 375–394.

Publications

Refereed Journal Articles

- Auger, A.-T.; Groussin, O.; Jorda, L.; R.El-Maarry, M.; Bouley, S.; Séjourné, A.; Gaskell, R.; Capanna, C.; Davidsson, B.; Marchi, S. ; **Höfner, S.**; Lamy, P.L.; Sierks, H.; Barbieri, C.; Rodrigo, R.; Koschny, D.; Rickman, H.; Keller, H.U.; Agarwal, J.; A’Hearn, M.F.; Barucci, M.A.; Bertaux, J.-L.; Bertini, I.; Cremonese, G.; Deppo, V. D.; Debei, S.; Cecco, M. D.; Fornasier, S.; Fulle, M.; Gutierrez, P.J.; Güttler, C.; Hviid, S.; Ip, W.-H.; Knollenberg, J.; Kramm, J.-R.; Kührt, E.; Küppers, M.; Lara, L.M.; Lazzarin, M.; Moreno, J.J. L.; Marzari, F.; Massironi, M.; Michalik, H.; Naletto, G.; Oklay, N.; Pommerol, A.; Sabau, L.; Thomas, N.; Tubiana, C.; Vincent, J.-B.; Wenzel, K.-P.: **Meter-scale thermal contraction crack polygons on the nucleus of comet 67P/Churyumov-Gerasimenko.** *Icarus* 301, pp. 173 - 188 (2018)
- Agarwal, J.; Corte, V. D.; Feldman, P. D.; Geiger, B.; Merouane, S.; Bertini, I.; Bodewits, D.; Fornasier, S.; Grün, E.; Hasselmann, P. ; Hilchenbach, M.; **Höfner, S.**; Ivanovski, S.; Kolokolova, L.; Pajola, M.; Rotundi, A.; Sierks, H.; Steffl, A. J.; Thomas, N.; A’Hearn, M. F.; Barbieri, C.; Barucci, M. A.; Bertaux, J.-L.; Boudreault, S.; Cremonese, G.; Deppo, V. D.; Davidsson, B.; Debei, S.; Cecco, M. D.; Deller, J. F.; Feaga, L. M.; Fischer, H.; Fulle, M.; Gicquel, A.; Groussin, O.; Güttler, C.; Gutiérrez, P. J.; Hofmann, M.; Hornung, K.; Hviid, S. F.; Ip, W.-H.; Jorda, L.; Keller, H. U.; Kissel, J.; Knollenberg, J.; Koch, A.; Koschny, D.; Kramm, J.-R.; Kührt, E.; Küppers, M.; Lamy, P. L.; Langevin, Y.; Lara, L. M.; Lazzarin, M.; Lin, Z.-Y.; Moreno, J. J. L.; Lowry, S. C.; Marzari, F.; Mottola, S.; Naletto, G.; Oklay, N.; Parker, J. W.; Rodrigo, R.; Rynö, J.; Shi, X.; Stenzel, O.; Tubiana, C.; Vincent, J.-B.; Weaver, H. A.; Zaprudin, B.: **Evidence of sub-surface energy storage in comet 67P from the outburst of 2016 July 03.** *Monthly Notices of the Royal Astronomical Society*, 469, pp. S606 - S625 (2017)
- Gicquel, A.; Rose, M.; Vincent, J.-B.; Davidsson, B.; Bodewits, D.; A’Hearn, M. F.; Agarwal, J.; Fougere, N.; Sierks, H.; Bertini, I. ; Lin, Z.-Y.; Barbieri, C.; Lamy, P. L.; Rodrigo, R.; Koschny, D.; Rickman, H.; Keller, H. U.; Barucci, M. A.; Bertaux, J.-L.; Besse, S.; Boudreault, S.; Cremonese, G.; Deppo, V. D.; Debei, S.; Deller, J.; Cecco, M. D.; Frattin, E.; El-Maarry, M. R.; Fornasier, S.; Fulle, M.; Groussin, O.; Gutiérrez, P. J.; Gutiérrez-Marqués, P.; Güttler, C.; **Höfner, S.**; Hofmann, M.; Hu, X.; Hviid, S. F.; Ip, W.-H.; Jorda, L.; Knollenberg, J.; Kovacs, G.; Kramm, J.-R.; Kührt, E.; Küppers, M.; Lara, L. M.; Lazzarin, M.; Moreno, J. J. L.; Lowry, S.;

- Marzari, F.; Masoumzadeh, N.; Massironi, M.; Moreno, F.; Mottola, S.; Naletto, G.; Oklay, N.; Pajola, M.; Preusker, F.; Scholten, F.; Shi, X.; Thomas, N.; Toth, I.; Tubiana, C.: **Modelling of the outburst on 2015 July 29 observed with OSIRIS cameras in the Southern hemisphere of comet 67P/ChuryumovGerasimenko.** *Monthly Notices of the Royal Astronomical Society* 469, 178G (2017)
- **Höfner, S.;** Vincent, J.-B.; Blum, J.; Davidsson, B. J. R.; Sierks, H.; El-Maarry, M. R.; Deller, J.; Hofmann, M.; Hu, X.; Pajola, M. ; Barbieri, C.; Lamy, P. L.; Rodrigo, R.; Koschny, D.; Rickman, H.; Keller, H. U.; A’Hearn, M. F.; Auger, A.-T.; Barucci, M. A.; Bertaux, J.-L.; Bertini, I.; Bodewits, D.; Cremonese, G.; Deppo, V. D.; Debei, S.; Cecco, M. D.; Fornasier, S.; Fulle, M.; Gicquel, A.; Groussin, O.; Gutiérrez, P. J.; Gutiérrez-Marqués, P.; Güttler, C.; Hviid, S. F.; Ip, W.-H.; Jorda, L.; Knollenberg, J.; Kovacs, G.; Kramm, J.-R.; Kührt, E.; Küppers, M.; La Forgia, F.; Lazzarin, M.; Lopez-Moreno, J. J.; Marzari, F.; Michalik, H.; Moissl-Fraund, R.; Moreno, F.; Mottola, S.; Naletto, G.; Oklay, N.; Preusker, F.; Scholten, F.; Shi, X.; Thomas, N.; Toth, I.; Tubiana, C.; Zitzmann, S.: **Thermophysics of fractures on comet 67P/Churyumov-Gerasimenko.** *Astronomy and Astrophysics* 608, A121 (2017)
 - Hu, X.; Shi, X.; Sierks, H.; Fulle, M.; Blum, J.; Keller, H. U.; Kührt, E.; Davidsson, B.; Güttler, C.; Gundlach, B. ; Pajola, M.; Bodewits, D.; Vincent, J.-B.; Oklay, N.; Massironi, M.; Fornasier, S.; Tubiana, C.; Groussin, O.; Boudreault, S.; **Höfner, S.;** Mottola, S.; Barbieri, C.; Lamy, P. L.; Rodrigo, R.; Koschny, D.; Rickman, H.; A’Hearn, M.; Agarwal, J.; Barucci, M. A.; Bertaux, J.-L.; Bertini, I.; Cremonese, G.; Da Deppo, V.; Debei, S.; De Cecco, M.; Deller, J.; El-Maarry, M. R.; Gicquel, A.; Gutierrez-Marques, P.; Gutiérrez, P. J.; Hofmann, M.; Hviid, S. F.; Ip, W.-H.; Jorda, L.; Knollenberg, J.; Kovacs, G.; Kramm, J.-R.; Küppers, M.; Lara, L. M.; Lazzarin, M.; Lopez-Moreno, J. J.; Marzari, F.; Naletto, G.; Thomas, a. N.: **Seasonal erosion and restoration of the dust cover on comet 67P/Churyumov-Gerasimenko as observed by OSIRIS onboard Rosetta.** *Astronomy and Astrophysics* 604, A114 (2017)
 - Pajola, M.; **Höfner, S.;** Vincent, J. B.; Oklay, N.; Scholten, F.; Preusker, F.; Mottola, S.; Naletto, G.; Fornasier, S.; Lowry, S. ; Feller, C.; Hasselmann, P. H.; Güttler, C.; Tubiana, C.; Sierks, H.; Barbieri, C.; Lamy, P.; Rodrigo, R.; Koschny, D.; Rickman, H.; Keller, H. U.; Agarwal, J.; A’Hearn, M. F.; Barucci, M. A.; Bertaux, J.-L.; Bertini, I.; Besse, S.; Boudreault, S.; Cremonese, G.; da Deppo, V.; Davidsson, B.; Debei, S.; de Cecco, M.; Deller, J.; Deshapriya, J. D. P.; El-Maarry, M. R.; Ferrari, S.; Ferri, F.; Fulle, M.; Groussin, O.; Gutierrez, P.; Hofmann, M.; Hviid, S. F.; Ip, W.-H.; Jorda, L.; Knollenberg, J.; Kovacs, G.; Kramm, J. R.; Kührt, E.; Küppers, M.; Lara, L. M.; Lin, Z.-Y.; Lazzarin, M.; Lucchetti, A.; Lopez Moreno, J. J.; Marzari, F.; Massironi, M.; Michalik, H.; Penasa, L.; Pommerol, A.; Simioni, E.; Thomas, N.; Toth, I.; Baratti, E.: **The pristine interior of comet 67P revealed by the combined Aswan outburst and cliff collapse.** *Nature Astronomy* 1, 0092 (2017)
 - Pajola, M.; Lucchetti, A.; Fulle, M.; Mottola, S.; Hamm, M.; Da Deppo, V.; Penasa, L.; Kovacs, G.; Massironi, M.; Shi, X. ; Tubiana, C.; Güttler, C.; Oklay,

- N.; Vincent, J. B.; Toth, I.; Davidsson, B.; Naletto, G.; Sierks, H.; Barbieri, C.; Lamy, P. L.; Rodrigo, R.; Koschny, D.; Rickman, H.; Keller, H. U.; Agarwal, J.; A'Hearn, M. F.; Barucci, M. A.; Bertaux, J. L.; Bertini, I.; Cremonese, G.; Debei, S.; De Cecco, M.; Deller, J.; El Maarry, M. R.; Fornasier, S.; Frattin, E.; Gicquel, A.; Groussin, O.; Gutierrez, P. J.; **Höfner, S.**; Hofmann, M.; Hviid, S. F.; Ip, W. H.; Jorda, L.; Knollenberg, J.; Kramm, J. R.; Kührt, E.; Kuppers, M.; Lara, L. M.; Lazzarin, M.; Moreno, J. J. L.; Marzari, F.; Michalik, H.; Preusker, F.; Scholten, F.; Thomas, N.: **The pebbles/boulders size distributions on Sais: Rosetta's final landing site on comet 67P/Churyumov-Gerasimenko.** *Monthly Notices of the Royal Astronomical Society* 469, pp. 636 - 645 (2017)
- Agarwal, J.; A'Hearn, M. F.; Vincent, J.-B.; Güttler, C.; **Höfner, S.**; Sierks, H.; Tubiana, C.; Barbieri, C.; Lamy, P. L.; Rodrigo, R.; Koschny, D.; Rickman, H.; Barucci, M. A.; Bertaux, J.-L.; Bertini, I.; Boudreault, S.; Cremonese, G.; Da Deppo, V.; Davidsson, B.; Debei, S.; De Cecco, M.; Deller, J.; Fornasier, S.; Fulle, M.; Gicquel, A.; Groussin, O.; Gutiérrez, P. J.; Hofmann, M.; Hviid, S. F.; Ip, W.-H.; Jorda, L.; Keller, H. U.; Knollenberg, J.; Kramm, J.-R.; Kührt, E.; Küppers, M.; Lara, L. M.; Lazzarin, M.; Lopez Moreno, J. J.; Marzari, F.; Naletto, G.; Ockay, N.; Shi, X.; Thomas, N.: **Acceleration of individual, decimetre-sized aggregates in the lower coma of comet 67P/Churyumov-Gerasimenko.** *Monthly Notices of the Royal Astronomical Society* 462, pp. S78 - S88 (2016)
 - Davidsson, B. J. R.; Sierks, H.; Güttler, C.; Marzari, F.; Pajola, M.; Rickman, H.; A'Hearn, M. F.; Auger, A.-T.; El-Maarry, M. R.; Fornasier, S.; Gutierrez, P. J.; Keller, H. U.; Massironi, M.; Snodgrass, C.; Vincent, J.-B.; Barbieri, C.; Lamy, P. L.; Rodrigo, R.; Koschny, D.; Barucci, M. A.; Bertaux, J.-L.; Bertini, I.; Cremonese, G.; Da Deppo, V.; Debei, S.; De Cecco, M.; Feller, C.; Fulle, M.; Groussin, O.; Hviid, S. F.; **Höfner, S.**; Ip, W.-H.; Jorda, L.; Knollenberg, J.; Kovacs, G.; Kramm, J.-R.; Kuehrt, E.; Kueppers, M.; La Forgia, F.; Lara, L. M.; Lazzarin, M.; Lopez Moreno, J. J.; Moissl-Fraund, R.; Mottola, S.; Naletto, G.; Ockay, N.; Thomas, N.; Tubiana, C.: **The primordial nucleus of comet 67P/Churyumov-Gerasimenko.** *Astronomy and Astrophysics* 592, A63 (2016)
 - Gicquel, A.; Vincent, J.-B.; Agarwal, J.; A'Hearn, M. F.; Bertini, I.; Bodewits, D.; Sierks, H.; Lin, Z.-Y.; Barbieri, C.; Lamy, P. L.; Rodrigo, R.; Koschny, D.; Rickman, H.; Keller, H. U.; Barucci, M. A.; Bertaux, J.-L.; Besse, S.; Cremonese, G.; Da Deppo, V.; Davidsson, B.; Debei, S.; Deller, J.; De Cecco, M.; Frattin, E.; El-Maarry, M. R.; Fornasier, S.; Fulle, M.; Groussin, O.; Gutiérrez, P. J.; Gutiérrez-Marqués, P.; Güttler, C.; **Höfner, S.**; Hofmann, M.; Hu, X.; Hviid, S. F.; Ip, W.-H.; Jorda, L.; Knollenberg, J.; Kovacs, G.; Kramm, J.-R.; Kührt, E.; Küppers, M.; Lara, L. M.; Lazzarin, M.; Moreno, J. J. L.; Lowry, S.; Marzari, F.; Masoumzadeh, N.; Massironi, M.; Moreno, F.; Mottola, S.; Naletto, G.; Ockay, N.; Pajola, M.; Pommerol, A.; Preusker, F.; Scholten, F.; Shi, X.; Thomas, N.; Toth, I.; Tubiana, C.: **Sublimation of icy aggregates in the coma of comet 67P/Churyumov-Gerasimenko detected with the OSIRIS cameras on board Rosetta.** *Monthly Notices of the Royal Astronomical Society* 462, pp. S57 - S66 (2016)

- Gicquel, A.; Vincent, J.-B.; Agarwal, J.; A’Hearn, M. F.; Bertini, I.; Bodewits, D.; Sierks, H.; Li, Z.-Y.; Barbieri, C.; Lamy, P. L. ; Rodrigo, R.; Koschny, D.; Rickman, H.; Keller, H. U.; Barucci, M. A.; Bertaux, J.-L.; Besse, S.; Cremonese, G.; Da Deppo, V.; Davidsson, B.; Debei, S.; Deller, J.; De Cecco, M.; Frattin, E.; El-Maarry, M. R.; Fornasier, S.; Fulle, M.; Groussin, O.; Gutierrez, P. J.; Gutiérrez-Marqués, P.; Güttler, C.; **Höfner, S.**; Hofmann, M.; Hu, X.; Hviid, S. F.; Ip, W.-H.; Jorda, L.; Knollenberg, J.; Kovacs, G.; Kramm, J.-R.; Kuehrt, E.; Kueppers, M.; Lara, L. M.; Lazzarin, M.; Lopez Moreno, J. J.; Lowry, S.; Marzari, F.; Masoumzadeh, N.; Massironi, M.; Moreno, F.; Mottola, S.; Naletto, G.; Oklay, N.; Pajola, M.; Pommerol, A.; Preusker, F.; Scholten, F.; Shi, X.; Thomas, N.; Toth, I.; Tubiana, C.: **Sublimation of icy aggregates in the coma of comet 67P/Churyumov-Gerasimenko detected with the OSIRIS cameras on board Rosetta.** *Monthly Notices of the Royal Astronomical Society* 462, pp. S57 - S66 (2016)

- Pajola, M.; Lucchetti, A.; Vincent, J.-B.; Oklay, N.; El-Maarry, M. R.; Bertini, I.; Naletto, G.; Lazzarin, M.; Massironi, M.; Sierks, H. ; Barbieri, C.; Lamy, P.; Rodrigo, R.; Koschny, D.; Rickman, H.; Keller, H. U.; Agarwal, J.; A’Hearn, M. F.; Barucci, M. A.; Bertaux, J.-L.; Boudreault, S.; Cremonese, G.; Da Deppo, V.; Davidsson, B.; Debei, S.; De Cecco, M.; Deller, J.; Fornasier, S.; Fulle, M.; Gicquel, A.; Groussin, O.; Gutierrez, P. J.; Güttler, C.; Hofmann, M.; **Höfner, S.**; Hviid, S. F.; Ip, W.-H.; Jorda, L.; Knollenberg, J.; Kramm, J.-R.; Kuehrt, E.; Küppers, M.; La Forgia, F.; Lara, L. M.; Lee, J.-C.; Lin, Z.-Y.; Lopez Moreno, J. J.; Marzari, F.; Michalik, H.; Mottola, S.; Preusker, F.; Scholten, F.; Thomas, N.; Toth, I.; Tubiana, C.: **The southern hemisphere of 67P/Churyumov-Gerasimenko: Analysis of the preperihelion size-frequency distribution of boulders $\geq 7\text{m}$.** *Astronomy and Astrophysics* 592, L2 (2016)

- Shi, X.; Hu, X.; Sierks, H.; Güttler, C.; A’Hearn, M.; Blum, J.; El-Maarry, M. R.; Kuehrt, E.; Mottola, S.; Pajola, M. ; Oklay, N.; Fornasier, S.; Tubiana, C.; Keller, H. U.; Vincent, J.-B.; Bodewits, D.; **Höfner, S.**; Lin, Z.-Y.; Gicquel, A.; Hofmann, M.; Barbieri, C.; Lamy, P. L.; Rodrigo, R.; Koschny, D.; Rickman, H.; Barucci, M. A.; Bertaux, J.-L.; Bertini, I.; Cremonese, G.; Da Deppo, V.; Davidsson, B.; Debei, S.; De Cecco, M.; Fulle, M.; Groussin, O.; Gutierrez, P. J.; Hviid, S. F.; Ip, W.-H.; Jorda, L.; Knollenberg, J.; Kovacs, G.; Kramm, J.-R.; Küppers, M.; Lara, L. M.; Lazzarin, M.; Lopez-Moreno, J. J.; Marzari, F.; **Naletto, G.**; **Thomas, N.**: **Sunset jets observed on comet 67P/Churyumov-Gerasimenko sustained by subsurface thermal lag.** *Astronomy and Astrophysics* 586, A7 (2016)

- Vincent, J.-B.; A’Hearn, M. F.; Lin, Z.-Y.; El-Maarry, M. R.; Pajola, M.; Sierks, H.; Barbieri, C.; Lamy, P. L.; Rodrigo, R.; Koschny, D. ; Rickman, H.; Keller, H. U.; Agarwal, J.; Barucci, M. A.; Bertaux, J.-L.; Bertini, I.; Besse, S.; Bodewits, D.; Cremonese, G.; Da Deppo, V.; Davidsson, B.; Debei, S.; De Cecco, M.; Deller, J.; Fornasier, S.; Fulle, M.; Gicquel, A.; Groussin, O.; Gutierrez, P. J.; Gutiérrez-Marqués, P.; Güttler, C.; **Höfner, S.**; Hofmann, M.; Hviid, S. F.; Ip, W.-H.; Jorda, L.; Knollenberg, J.; Kovacs, G.; Kramm, J.-R.; Kuehrt, E.; Kueppers, M.; Lara, L. M.; Lazzarin, M.; Lopez Moreno, J. J.; Marzari, F.; Massironi, M.; Mottola,

- S.; Naletto, G.; Oklay, N.; Preusker, F.; Scholten, F.; Shi, X.; Thomas, N.; Toth, I.; Tubiana, C.: **Summer fireworks on comet 67P**. *Monthly Notices of the Royal Astronomical Society* 462, pp. S184 - S194 (2016)
- Vincent, J.-B.; Oklay, N.; Pajola, M.; **Höfner, S.**; Sierks, H.; Hu, X.; Barbieri, C.; Lamy, P.; Rodrigo, R.; andand H. Rickman, D. K. ; Keller, H. U.; A'Hearn, M.; Barucci, M. A.; Bertaux, J.-L.; Bertini, I.; Besse, S.; Bodewits, D.; Cremonese, G.; Deppo, V. D.; Davidsson, B.; Debei, S.; Cecco, M. D.; El-Maarry, M. R.; Fornasier, S.; Fulle, M.; Groussin, O.; Gutiérrez, P. J.; Gutiérrez-Marqués, P.; Güttler, C.; Hofmann, M.; Hviid, S. F.; Ip, W.-H.; Jorda, L.; Knollenberg, J.; Kovacs, G.; Kramm, J.-R.; Kührt, E.; Küppers, M.; Lara, L. M.; Lazzarin, M.; Lin, Z.-Y.; Moreno, J. J. L.; Lowry, S.; Marzari, F.; Massironi, M.; Moreno, F.; Mottola, S.; Naletto, G.; Preusker, F.; Scholten, F.; Shi, X.; Thomas, N.; Toth, I.; Tubiana, C.: **Are fractured cliffs the source of cometary dust jets? Insights from OSIRIS/Rosetta at 67P**. *Astronomy and Astrophysics* 587, A14 (2016)
 - El-Maarry, M. R.; Thomas, N.; Gracia-Berna, A.; Marschall, R.; Auger, A.-T.; Groussin, O.; Mottola, S.; Pajola, M.; Massironi, M.; Marchi, S. ; **Höfner, S.**; Preusker, F.; Scholten, F.; Jorda, L.; Kührt, E.; Keller, H. U.; Sierks, H.; A'Hearn, M. F.; Barbieri, C.; Barucci, M. A.; Bertaux, J.-L.; Bertini, I.; Cremonese, G.; Da Deppo, V.; Davidsson, B.; Debei, S.; De Cecco, M.; Deller, J.; Güttler, C.; Fornasier, S.; Fulle, M.; Gutierrez, P. J.; Hofmann, M.; Hviid, S. F.; Ip, W.-H.; Knollenberg, J.; Koschny, D.; Kovacs, G.; Kramm, J.-R.; Küppers, M.; Lamy, P. L.; Lara, L. M.; Lazzarin, M.; Lopez Moreno, J. J.; Marzari, F.; Michalik, H.; Naletto, G.; Oklay, N.; Pommerol, A.; Rickman, H.; Rodrigo, R.; Tubiana, C.; Vincent, J.-B.: **Fractures on comet 67P/Churyumov-Gerasimenko observed by Rosetta/OSIRIS**. *Geophysical Research Letters* 42 (13), pp. 5170 - 5178 (2015)
 - Guilbert-Lepoutre, A.; Besse, S.; Mousis, O.; Ali-Dib, M.; **Höfner, S.**; Koschny, D.; Hager, P.: **On the Evolution of Comets**. *Space Science Reviews* 197, pp. 271 - 296 (2015)
 - Vincent, J.-B.; Bodewits, D.; Besse, S.; Sierks, H.; Barbieri, C.; Lamy, P.; Rodrigo, R.; Koschny, D.; Rickman, H.; Keller, H. U. ; Agarwal, J.; A'Hearn, M. F.; Auger, A.-T.; Barucci, M. A.; Bertaux, J.-L.; Bertini, I.; Capanna, C.; Cremonese, G.; Da Deppo, V.; Davidsson, B.; Debei, S.; De Cecco, M.; El-Maarry, M. R.; Ferri, F.; Fornasier, S.; Fulle, M.; Gaskell, R.; Giacomini, L.; Groussin, O.; Guilbert-Lepoutre, A.; Gutierrez-Marques, P.; Gutierrez, P. J.; Güttler, C.; Hoekzema, N.; **Höfner, S.**; Hviid, S. F.; Ip, W.-H.; Jorda, L.; Knollenberg, J.; Kovacs, G.; Kramm, R.; Kührt, E.; Küppers, M.; La Forgia, F.; Lara, L. M.; Lazzarin, M.; Lee, V.; Leyrat, C.; Lin, Z.-Y.; Lopez Moreno, J. J.; Lowry, S.; Magrin, S.; Maquet, L.; Marchi, S.; Marzari, F.; Massironi, M.; Michalik, H.; Moissl, R.; Mottola, S.; Naletto, G.; Oklay, N.; Pajola, M.; Preusker, F.; Scholten, F.; Thomas, N.; Toth, I.; Tubiana, C.: **Large heterogeneities in comet 67P as revealed by active pits from sinkhole collapse**. *Nature* 523 (7558), pp. 63 - 66 (2015)
 - Vincent, J.-B.; Oklay, N.; Marchi, S.; **Höfner, S.**; Sierks, H.: **Craters on comets**. *Planetary and Space Science* 107, pp. 53 - 63 (2015)

Conference Proceedings

- **Höfner, S.;** Vincent, J.B.; Sierks, H.; Blum, J.: *A Numerical Modeling Approach to Cometary Nucleus Surface Roughness Determination* (oral), European Planetary Science Congress 2013, University College London, UK, September 8-13, 2013
- **Höfner, S.;** Vincent, J.B.; Sierks, H.; Blum, J.: *Thermal wave and geomorphologic features on cometary nuclei* (oral), Asteroids Comets Meteors 2014, Helsinki, June 30-July 5, 2014
- **Höfner, S.;** Vincent, J.B.; Sierks, H.; Jorda, L.; Blum, J.: *Where do we expect activity on 67P/CG? A thermo-physical point of view* (poster), European Geosciences Union General Assembly, Vienna, Austria, April 12-17, 2015

Acknowledgements

The acknowledgements are not included in the online version.

Curriculum Vitae

The curriculum vitae is not included in the online version.